Rationale Design of Up-Converting Inorganic Nanoparticles Towards Advanced Optical Applications

Ph.D. student: Fabrizio Guzzetta

Thesis Director and Supervisor: Beatriz Julián-López

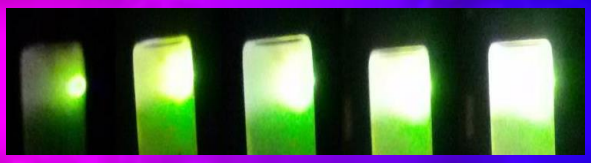

Julio 2018

UNIVERSITAT JAUME·I

Programa de Doctorado en Ciencias

Escuela de Doctorado de la Universitat Jaume I

Rationale Design of Inorganic Up-Converting Nanoparticles Towards Advanced Optical Applications

---

Memoria presentada por Fabrizio Guzzetta para optar al grado de doctor por la Universitat Jaume I

Fabrizio Guzzetta

Prof. Beatriz Julián-López

Castellón de la Plana, Julio 2018

- F.G. would like to thank the **Generalitat Valenciana** for the **"Santiago Grisolía" Scholarship** (GRISOLIA/2014/018) for funding the Ph.D. position that has permitted carry out the research.
- F.G. would like to thank the **Gonel-Balaguer Hermanos Foundation** from the **Universitat Jaume I** and the **COST Action MP 1202: Rational design of hybrid organic-inorganic interfaces (HINT)** for the economical contributions as a scholarship and stipend, towards the short stay at the Université Pierre et Marie Curie in Paris that has permitted to promote high impact research partnerships between the Instituto de nanomaterials Avanzados (INAM-UJI), Química Inorgánica y Órganica department and UJI as institution and the former.
- F.G. would like to thank the **COST Action MP 1202: Rational design of hybrid organic-inorganic interfaces (HINT)** for financing in form of scholarship the COST school "*Bottom - up approaches of hybrid materials: preparation and design*", held at the Jozef Stefan Institute, in Ljubljana, Slovenia, 26-28/05/2015.

"The principles of physics, as far as I can see, do not speak against the possibility of maneuvering things atom by atom.
It is not an attempt to violate any laws; it is something, in principle, that can be done, but in practice it has not been done because we are too big."

Richard P. Feynman (1959)

A me stesso, per la forza che ho avuto a rialzarmi

A mia moglie Ana Cecilia, che ha avuto la forza di aspettarmi

Alla mia famiglia, che non ha mai smesso di aiutarmi

This work (2014-2018) is dedicated to my family, which moral and sometimes financial support has been of great help in difficult moments, to my wife Ana that had the patience to wait for this day to happen and to me, who, after a long time of sacrifices and depression, finally realize this dream. It is also dedicated to all the people who encouraged me not to give up, starting from my thesis director, Beatriz Julián-López.

Acknowledgements

This work, outcome of a three years journey in a wonderful part of Spain, has been carried out by me. However, as always, it could not be done without the help of people both in the private and in the working life that helped me growing both as a man and as a professional. Therefore, here there is a list of persons that I want to thank. First of all I want to thank – equally – my family, dad (Salvatore), mum (Vincenza), brother (Giorgio), my wife (Ana Cecilia), and my thesis director, Beatriz Julián-López to have given me this opportunity and to have believed in me when no one would have bet a penny in my favor. Furthermore I want to thank my advisor to have helped me in understanding the academic world far better than I previously did and to have been present both in my academic and private life as a friend. Secondly I want to thank the Generalitat Valenciana, from which I have benefitted economically these three years through a Grisolía doctoral scholarship. I want to thank the personnel at the Servicio Central de Instrumentación Científica whose friendship and technical knowledge has helped me in achieving the amazing results presented in this manuscript, especially since I was coming from a different scientific background. I thank them both for their professional advice, troubleshooting abilities and friendship along these years. I want to thank all the professors, researchers and student I have met along the way at the Instituto Universitario de Nanomateriales Avanzados (INAM) within the Universitat Jaume I, in particular my friends Francisco y Fernando, who were my labmates that introduced me to this new chapter in my scientific production and professors Juan Miravet and Francisco Honrubia at the department of Organic and Inorganic Chemistry for their collaboration to the formation of the soft-matter hybrids. Beyond the Universitat Jaume I, I want to thank, in particular Prof. Anna Roig Serrá and Ramón y Cajal researcher Anna Larromaine, at the Instituto de Ciencia de Materiales de Barcelona – Consejo Superior de Investigación Científica (ICMAB-CSIC) and Niki Baccile and all the others at the Université Pierre et Marie Curie (UPMC) and Bruno Viana at the Ecóle Nationale Superieur de Chemie for their help with the experiments and projects during my 3 and a half months stay in Paris, thanks to whom I have learnt a lot on microwave synthesis and with whom I have established a relation based on cordiality and mutual respect, both for their scientific production and for the moral and kindness behavior in my regards. Thanks to them we achieved very interesting results that will soon be published in highly ranked journals, helping me in building a reliable and strong

academic reputation, along with my supervisor. I do not want to forget all the other wonderful people I have met in these years in Castellón, that I am proud to call friends, and which are a list so long that I beg pardon if I forget some of them. Ana Sandhy to be such a good friend who has always been present when things were not so clear and when my wife had health problems, Sulejman and Mercedes, Francesco, a friend that is like my brother here in Castellón, Melín (Amelia), Carles, Carlos, Gabi, Viktorija, Saturday, Prisca, Elvin, Nuno, Marco, Tuyen, Sandheep, Andy, (to be such a good friend and advisor, who with his family has taken a good care of us), Rob, Yvonne, Tahiri, Ernestina and all the other people that has been with us showing their care and their sympathy toward me (and my wife) all these years. To all of them there is a big Thank You from my heart, and all of you have a special place in my life.

¡¡¡Y ahora… que empiece la fiesta!!!

Index

Chapter 1 – *"Up-converting Nanophosphors: An Introduction"*

Chapter 2 – *"Rationalizing Crystals Size and Phase: Impact of Several Reaction Parameters on the Solvothermal Synthesis of $NaYF_4$:Yb,Ln"*

Chapter 1

Up-converting Nanophosphors: An Introduction

1.1 Introduction

The visionary quote *"[there] is plenty of room at the bottom"*, by Feynman, at the American Physical Society annual meeting,[1] challenged scientists to pursue new synthetic routes to limit condensed matter size at the nanoscale, and engineers to design nanotechnology-based life-easing devices. The exponential growth of nanotechnology has paved the road for industrial marketing of nanomaterials through new, smaller sized, thinner designed, and more powerful devices than the previous generations (43 nanomaterials in 1,680,392 articles, 177,083 patents and 2,919 products. Source: http://statnano.com/nanomaterials). These devices exhibit better performances with respect to previous generations due to the exploitation of nanomaterials' peculiar properties[2].

The development of nanomaterials spans for 30 years now; however, there is still an increasing demand in many areas of technological interest with universities designing specific groups devoted to the technological development of nanomaterials. For example, groups that work on specific nanomaterials preparations and functionalization towards applications to optics and photonics (https://www-png.materials.ox.ac.uk/), magnetism (https://nanomag.stanford.edu/), electronics (https://www.ecs.soton.ac.uk/research/nano), electrochemistry and, catalysis (http://www.nce.ulg.ac.be/), biology, biochemistry and medicine (https://www.chemistry.ucla.edu/materials-and-nanoscience, http://imsat.org/CBN.htm), have been born. New fields have arisen combining properties for the same class of nanomaterials, and so fields such as *optronics* (optics and electronics), *magnetronics* (magnetism and electronics), and so on, have been born. These new fields are at the core of quantum computing because of their ease of manipulating atomic spins[3] and have the aim to output more performing, smaller and more powerful computers.

The *"nano"*-revolution has led to a complete change in the fabrication processes, in an attempt to reduce environmental contamination[2,4,5], to make smaller sized devices, to moderate production costs[5] and to offer materials with new functionalities. A glance at the vast library of technical articles and at the number of patents related to the nano world, shows how much technology and science has improved, year by year, in the last decades. However, even if science has gone far in preparing nanomaterials and understanding their properties, still there is so much ahead to do: in fact, new skillful synthetic strategies must be used to manipulate matter to obtain high quality and quantity of nanomaterials with improved properties or showing new physical phenomena. These studies are directed towards understanding the formation of

materials and rationalizing their nucleation and growth, relating crystal structure and size with physical properties, and to their applications, which, indirectly leads to the discovery of new ground-breaking technologies which are changing the game's rules by the day (http://statnano.com/nanomaterials).

1.2 Nanomaterials: a brief overview

Nanomaterials are not visible to the naked eye: the term 'nano' (from Greek term 'νάνος') -meter means one billionth (10^{-9}) of a meter, which is far beyond our reachable vision limit. These materials are so small that they can be seen only under electron microscopes. As seen in Figure 1.1, (http://www.akronascent.com/tech-blog/nanoscale1, © Akronascent, 2017) nanoscale matter sizes are comprised between 1 and 1000 nm (1 μm), with a broad distribution that peaks around 100 nm (http://ec.europa.eu/environment/chemicals/nanotech/faq/definition_en.htm).
However, despite their small dimensions, their properties can be effectively studied by science -and applied in new technologies-, with the aim of maximizing their efficiency or proposing new device designs and increased performances.

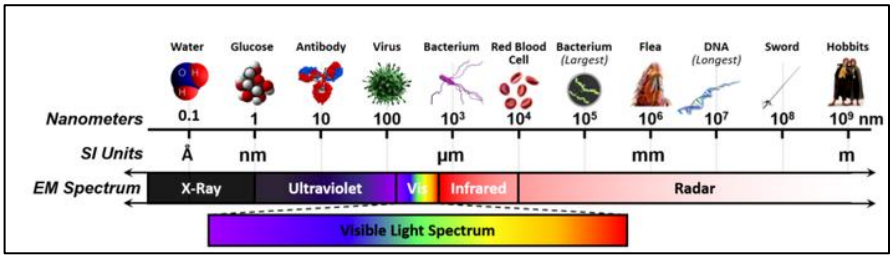

Figure 1.1: Different sizes of matter

The ultra-small sizes show large surface to volume ratios (http://www.trynano.org/nanomaterials/quantum-dots), which makes their physical properties unique and different from bulky systems. Size effects constitute a fascinating aspect of nanomaterials and have direct consequences on the evolution of structural, thermodynamic, electronic, spectroscopic, electromagnetic and chemical features of these finite systems with increasing size. Confinement of matter to a nanometric scale leads to altered crystal structures and highly defective surfaces[6,7] (Figure 1.2), which, in turn, determine their physical properties[8].

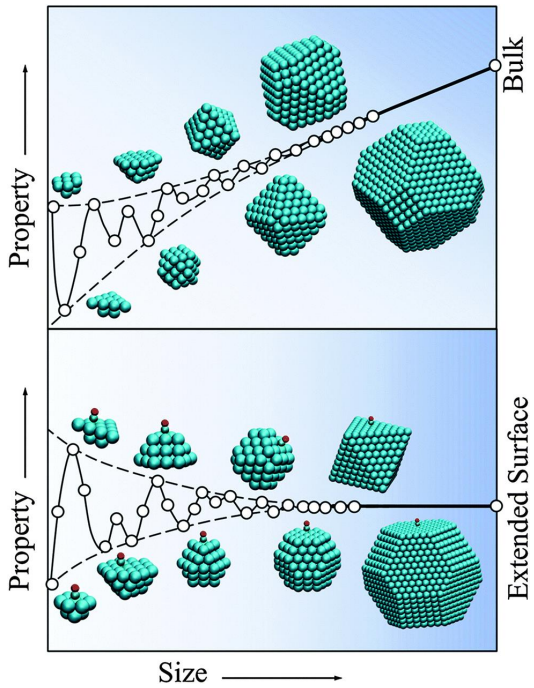

Figure 1.2: Variation of an arbitrary property with the nanoparticle size either towards the bulk (top panel) or towards the extended surface limit (bottom panel), illustrating the scalable and non-scalable regimes. Adapted from Viñes et al.[6].

Such structural alterations underlie the quantum effects[9] responsible for the new features that are visible only at the nanoscale (see Figure 1.3, http://www.akronascent.com/tech-blog/nanoscale2, © Akronascent, 2017, and https://nanocomposix.eu/pages/gold-nanoparticles-optical-properties, © Nanocomposix, 2017). The physical strengths of nanomaterials over bulky materials allow versatility for their embedding in a number of life-changing applications.

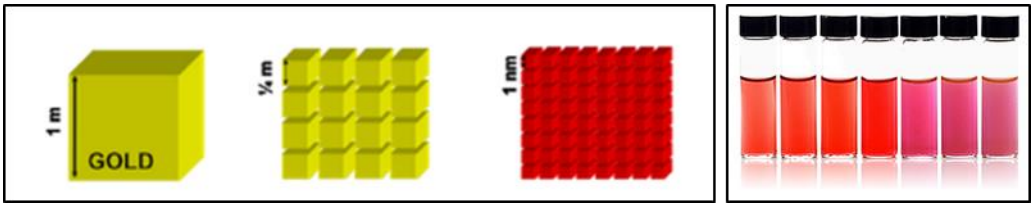

Figure 1.3: (Left) Bulk *vs* nano gold. (Right) The gold nanoclusters lose their bright yellow color and exhibit reddish tones, from red to violet depending on the size, local refractive index and aggregation of the nanoclusters.

1.2.1 Nanomaterials' dimensions

Nanomaterials may be zero-dimensional (0D), one-dimensional (1D), two-dimensional (2D) and three-dimensional (3D).

- 0-D nanomaterials are materials which present an isotropic growth and an overall geometrical shape such as sphere, polyhedral, prisms, stars, etc…[10–12] (Figure 1.4).

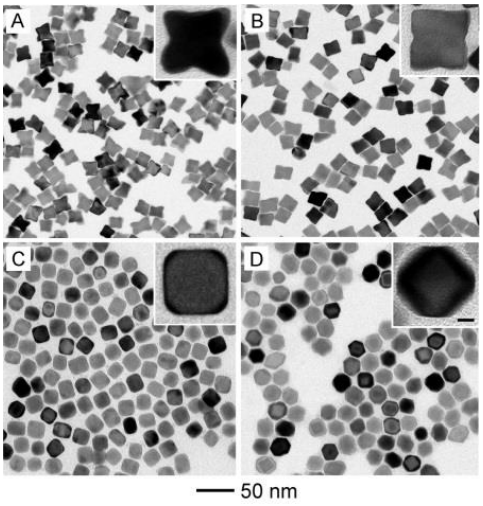

Figure 1.4: different shapes of 0D-nanomaterials (reprinted from Xia et al. [13])

- 1-D nanomaterials present an anisotropic growth in one direction, and properties directionally dependent. Nanotubes[14], nanorods[15] and nanowires[16] are part of this family of nanomaterials (Figure 1.5).

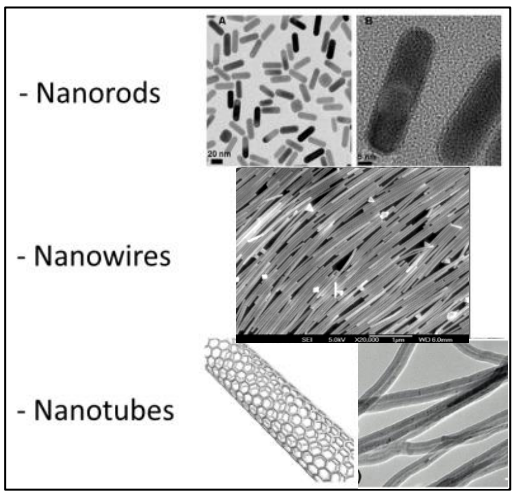

Figure 1.5: Differences between nanorods[17], nanowires (image adapted from Tao et al.[18]) and nanotubes **left:** computer drawing of a nanotube (http://www.3dchem.com/Buckytube.asp), **right:** image adapted from Laurila[19] ,. The aspect ratio (longitudinal size *vs* latitudinal size) increases exponentially from nanorods to nanotubes.

- 2-D nanomaterials are generally composed of mono- or bi- layers of planar systems. Graphene[20] is a good example of 2-D nanomaterial (Figure 1.6).

Figure 1.6: graphene sheet (topview) by James Hedberg / CC BY-NC-SA 3.0

- A recent discovery is that DNA strands help in the formation of 3-D nanoarchitectures of stacked nanoparticles, with ordered and organized helicoidal arrangements[21,22]. These organized 3-D architectures present novel properties, which differ from the nanoparticles alone or in dispersion[22] (Figure 1.7).

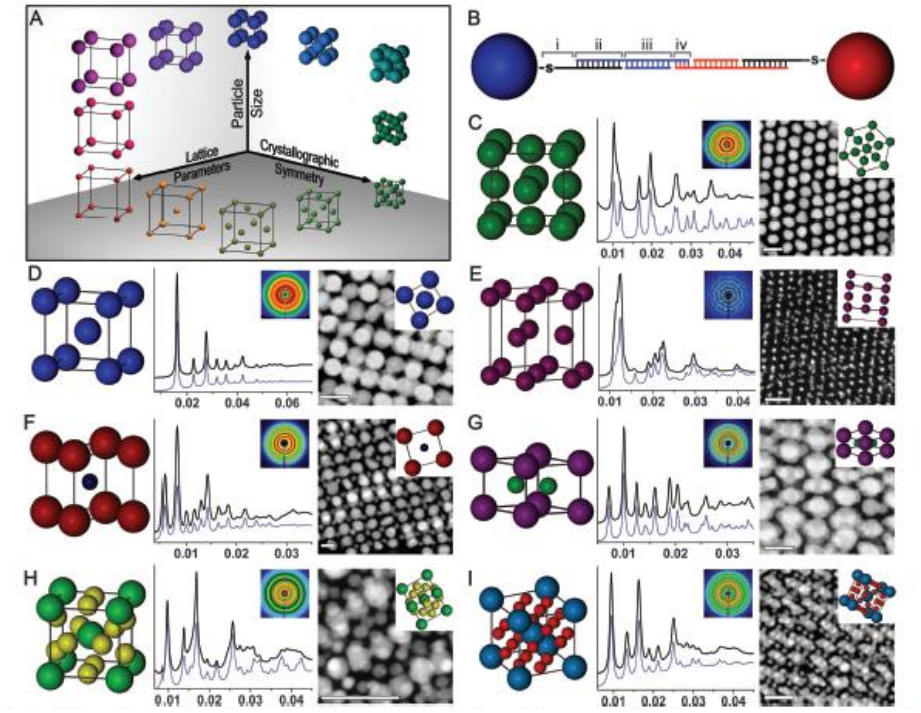

Figure 1.7: Nanoparticles-based superlattices that change their configuration upon the DNA strands covering their surface. Adapted from Macfarlane et al.[22]

0-D nanomaterials can be synthesized in a manifold of different shapes. Different geometries and sizes are important for the tuning of their physical properties[23]. The case depicted in Figure 1.8, shows gold nanoparticles prepared in water/organic media, with PVP (polyvynilpirrolidone). The difference in the organic solvent drives the binding of the polymer to different gold seed sites and the light absorbance is strongly affected[23].

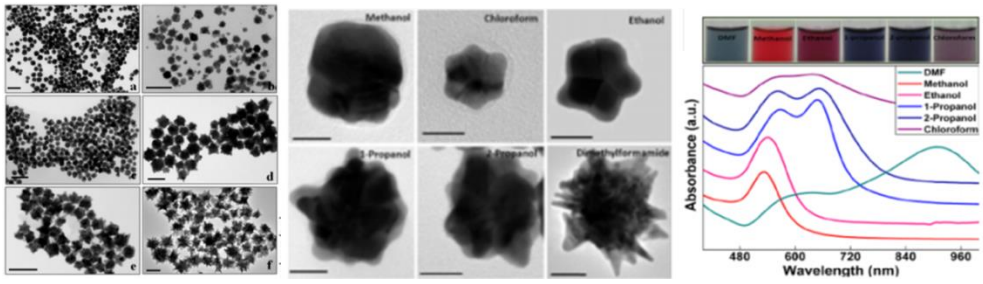

Figure 1.8: (Left) TEM images (scale bar = 100 nm) of as-prepared anisotropic Au nanoparticles in different solvents **(a)** methanol, **(b)** chloroform, **(c)** ethanol, **(d)** 1-propanol,

(e) 2-propanol, and **(f)** dimethylformamide; **(center)** high magnification (scale bar = 20 nm) TEM images; **(right)** UV-Vis spectra for the various Au nanoparticles and their respective color when dispersed in solution. Adapted from Kedia et al.[23].

Synthesizing a definite crystal structure, with nano-sized dimensions, and with a definite geometry is not an easy task. The correlation between the physical properties and the geometrical constraints (crystal phase, size and geometry of the crystals) sometimes can be rationalized, to certain extents, upon a model of nucleation and growth, especially in seed-mediated nanoparticles synthesis[24]. The crystal seeds and short radius nanoparticles, once formed, will grow in order to reduce or minimize lattice energy. The growth of the crystal up to a desired size/shape permits, in turn, modulation of the physical properties[23]. However, the shorter the diameter of the nanoparticle, the more defective its surface will be and this increases the surface energy of the crystal,[6] making the crystals more reactive and more prone to coalescence while aging.

The general model of nucleation and growth of inorganic 0-D nanomaterials is the so-called Ostwald ripening. IUPAC define the process as the *"dissolution of small crystals or sol particles and the redeposition of the dissolved species on the surfaces of larger crystals or sol particles"* [25].

The process occurs because smaller particles, presenting a predominant surface over the spherical volume, suffer from higher surface energy, in comparison with single crystal systems or larger particles. This surface energy of the particles increases the overall Gibbs energy of the bulk nanoparticle that leads to an apparent higher solubility, since solvation helps diminish the overall energy.[24]

In polyphasic systems, crystals can nucleate in one crystal lattice and, at a certain radius, thermodynamics takes over and the lattice rearranges into a more stable crystalline structure.[26] These structural changes depending on the crystal size (and shape) in polyphasic nanomaterials are very hard to model. Nonetheless, a number of models for nucleation and growth of nanomaterials have been built in an effort to describe this behavior[24,27].

It is also common that an *epitaxial* growth takes place to reduce the crystal lattice energy. In 0-D nanocrystals, one (or some) facets can concentrate residual energy, thus promoting atom stacking over those over-energized facets. These high-energy crystal planes promote an anisotropic growth, leading to 1-D (nanorods, nanotubes…)

or more complex (octapods, nanoflowers, nanostars…) structures, depending on the preferential directions of growth (Figure 1.9).[28]

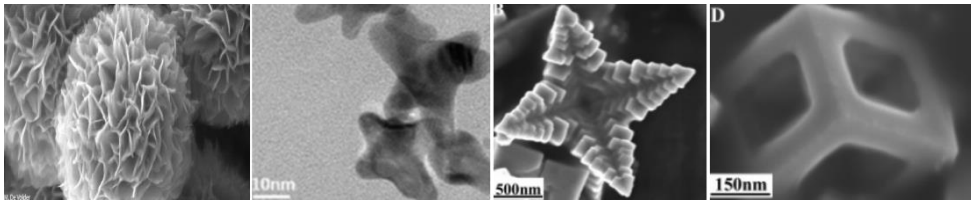

Figure 1.9: From left to right: TiO_2 Nanoflowers (adapted from https://www.nanomanufacturing.eng.cam.ac.uk/NanoScapes/Others/tio2-nanoflowers.jpg); nanostars[29], octapods and hollow cubes[30].

The complex physicochemical processes involved in the formation and growth of nanocrystals deserve more efforts towards the design of the nanomaterials and enforce rationale synthetic routes towards the desired size, crystal phase and final properties[10,11]. However, since the reaction conditions drastically affect the crystal lattice stabilities, the sizes and geometries of the crystals (*polymorphs*) for a defined material composition, these studies become fundamental for drawing more exact phase diagrams, associating geometric constraints to a lattice type and describing, this way, crystal phase evolution in dependence of reaction conditions and parameters.[13,23,26,30,31].

1.2.2 Synthetic approaches on the formation of nanomaterials

Two main approaches are used in the preparation of nanomaterials: top-down and bottom-up (Figure 1.10) [32]. The first approach is to prepare nanomaterials by removing matter from larger blocks: it is an iterative synthetic route that is carried out until the desired size is achieved. Generally, this kind of approach makes use of physical synthetic techniques such as milling, crushing, laser ablation, and so on, and produce nanomaterials which suffer from contamination, lower crystallinity and high polydispersity[33]. Moreover, frequent maintenance of instrumentations or long synthetic times are generally required for the physical processing of materials.

In contrast with top-down approaches, bottom-up approaches begin at the atomic scale and build up structures. To spatially limit the growth at the nanoscale several synthetic strategies[33] using chemical routes such as sol-gel[34], thermal decomposition [35], hydro- or solvothermal[36,37], self-assembly[38], electrodeposition[39,40] and microwave-assisted techniques[41] are widely employed in the preparation of nanomaterials, These synthetic methods require careful manipulation of the precursor solutions for limiting

growth, such as the use of very diluted solutions[42], high boiling solvents[43], the preparation of bulky precursors,[37] and complexes [44,45], and/or emulsions (W/O mostly)[46,47].

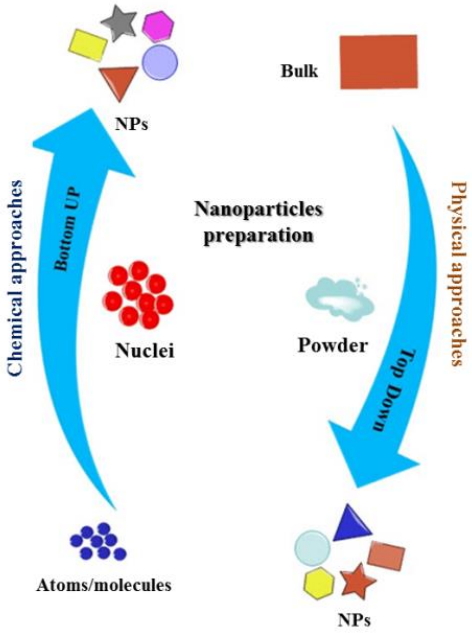

Figure 1.10: Top-down versus bottom-up approaches for the preparation of nanomaterials, adapted from Ovais et al.[32]

Chemical methods offer several advantages over the physical ones because the bottom-up approach produces nanostructures with better uniformity and quality (less defects, homogeneous composition, short- and long-range ordering…). Furthermore, the chemical methods can be industrially scalable for economically feasible mass production [32,33].

In fact, in order to engineer matter at the nanoscale, chemical synthetic bottom-up strategies make use of assemblies of smaller subunits, which are composed of labile complexes of the metal ions that will constitute the inorganic core of the nanomaterials. These precursors are building blocks around which the crystal generates[37,42–44,46].

Nevertheless, the bottom-up approach for the synthesis of nanomaterials is not exempted from certain, intrinsic drawbacks of the chemical processing:

agglomeration, [48] polycrystallinity of solids (most of the time)[49], and byproduct contamination[50], are some of the difficulties met in building up nanostructures.

To avoid such drawbacks, and in an effort to purify reaction products, as well as to preserve physical qualities of the nanomaterials, surface modification is usually performed. These strategies are devoted to the maintenance (or improvement) of the physical properties [51] while maintaining small crystal size (or slightly larger) and avoid coalescence[48].

1.2.3 Nanomaterials surface modification strategies

Nanomaterials can be both organic[52–55] and inorganic in nature[26,30,56–58]; however, most frequently, nanomaterials are composed of an inorganic core and an organic (surfactant) shell[59–61]; that permits ease of dispersion in a range of solvents. The surfactant shell, most of the time, does a poor job in protecting the core of the nanomaterial as this degrades over time. Due to the fast degradation of surfactants, the shelf life of nanomaterials is limited due to coalescence and aging, ease of contamination, aggregation of the nanomaterials and high polydispersity around a central size. However, very few reports have described this behavior.[62]These drawbacks limit their dispersability in solvents[62] and dim the unique physical phenomena of the nanomaterials, making bulkier materials and changing their physical properties.[62] Generally, surfactant-based organic layers are more soluble in organic solvents rather than water; however, some polymers, such as polyethyleneglycol (PEG)[63], polyvynilpirrolidone (PVP)[64], polyacrilic acid (PAA)[65] are water soluble and, as a plus, present low or mild toxicity. Therefore, in view of bio-medical, phytologic and pharmaceutical applications of nanomaterials, biocompatible polymers are commonly used to coat the surfaces in order to switch from hydrophobic to hydrophilic ones. Moreover, it has been shown that the chemical nature of the surfactant has a direct impact on the physical properties of the nanomaterials[60]. To resolve these and other issues, responsible for masking the full potential of nanomaterials, manipulation of these external shells permits:

a) Switching from hydrophobic to hydrophilic surfaces (and vice versa)[66,67]
b) Limiting nanomaterial growth, aggregation and coalescence[68,69]
c) Maintaining, improving or modulating physical properties[59,60] (see Figure 1.11)

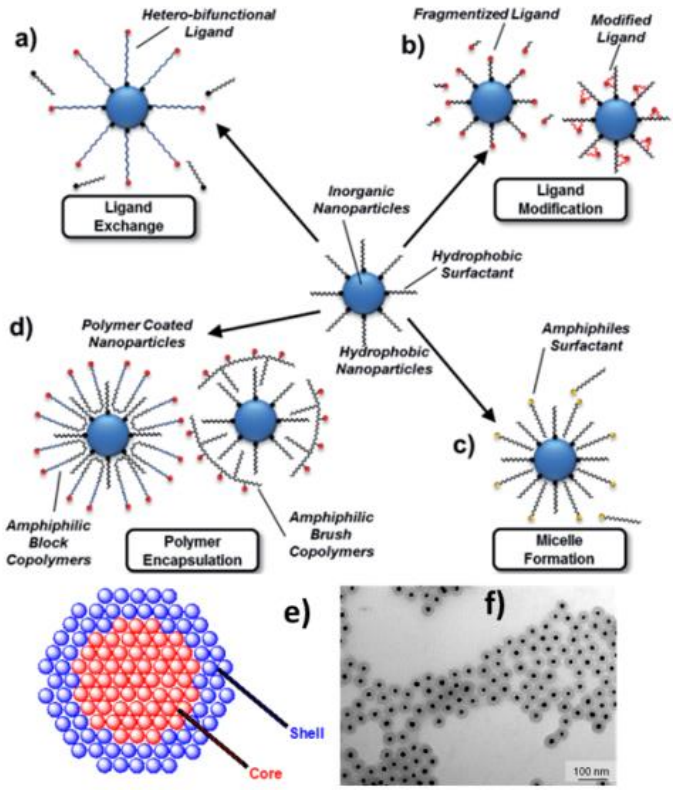

Figure 1.11: Ligand modification/replacement strategies **(a-d)**: **a)** Ligand Exchange, **b)** Ligand Modification, **c)** Micelle Formation and **d)** Polymer Encapsulation;[70] **e)-f)**: Core-Shell schematization of a nanoparticle (adapted from By Akcook8 - Own work, CC BY-SA 3.0) and core-shell nanoparticles relative TEM image (http://www.hiqnano.com/products/silica-nanoparticles-2/core-shell-silica-nanoparticles/) respectively.

Thanks to the possibility of manipulating the external shell, chemical reactions on the surfactant systems are performed with the nanomaterials' fate in mind. Indeed surface modification is used generally to protect the core, to magnify its unique properties.[71]

Efforts to modify the external layers of nanomaterials have led to a relatively large number of chemical manipulations and techniques (see Figure 1.12): ligand chemical modification **(A)**, ligand exchange **(B)** as well as core-shell procedures **(C)**.

(A) When prepared in inverse emulsions[46–48], inorganic nanomaterials are generally prepared with a layer of water-insoluble molecules. In an effort to make the former water soluble, one of the strategies is to chemically modify the water

insoluble layer with surgical-precision manipulations (such as chemical oxidation). However, these techniques suffer from heavy solid by-product formation and so the unavoidable contamination of the nanomaterials, [66]which results in a reduced product recovery yield.

(B) Ligand exchange is a formidable technique to convert water-insoluble nanoparticles into water soluble ones. This technique is based on the solubility of the two different ligands in polar and non-polar solvents. Relatively high temperatures and long times are generally required to reach a complete conversion of the ligand on the nanoparticle surface[72,73]. This process is a multi-step one: therefore, the first step is to remove the weakly adsorbed ligand, which leaves the nanoparticle naked, and a successive substitution of the reactive nanoparticle with the desired ligand.

(C) Grafting foreign or matrix-based inorganic layers[28,69,73,74] on nanoparticle surfaces prevent the core nanoparticle from fast growth, aggregation or coalescence with neighboring nanoparticles, keeping[59,60] or magnifying [71] the desired physical properties. Building one or more *shells* of inorganic materials around a central core (*core-shell* technique)[69], permits: **a)** maintenance of physical properties, **b)** modulation of the physical properties[75,76] and **c)** addition of external physical properties for dual-mode nanoparticle preparation[77]. The physical properties and the size of the shell(s) mainly depend on the fate of the nanoparticles, and also are strongly related to its (or theirs) chemical nature or composition(s)[78–81].

These techniques will be further discussed and in a deeper fashion when applied to the main argument of this manuscript, to up-converting nanoparticles (UCNPs).

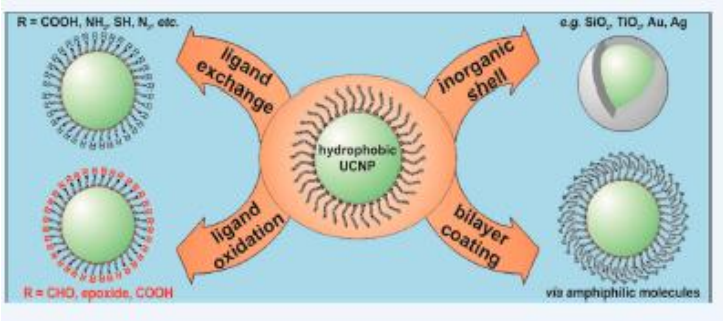

Figure 1.12: Scheme of hydrophobic-to-hydrophilic surface switching techniques through surfactant layer chemical manipulation in UCNPs.[66]

1.3 Optically active nanomaterials

The global optic and photonics market size was quoted as 450 Billion dollars in 2015, and has an estimated forecast of 725 Billion dollars by 2021 (http://www.marketsandmarkets.com/Market-Reports/photonics-market-88194993.html?gclid=CKP76uuzsNMCFdVAGwodBrQD4Q) and expanding to 980 Billion dollars by 2024 (http://www.grandviewresearch.com/press-release/global-photonics-market). This huge economic forecast (about 38% increment in 6 years and more than double in 9 years) makes the quest for high-quality, optically active, nanomaterials alluring in both academic and industrial fields are discovered every day. Literature on optically active nanomaterials and related optical and photonic effects is very rich and intriguing[44,60,66,75,77–81]. With this perspective, an increasing number of research groups are working on bio-medical, pharmaceutical and technological applications of optical nanomaterials[17,67,82–84]. In industry, optical nanotechnology has permitted a change in labor habits, i.e. the use of more and more sophisticated computers with unprecedented resolution and definition of the images; optical nanotechnology has been used in the industrial manufacture in a multitude of devices, from high-resolution, high definition TV and computer screens, medical imaging instruments, optically activated hard drives, touch-screen devices and smart displays, etc. Furthermore, optically active nanotechnology has been used in energy harvesting devices (photovoltaic[85–88], solar fuel[89,90]), and sensing[91,92].

Despite the large number of discoveries and new-marketed devices, optics- and photonics-based nanotechnology is showing an ever-increasing rate of turnover, due to the fast discoveries in new optical phenomena. Solar light conversion is one of the most quoted themes in literature. Nanostructures are helping in harvesting a larger part of the solar spectrum beyond the visible photons, (1) providing a large surface area to boost the electrochemical reaction[89,93] or molecular and hybrid (i.e. composite materials of an organic matrix embedding inorganic nanocrystals) light harvesting systems[38,94–96], (2) generating optical effects to improve optical absorption (for energy harvesting) and energy conversion in solar cells in effort to gain high efficiency, and (3) giving rise to high crystallinity and/or porous structures for photoelectrochemical sensing[91,92].

For example, semi-conducting crystals may have a two-way employment: irradiation with light sources of energies similar to their bandgap[97] permits electrons to jump from the valence band to the conduction band, giving out a photocurrent.

Additionally, a current higher or equal to the bandgap can be provided to such systems, exciting electrons in the valence band up to the conduction band, and upon relaxation emit bright, monochromatic light, whose wavelength mainly depends on the bandgap of the semiconductor, strictly related to the size and the chemical nature of the crystals (quantum dots)[98,99]. These materials are highly requested in the market due to their versatility in a number of industrially relevant processes: they can help other systems to perform catalysis and photocatalysis[97], water splitting ($BiWO_6$ is the most established water splitter,[100–102]), transform light into current in photovoltaic systems or electricity into light (LEDs).[97–99]

The optics and photonics, electronics, energy-harvesting and energy storage industries are looking towards a number of new optical nanomaterials. In fact, besides semi-conductors, that are widely employed in technological advancements[97–99], and whose job is to convert electrical signal into optical emissions or vice versa, spectral converters, with the ability to convert between photons of two different specific wavelengths, are a relevant class of optically-active material. Normally, these converters are excited by high-energy wavelengths and the outcoming converted energy is in the form of low energy photons (*down-converters*). For example, organic fluorophores are an important class of down-converters. The physics and chemistry of these materials is well known, and many pages describing their physical behavior in interacting with light have been written. Thanks to these many pages of literature, today, a database comprising the most known organic fluorophores has been created (http://www.fluorophores.tugraz.at/).

However, nowadays, technology is moving towards infrared (IR) energies absorbing-visible (Vis) radiation emitting materials, with increasing interest. The low excitation energy permits a wide range of opportunities for these materials, both in the technological [27,94,103–106] and biological fields[67,82,83,91,92,107]. The *up-conversion* process (i.e. generation of higher energy photons from low energy photons) is a non-linear process, based on a subsequential absorption of two or more low-energy photons, which permit quantum leaps of the electrons into higher energy (*excited*) states[27,108]. The energized electrons relax down to the ground state, and in doing so emit photons of visible light. This class of materials includes Triplet – Triplet Annihilators (TTA) and inorganic Up-Converters (UC), which, currently, show optical phenomena that are at the base of cutting-edge technologies[94,103,109] and biomedicine[110].

1.3.1 Up-converting systems

Up-converting materials represent a large subgroup of luminescent materials, whose peculiarity is to convert lower energy photons in higher energy photons (anti-Stokes emissions). Several up-converting processes have been studied, both from organic and organometallic structures, and in inorganic nano and microcrystals [27,60,108,111–115].

Organic and organo-metallic up-converters rely on a process called sensitized TTA (Figure 1.13). IUPAC define TTA as *"Two atoms or molecular entities both in a triplet state often interact (usually upon collision) to produce one atom or molecular entity in an excited singlet state and another in its ground singlet state. This is often, but not always, followed by delayed fluorescence"* [25].

Triplet–triplet annihilation (TTA) shows great promise as an up-conversion phenomenon: it needs low excitation power density. For example, it can be activated by solar light and it is quite efficient, with relatively high up-conversion quantum yields (up to 10%)[111,113].

Another advantage of the TTA phenomenon is its readily tunable excitation/emission wavelengths and strong absorption of excitation light. Its emission mechanism involves energy transfer between a sensitizer molecule (donor) and an acceptor/annihilator that, ultimately, emits the up-converted visible frequency.

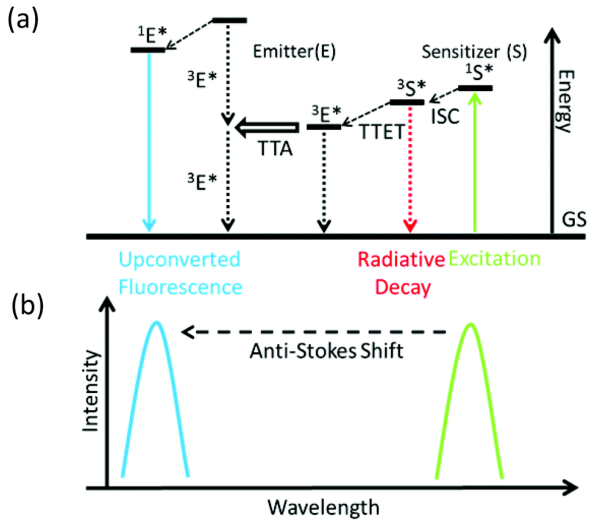

Figure 1.13: **upper:** general scheme sensitized TTA Jablonski diagram.[116]; **lower:** Anti-Stokes shift of the emissions (high energy end) from low-energy excitation.

The main drawback of the TTA systems is the low long-lasting stability and photobleaching (diminution of the emissions intensity due to degradation of the emitting system in function of the high-brilliance/ high energy of the irradiation source over time), since the labile organic matter is more prone to degradation than inorganic crystals[112–114]. Furthermore, the organic moieties present short-lived states (in the order of nanoseconds) in comparison to fully inorganic up-converters (micro or milliseconds), due to the lack of intermediate, metastable states and forbidden emissions. Another important drawback is that this effect is shown in non-aqueous solutions,[112] especially in organic non-polar or slightly polar solvents, and a preferred orientation between the donor and the acceptor is sometimes required for the energy transfer to be efficient, while an inorganic up-converter can emit in a solid state too.

Inorganic nano-sized up-converters are very different from TTA systems, even though the up-converting overall mechanism is quite similar, the sequential absorption of two or more low-energy photons and the emission of one or higher energy photons.

They are based on crystalline networks that incorporate lanthanide trivalent cations in their structure. Thus, the UC phenomenon is generally performed by lanthanide ion pairs unevenly distributed around a low-phonon crystal host. In these materials, *f to f* transitions are Laporte and (sometimes) spin forbidden, which render the emissions long-lived. Very little or no photobleaching [117,118] is observed over a large time span (2h or more). The rigid inorganic lattice, opposite to the fragile organic framework of TTA systems, makes them more resistant to degradation from external agents [27,105,115,119]. Surface modification can render inorganic up-converting nanocrystals (UCNPs) water soluble and core-shell approaches limit the number of surface defects[66,77,79,81] improving greatly emission efficiency. The advantage of having water-soluble nanocrystals that show limited toxicity and high brilliance give rise to a multitude of opportunities for biochemical, pharmacological and medical technologies in imaging. Despite the lack of molar absorptivity of lanthanide ions, inorganic up-converting system can be helped through the insertion of sensing ions or antenna molecules, which aid the energy transfer.

1.3.2 Up-converting photoluminescence in lanthanide-based systems: spectral properties and mechanisms

Up-conversion (UC) properties within inorganic crystals have been discovered by Auzel [108] about sixty years ago.

Lanthanide-based up-conversion is intimately related to the electronic distribution over excited levels. The latter must be arranged in a ladder-like structure (as in Figure 1.14) where the excited levels are separated by an almost equal energy difference. Light harvesting, energy-transferring lanthanides must provide few excited levels (preferably one ground and one excited, with the others too far away in energy in order to maximize energy transfer efficiency) and must be capable of absorbing NIR (980 or 808 nm) photons.

These processes depend on the electronic configurations of lanthanide (Ln^{3+}) cations. To observe these unusual optical phenomena, non-linear processes are involved: in fact, multiple photons of low energy excitation (usually NIR wavelengths) are absorbed by one set of sensing lanthanide ions, with suitable electronic level separation, which then transfer the harvested energy to excited levels, pumping of another set of lanthanide ions responsible for the emissions. The high-energy filled excited states of the latter sets of lanthanides relax down to the ground state, emitting visible (anti-Stokes) photons. The presence of filled $5s^2$ and $5p^6$ sub-shells shields the *4f* orbitals, (http://www.cchem.berkeley.edu) responsible for the whole up-conversion process.

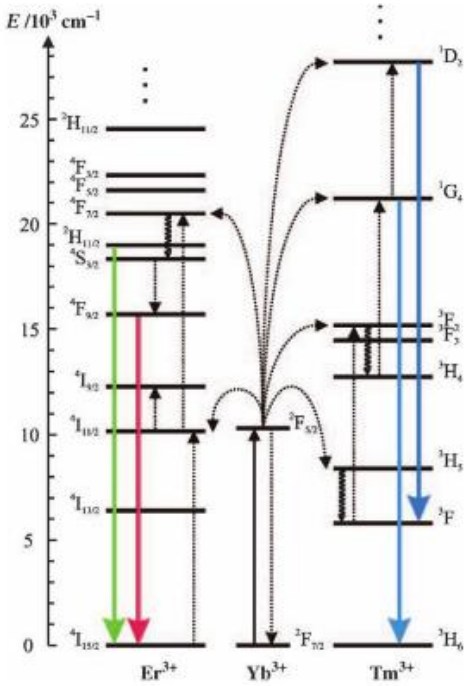

Figure 1.14: (left) Ladder like structure of the emitting Ln(III) ion. In black is the absorption of the NIR photons from Yb ions**; (right)** energy transfer and relative emission lines from Yb to Er and Yb to Tm pairs[27]

The different electronic configurations of the lanthanides (Figure 1.15) allow for the availability of different emissions, spanning from UV to NIR and freedom of choice for the dominant emissions.[27,108,110,120] Their fine tuning[27,75,121] is permitted through manipulation of the up-converting ions concentrations, host crystal structures (and chemical nature), core-shell strategies and multiple co-doping.[75,77,79,121]

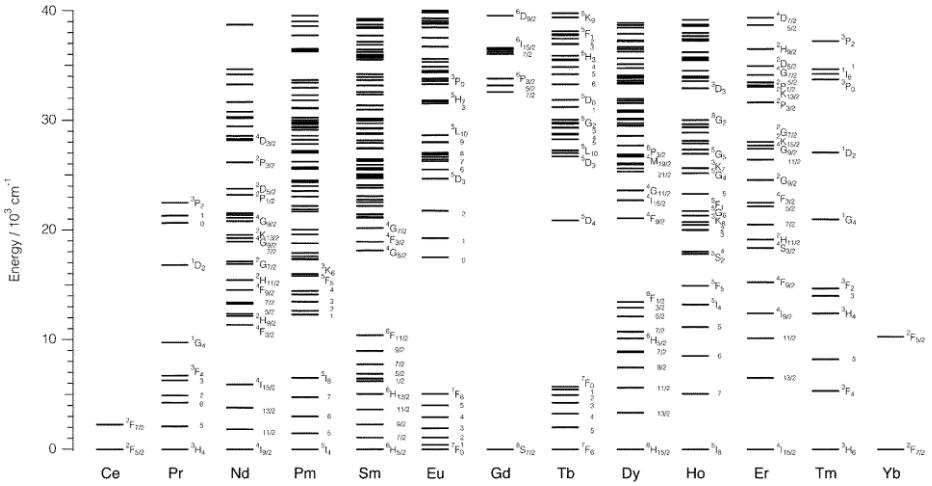

Figure 1.15: Energy levels of trivalent lanthanide ions.[122]

Since the electronic states of the lanthanides are energy-quantized, the resulting emissions will promote single-photon emissions, and therefore the resulting spectra will appear with narrow, spiked multi-band signals. Each band of the spectrum is characteristic of a particular *f-f* transition and its position is attributed to the energy difference between the excited and ground states. Organic fluorophores and up-converting TTA systems, instead, show broad-banded spectra, which comes from the fast relaxation of excited states (S_1, S_2, S_3, …) that relax down to the ground state (S_0). One example of emission spectra for both organic and inorganic UC systems are shown in Figure 1.16 (http://www.cchem.berkeley.edu).

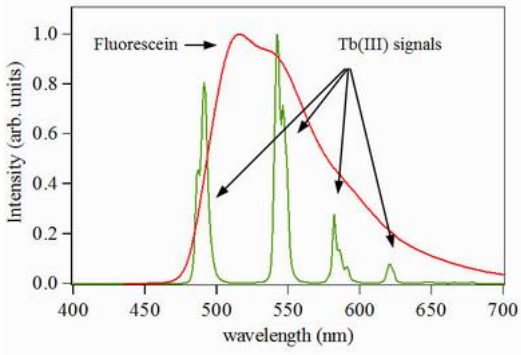

Figure 1.16: Overlap of Tb(III) emission and fluorescein (organic). Inorganic emitters show discrete emission lines due to the quantized excited states that relax down to the ground state. © Berkeley, 2017 http://www.cchem.berkeley.edu

Several multi-photon processes have been proposed in the literature [27,110,123] to explain the UC phenomenon. However, the most frequently reported are Energy Transfer Up-conversion (ETU), Excited State Absorption (ESA) and with minor frequency Photon Avalanche (PA). All mechanisms are based on the sequential absorption of two or more photons by metastable, long-lived energy states of Ln^{3+} ions, which emit the surplus energy in the form of visible photons (Figure 1.17).

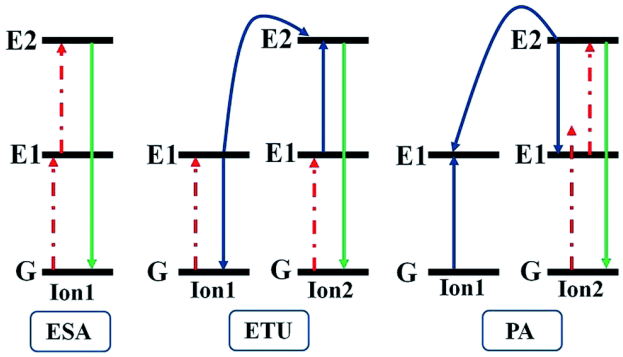

Figure 1.17: ESA, ETU and PA mechanisms[123].

Under the ESA mechanism, excitation takes the form of successive absorption of pump photons by a single ground state ion. If a photon promotes an electron from the ground state to the E1 state, a second photon will produce emission upon the excitation of the electron from the E1 to the higher – lying E2 level (up-conversion).

The ETU mechanism is similar to ESA, however it needs at least two neighboring ions for the energy transfer to occur. In this mechanism, the ion 1 (sensitizer) is excited by wavelengths with energy similar to the separation of the electronic states from its ground state to its excited state (metastable). The harvested energy is then transferred to the ion 2 (emitter), which is then excited from its ground state G to its excited state E1 (mechanism known as *activator*) exciting ion 2 to its excited level E2, while ion 1 relaxes back to its ground state G. The dopant concentrations that determine the average distance between neighboring dopant ions has a strong influence on the UC efficiency of an ETU conversion process. In contrast, the ESA mechanism is independent of the dopant concentration due to its single-ion emission characteristic.

Photon avalanche features an unusual pump mechanism requiring non-resonant, higher pump intensity. The process starts with the population of E1 level by a weak, non-resonant GSA followed by a resonant ESA populating the higher-lying emitting E2 energy level. Thereafter, a cross-relaxation between the excited ion and a

neighboring ground-state ion occurs resulting in both ions populating the intermediate energy level E1. The two ions then again populate the level E2 via ESA to further initiate cross-relaxation, leading to a looping process. Thus, the upconversion emission produced by photon avalanche is very strong. The PA process is considered to be the most efficient upconversion process. However, the emission response is delayed due to the looping processes with a rise time up to a few seconds. Also the weak GSA and the high pump threshold limit the use of PA.[124,125] In fact, only a few nanomaterials have shown PA-based upconversion[126–128].

Fine-tuning of the lanthanide emissions is performed for a number of applications. Since each lanthanide has a unique electronic structure, each spectrum will show different emission lines whose position depends upon the energy difference between the excited electronic levels and ground state. For example, Er^{3+} and Ho^{3+} show emissions predominantly in the green (Er^{3+}: 527, 542 nm deriving from the $^2H_{11/2}$, $^4S_{3/2} \rightarrow {}^4I_{15/2}$ transitions, respectively- and Ho^{3+}: 547 nm from $^5S_2 \rightarrow {}^5I_8$) and red ($Er^{3+}$: 656 from $^4F_{9/2} \rightarrow {}^4I_{15/2}$ and Ho^{3+}: 657 nm from $^5F_5 \rightarrow {}^5I_8$), while Tm^{3+} shows emissions in the UV (350 nm from $^1I_6 \rightarrow {}^3H_6$ and 360 nm from $^1D_2 \rightarrow {}^3H_6$ transition), blue (456 nm from $^1D_2 \rightarrow {}^3F_4$ and 476 nm from $^1G_4 \rightarrow {}^3H_6$), red (652 nm from $^1G_4 \rightarrow {}^3F_4$) and NIR (800 nm from $^3H_4 \rightarrow {}^3H_6$) regions of the radiation spectrum.

To give rise to UC emissions from the elements above, the most used sensitizers are $Yb^{3+}$and Nd^{3+}, which absorb at 980 nm ($^2F_{5/2} \rightarrow {}^2F_{7/2}$),[129–131] and 808 nm ($^4F_{5/2} \rightarrow {}^4I_{9/2}$), respectively [132], but other lanthanide ions such as Ce[133,134], among others, have been used as sensing ions for UC.

The up-conversion phenomenon is a non-linear process, and therefore the emission intensity is strongly coupled to the laser excitation energy, in particular with the power density (after beam focusing on the sample). Power optical density, in W/cm^2, is calculated dividing the read output power by the geometrical area (circle) of the focused beam calculated in cm^2. It must be noticed that, in the most common fluorescence experiments (illustrated in Figure 1.18), the emitted light is registered at 90°. Since the fluorescence has no preferential direction, only a fringe of the emissions intensities are recorded, which do not allow for quantitative results. More sophisticated setups are required for measuring QY of the UC photoluminescence.

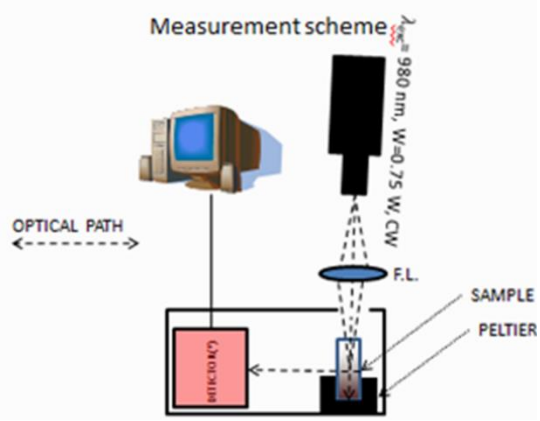

Figure 1.18: Scheme for one of the set-ups used for the determination of UCNPs emissions.

The relation between the intensity of upconversion photoluminescence (P) and the power of excitation pump laser (P) is depicted in equation (1.1)

$$I_{UCPL} \propto P_{Dexc}^{n} \qquad (1.1)$$

where n is the number of excitation photons required to produce the upconversion photoluminescence (UCPL) at a defined power density output. The fluctuations of this index are dependent on the laser power scale, area of the focused beam and detector sensitivity. In addition, scattering effects may diffuse light making this n parameter fluctuate too. However, generally in well-dispersed systems, these effects of light scattering are negligible[133–135]. Therefore, n is linked to the number of photons absorbed by the sensing ions and can be obtained from the slope of a log–log plot of intensity vs. excitation power density.

In this plot, two regimes can be found: a linear regime, where the intensity increases as the power output increases, and a saturation regime for high excitation density where emission intensity is constant. Generally, for red and green emissions, *n* (the number of photons needed for a certain emission) approximates to 2, while for blue emissions it approximates to 3 (see Figure 1.19).

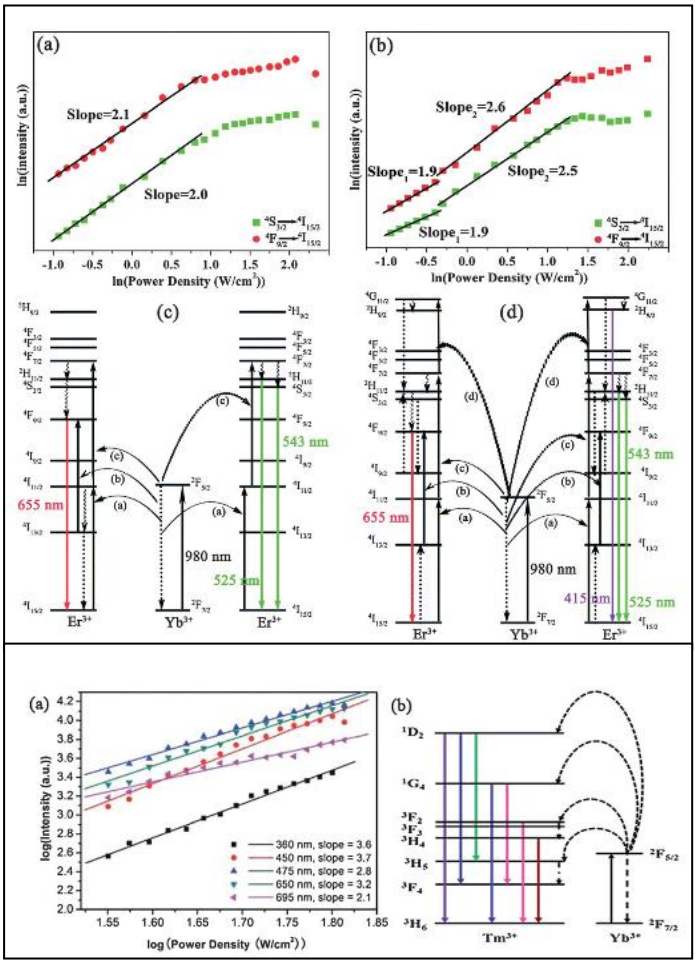

Figure 1.19: Examples of log–log plots of intensity vs. excitation power density for **(top)** Yb,Er[135,136] and **(bottom)** Yb,Tm[135,137] in α and β - $NaYF_4$ nanocrystals and $NaREF_4$ with their relative emission diagrams.

Therefore, UC green or red processes are only 2 photon absorption-dependent processes, because the energy needed for these emissions comes from the absorption of 2 NIR photons, while blue emissions are 3-photon processes because getting UC high-energy emissions, requires the absorption of 3 NIR photons. Obviously, it has impact on the emission efficiencies: the green and red emitters are far much more performant than the respective blue emitters.

In systems where there is no ladder-like energy distribution, it is also possible to detect UC emission thanks to *cooperative sensitization* phenomena. Very few works

describe this phenomenon because it is rare. However, it is relevant to mention it in this section since in our research we have achieved a UC nanomaterial with such effects. This process, called cooperative sensitization up-conversion (CSU), involves interaction between three ion centers, as shown in Figure 1.20, left. Ion 1 and ion 3 are generally sensitizers and are simultaneously excited to their E1 levels from their G levels. Then, the energies are simultaneously translated to the ion 2 (emitter) which relaxes down emitting up-converted light[138]. The CSU process is observed in Yb,Tb co-doped systems, in which Tb^{3+} emitting levels are much higher in energy than the energy provided by just one neighboring Yb ion. This process is generally found at temperatures above 100 ºK, while a dimer Yb-Tb would explain better the CSU mechanism below 10 ºK (Figure 1.20 right)[138].

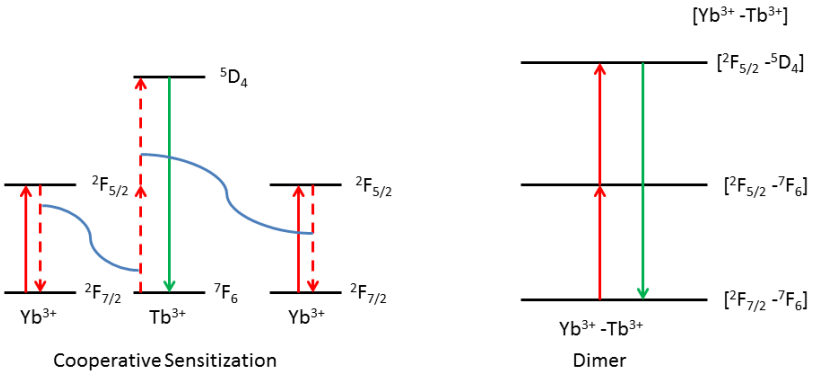

Figure 1.20: Up-conversion mechanisms for Yb,Tb co-doped crystals: **a)** high temperature CSU model, **b)** low temperature "dimer" mode. Adapted from Salley, Valiente and Guedel,[138].

1.3.3 Effects of "nano" size and composition in the UCPL

For many decades, up-conversion was observed in single crystal experiments[108]. The development of up-converting (UC) nanocrystal research has evoked increasing interest with the progress of nanoscience[27]. However, the crystal engineering for UC nanophosphors present strict requirements that must be fulfilled in preparing high-efficiency, high brilliance and easy dispersible small dimension up-converters. The most important points affecting the up-conversion photoluminescence (UCPL) will be revised in this section.

The effect of nano size

In comparison with bulk luminescent material, small luminescent particles show a classical drawback, namely poor luminescent efficiency. It comes directly from the geometrical constraints and the highly defective surfaces of nanocrystals, which

exhibit unsaturated coordination of metals, ion vacancies or atom lattice misplacements responsible for increased phonon vibrations and enhances non-radiative paths rather than the emitting ones. For example, in Figure 1.21, it is shown how the size of the nanocrystals (which goes from 150 nm to 8 nm), affects emissions in function of the power density output. Emissions were recorded from 1 W/cm^2 to 10^6 W/cm^2, however, while the full power scale (logP_D is 0 to 6) can be used for 150 nm nanocrystals, signals from 8 nm analogues can be recorded only using very high output densities, due to the large surface to bulk ratio. This large increase in vibrational energy and of the number and nature of the defects, thus, decreases emission probability for the UC photoluminescence[139].

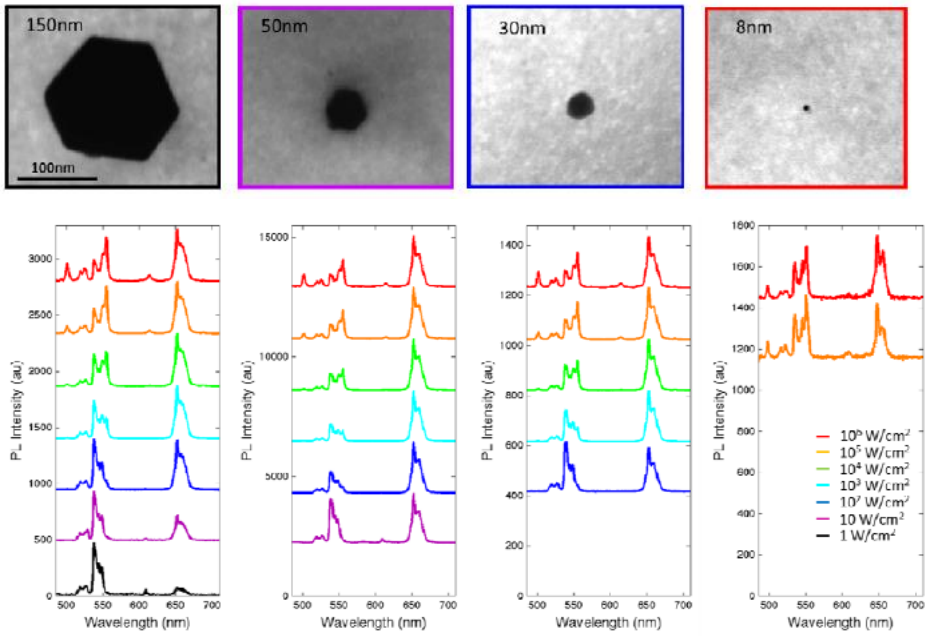

Figure 1.21: Size-dependent emission of various single-upconverting nanoparticles. Spectra are mounted in function of the lasing power (black 1 W/cm^2 to red 10^6W/cm^2) [139]

The lattice distortion

From a crystallographic point of view, the chemical nature and structure of isotropic crystals determines interatomic distances between ions, their relative (fixed) lattice positions and symmetry (Wickoff), as well as their relative coordination environments[140,141]. However, the insertion of foreign atoms (doping), in isotropic

host lattices, alters the relative inter-atomic distances to a certain extent[27], provokes distortions of the crystal lattice[27], and causes crystal stress and strain[27].

In highly doped systems where the total doping is about 20.5-22% of the total cation substitution with especially Ln^{3+} ions, which show larger coordination numbers, these distortions can alter heavily the phonon distribution and the lattice motions. However, despite the increased phonon distribution modes, the insertion of Ln ions is unavoidable for UC processes. These distortions are at the base of "*self-induced*" increased phonon energy (as compared to same-size, same composition isotropic crystals)[24,27,135,142,143].

From the optical point of view, bright emissions are obtained if few requirements are respected: first of all, to ensure efficient energy transfer, doping of the sensitizer must be in large quantities (≥5 times), with respect to the emitting lanthanides (normally 0.1-5 atom %).[135,144] Literature reports an optimum for sensing and emitting ions to ensure bright emissions. Doping quantities, therefore, are important for bright emissions: too low or too high concentrations of ions will dim emissions for a given compound. Normally, for up-conversion pairs such as Yb:Er and Yb: Ho the lanthanide relative quantities are about 10:1, however, when the ion pair is Yb: Tm, this ratio falls to 40:1 because Tm ions are very concentration sensitive.

Ensuring adequate hosting of lanthanide trivalent ions means including cations with similar atomic radii in the host crystal lattice. Similar sized cations greatly reduce distortions and allow a more effective inclusion of Ln ions. The latter, however present larger coordination numbers (see Table 1.1).

Cation	Ionic radius (Å)	Covalent radius in 6-9 coordination (Å)
$\mathbf{Y^{3+}}$	0.90	1.04-1.21
$\mathbf{Yb^{3+}}$	0.87	1.01-1.18
$\mathbf{Er^{3+}}$	0.89	1.03-1.20
$\mathbf{Tm^{3+}}$	0.88	1.02- 1.19
$\mathbf{Ho^{3+}}$	0.90	1.04-1.26

Table 1.1: Ionic and covalent (with coordination 6-9) radii found in crystals (copyrights to "Database of Ionic Radii" http://abulafia.mt.ic.ac.uk/shannon/ptable.php)

The host (phonon energy)

Metal oxides[128,145] and fluorides[46,77,146–149] are by far the most studied crystal hosts for up-conversion processes because these anions-derived crystal structures greatly reduce phonon energy, maximizing radiative paths and thus emission intensity.

In fact, collaborative lattice vibrations (phonons) greatly dim or quench emission brightness through preferential non-radiative decays: to design bright UC nanostructures, the lowest phonon energy possible is desired (see Table 1.2).

Material	**Phonon energy (cm^{-1})**
Phosphate glass	1200
Silica glass	1100
Fluoride glass	550
Chalcogenide glass	400
Y_2O_3	550
ZrO_2	500
$NaYF_4$	350
LaF_3	300
$LaCl_3$	240
YVO_4	890
Y_2O_2S	520
GdOCl	500
$LaPO_4$	1050

Table 1.2: Host crystals and relative phonon energy[24].

Lattice phonon energy is of great importance in selecting a host matrix for UC materials. Its influence on the non-radiative transition rate, k_{nr}, can be expressed as

$$k_{nr} = \beta e^{-\alpha(\Delta E - \frac{h\omega}{2\pi})} \qquad (1.2)$$

for low phonon numbers and

$$k_{nr} = \beta e^{-\alpha(\Delta E)} \qquad (1.3)$$

for phonon numbers above two or three, where β and α are constants unique to each host matrix, E is the energy gap between the two electronic states of interest, and hω/2π is the maximum phonon energy for the host matrix. How phonon vibrations affect emissions must be accounted for when designing a rationale formulation for the crystal engineering of nanostructures, and in particular for UC nanocrystals.

Alterations in the relative intensity of emissions

The alteration of the emission intensities can be related to a change in population of excited levels and also a modification of the energy transfer mechanisms. Analysis of intensity ratios between different transitions is performed routinely when understanding the up-conversion process[150].

The intensity of the emission bands is related to different parameters. Some of them depend on the nature of the crystals (chemical structure, crystalline phase, doping concentration, number and nature of defects, etc.) that may limit emission brightness for some (or all) transitions, or alter emission mechanisms [27,125,135,142]. Other effects involve external agents. For instance, OH- residues and organic matter (from solvent, surfactant layers, energy transfer fluorophores, etc) acts as quenchers for visible emissions and use NIR radiation to vibrate, then reducing selectively one [24,60,82] , or all emissions[143,151–153] from up-conversion spectra. To counteract this drawback, core–shell architectures are prepared[27,69,77,79].

Emission intensities are also affected by other factors such as temperature, (which greatly increases phonon vibration frequency), aging (due to the highly energetic nature of nanocrystals) and coalescence (this latter, sometimes, may come directly from the aging process) [115,119,120,125,135,142,154–156], and high lasing power density[135,142,157,158] or detector saturation.

The efficiency in nano systems

The quantum yield is defined as the ratio of the number of emitted photons to the number of absorbed photons. For an n-photon UC-process, the theoretical maximum for QY is 100/n %, e.g., for a two-photon process, the maximum QY is 50%. However, the observed QYs of UCNPs are usually much lower due to the energy losses in UC processes[131]. The QY of UCNPs must be analyzed by using the absolute

QY measurement due to the power dependency and the lack of standardized UCNP reference materials for a relative measurement method.

For the most efficient Er,Yb-$NaYF_4$ standard material, up-converting quantum yield is found in the order of 15% in single crystals, while they fall as low as 1-4% for nanostructured (20-100 nm) crystals[24]. Obviously, nanomaterials show lower quantum yields on account of the defective nature of the surface, increased phonon energy and of low-strength shielding of organic shell layers (for non-core-shell structures).

To limit the huge decrease in efficiency of the nanomaterials, synthetic strategies have been developed to crystal-engineer emission-modulated materials through core-shell architectures, [77,79,136,159] multi-modal magneto-optic materials[77], and surface functionalization techniques. [27,66,82,160]

1.4 Fluorides in up-conversion

Rare-earth doped, complex fluoride materials are dominating the panorama of UC nanomaterials due to their bright emissions and lower lattice phonon vibration as compared to the oxide structures (see Table 1.2). Systems such as $NaYF_4$:Yb,Ln[147,161,162], $BaYF_5$:Yb,Ln [163], CaF_2:Yb,Ln[164,165], LaF_3:Yb,Ln,[146,149,166] and so on are considered, for the reasons explained above, among the brightest up-converters systems. In particular, nano-sized $NaLn^1F_4$:Yb, Ln^2 (Ln^1= Gd, Y, La, Yb, Dy, etc. and Ln^2= Er, Ho, Tm, Tb, etc.) are studied because: (i) they present low phonon energy (350-500 cm^{-1})[24], (ii) there are well established synthetic routes and (iii) they have a variety of marketable opportunities for technological and biotechnological exploitation of their UC processes. The main strengths, especially in the bio-technological fields, are due to the low-energy excitation that provokes low autofluorescence of biological tissues (excitation in the transparent region of tissues), high penetration depth of the NIR light, high brightness of the emission, mild (or low) cytotoxicity towards cells and ease of biocompatibilization[67,82,160,164,167]. This makes these materials widely appreciated for *in vitro* and *in vivo* imaging studies: bio-imaging[77], theranostics[168], and photothermal therapy[88,169] are, nowadays, the most sought biological applications. More recently, since the dependence of UC luminescence on the temperature has been rationalized, these nanomaterials have been proposed as thermo-responsive nanometric devices. Moreover, UC nanofluorides offer other favorable properties such as high photostability[117], tunable emission wavelengths[75] and high detection sensitivity [105,164,170], which are important when thinking about bio-technological exploitation of optical materials.

However, beyond the adaptability and utility of these materials in diverse fields of application, and despite the large number of papers and reviews, which show how much the knowledge of these materials has increased in the 50 years from their discovery, there is still so much to learn about their crystal formation, size and luminescence relations.

1.5 $NaYF_4$: Yb, Ln^{3+} nanophosphors. Synthetic routes and surface modification

The most efficient UC phosphor to date is pure hexagonal $NaYF_4$:Yb,Er (where Yb^{3+} and Er^{3+} are substitutional ions with Y^{3+}, in concentrations of 18-20 atom % and 1-2 atom% respectively). It was introduced by Menyuk *et al.* in 1972 [171]. This inorganic phosphor permits emissions in the green and red regions of the visible spectrum. The most efficient UC phosphor for emissions in the UV and blue range is pure hexagonal $NaYF_4$:Yb,Tm (where Yb^{3+} and Tm^{3+} are substitutional ions with Y^{3+}, in concentrations of 18-20 atom % and ~ 0.5atom% respectively,). This material was introduced by and Kano *et al.* in 1973[172,173]. Both up-converting nanophosphors have been extensively studied and proposed for several technological applications, such as lasers,[124,174] solar cells,[58,120,155,175] waveguides, [176,177] and display devices[178]. Today there is a completely new focus on these bright light emitting nanophosphors in various biological[105,179,180], biomedical[160,168,181,182], and botanical[183–186] applications, as tagging labels and photosynthesis activators. Furthermore, new studies look towards the investigation of the temperature-dependent emission, as nanothermometers[187]. This new focus makes UCNPs promising alternatives to organic dyes or quantum dots in some applications.

The existence of two crystal structures has been studied from a crystallographic and optical point of view: α (cubic)[188] and β (hexagonal)[189] phases show very different UC emission intensities.

Cubic (α-) $NaYF_4$:Yb,Er is much less emitting (around 10 times less) than hexagonal (β-) $NaYF_4$:Yb,Er [190]. The different optical response lies on the different coordination environments around the lanthanides, different inter-lanthanide distances, different phonon energies, and so on. Altogether, these effects will impact the emission efficiency and the intensity ratios.

Lanthanides lattice positions and Wyckoff symmetries are very different in the two crystalline environments[190] (see Table 1.3 and Figure 1.22), and as soon as the hexagonal lattice is formed, their atomic position will adjust to the position symmetry of the most stable lattice.

Ion	Cubic lattice Wyckoff position symmetry	Hexagonal lattice Wyckoff position symmetry
Yb^{3+}	4 a	1 a/1 f
Ln^{3+}	4 a	1a/ 1 f
Y^{3+}	4 a	1 a/ 1 f
Na^{+}	4 a	1 f/2 h
	Volume unit cell=164 Å ^{3}	**Volume unit cell = 106Å^3**

Table 1.3: Crystal cations positions, symmetry, and relative volume of the unit cell[191]

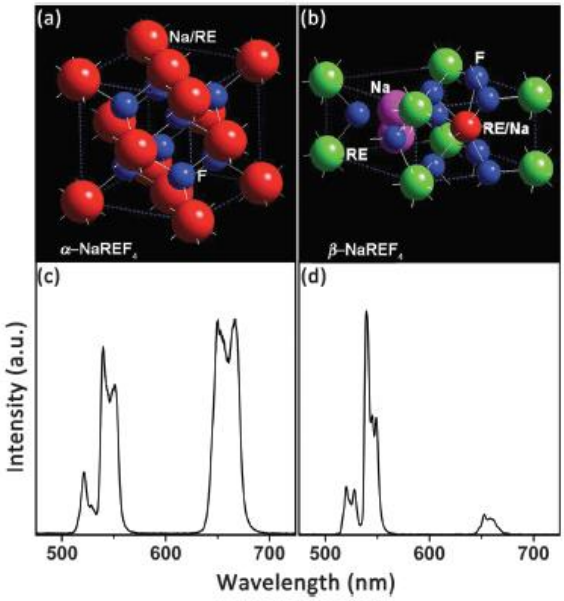

Figure 1.22: Structure and relative emissions of α and β – $NaYF_4$:Yb,Er. Adapted from Dong et al.[190]

One of the main differences that can be seen is that the hexagonal unit cell shrinks significantly, leaving the rare earth (RE) cations much closer together, potentiating the energy transfer between the sensitizer and the activator. Furthermore, there are several combinations where the RE ions can substitute for the original Y (or Na) ions.

Therefore, there are more Ln ions per hexagonal unit cell as compared to the cubic one [190,191].

Crystal structure has also a direct impact on the emissions efficiencies and colors. Cubic or mixed phase systems show different spectra[191], as depicted in Figure 1.22, e.g. in cubic $NaYF_4$:Yb,Er, for example, the most intense emission in the cubic phase is red, while in the hexagonal one it is green. A mixture of phases generally gives out an average intensity for both emissions and the relative intensity depends on the relative amounts of the different phases.[191] In the latter case, the formation of powders composed of mixture of crystals the relation of intensities is altered.[190,191] The formation of cubic or hexagonal structures, then, can be used as a strategy to look for the main color of the emission in optical applications.[192]

It is known, up to now, that the formation of high quality, pure β-$NaYF_4$:Yb,Ln crystals is a multi-step process. Nucleation of the crystals passes for an initially slow kinetics due to nucleation in the cubic crystal lattice (simpler), until a cubic to hexagonal transition is reached. At present, the main drawback probably resides in the very different kinetics of growth rate for the two crystal phases[193], which depends on the poorly understood crystal phase diagram and cubic to hexagonal transition parameters[191,193]. Results have demonstrated that the α-phase is the kinetically more favored, and always formed first[191,193], while the β-phase is thermodynamically more stable.[190,191,193]

When the crystal reaches the opportune size for the cubic to hexagonal transition, the growth rate steeply increases due to the high–energy facet of the plane (0001)[24,194], that initiates the formation of elongated crystals (nanorods). The kinetics of crystal formation, if not stopped, leads to submicron, and micron-sized crystals (anisotropic epitaxial growth) which lead to the formation of needle (or rod) shaped crystals (see Figure 1.23).

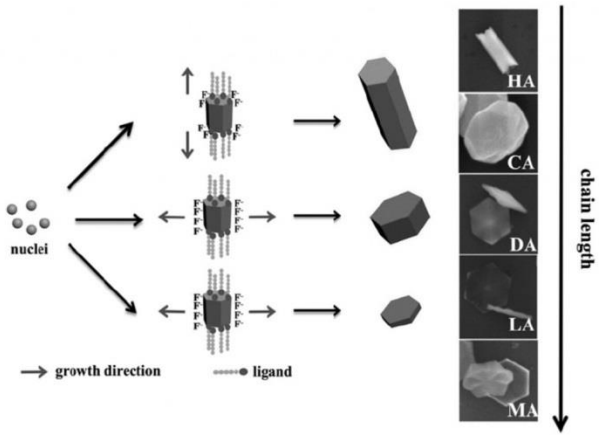

Figure 1.23: Schematic diagram of the growth processes of β-$NaYF_4$. Adapted from Wu et al.[195]

Due to the causes above described, it is practically difficult to control particle size and phase.

The main reason is because the growth of β-UCNPs needs an α → β transition process. If the reaction is stopped while in the middle of the transformation from α to β, the product will be consisting of only mixed phase crystals with nonuniform particle size distribution. Therefore, to achieve pure β-UCNPs, the α → β phase transition must be completed, and the size that has to be focused will derive from the outcome of the kinetic process of the transition, rather than determined by reaction time.[194]

It also has been found that the nature of the lanthanide ion plays a key role in driving the crystallization process towards one or another phase, under the same synthetic conditions, as demonstrated by F. Wang *et al.* (Figure 1.24).

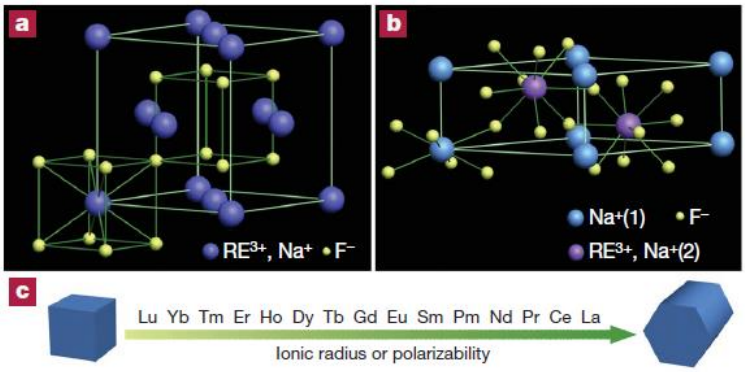

Figure 1.24: (a-b) Phase transformation in $NaREF_4$ structures by lanthanide doping, (c) General trend of phase transition from cubic to hexagonal as a function of ionic radius (or polarizability) of the lanthanide dopant ions.[196]

Variations of the crystal chemistry including complete exchange of Y with pure lanthanide components [196] or triple doping with various transition metals, including Sc^{3+} [121], Bi^{3+}[197], Fe^{3+} [198] and Mn^{2+} [199], have revealed the importance of similar-radii cations in emission modulation as well as counter-cations such as Na^+ which have been completely or partially substituted with K^+, [121] Li^+ [188] or Rb^+ [200], to determine counter-cation size effects. All these studies have been reported in order to rationalize atomic-radius driven crystallization.

1.5.1. Synthetic routes of UC $NaYF_4$

Concerning the synthesis of high quality UC $NaYF_4$ nanocrystals, several methods of preparation have already been established to produce high quality nanomaterials (as reported in Table 1.4).

Different wet chemistry approaches such as coprecipitation [125,201] (A), thermal decomposition of precursors in high-boiling organic solvents [179,194,202,203] (B), hydro– and solvo-(C) thermal synthesis [204–211], and more recently microwave assisted and microwave hydro - and solvo – thermal syntheses [49,188,197,212,213] (D) have been used in order to produce high quality nanomaterials. The main considerations on these approaches are listed below:

Method	Hosts	Remarks
Co-precipitation	LaF_3 $NaYF_4$ $LuPO_4$ $YbPO_4$	Fast growth rate without the need for costly equipment and complex procedures. Post-heat treatment typically required.
High Temperature Thermolysis	LaF_3 $NaYF_4$ GdOF	Expensive, air-sensitive metal precursors. High quality, monodisperse nanocrystals. Toxic by-products.
Hydro(solvo)thermal synthesis	LaF_3 $NaYF_4$ $La_2(MoO_4)_3$ YVO_4	Cheap raw materials. No post heat treatment. Excellent control over particle size and shape. Specialized reaction vessels required.
Sol-gel processing	ZrO_2 TiO_2 $BaTiO_3$	Cheap raw materials. Calcinations at high temperatures required.
Combustion Synthesis	Y_2O_3 Gd_2O_3 La_2O_2S	Time and energy saving. Considerable particle aggregation.
Flame Synthesis	Y_2O_3	Time saving and readily scalable. Suitable for preparing oxide-based nanomaterials
Microwave assisted	Oxides, TiO_2, ZrO_2, SiO_2 $NaYF_4$	Fast reaction kinetic, low temperature gradient and relatively high temperatures. Ease of scalability. Use of polar solvents only

Table 1.4: Synthetic routes for preparation of several UC nanostructures.[24]

A) The co-precipitation method requires the formation of non-soluble salts in confined emulsion at room (or low) temperature [214]. However, this method is quite abandoned because of the poor quality of the crystals and the weak emissions deriving from the synthesis [125,201].

B) The most widely used synthetic route is thermolysis or thermal decomposition of precursors in high–boiling organic solvents [35,194,202]. This route, despite the synthetic advantages that it gives (almost always a pure hexagonal phase [215,216], with very narrow size distributions[215] and small diameters [215]) to the particles, needs harmful precursors, a carefully controlled inert atmosphere and high temperature, making this synthetic route very hard to manage and prone to danger in the laboratory.

C) Hydro– and solvo– thermal routes are very simple synthetic strategies that give generally high quality nanocrystals [10,36,211,217–221] due to the high temperature and autogenous pressure that generates inside the autoclave container; however,

since most autoclaves do not have control over pressure and homogenization, particles are generally aggregated and bulkier, with sub-micron sizes[36,217,222,223]. Another drawback of this synthetic route lies in the long reaction kinetic (sometimes more than 24 hours are needed to complete one synthesis [220]) needed to complete the formation of the materials.

D) Microwave-assisted synthesis uses homogeneous heating, which generates crystalline solids in few minutes and that gives the freedom for controlled morphology and size of the derived product through an accurate tuning of synthetic conditions. One requirement for the microwave-assisted synthesis is the use of a polar solvent as the reaction medium: non-polar or low-polarity solvents are generally insensitive to microwave irradiation and so the reaction medium (solvent or mixtures) would not be as effective. Microwave assisted synthesis incorporates the qualities of both hydro/solvo-thermal and thermal decomposition routes, with the advantages of homogeneous heating within the reaction vessel, faster reactions (a microwave assisted synthesis generally ends within minutes), and lower reaction temperatures, giving uniform-high quality, pure hexagonal and highly crystalline nanostructures.

Figure 1.25 shows the pros and cons of the various routes to prepare UC-$NaYF_4$ nanocrystals.

Synthetic route	Pros	Con
Solid state	- High-energy milling/crushing, - Robust reactors (high pressure)	- Low crystallinity of the as-prepared materials - Polydispersity - Cross-contamination - Little control over reaction - Low emissions
Co-precipitation	- easy synthetic route - Generally low-temperature	- No control over phase and size - Poor crystallinity - Low emissions
HTT (High Temperature Thermolysis)	- Control over crystalline phase and size - Good luminescence - Uniform size/low polydispersity - Number of nucleation and growth models	- High temperature (over 300°C) - Harmful synthetic precursors - (sometimes) poor crystallinity or contamination from by products of the thermolysis - Rigorous control of the atmosphere
Solvothermal	- Good crystalline phase control - Good luminescence - Autogenous pressure generation (helps crystallinity - Robust autoclave vessels - Ease of use (widely used synthetic route for nucleation and growth of a number of inorganic nanocrystals.	- No control over size (generally sub-micron or micron sized aggregates) - No reaction control (requires preparation of precursors - Lower T as compared to HTT - No agitation (mostly) - No nucleation and growth modeling - long reaction times
Microwave assisted (solvothermal)	- Short reaction times - Highly crystalline solids - Autogenous pressure generated (lower than pure ST) - Focused and local heating (no heat gradients) - Agitation included - Possibility of different temperature ramps	- Difficult scaling up to larger systems - Scarce quantities of precursors and limited solvent volumes - Only highly polar solvent can be used (hydrothermal synthesis better than solvothermal) - Difficult (sometimes) cleaning of prepared materials

Figure 1.25: $NaYF_4$:Yb,Ln principal synthetic strategies, strengths and weaknesses

The most studied reaction for the synthesis of high-quality, nano-sized, bright $NaYF_4$:Yb,Ln up-converters is certainly high temperature thermolysis. The large numbers of crystal nucleation and growth models of $NaYF_4$:Yb, Ln, published in literature, are mostly limited to this synthetic route.[203,204,216,224]

In this PhD work, we are especially interested in the solvothermal route because of the easy procedure and high crystallinity and brightness of the nanomaterials. However, to date, solvo-thermal modeling of UCNPs nucleation and growth has not been thoroughly studied yet, due to the intrinsic difficulties given by the limited control over reaction conditions, lack of visual observation and the thermal inertia of the reactors and the different pressure/temperature conditions that are found in autoclaves as compared to the glassware-based syntheses.[220]

The lack of detailed models for nano-sized UC materials under solvothermal conditions is giving an opportunity for a deeper study of the nucleation and growth of nano-sized $NaYF_4$: Yb, Ln. It is known that preparation of such crystals, under solvothermal conditions, generally form micro or sub-micro sized systems [36,211,223] (see Figure 1.26).

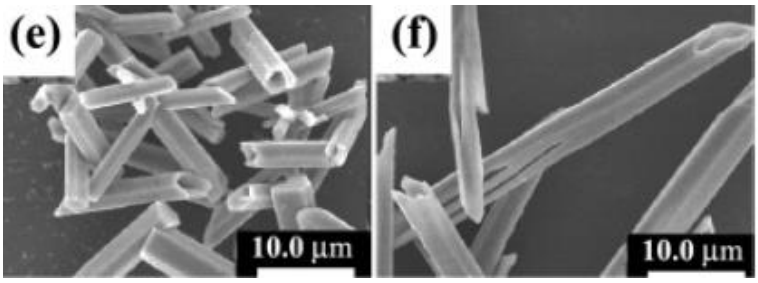

Figure 1.26: SEM images of $NaYF_4$ hydrothermally synthesized at 220 °C for 48 h[211]

As described before, the crystal transition phases pass from re-dissolution of sacrificial cubic nanostructures that evolve into hexagonal nanostructures, according to Ostwald ripening process, and, suddenly, the continuous enlargement of the latter to form large crystals. However, the process of blocking the hexagonal structure to nano-sized crystals especially under solvothermal synthesis is very difficult to manage, due to the inner systematic drawbacks depicted above, and to not well-defined phase transition parameters. These parameters depend on the employed solvents, on the complexes formed by precursors, the solvent-exposed environment around the lanthanides and the temperature and pressure[37,50,196,211] inside the vessel.

In literature, UC $NaYF_4$ nanocrystals prepared by solvothermal routes have a wide particle distribution, going from 5 nm to 500 nm and more[24]. Furthermore, the small particles (of around 5 nm) are mostly cubic α-crystals [204], while the brighter β-crystals have very big sizes (200-500 nm)[211]. The lack of small (< 50 nm) hexagonal UC crystals under solvothermal conditions, then, opens up the doors for the study of the hexagonal crystal formation[194], nucleation and growth under solvothermal conditions. In addition, since the cubic to hexagonal transition process is still poorly understood, the study of UC pure hexagonal nanocrystals becomes intriguing because of the possibility of offering new parameters affecting transition such as the influence of time, temperature, direct or inverse emulsion system, and so on. Understanding these effects on the nucleation and growth of solvothermal synthesis of nano-sized up-converting crystals can provide a valid strategy to elucidate the phase diagram from both the solid and the solution point of view [24,37,50,194,220].

Despite the large number of studies published, one of the biggest challenges that the scientific community at large is facing, up to now, is to find an efficient and scalable synthetic route for the preparation of pure, nano-sized and brightly emitting β-$NaYF_4$:Yb, Ln crystals.

Chemical strategies for surface modification of UCNPs

The most efficient synthetic methods for $NaYF_4$ nanoparticles yield hydrophobic materials[35,185,216]. However, water-dispersibility is needed for the major fields of application of UCNPs. Surface modification strategies have been designed mostly for improving nanocrystals´ surface architecture[66,74,82,160], to switch from hydrophobic to hydrophilic surfaces[66,82], and to functionalize nanocrystal surface, [59,67,72,107,179] in sight of bio-technological marketable opportunities, offered by biochemical and medical exploitation of the up-conversion phenomenon[27,66,82,160,185].

Numerous methods have been reported as employable strategies to efficiently render the UCNPs dispersible in aqueous systems. These surface modification techniques not only help in switching between hydrophobic and hydrophilic surfaces, but also, in some cases, reduce or eliminate emission quenching effects due to the very defective surface, and protect them from external quenching agents. These strategies can be divided into four categories and include:

- **(A)** chemical modification of the hydrophobic (typically oleate) ligand on the surface,
- **(B)** addition of an extra layer,
- **(C)** addition of a thin shell on top of the UCNP,

- **(D)** complete replacement of the original ligand by another one.

Of these ligand functionalizations, ligand oxidation under heavy conditions, addition of amphiphilic compounds between the hydrophobic tails, are reported but by far the most used is core-shell or core-multi shell nanocrystal engineering.

Surfactant-based layers have a direct impact on UCNPs´ emissions [60], and besides, they leave the emitting core exposed to the liquid-solid interface, and so to a number of quenchers that can dim emission brightness.

Core-shell architectures, on the other hand, are robust and relatively small, protect the core from directly touching the solid-liquid interface and greatly reduce core-related surface defects, coalescence between neighboring.

The main drawback is that the slightly larger dimension of the crystals [69,74] can be detrimental in some cases [69,74]. Core-shell (or core–multi-shell) designs reduce the concentration of surface defects, and, at the same time, the shell layer acts as a protective shield from external quenchers [69,77,79,225]. The reduced number of surface defects, moreover, enhances emission reducing the vibrational quenching due to occupation of surface atom vacancies with atoms pertinent to the shell layer: the result is shown in higher luminescence and, therefore, efficiency. Successive shells onto the UC core can be made of soft matter (often polymers) [59,72,226], functionalized silica, metals (e.g. Au, Ag)[227], and functional oxides (TiO_2, SiO_2, ZrO_2 etc…) [79,159,225]. However, the most employed shell is the matrix ($NaYF_4$), with different (or not) lanthanide doping in an effort to modulate wavelength color[77,228].

UCNPs and its native ligand	**Shell**	**Application**	**Ref**
$NaYF_4$:Yb,Tm/Er@Oleate	SiO_2	Imaging, drug delivery	79
$NaYF_4$:Yb,Tm/Er@Oleate/SiO_2	TiO_2	Dye sensitized solar cells, photocatalysis	58,159,225
$NaYF_4$:Yb,Tm@oleate	Au	Plasmonic-UC modulation	229
$NaYF_4$:Yb,Er@oleylamine	Ag	Imaging, photothermal therapy	230
$NaYF_4$:Yb,Tm/Er@ Oleate	$NaGdF_4$	Dual Fluorescence and MRI	77,231
$NaYF_4$:Yb,Tm@ Oleate,	$NaYF_4$	Multiple applications	228

Table 1.5: core-shell architectures and applications for different UCNPs.

Core shell engineering is also used in other aspects: emission enhancements (emission can be many-fold more intense under core-shell architectures [228]), emission color modulation and tuning [27,115,125], or selective enhancement of one specific emission, at the expense of the other emissions, driving emitting paths in one or a few directions as, for example in Shen et al.[232]. Moreover, core-shell structures have been designed with the aim of using UC emission monochromatically.[233] The shells were filled with wavelength-selective bypass filters, which have permitted monochromatic light from different regions of the visible spectrum using core-shell UCNPs (see Figure 1.27).

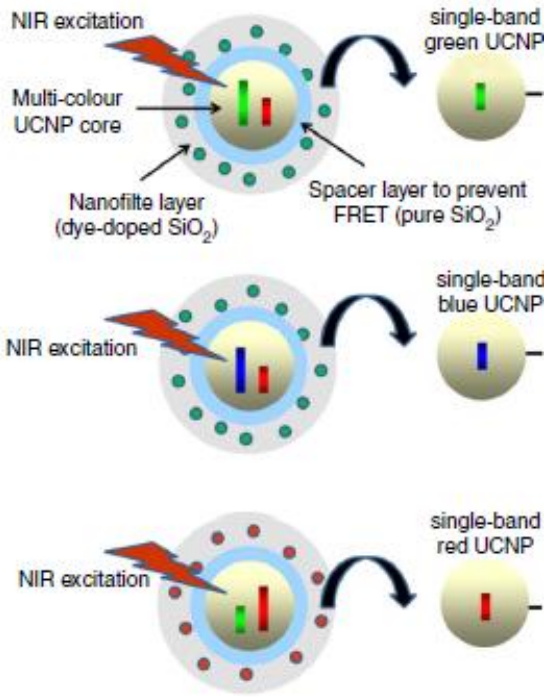

Figure 1.27: Scheme of selectively filtered radiation of upconverting nanoparticles Adapted from Zhou et al.[233].

The main field of application for core-shell UCNPs architecture is without doubt the biochemical field. However, other fields such as photocatalysis, photovoltaic devices, security or sensing may have a good use for core-shell UCNPs architectures.

Mono-chromatic narrow-band emissions can be useful, in fact for a manifold of technologies such as smart screen, smart coatings, sensing, biomedical fluorescent labels and heterogeneous photocatalysis. Moreover, they can find application in

pharmacological formulation for a more precise detection of the immune response to active components for cancer detection

.

1.6 Justification of the research work

The hydro(solvo)thermal synthesis of inorganic crystals is not a new synthetic technique. The main strength of this technique relies on the relatively high temperature and pressure of the vessel in which the crystals are grown. The main drawbacks, as we depicted above, are the great thermal inertia, the lack of visual observation and long reaction times for the preparation of the crystals. This synthetic route is generally used for growing large crystalline systems and porous systems such as zeolites and metal organic frameworks (MOFs) [234]. However, lately, this route has served for the preparation of several inorganic nanomaterials, including the very small quantum dots (QDs) [235]. The advantages it has to offer over the classic glassware-based synthetic techniques include the larger scalability of the reaction products and the relative high pressure within the vessel, which lead to the formation of highly crystalline materials.[218,220]. The high pressure is formed from the autogenous evaporation of high-temperature boiling mixtures (or solvents) and facilitates the conditions for the germination and nucleation of the crystals; secondly, the thermodynamic regime operating in this process permits higher quality nanocrystals.

Despite all of these advantages, however, very few reports have been written with the aim of describing the formation of the crystals within the autoclaves, and even fewer studies describe a rational model for limiting the crystal size in a solvothermal procedure.

To obtain high-quality, pure hexagonal phase Lanthanide doped $NaYF_4$ nanocrystals, through solvo-thermal synthesis is still challenging because it either gives small-sized (size of about 5 nm) cubic UCNPs or large crystals between 200 nm to 500 nm, even more. The former lack efficient emissions while maintaining a small size, suitable for biological and technological nano-based applied research; the latter definitely show pure hexagonal phase, however they are too big for nano-based technology especially for biological and biomedical-based tagging experiments.

In the context of this work, then, a synthetic route for the synthesis of $NaYF_4$:Yb,Ln has been studied and a scheme of crystal growth has been formulated. This work attempts to rationalize a systematic study of a reported synthetic route for UC nanocrystals in solvothermal mixtures [47,50,170,236]. This work intends to impact the poor literature by trying to understand the effect of various reaction parameters on the nucleation and growth models for these experiments.

Besides this fundamental work, the inclusion of the synthesized UC nanocrystals of 20 to 50 nm in soft-matter matrices was investigated. In literature, there are many reports[154,237–239] on supramolecular systems embedding a wide variety of optical nanocrystals such as plasmonics [240], QDs[241–243] or carbon nanotubes[244,245]. Inspired by these works and a recent references based on near-infrared light-sensitive supramolecular gels[246], we decided to prepare supramolecular systems from Naphtalimide (Naf)-based, hand-made fibrillary networks incorporating the previously synthesize UC nanocrystals. The luminescence dependence of the system was studied as a function of the temperature and the sol-gel transition.

With the aim of increasing the surface functionality of the UCNPs, core-shell systems based on silica and functionalized silica–coated UCNPs were also performed. The core-shell structures were prepared in a two-step reaction, changing from oleic acid (OA) to polyvynilpirrolidone (PVP) and successively transforming into core- silica shell architectures. The switch from hydrophobic to hydrophilic surface and the optical activity of the materials was evaluated.

Great attention, today, is also paid to drug-delivery novelties and poly-functional mesostructured systems. Drug-delivery systems are generally based upon micron-sized vesicles prepared in a variety of fashions from bio-polymers[247] or bio-based organic surfactants[248] and so on, that encapsulate a variety of functional nanoparticles and drugs[249]. Generally, spotting-delivery composites, including UCNPs, amphiphilic biopolymers are used[250,251]. Under this premise, and knowing the importance that UCNPs are recovering in bio-based imaging, and the ease of their bio-compatibilization, encapsulation of the as-synthesized UCNPs within bio-surfactants based vesicles was studied. The formation of the bio-surfactant vesicles passes through a series of pH changes. Some experiments were done in order to successfully incorporate the up-converting nanocrystals inside these biosurfactant microcapsules. The most relevant outcomes of these experiments will be exposed in this PhD manuscript.

Finally, the novelty of microwave-assisted (MW) synthesis, which limits the heat gradient due to fast and homogeneous heating, has been used in the formation of UCNPs. This novel synthetic route has always shown to produce very small-sized structures. However, only cubic or mixed phase crystals were discovered for $NaYF_4$:Yb,Ln nanoparticles under micro-wave heated reactions[41,49,188,252]. The main drawback of this synthetic route is the use of highly polar solvents which may act as solvent and reactant and change the compound composition. Despite this, the

interaction of MW heating with polar solvents opens up the possibility for low temperature syntheses[41,49,188,252] and very fast crystal growth kinetics [41,49,188,252] which dramatically diminish reaction times compared to solvothermal ones. Therefore, the last part of this PhD work is devoted to prepare $NaYF_4$:Yb,Ln nanoparticles of small size and pure hexagonal phase by using microwave-based procedures.

1.7 Objectives of the present work

The aims of this work are:

To shed light on the formation of β-$NaYF_4$:Yb, Ln (Ln= Er, Ho, Tm) nanocrystals, benchmarked with pure $NaYF_4$, under solvothermal conditions, establishing connections between crystal phase and size of the UCNCs with reaction parameters, and to suggest a nucleation-growth model. Experimental findings will be analyzed in order to demonstrate size and structure(s) relations and relative optical activity.

Secondly, particular applications of the solvothermal UCNPs will be presented:

(i) A one-pot synthesis of composite systems formed of Naphtalimide-based fibrillary monomers and solvothermal UCNPs. UCNPs included Yb as the sensitizer (hence 980 nm radiation of excitation will be used) and Er/Tm as the chosen activators. The energy transfer between the $NaYF_4$:Yb,Tm and the organic chromophore anchored onto the fibrillary monomers will be study as a function of the temperature and, specifically on the sol-gel transition temperature.

(ii) A bio-based application of the solvo-thermal prepared UCNPs will deal with the incorporation of nanocrystals into glycolipid-based pH-dependent vesicles with the aim of studying the entrapment of the crystals within the vesicles and determining the robustness of the composite in solution, through optical – based studies, dynamic light scattering (DLS) and kinetic experiments. The study will comprise DRX study of the encapsulated UCNPs, in order to understand if the pH-dependency of the vesicles´ formation will ruin the nanoparticles crystalline structure.

Finally, this work will describe the formation of pure hexagonal nanorods through MW-assisted synthesis. This study will identify a potentially exploitable feature of the synthetic route, which will permit post-synthetic coating: the possibility of coating the nanorods post-synthesis will permit ease of dispersion and therefore freedom of choice of the solvent dispersions dependent upon the fate of the UC nanorods

1.8 Bibliography

(1) Feynman, R. P. *Eng. Sci.* **1960**, 22–36.

(2) Tegart, G. *Nanotechnology* **2002**, *II*, 1–12.

(3) Buhrman, R. A.; Daughton, J. M.; Roukes, M. L. **2003**, No. August.

(4) Gottschalk, F.; Nowack, B. *Nanotechnology* **2014**, *5* (2), 1670.

(5) OECD International Futures Programme. *Allianz* **2007**, 46.

(6) Viñes, F.; Gomes, J. R. B.; Illas, F. *Chem. Soc. Rev.* **2014**, *43* (14), 4922–4939.

(7) Borisenko, V. E.; Ossicini, S. *What is What in the Nanoworld*; 2008.

(8) Lloyd-Hughes, J.; Jeon, T. I. *J. Infrared, Millimeter, Terahertz Waves* **2012**, *33* (9), 871–925.

(9) Roduner, E. *Chem. Soc. Rev.* **2006**, *35* (7), 583.

(10) Altavilla, C.; Ciliberto, E. *Inorganic nanoparticles : synthesis, applications, and perspectives*; CRC Press: Boca Raton, FL :, 2011.

(11) Burda, C.; Chen, X.; Narayanan, R.; El-Sayed, M. A. *Chemical Reviews*. 2005, pp 1025–1102.

(12) Tevet, O.; Goldbart, O.; Cohen, S. R.; Rosentsveig, R.; Popovitz-Biro, R.; Wagner, H. D.; Tenne, R. *Nanotechnology* **2010**, *21* (36).

(13) Xia, X.; Xie, S.; Liu, M.; Peng, H.-C.; Lu, N.; Wang, J.; Kim, M. J.; Xia, Y. *Proc. Natl. Acad. Sci.* **2013**, *110* (17), 6669–6673.

(14) Cheng, Z.; Chai, R.; Ma, P.; Dai, Y.; Kang, X.; Lian, H. **2013**.

(15) Kumar, A.; Tripathi, S. K.; Deshmukh, A. D. *Adv. Mater. Lett.* **2015**, *6* (8), 701–705.

(16) Chen, W.; Wang, Z.; Zhi, C.; Zhang, W. *Compos. Sci. Technol.* **2016**, *130*, 63–69.

(17) Cai, X.; Wang, C. L.; Chen, H. H.; Chien, C. C.; Lai, S. F.; Chen, Y. Y.; Hua, T. E.; Kempson, I. M.; Hwu, Y.; Yang, C. S.; Margaritondo, G. *Nanotechnology* **2010**, *21* (33).

(18) Tao, A.; Kim, F.; Hess, C.; Goldberger, J.; He, R.; Sun, Y.; Xia, Y.; Yang, P. *Nano Lett.* **2003**, *3* (9), 1229–1233.

(19) Laurila, T. *Phys. Scr.* **2015**, *90* (9).

(20) Ferrari, A. C.; Meyer, J. C.; Scardaci, V.; Casiraghi, C.; Lazzeri, M.; Mauri, F.; Piscanec, S.; Jiang, D.; Novoselov, K. S.; Roth, S.; Geim, A. K. *Phys. Rev. Lett.* **2006**,

97 (18), 1–4.

(21) Jones, M. R.; MacFarlane, R. J.; Lee, B.; Zhang, J.; Young, K. L.; Senesi, A. J.; Mirkin, C. A. *Nat. Mater.* **2010**, *9* (11), 913–917.

(22) Macfarlane, R. J.; Lee, B.; Jones, M. R.; Harris, N.; Schatz, G. C.; Mirkin, C. A. *Science (80-.).* **2011**, *334* (6053), 204–208.

(23) Kedia, A.; Kumar, P. S. *J. Phys. Chem. C* **2012**, *116* (44), 23721–23728.

(24) Zhang, F. *Photon Upconversion Nanomaterials*; 2015.

(25) IUPAC. *Blackwell Sci. Publ. Oxford* **2014**, 1670.

(26) Dambournet, D.; Belharouak, I.; Amine, K. *Chem. Mater.* **2010**, *22* (3), 1173–1179.

(27) Haase, M.; Schäfer, H. *Angew. Chemie - Int. Ed.* **2011**, *50* (26), 5808–5829.

(28) Johnson, N. J. J.; Korinek, A.; Dong, C.; Van Veggel, F. C. J. M. *J. Am. Chem. Soc.* **2012**, *134* (27), 11068–11071.

(29) Jalani, G.; Cerruti, M. *Nanoscale* **2015**, *7* (22), 9990–9997.

(30) Bashouti, M.; Lifshitz, E. *Inorg. Chem.* **2008**, *47* (2), 678–682.

(31) Millstone, J. E.; Hurst, S. J.; Métraux, G. S.; Cutler, J. I.; Mirkin, C. A. *Small* **2009**, *5* (6), 646–664.

(32) Ovais, M.; Raza, A.; Naz, S.; Islam, N. U.; Khalil, A. T.; Ali, S.; Khan, M. A.; Shinwari, Z. K. *Appl. Microbiol. Biotechnol.* **2017**, *101* (9), 3551–3565.

(33) Brabazon, D.; Pellicer, E.; Zivic, F.; Sort, J.; Baró, M. D.; Grujovic, N.; Choy, K. L. *Commer. Nanotechnologies-A Case Study Approach* **2017**, 1–315.

(34) Lin, J. Y.; Hsueh, Y. L.; Huang, J. J. *J. Solid State Chem.* **2014**, *214*, 2–6.

(35) Chen, J.; Zhao, J. X. *Sensors* **2012**, *12* (3), 2414–2435.

(36) Li, C.; Quan, Z.; Yang, J.; Yang, P.; Lin, J. *Inorg. Chem.* **2007**, *46* (16), 6329–6337.

(37) Wang, M.; Zhu, Y.; Mao, C. *Langmuir* **2015**, *31* (25), 7084–7090.

(38) Sanchez, C.; Rozes, L.; Ribot, F.; Laberty-Robert, C.; Grosso, D.; Sassoye, C.; Boissiere, C.; Nicole, L. *Comptes Rendus Chim.* **2010**, *13* (1–2), 3–39.

(39) Wang, S.; Sun, Z.; Yan, E.; Sun, L.; Huang, N.; Zang, W.; Ni, L.; Wang, Q.; Gao, Y.; Jiang, X.; Bai, X.; Tang, F. *Int. J. Electrochem. Sci.* **2014**, *9* (2), 549–561.

(40) Guo, X.; Zheng, D.; Hu, N. *J. Phys. Chem. B* **2008**, *112* (48), 15513–15520.

(41) Chen, X.; Wang, W.; Chen, X.; Bi, J.; Wu, L.; Li, Z.; Fu, X. *Mater. Lett.* **2009**.

(42) Mansouri, S. S.; Ghader, S. *Arab. J. Chem.* **2009**, *2* (1), 47–53.

(43) Mourdikoudis, S.; Liz-Marzán, L. M. *Chem. Mater.* **2013**, *25* (9), 1465–1476.

(44) Lu, X.; Yavuz, M. S.; Tuan, H.; Korgel, B. A.; Xia, Y. **2008**, 3–5.

(45) Zheng, N.; Fan, J.; Stucky, G. D. *J. Am. Chem. Soc.* **2006**, *128* (20), 6550–6551.

(46) Sanchez-Dominguez, M.; Pemartin, K.; Boutonnet, M. *Curr. Opin. Colloid Interface Sci.* **2012**, *17* (5), 297–305.

(47) Capek, I. *Adv. Colloid Interface Sci.* **2004**, *110* (1–2), 49–74.

(48) Buchold, D. H. M.; Feldmann, C. *Adv. Funct. Mater.* **2008**, *18* (7), 1002–1011.

(49) Mi, C.; Tian, Z.; Cao, C.; Wang, Z.; Mao, C.; Xu, S. **2011**.

(50) Wang, M.; Liu, J. L.; Zhang, Y. X.; Hou, W.; Wu, X. L.; Xu, S. K. *Mater. Lett.* **2009**, *63* (2), 325–327.

(51) Kannan, P.; Rahim, F. A.; Chen, R.; Huang, L.; Sun, H.; Kim, D. R. **2013**, 1–13.

(52) Shatrohan Lal, R. K. *J. Nanomater. Mol. Nanotechnol.* **2014**, *3* (4).

(53) Debuigne, F.; Jeunieau, L.; Wiame, M.; Nagy, J. B. *Langmuir* **2000**, *16* (20), 7605–7611.

(54) Margulis-Goshen, K.; Magdassi, S. *Curr. Opin. Colloid Interface Sci.* **2012**, *17* (5), 290–296.

(55) Chen, O.; Zhuang, J.; Guzzetta, F.; Lynch, J.; Angerhofer, A.; Cao, Y. C. *J. Am. Chem. Soc.* **2009**, 7–8.

(56) Cao, S.-W.; Zhu, Y.-J.; Chang, J. *New J. Chem.* **2008**, *32* (9), 1526.

(57) Zhang, X.; Qin, J.; Xue, Y.; Yu, P.; Zhang, B.; Wang, L.; Liu, R. *Sci. Rep.* **2014**, *4*, 4–11.

(58) Qu, B.; Jiao, Y.; He, S.; Zhu, Y.; Liu, P.; Sun, J.; Lu, J.; Zhang, X. *J. Alloys Compd.* **2016**, *658*, 848–853.

(59) Liras, M.; González-Béjar, M.; Peinado, E.; Francés-Soriano, L.; Pérez-Prieto, J.; Quijada-Garrido, I.; García, O. *Chem. Mater.* **2014**, *26* (13), 4014–4022.

(60) Tan, M. C.; Al-Baroudi, L.; Riman, R. E. *ACS Appl. Mater. Interfaces* **2011**, *3* (10), 3910–3915.

(61) Limaye, M. V; Singh, S. B.; Date, S. K.; Kothari, D.; Reddy, V. R.; Gupta, A.; Sathe,

V.; Choudhary, R. J.; Kulkarni, S. K. **2009**, 9070–9076.

(62) Mudunkotuwa, I. A.; Pettibone, J. M.; Grassian, V. H. *Environ. Sci. Technol.* **2012**, *46* (13), 7001–7010.

(63) Anbarasu, M.; Anandan, M.; Chinnasamy, E.; Gopinath, V.; Balamurugan, K. *Spectrochim. Acta - Part A Mol. Biomol. Spectrosc.* **2015**, *135*, 536–539.

(64) Mohamed, T.; Matou-Nasri, S.; Farooq, A.; Whitehead, D.; Azzawi, M. *Int. J. Nanomedicine* **2017**, *12*, 8813–8830.

(65) Fresnais, J.; Yan, M.; Courtois, J.; Bostelmann, T.; Bée, A.; Berret, J. F. *J. Colloid Interface Sci.* **2013**, *395* (1), 24–30.

(66) Muhr, V.; Wilhelm, S.; Hirsch, T.; Wolfbeis, O. S. *Acc. Chem. Res.* **2014**, *47* (12), 3481–3493.

(67) Sperling, R. a; Parak, W. J. *Philos. Trans. A. Math. Phys. Eng. Sci.* **2010**, *368* (1915), 1333–1383.

(68) Malik, V.; Petukhov, A. V.; He, L.; Yin, Y.; Schmidt, M. *Langmuir* **2012**, *28* (41), 14777–14783.

(69) Kudera, S.; Maus, L.; Zanella, M.; Pelaz, B.; Zhang, Q.; Parak, W. J.; del Pino, P.; Parak, W. J. *Ref. Modul. Mater. Sci. Mater. Eng.* **2016**, No. September 2017.

(70) Mpinga, C. N.; Eksteen, J. J.; Aldrich, C.; Dyer, L. *Hydrometallurgy* **2018**, *178* (March), 88–96.

(71) Li, J. F.; Zhang, Y. J.; Ding, S. Y.; Panneerselvam, R.; Tian, Z. Q. *Chem. Rev.* **2017**, *117* (7), 5002–5069.

(72) J. C. Boyer, N. J. J. Johnson, F. C. J. M. V. V. *Chem. Mater.* **2009**, *21*, 2010–2012.

(73) Johnson, N. J. J.; Sangeetha, N. M.; Boyer, J.-C.; van Veggel, F. C. J. M. *Nanoscale* **2010**, *2* (5), 771.

(74) Hirsh, D. A.; Johnson, N. J. J.; Van Veggel, F. C. J. M.; Schurko, R. W. *Chem. Mater.* **2015**, *27* (19), 6495–6507.

(75) Huang, X. *Opt. Mater. Express* **2016**, *6* (7), 2165.

(76) Edalat, F. **2012**, *40* (6), 1301–1315.

(77) Wen, H. Q.; Peng, H. Y.; Liu, K.; Bian, M. H.; Xu, Y. J.; Dong, L.; Yan, X.; Xu, W. P.; Tao, W.; Shen, J. L.; Lu, Y.; Qian, H. S. *ACS Appl. Mater. Interfaces* **2017**, *9* (11), 9226–9232.

(78) Li, Y.-W.; Dong, L.; Huang, C.-X.; Guo, Y.-C.; Yang, X.-Z.; Xu, Y.-J.; Qian, H.-S.

RSC Adv. **2016**, *6* (59), 54241–54248.

(79) Geitenbeek, R. G.; Prins, P. T.; Albrecht, W.; Van Blaaderen, A.; Weckhuysen, B. M.; Meijerink, A. *J. Phys. Chem. C* **2017**, *121* (6), 3503–3510.

(80) Pinho, L.; Rojas, M.; Mosquera, M. J. *Appl. Catal. B Environ.* **2015**, *178*, 144–154.

(81) Ye, X.; Cai, S.; Zheng, C.; Xiao, X.; Hua, N.; Huang, Y. *Appl. Surf. Sci.* **2015**, *345*, 279–285.

(82) Wilhelm, S.; Kaiser, M.; Wurth, C.; Heiland, J.; Carrillo-Carrion, C.; Muhr, V.; Wolfbeis, O. S.; Parak, W. J.; Resch-Genger, U.; Hirsch, T. *Nanoscale* **2015**, *7* (4), 1403–1410.

(83) Beyazit, S.; Ambrosini, S.; Marchyk, N.; Palo, E.; Kale, V.; Soukka, T.; Tse Sum Bui, B.; Haupt, K. *Angew. Chemie - Int. Ed.* **2014**, *53* (34), 8919–8923.

(84) Buso, D.; Jasieniak, J.; Lay, M. D. H.; Schiavuta, P.; Scopece, P.; Laird, J.; Amenitsch, H.; Hill, A. J.; Falcaro, P. *Small* **2012**, *8* (1), 80–88.

(85) Leguy, A.; Hu, Y.; Campoy-Quiles, M.; Alonso, M. I.; Weber, O. J.; Azarhoosh, P.; van Schilfgaarde, M.; Weller, M. T.; Bein, T.; Nelson, J.; Docampo, P.; Barnes, P. R. F. *Chem. Mater.* **2015**, *27*, 3397–3407.

(86) Yang, W.; Li, X.; Chi, D.; Zhang, H.; Liu, X. *Nanotechnology* **2014**, *25*, 482001.

(87) Mase, J.; Razgoniaev, A. *Photochem. Photobiol. …* **2015**.

(88) Cheng, L.; Yang, K.; Li, Y.; Chen, J.; Wang, C.; Shao, M.; Lee, S. T.; Liu, Z. *Angew. Chemie - Int. Ed.* **2011**, *50* (32), 7385–7390.

(89) Tachibana, Y.; Vayssieres, L.; Durrant, J. R. *Nat. Photonics* **2012**, *6* (8), 511–518.

(90) Nocera, D. G.; Nash, M. P. **2007**, *104* (42).

(91) Yan, L.; Chang, Y.-N.; Yin, W.; Liu, X.; Xiao, D.; Xing, G.; Zhao, L.; Gu, Z.; Zhao, Y. *Phys. Chem. Chem. Phys.* **2014**, *16* (4), 1576–1582.

(92) Vilela, P.; El-Sagheer, A.; Millar, T. M.; Brown, T.; Muskens, O. L.; Kanaras, A. G. *ACS Sensors* **2017**, *2* (1), 52–56.

(93) Gust, D.; Moore, T. A.; Moore, A. L. *Acc. Chem. Res.* **2009**, *42* (12), 1890–1898.

(94) Felip-León, C.; Guzzetta, F.; Julián-López, B.; Galindo, F.; Miravet, J. F. *J. Phys. Chem. C* **2017**, *121* (39).

(95) Pan, F.; Huang, M.; Song, J.; Wu, M.; Xu, M. *Chem. Phys. Lett.* **2016**, *657*, 107–112.

(96) Sanchez, C.; Julián, B.; Belleville, P.; Popall, M. *J. Mater. Chem.* **2005**, *15* (35–36), 3559–3592.

(97) Li, J.; Zhang, J. Z. *Coord. Chem. Rev.* **2009**, *253* (23–24), 3015–3041.

(98) Alivisatos, A. P. *Science (80-.).* **1996**, *271* (5251), 933–937.

(99) Woggon, U. **1997**, No. Nr. 136, 175–179.

(100) Qian, X.; Yue, D.; Tian, Z.; Reng, M.; Zhu, Y.; Kan, M.; Zhang, T.; Zhao, Y. *Appl. Catal. B Environ.* **2016**, *193*, 16–21.

(101) He, D.; Wang, L.; Li, H.; Yan, T.; Wang, D.; Xie, T. *CrystEngComm* **2011**, *13* (12), 4053.

(102) Shi, H.; Huang, X.; Tian, H.; Lv, J.; Li, Z.; Ye, J.; Zou, Z. *J. Phys. D. Appl. Phys.* **2009**, *42* (12), 0–5.

(103) Gonell, F.; Haro, M.; Sánchez, R. S.; Negro, P.; Mora-Seró, I.; Bisquert, J.; Julián-López, B.; Gimenez, S. *J. Phys. Chem. C* **2014**, *118* (21), 11279–11284.

(104) Si, H. Y.; Yuan, D.; Chen, J. S.; Chow, G. M.; Zhang, H. L. *J. Colloid Interface Sci.* **2011**, *353* (2), 569–573.

(105) Hao, S.; Chen, G.; Yang, C. *Theranostics* **2013**, *3* (5), 331–345.

(106) Liu, X.; Yan, C.-H.; Capobianco, J. A. *Chem. Soc. Rev.* **2015**.

(107) Sedlmeier, A.; Gorris, H. H. *Chem. Soc. Rev.* **2015**, *44* (6), 1156–1526.

(108) Auzel, F. *Chem. Rev.* **2004**, *104* (1), 139–173.

(109) Bednarkiewicz, A.; Nyk, M.; Samoc, M.; Strek, W. *J. Phys. Chem. C* **2010**, *114* (41), 17535–17541.

(110) Chen, G.; Yang, C.; Prasad, P. N.; Chen, N. *Acc. Chem. Res.* **2013**, *46* (7), 1474–1486.

(111) Zhao, J.; Ji, S.; Guo, H. *RSC Adv.* **2011**, *1* (6), 937.

(112) Singh-Rachford, T. N.; Castellano, F. N. *Coord. Chem. Rev.* **2010**, *254* (21–22), 2560–2573.

(113) Cheng, Y. Y.; Khoury, T.; Clady, R. G. C. R.; Tayebjee, M. J. Y.; Ekins-Daukes, N. J.; Crossley, M. J.; Schmidt, T. W. *Phys. Chem. Chem. Phys.* **2010**, *12* (1), 66–71.

(114) Sternlicht, H.; Nieman, G. C.; Robinson, G. W. *J. Chem. Phys.* **1963**, *38* (6), 1326–1335.

(115) Gnach, A.; Bednarkiewicz, A. .

(116) Lee, S. H.; Ayer, M. A.; Vadrucci, R.; Weder, C.; Simon, Y. C. *Polym. Chem.* **2014**, *5* (24), 6898–6904.

(117) Wu, S.; Han, G.; Milliron, D. J.; Aloni, S.; Altoe, V.; Talapin, D. V.; Cohen, B. E.; Schuck, P. J. *Proc. Natl. Acad. Sci.* **2009**, *106* (27), 10917–10921.

(118) Chen, C.; Li, C.; Shi, Z. *Adv. Sci.* **2016**, *3* (10).

(119) Chen, G.; Yang, C.; Prasad, P. N. *Acc. Chem. Res.* **2013**.

(120) van der Ende, B. M.; Aarts, L.; Meijerink, A. *Phys. Chem. Chem. Phys.* **2009**, *11* (47), 11081–11095.

(121) Kale, V.; Soukka, T.; Hölsä, J.; Lastusaari, M. *J. Nanoparticle Res.* **2013**, *15* (8).

(122) Dieke, G. H. *Spectra and Energy Levels of Rare Earth Ions in Crystals*, 3rd ed.; Interscience, A. I. of P. H., Ed.; McGraw-Hill, 1968.

(123) Ramasamy, P.; Manivasakan, P.; Kim, J. *RSC Adv.* **2014**, *4* (66), 34873–34895.

(124) Joubert, M.-F. *Opt. Mater. (Amst).* **1999**, *11* (2–3), 181–203.

(125) Wang, F.; Liu, X. *Chem. Soc. Rev.* **2009**, *38* (4), 976.

(126) Auzel, F.; Chen, Y. *J. Lumin.* **1995**, *65* (1), 45–56.

(127) Rathaiah, M.; Martín, I. R.; Babu, P.; Linganna, K.; Jayasankar, C. K.; Lavín, V.; Venkatramu, V. *Opt. Mater. (Amst).* **2015**, *39*, 16–20.

(128) Xiao, Q.; Zhu, H.; Tu, D.; Ma, E.; Chen, X. *J. Phys. Chem. C* **2013**, *117* (20), 10834–10841.

(129) Zhang, Q. Y.; Li, T.; Jiang, Z. H.; Ji, X. H.; Buddhudu, S. *Appl. Phys. Lett.* **2005**, *87* (17), 1–3.

(130) Roeser, F.; Jauregui, C.; Limpert, J.; Tünnermann, A. *Opt. Express* **2008**, *16* (22), 17310.

(131) Boyer, J.-C.; van Veggel, F. C. J. M. *Nanoscale* **2010**, *2* (8), 1417.

(132) Wang, D.; Xue, B.; Kong, X.; Tu, L.; Liu, X.; Zhang, Y.; Chang, Y.; Luo, Y.; Zhao, H.; Zhang, H. *Nanoscale* **2015**, *7* (1), 190–197.

(133) Meyssamy, H.; Riwotzki, K.; Kornowski, A.; Naused, S.; Haase, M. *Adv. Mater.* **1999**, *11* (10), 840–844.

(134) Jang, H. S.; Woo, K.; Lim, K. *Opt. Express* **2012**, *20* (15), 17107–17118.

(135) Dong, H.; Sun, L.-D. D.; Yan, C.-H. H. *Nanoscale* **2013**, *5* (13), 5703–5714.

(136) Mai, H. X.; Zhang, Y. W.; Sun, L. D.; Yan, C. H. *J. Phys. Chem. C* **2007**, *111* (37), 13721–13729.

(137) Yin, A.; Zhang, Y.; Sun, L.; Yan, C. *Nanoscale* **2010**, *2* (6), 953.

(138) Salley, G. M.; Valiente, R.; Guedel, H. U. *J. Lumin.* **2001**, *94–95*, 305–309.

(139) Gargas, D. J.; Chan, E. M.; Ostrowski, A. D.; Aloni, S.; Virginia, M.; Altoe, P.; Barnard, E. S.; Sanii, B.; Urban, J. J.; Milliron, D. J.; Cohen, B. E.; Schuck, P. J. .

(140) Mccusker, L. B.; Dreele, R. B. Von; Cox, D. E.; Loue È R D, D.; Scardi, P. *Int. Union Crystallogr. J. Appl. Crystallogr. J. Appl. Cryst* **1999**, *32*, 36–50.

(141) Massa, W. *Crystal structure determination*, 2nd transl.; Gould, R. O., Ed.; Springer Berlin / Heidelberg: Berlin Heidelberg, 2013.

(142) Bunzli, J. G.; Eliseeva, S. V. *Springer Ser. Fluoresc.* **2011**, No. July 2010, 1–45.

(143) Xue, X.; Uechi, S.; Tiwari, R. N.; Duan, Z.; Liao, M.; Yoshimura, M.; Suzuki, T.; Ohishi, Y. *Opt. Mater. Express* **2013**, *3* (7), 989–999.

(144) Nadort, A.; Zhao, J.; Goldys, E. M. *Nanoscale* **2016**, *8* (27), 13099–13130.

(145) Soukka, T.; Kuningas, K.; Rantanen, T.; Haaslahti, V.; Lövgren, T. *J. Fluoresc.* **2005**, *15* (4), 513–528.

(146) Pichaandi, J.; Van Veggel, F. C. J. M.; Raudsepp, M. *ACS Appl. Mater. Interfaces* **2010**, *2* (1), 157–164.

(147) Gao, Y.; Hu, Y.; Ren, P.; Zhou, D.; Qiu, J. *J. Eur. Ceram. Soc.* **2016**, *36* (11), 2825–2830.

(148) Kannan, P.; Abdul Rahim, F.; Chen, R.; Teng, X.; Huang, L.; Sun, H.; Kim, D. H. *ACS Appl. Mater. Interfaces* **2013**, *5* (9), 3508–3513.

(149) Cooper, D. R.; Kudinov, K.; Tyagi, P.; Hill, C. K.; Bradforth, S. E.; Nadeau, J. L. *Phys. Chem. Chem. Phys.* **2014**, *16* (24), 12441–12453.

(150) Page, R. H.; Schaffers, K. I.; Waide, P. A.; Tassano, J. B.; Payne, S. A.; Krupke, W. F.; Bischel, W. K. *J. Opt. Soc. Am. B* **1998**, *15* (3), 996–1008.

(151) Rabouw, F. T.; Prins, P. T.; Villanueva-Delgado, P.; Castelijns, M.; Geitenbeek, R. G.; Meijerink, A. *ACS Nano* **2018**, acsnano.8b01545.

(152) Arppe, R.; Hyppänen, I.; Perälä, N.; Peltomaa, R.; Kaiser, M.; Würth, C.; Christ, S.; Resch-Genger, U.; Schäferling, M.; Soukka, T. *Nanoscale* **2015**, *7* (27), 11746–11757.

(153) Yuan, D.; Tan, M. C.; Riman, R. E.; Chow, G. M. *J. Phys. Chem. C* **2013**, *117* (25), 13297–13304.

(154) Carlos, L. D.; Ferreira, R. a S.; de Zea Bermudez, V.; Julián-López, B.; Escribano, P. *Chem. Soc. Rev.* **2011**, *40* (2), 536–549.

(155) Correia, S. F. H.; De Zea Bermudez, V.; Ribeiro, S. J. L.; André, P. S.; Ferreira, R. a S.; Carlos, L. D. *J. Mater. Chem. A* **2014**, *2* (16), 5580–5596.

(156) Binnemans, K. *Chem. Rev.*, **2009**, *109*, 4283–4374.

(157) Esipova, T. V; Ye, X.; Collins, J. E.; Sakadži, S.; Mandeville, E. T.; Murray, C. B.; Vinogradov, S. A. .

(158) Pollnau, M.; Gamelin, D.; Lüthi, S.; Güdel, H.; Hehlen, M. *Phys. Rev. B - Condens. Matter Mater. Phys.* **2000**, *61* (5), 3337–3346.

(159) Tang, Y.; Di, W.; Zhai, X.; Yang, R.; Qin, W. *ACS Catal.* **2013**, *3* (3), 405–412.

(160) Wolfbeis, O. S. *Chem. Soc. Rev. Chem. Soc. Rev* **2015**, *44* (44), 4743–4768.

(161) Teshima, K.; Lee, S. *Cryst. Growth Des.* **2011**, *11*, 995–999.

(162) Chen, G.; Ohulchanskyy, T. Y.; Kumar, R.; Ågren, H.; Prasad, P. N. *ACS Nano* **2010**, *4* (6), 3163–3168.

(163) Du, H.; Zhang, W.; Sun, J. *J. Alloys Compd.* **2011**, *509* (7), 3413–3418.

(164) Misiak, M.; Skowicki, M.; Lipiński, T.; Kowalczyk, A.; Prorok, K.; Arabasz, S.; Bednarkiewicz, A. *Nano Res.* **2017**, *10* (10), 3333–3345.

(165) Pedroni, M.; Piccinelli, F.; Passuello, T.; Giarola, M.; Mariotto, G.; Polizzi, S.; Bettinelli, M.; Speghini, A. *Nanoscale* **2011**, *3* (4), 1456.

(166) Peijzel, P. S.; Meijerink, A.; Wegh, R. T.; Reid, M. F.; Burdick, G. W. *J. Solid State Chem.* **2005**, *178* (2 SPEC. ISS.), 448–453.

(167) Zheng, W.; Huang, P.; Tu, D.; Ma, E.; Zhu, H.; Chen, X. *Chem. Soc. Rev.* **2015**, *44* (6), 1379–1415.

(168) Zhan, Q.; He, S.; Qian, J.; Cheng, H.; Cai, F. *Theranostics* **2013**, *3* (5), 306–316.

(169) Xue, X.; Wang, F.; Liu, X. *J. Mater. Chem.* **2011**, *21* (35), 13107.

(170) Wang, M.; Li, M.; Yang, M.; Zhang, X.; Yu, A.; Zhu, Y.; Qiu, P.; Mao, C. *Nano Res.* **2015**, *8* (6), 1800–1810.

(171) Menyuk, N.; Dwight, K.; Pierce, J. W. *Appl. Phys. Lett.* **1972**, *21* (4), 159–161.

(172) Kano, T. 1561–1564.

(173) Auzel, F. *J. Electrochem. Soc.* **1975**, *122* (1), 101.

(174) Zhang, Y.; Pasquale, N.; Lee, K. B. *Angew. Chemie - Int. Ed.* **2014**, *53* (52).

(175) Zhang, X. D.; Jin, X.; Wang, D. F.; Xiong, S. Z.; Geng, X. H.; Zhao, Y. *Phys. Status*

Solidi Curr. Top. Solid State Phys. **2010**, *7* (3–4), 1128–1131.

(176) Hoven, G. Van Den; Snoeks, E. *J. Appl. …* **1996**, *79* (3), 12–14.

(177) Huang, X.; Cutinha, N.; Alcázar de Velasco, A.; Chandler, P. .; Townsend, P. . *Nucl. Instruments Methods Phys. Res. Sect. B Beam Interact. with Mater. Atoms* **1998**, *142*, 50–60.

(178) Park, B. J.; Hong, A. R.; Park, S.; Kyung, K. U.; Lee, K.; Jang, H. S. *Sci. Rep.* **2017**, *7* (November 2016), 1–11.

(179) Wang, M.; Abbineni, G.; Clevenger, A.; Mao, C.; Xu, S. *Nanomedicine Nanotechnology, Biol. Med.* **2011**, *7* (6), 710–729.

(180) Sedlmeier, A.; Gorris, H. H. *Chem. Soc. Rev.* **2015**, *44* (2009), 1156–1526.

(181) Yu, X.; Li, M.; Xie, M.; Chen, L.; Li, Y.; Wang, Q. *Nano Res.* **2010**, *3* (1), 51–60.

(182) Jia, X.; Yin, J.; He, D.; He, X.; Wang, K.; Chen, M.; Li, Y. *J. Biomed. Nanotechnol.* **2013**, *9* (12), 2063–2072.

(183) Wu, X.; Hu, P.; Hu, S.; Chen, Z.; Yan, H.; Tang, Z.; Xi, Z.; Yu, Y.; Dai, G.; Liu, Y. *J. Rare Earths* **2016**, *34* (2), 208–220.

(184) Peng, J.; Sun, Y.; Liu, Q.; Yang, Y.; Zhou, J.; Feng, W.; Zhang, X.; Li, F. *Nano Res.* **2012**, *5* (11), 770–782.

(185) Wilhelm, S. *ACS Nano* **2017**, *11* (11), 10644–10653.

(186) Hischemöller, A.; Nordmann, J.; Ptacek, P.; Mummenhoff, K.; Haase, M. *J. Biomed. Nanotechnol.* **2009**, *5* (3), 278–284.

(187) Vetrone, F.; Naccache, R.; Zamarrón, A.; De La Fuente, A. J.; Sanz-Rodríguez, F.; Maestro, L. M.; Rodriguez, E. M.; Jaque, D.; Sole, J. G.; Capobianco, J. A. *ACS Nano* **2010**, *4* (6), 3254–3258.

(188) Wang, H. Q.; Nann, T. *ACS Nano* **2009**.

(189) Na, H.; Woo, K.; Lim, K.; Jang, H. S. *Nanoscale* **2013**, *5* (10), 4242–4251.

(190) Dong, H.; Sun, L.-D. D.; Yan, C.-H. H. *Chem. Soc. Rev.* **2015**, *44* (6), 1608–1634.

(191) Klier, D. T.; Kumke, M. U. *J. Mater. Chem. C* **2015**, *3* (42), 11228–11238.

(192) Wang, F.; Liu, X. *Acc. Chem. Res.* **2014**.

(193) Naccache, R.; Yu, Q.; Capobianco, J. A. *Adv. Opt. Mater.* **2015**, *3* (4), 482–509.

(194) Shan, J.; Ju, Y. *Nanotechnology* **2009**, *20* (27), 275603.

(195) Wu, S.; Liu, Y.; Chang, J.; Zhang, S. *CrystEngComm* **2014**, *16* (21), 4472–4477.

(196) Wang, F.; Han, Y.; Lim, C. S.; Lu, Y.; Wang, J.; Xu, J.; Chen, H.; Zhang, C.; Hong, M.; Liu, X. *Nature* **2010**, *463* (7284), 1061–1065.

(197) Niu, N.; He, F.; Gai, S.; Li, C.; Zhang, X.; Huang, S.; Yang, P. .

(198) Tang, J.; Chen, L.; Li, J.; Wang, Z.; Zhang, J.; Zhang, L.; Luo, Y.; Wang, X. *Nanoscale* **2015**, *7* (35), 14752–14759.

(199) Tian, G.; Gu, Z.; Zhou, L.; Yin, W.; Liu, X.; Yan, L.; Jin, S.; Ren, W.; Xing, G.; Li, S.; Zhao, Y. *Adv. Mater.* **2012**, *24* (9), 1226–1231.

(200) Ahmad, S.; Nagarajan, R.; Raj, P.; Prakash, G. V. *Inorg. Chem.* **2014**, *53* (19), 10257–10265.

(201) Gao, S.; Qiu, P.; Zhou, N.; Chen, H.; Zhang, C.; Gao, G.; Cui, D. *Nanoscale* **2013**, *5* (207890), 11512–11525.

(202) Shyichuk, A. **2015**.

(203) Liu, Q.; Sun, Y.; Yang, T.; Feng, W.; Li, C.; Li, F. *J. Am. Chem. Soc* **2011**, *133*, 17122–17125.

(204) Zhang, F.; Li, J.; Shan, J.; Xu, L.; Zhao, D. *Chem. - A Eur. J.* **2009**, *15* (41), 11010–11019.

(205) Shan, J.; Qin, X.; Yao, N.; Ju, Y. *Nanotechnology* **2007**, *18* (44).

(206) Gainer, C. F.; Romanowski, M. *J. Innov. Opt. Health Sci.* **2014**, *7* (2), 1330007.

(207) Wang, L.; Li, Y. 1–4.

(208) Wang, L.; Li, Y. *Nano Lett.* **2006**, *6* (8), 1645–1649.

(209) Wang, X.; Zhuang, J.; Peng, Q.; Li, Y. *Nature* **2005**, *437* (7055), 121–124.

(210) Li, P.; Peng, Q.; Li, Y. *Adv. Mater.* **2009**, *21* (19), 1945–1948.

(211) Zhuang, J.; Liang, L.; Sung, H. H. Y.; Yang, X.; Wu, M.; Williams, I. D. *Inorg. Chem.* **2007**, *46* (13), 2324–2329.

(212) Panda, A. B.; Glaspell, G.; El-Shall, M. S. *J. Phys. Chem. C* **2007**, *111* (5), 1861–1864.

(213) Bondioli, F.; Ferrari, A. M.; Leonelli, C.; Siligardi, C.; Pellacani, G. C. *J. Am. Ceram. Soc.* **2001**, *84* (11), 2728–2730.

(214) Kandpal, N. D.; Sah, N.; Loshali, R.; Joshi, R.; Prasad, J. *J. Sci. Ind. Res.* **2014**, *73* (February), 87–90.

(215) Yan, C.; Zhao, H.; Perepichka, D. F.; Rosei, F. *Small* **2016**, 3888–3907.

(216) Boyer, J.-C.; Vetrone, F.; Cuccia, L. A.; Capobianco, J. A. *J. Am. Chem. Soc.* **2006**, *128* (23), 7444–7445.

(217) Y, N. L.; Yb, D.; Zhuang, J.; Liang, L.; Sung, H. H. Y.; Yang, X.; Wu, M.; Williams, I. D. *Inorg. Chem.* **2007**, *46* (13), 2324–2329.

(218) Walton, R. I. *Chem. Soc. Rev.* **2002**, *31*, 230–238.

(219) Chen, Z.; Tian, Q.; Song, Y.; Yang, J.; Hu, J. *J. Alloys Compd.* **2010**, *506* (2), 12–14.

(220) Demazeau, G. *Res. Chem. Intermed.* **2011**, *37* (2–5), 107–123.

(221) Dawson, W. J. *Am. Ceram. Soc. Bull.* **1988**, *67* (10), 1673–1678.

(222) Rahman, P.; Green, M. *Nanoscale* **2009**, *1* (2), 214–224.

(223) Li, C.; Lin, J. *J. Mater. Chem.* **2010**, *20* (33), 6831.

(224) Chang, H.; Xie, J.; Zhao, B.; Liu, B.; Xu, S.; Ren, N.; Xie, X.; Huang, L.; Huang, W. *Nanomaterials* **2015**, *5*, 1–25.

(225) Yang, Y.; Zhou, P.; Xu, W.; Xu, S.; Jiang, Y.; Chen, X.; Song, H. *J. Mater. Chem. C* **2016**, *4* (4), 659–662.

(226) Budijono, S. J.; Shan, J.; Yao, N.; Miura, Y.; Hoye, T.; Austin, R. H.; Ju, Y.; Prud'Homme, R. K. *Chem. Mater.* **2010**, *22* (2), 311–318.

(227) Ge, W.; Zhang, X. R.; Liu, M.; Lei, Z. W.; Knize, R. J.; Lu, Y. *Theranostics* **2013**, *3* (4), 282–288.

(228) Jin, L. M.; Chen, X.; Siu, C. K.; Wang, F.; Yu, S. F. *ACS Nano* **2017**, *11* (1), 843–849.

(229) Saboktakin, M. **2013**.

(230) Dong, B.; Xu, S.; Sun, J.; Bi, S.; Li, D.; Bai, X.; Wang, Y.; Wang, L.; Song, H. *J. Mater. Chem.* **2011**, *21* (17), 6193.

(231) Chen, H.; Guan, Y.; Wang, S.; Ji, Y.; Gong, M.; Wang, L. *Langmuir* **2014**, *30* (43), 13085–13091.

(232) Shen, J.; Chen, G.; Ohulchanskyy, T. Y.; Kesseli, S. J.; Buchholz, S.; Li, Z.; Prasad, P. N.; Han, G. *Small* **2013**, *9* (19), 3213–3217.

(233) Zhou, L.; Wang, R.; Yao, C.; Li, X.; Wang, C.; Zhang, X.; Xu, C.; Zeng, A.; Zhao, D.; Zhang, F. *Nat Commun* **2015**, *6*, 1–10.

(234) Sun, Y.; Zhou, H. C. *Sci. Technol. Adv. Mater.* **2015**, *16* (5).

(235) Hongren, L.; Feng, L.; Aimin, D. *Luminescence* **2015**, *30* (6), 740–744.

(236) Shan, S.; Wang, X.; Jia, N. **2011**, 3–7.

(237) Trickett, K.; Brice, H.; Myakonkaya, O.; Eastoe, J.; Rogers, S. E.; Heenan, R. K.; Grillo, I. *Soft Matter* **2010**, *6* (6), 1291–1296.

(238) Escribano, P.; Julián-López, B.; Planelles-Aragó, J.; Cordoncillo, E.; Viana, B.; Sanchez, C. *J. Mater. Chem.* **2008**, *18* (1), 23.

(239) Peveler, W. J.; Bear, J. C.; Southern, P.; Parkin, I. P. *Chem. Commun.* **2014**, *50* (92), 14418–14420.

(240) Sangeetha, N. M.; Maitra, U. *Chem. Soc. Rev.* **2005**, *34* (10), 821–836.

(241) Yan, X.; Cui, Y.; He, Q.; Wang, K.; Li, J. *Adv. Mater.* **2008**, *20* (23), 1522–1526.

(242) Gaponik, N.; Wolf, A.; Marx, R.; Lesnyak, V.; Schilling, K.; Eychmüller, A. *Adv. Mater.* **2008**, *20* (22), 4257–4262.

(243) Bardelang, D.; Zaman, M. B.; Moudrakovski, I. L.; Pawsey, S.; Margeson, J. C.; Wang, D.; Wu, X.; Ripmeester, J. A.; Ratcliffe, C. I.; Yu, K. *Adv. Mater.* **2008**, *20* (23), 4517–4520.

(244) Srinivasan, S.; Babu, S. S.; Praveen, V. K.; Ajayaghosh, A. *Communications* **2008**, 5746–5749.

(245) Nobusawa, K.; Ikeda, A.; Kikuchi, J. I.; Kawano, S. I.; Fujita, N.; Shinkai, S. *Angew. Chemie - Int. Ed.* **2008**, *47* (24), 4577–4580.

(246) Duan, P.; Yanai, N.; Nagatomi, H.; Kimizuka, N. *J. Am. Chem. Soc.* **2015**, *137* (5), 1887–1894.

(247) Singh, A. V. *Pharmacologyonline* **2011**, *1* (May), 666–674.

(248) Kaur, P.; Garg, T.; Rath, G.; Murthy, R. S. R.; Goyal, A. K. *Drug Deliv.* **2016**, *23* (3), 727–738.

(249) Ladj, R.; Bitar, A.; Eissa, M. M.; Fessi, H.; Mugnier, Y.; Le Dantec, R.; Elaissari, A. *Int. J. Pharm.* **2013**, *458* (1), 230–241.

(250) Wang, H. J.; Shrestha, R.; Zhang, Y. *Part. Part. Syst. Charact.* **2014**, *31* (2), 228–235.

(251) Bazylińska, U.; Wawrzyńczyk, D.; Kulbacka, J.; Fraçkowiak, R.; Cichy, B.; Bednarkiewicz, A.; Samoć, M.; Wilk, K. A. *Sci. Rep.* **2016**, *6* (April).

(252) Niu, N.; He, F.; Gai, S.; Li, C.; Zhang, X.; Huang, S.; Yang, P.; Wang, H. Q.; Nann, T.; Panda, A. B.; Glaspell, G.; El-Shall, M. S.; Niu, N.; He, F.; Gai, S.; Li, C.; Zhang, X.; Huang, S.; Yang, P.; Mi, C.; Tian, Z.; Cao, C.; Wang, Z.; Mao, C.; Xu, S. *J. Mater. Chem.* **2012**, *22* (40), 21613.

Chapter 2

Rationalizing Crystals Size and Phase: Impact of Several Reaction Parameters on the Solvothermal Synthesis of $NaYF_4$:Yb,Ln

2.1. Solvothermal synthesis of UC Nano $NaYF_4$:Yb,Ln

2.1.1. Fundamentals and antecedents

Rabenau defined hydrothermal synthesis as the use of water as a solvent in a sealed reaction container when the temperature is raised above 100 °C. Clearly the definition can be extended further to solvothermal chemistry being the use of a sealed reaction vessel and temperature above the boiling point of the solvent used. Under these conditions, autogenous pressure (i.e. self-developing and not externally applied) is developed. The pressure within the sealed reaction container is found to increase dramatically with temperature, but also will depend on other experimental factors, such as the percentage fill of the vessel and any dissolved salts.[1]

Solvothermal synthesis is one of the most used synthetic bottom-up routes for preparation of several inorganic nanomaterials.[1–8] It presents advantages over glass-based synthetic techniques, such as the formation of autogenous pressure which helps the formation of crystals, and these conditions of higher pressure at a defined temperature are impossible, or, at least very hard to reach (or handle) with normal laboratory glassware reactions (risk of glass breaking, explosions…) because the solvent or the mixtures must be above their boiling points.[1,7] The formation of the autogenous pressure, therefore, need a very robust and thick autoclave systems, built to be resistant to the dramatic conditions arising in solvothermal reactions.

The autoclave armatures are built with stainless steel, in order to be resistant to corrosion and provide the necessary safety conditions to handle the conditions of pressure and temperature under which the reaction is carried. Within the stainless armature is lodged a Teflon-lined reactor where the reaction takes place. The Teflon plastic gives chemical inertia to the system (hard to react even at very acidic or basic conditions), avoiding container-based reaction contamination. The passages to build the complete autoclave system are presented in Figure 2.1.

Figure 2.1: The mounting steps for the autoclave vessel ready to be introduced in the oven.

The autogenous pressure formed within the sealed autoclave system under high temperatures is generated by the vapors of the solvent or mixtures which are often beyond their boiling point, through a gas-liquid equilibrium and depends directly from the solvent or the mixture of solvents and the chemicals dissolved within. For each model of Teflon-lined vessel, there is a maximum value of filling or maximum filling factor (defined by the factory maker) to avoid over-pressurization of the autoclave. In general, it ranges between 65-75% of the vessel's capacity.

In most cases, it is possible to estimate pressure at the reaction temperature through parametric models[1,7], depending on the solvent or mixture used and its (or theirs) physico-chemical characteristics. The most useful parameter to estimate the pressure is the *acentric factor*, first proposed by Pitzer[9] as a measure of the amount by which the thermodynamic properties of a particular substance differ from those predicted by the Principle of the Corresponding States. This principle strictly applies only to a fluid (liquid or gas) comprised of spherical molecules. Fluids containing nonspherical molecules, or those with polar groups, show systematic deviations in their thermodynamic properties from their spherical counterparts. It is these deviations which are correlated with the acentric factor.

The acentric factor is defined as:

$$\omega = -1.000 - log_{10}\frac{P_\sigma}{P^c} \qquad (2.1)$$

Where -1.000 is a coefficient (that may vary depending on the deviation of the solvent from being formed of spherical molecules) and where P^c is the critical pressure and P_σ is the vapor pressure at temperature T where $T/T^c = 0.7$ and T^c is the critical temperature. (http://www.thermopedia.com/content/287/).

In terms of practical considerations, when hydro(solvo)thermal synthesis is employed, the most revealing physico-chemical data are those describing the pressure developed inside a sealed reaction vessel as a function of percentage fill of the container and the temperature employed. Figure 2.2 shows a graph obtained from these data (using water as only solvent) and demonstrates first the dramatic rise in pressure when high percentage fill of reaction vessel is used, and second how the pressure inside the reaction container can be controlled by choice of temperature and/or the volume of solvent used. Modeling pressure and temperature within solvothermal autoclaves synthesis permits to draw improved phase diagrams for the crystallization of

nanomaterials; most modern autoclaves, however, permit to read directly the inner vessel temperature and pressure.

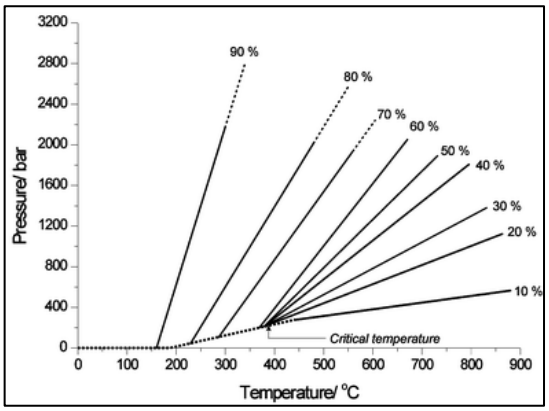

Figure 2.2: Pressure as a function of temperature and percentage fill of water in a sealed vessel (from Rabenau).[1]

The hydro- and solvothermal process is used to prepare materials with different geometries, sizes and morphologies (thin films, bulk powders, single crystals and nanocrystals with 1D, 2D and 3D extension), which can be controlled by manipulating the solvent supersaturation, concentration of the reagents, reaction time and temperature, etc. This method can be used to prepare thermodynamically stable and metastable states including novel materials that cannot be easily formed from other synthetic routes.[4,10,11] Besides the great versatility for inorganic crystals' synthesis, other advantages include scaling-up of reactions and promotion of larger recovery yields.[12,13]

However, as all synthetic routes, this one is not, as well, exempted by drawbacks. Most common autoclaves lack of stirring device and do not allow homogeneous mixing during reaction; furthermore, do not permit an accurate reading of reaction conditions of pressure and temperature: To have an estimate idea of the temperature it is possible to read the nominal temperature on the screen of the ovens. However, in most cases, this assumption cannot be valid; an inhomogeneous heat gradient in the oven heating room must be considered. This heat gradient may substantially change the synthetic conditions within the reaction vessel.

Moreover, the strict limitations inherent to construction of the autoclave reactor lack of direct observation of the reaction evolution (e.g. color changes, bubble formation, rapid evaporation, formation of precipitates etc.). Another variable, which must be set, is reaction time because the thermal inertia of the autoclave (slow cooling rate of

the stainless steel recipient) does not permit a perfect control on the real reaction end-point.

Furthermore, the use of relatively high temperatures, very often far beyond the boiling points of common solvents, makes solvothermal syntheses need high-boiling solvents: low-boiling solvents will tend to escape under gas form. This issue will limit the range of usable solvents for the solvothermal synthesis, and force the scientists to think through the reaction and the conditions to use to reach the desired materials.

All those issues can be partially overcome through iterative analysis of reaction parameters, which can lead, finally, to a nucleation and growth model of nanomaterials in function of the solvothermal parameters, solvent mixtures and inorganic precursors.

Solvothermal synthesis is, generally, a slow process (hours, if not days), as already described, and in those conditions, the crystal formation is mostly thermodynamically controlled. However, the synthesis of small nanoparticles in solution is essentially a kinetically controlled process.[1,7,10] Therefore, special precautions must be taken into account when the crystal presents two or more lattice structures that are both stable: shorter times and low temperatures lead to the kinetically more stable phase and larger times and higher temperatures promote the phase transition towards the formation of the thermodynamically stable phase, and often accompanied of large sized-crystals.

In any case, solvothermal syntheses produce agglomeration and/or coalescence and polydispersity of the nanocrystals. Sometimes, polycrystallinity is an easy outcome from wrongly estimated conditions of nucleation and growth of nanocrystals. All these issues arise, among other reasons, because of the lack of agitation during solvothermal reaction.

Solvothermal preparation of upconverting nanostructures based on rare-earth ions doped $NaYF_4$ was developed by Wang et al. mentioning it first in 2005 and studied with more details in 2006[14] The reaction was based on liquid–solid–solution (LSS) growth of the particles. The synthesis was based on a phase transfer and separation occurring at the interfaces of the liquid–solid and solid–solution phases. The LSS reaction was initially thought for the preparation of small nanoparticles of noble metals to use as plasmon resonators. However, this LSS phase transfer and separation

process was extended to the synthesis of nanocrystals with a variety of compositions, including up-converting $NaYF_4$, when including NaF or NH_4F as source of F^- ions.[15]

This hydro(solvo)thermal route used sodium linoleate, linoleic acid, and ethanol which were added to aqueous solutions of lanthanide nitrates, as precursors at the core of the particles, and NaF or NH_4HF_2 as source of Fluorine. In the first case NaF was used also as a source of Na^+ ions. Reactions were performed at 100–200°C for about 8–10 h. The obtained $NaYF_4$ NPs were easily dispersible in nonpolar solvents such as cyclohexane and toluene and showed a spherical morphology with a very narrow size distribution, tunable from 6 to 10 nm by increasing the reaction temperature from 100 to 180°C. [16]

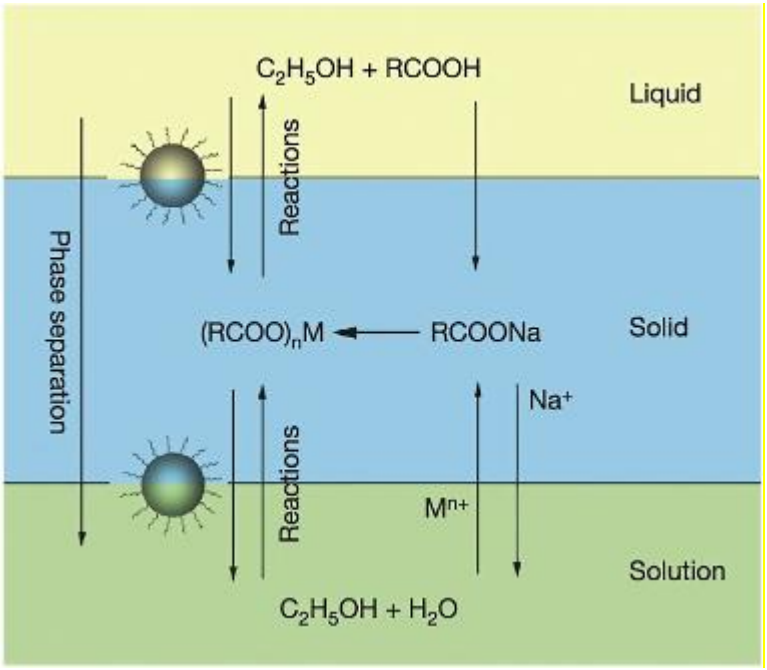

Figure 2.3: Liquid-solid-solution phase transfer synthetic strategy. Adapted from Wang *et al.* [14]

Although the LSS method brought improvements to the size and morphology of the NPs, the $NaYF_4$ particles obtained were synthesized in the α-phase with relatively low luminescence intensity.

The preparation of up-converting $NaYF_4$ structures through hydrothermal synthesis has been reported to create either very small (about 5 nm in diameter) nanoparticles

with cubic lattices[17] or very large structures (from about 200 nm to more than 2 μm) with hexagonal phase[18,19], as shown in Figure 2.4.

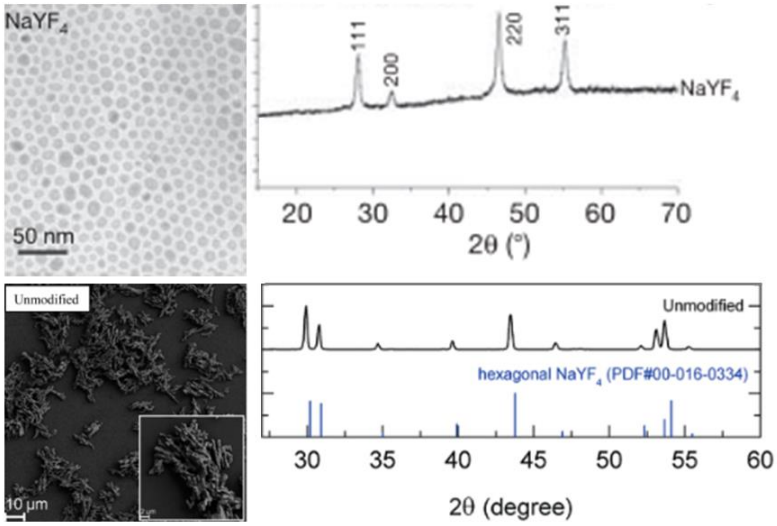

Figure 2.4: Hydro(solvo)thermal synthesis of UCNPs size 6-10 nm cubic (**upper left:** TEM image and **upper right:** XRD pattern, adapted from *Wang et al.*[14]) and large (2.2-2.7 μm) hexagonal crystals (**lower left:** SEM image and **lower right**: XRD pattern, adapted from Tan *et al.*[19])

Zhang and coworkers have reported hydrothermal preparation of up-converting $NaYF_4$, studying several parameters, and using oleic acid as stopper for the growth of the nanomaterials. Variation of several parameters has permitted to obtain various geometries and phases, as in Table 2.1. This study has allowed drawing a shape-parameter dependent plot where each of the geometry can be related to a particular variation of parameters.

Composition	Temperature (°C)	Time (h)	Phase	Shape	Size (nm)
$NaYF_4$	100	12	Cubic	Polyhedron	5.1±1.6
	180	48	Hexagonal	Disk	90±13x510±21
	230	12	Hexagonal	Tube	250±15x500±17

Table 2.1: Phase, shape, and size of $NaYF_4$ nanocrystals under different synthesis conditions. Adapted from Zhang *et al.*[20]

Riman and coworkers have shown that under hydrothermal conditions, large crystals, rod-shaped of 2.2-2.7 μm have been formed, and whose aggregation/optical properties are strongly dependent on the surfactant binding the surface of the crystals[19].

Li and coworkers have prepared several $NaMF_4$ where M were rare-earth metal ions, including Y^{3+} under hydrothermal conditions, obtaining hexagonal, micrometer-sized structures and studying the growth of the crystals and the effect of the surfactants binding the surface.[21]

However, not so many studies have been provided with solvothermal chemistry for the preparation of upconverting $NaYF_4$ nanocrystals. The most representative example of hydro(solvo)thermal synthesis is reported by Li and coworkers[21] who reported on a general "liquid-solid-solution (LSS)" (previously presented by Wang and coworkers[14]) strategy for the synthesis of monodisperse nanoparticles, whereby the reaction, phase transfer and separation take place at the interfaces.

To address the issue of spatial confinement for the formation and growth of small-sized nanomaterials, the use of labile precursors and surfactants such as ethylenediamine tetraacetic acid (EDTA)[22], cetyltrimethylammonuim bromide (CTAB)[8] or oleic acid (OA)[21] have been included. In the latter case The authors attributed this to the binding of the OA surfactant to surfaces that are parallel to the c-axis of the growing crystallites, which renders the epitaxial growth along the <001> directions and results in nanorods.[21]

A more interesting strategy is the use of water in oil (W/O) or oil in water (O/W) emulsions (figure 2.5).[23] The microemulsion method, for the preparation of nanoparticles utilizes the fact that the small size of reverse micelles, produced by certain combinations of water, oil (usually simple long-chain hydrocarbons), surfactant (which are amphiphilic molecules that are composed of long-chain organic molecules with a hydrophilic head and lipophilic tail), and an alcohol- or amine-based cosurfactants. These three-component systems are subject to continuous Brownian motion and thus frequent collisions, even at room temperature. A relatively small fraction of these collisions, e.g. one in thousand, results in the formation of a short-lived dimer, that during its ~100 ns lifetime permit the two aggregated reverse micelles exchange the contents of ions / crystallites dissolved within their aqueous cores before decoalescing, resulting in the eventual equilibrium distribution of all the contents[23]. In the preparation of nanoparticles of a definite shape/geometry, particular attention is placed on surfactants, which are often used to stabilize emulsions, and

generally are the ones that can specifically bind to particular crystal facets, leading to an alteration of the surface energies of the crystallographic structures and their relative growth rates[23].

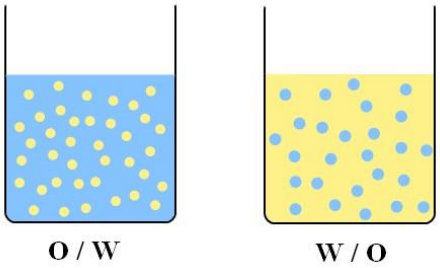

Figure 2.5: O/W and W/O emulsions (https://www.toppr.com/guides/chemistry/surface-chemistry/emulsions/).

The choice of surfactants in the emulsions is crucial for the formation of nanocrystals with specific surface properties. In fact, the use different surfactants lead to different results that alter the physical properties of the final product[19] as compared to naked particles. In Figure 2.6, the optical effects on UC microcrystals emissions provided by different organic surfactants capping the surface of the crystals are described.[19]

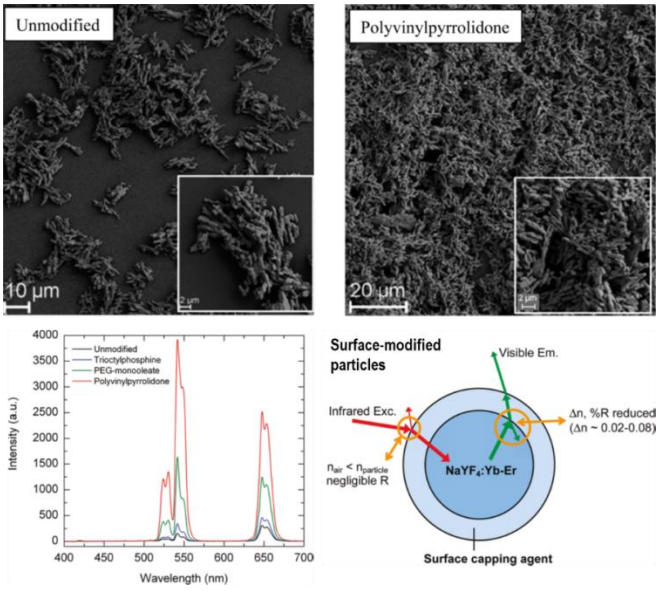

Figure 2.6: Effects of the surfactants grafted on the surfaces of UC microcrystals in the morphology (**A**- SEM images) and optical emission (**B**- UC emission spectra). **C)** Schematic

representation of reducing reflectance losses by reducing refractive index mismatches with surface capping agents[19].

It is evident, for example, that the grafting of polyvynilpyrrolidone (PVP) promotes a significant enhancement of the UC emission in comparison to the "naked" crystals and those coated with trioctylphosphine or PEG-monooleate. These $NaYF_4$ crystals show approximately the same size (2.20 to 2.7 μm) and are prepared under hydrothermal conditions: this article clearly shows how difficult it is to maintain matter at the nanoscale under hydrothermal route.

There are few examples for the solvothermal preparation of up-converting nanoparticles. Wang and coworkers have presented a solvothermal LSS route for the preparation of up-converting β-$NaYF_4$ with sizes of about 30 nm[24,25]and Tian and coworkers have studied the inclusion of Mn^{2+} ions as controlling ions for the preparation of hexagonal nanocrystals in inverse microemulsions[26]. He and co-workers[27] have prepared solvothermal prepared up-converting nanocrystals using fluorinated ionic liquids as source of F^- reactive medium. However, even though these studies have been poured out in the literature, still, the formation of pure hexagonal $NaYF_4$ is not completely clear. The efforts presented in this dissertation are devoted to shed some light into the formation of $NaYF_4$ nanostructures under LSS conditions and in microemulsions.

2.1.2. Synthetic procedure

The synthetic route employed in this study is based on the one reported by Wang *et al.*[24] in which a two-steps solvothermal synthesis of hexagonal $NaYF_4$:Yb,Er nanoparticles (labelled herein as UCNPs) of about 50 nm is described (see Figure 2.7). This protocol was selected because, as mentioned before, it was promising to obtain smaller sized, fully hexagonal $NaYF_4$:Yb,Ln with diameter below 50 nm. Therefore, modifications of the as-reported route have been studied in this PhD work to identify parameters that could lead to the formation of pure hexagonal UC nanocrystals.

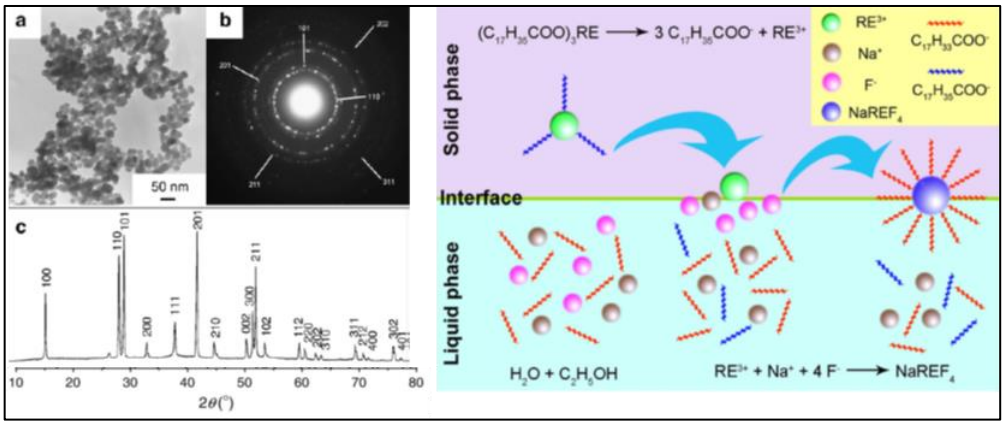

Figure 2.7: Characterization data for $NaY_{0.78}F_4$:$Yb_{0.20}$,$Er_{0.02}$ nanocrystals: (a) TEM image, (b) SAED pattern, (c) powder XRD pattern and (right) proposed mechanism for the formation of $NaREF_4$ nanoparticles at a solid–liquid interface.[24]

The first step of the synthesis is to prepare labile complexes of Y^{3+}, Yb^{3+} and Ln^{3+} (with Ln: Er, Tm, Ho) stearates from lanthanide nitrates and stearic acid. In a second step, these labile complexes are converted into crystalline $NaYF_4$:Yb,Ln through a solvothermal process that includes their emulsification in a mixture of water-oleic acid-ethanol ternary system using NaF as source of sodium and fluorine ions. It must be noticed that, using NaF as contemporary source of sodium and fluorine, and since the stoichiometry in the final crystal is Na:F 1:4, NaF can either be weighed as same equivalents of yttrium (intended as the sum of yttrium and the lanthanide ions) or as the total amount of F^- ions needed (which is 4 times higher in Na^+ ions). At the end, the choice is either to leave the system being F^- defective, or in excess of Na^+ ions. The excess of sodium ions has been reported to be driving the formation of the UC $NaYF_4$: Yb, Ln mostly in cubic lattices[24], even though, recently it has been

discovered, in a high temperature decomposition process, that joint action of NaCl and NaF or NH_4F and NaOH help the transition from cubic to hexagonal[28] (figure 2.8), therefore, in this case study the option of being F^- defective (with equimolar quantities of sodium and yttrium) was selected.

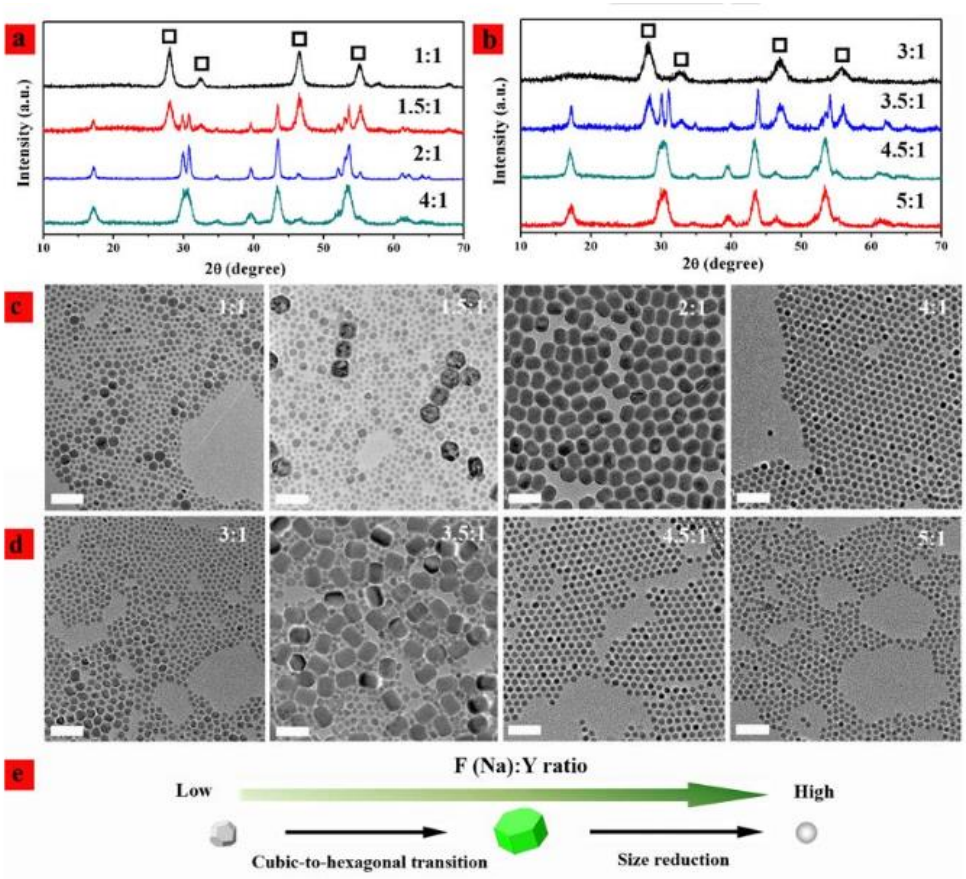

Figure 2.8: Conversion of cubic - phase to hexagonal - phase particles after heating for 30 min at 300 °C. **(a)** XRD patterns and **(c)** the corresponding TEM images of the nanocrystals obtained via the *"separate-method"* by varying Na:Y molar ratios from 1:1 to 4:1. **(b)** XRD patterns and **(d)** corresponding TEM images of the samples by varying the F:Y molar ratios from 3:1 to 5:1. Diffraction peaks corresponding to α-$NaYF_4$ are marked with square boxes. A gradual decrease in diffraction peak intensities for cubic - phase is observed as a function of increased Na(F):Y ratio. **(e)** General trend of phase transition from cubic to hexagonal and particle size as a function of Na(F):Y ratio. Scale bar: **(c, d)** 50 nm for TEM images.[28]

The three components emulsion (water, oil and an alcohol), usually called *pseudo-emulsion*, plays a determinant role on the nucleation/growth of UCNPs, and it also determines the crystal phase. Therefore, attempting to address nucleation and growth of nanocrystals under this solvothermal route passes through the iterative, accurate and precise analysis of various reaction parameters.

In this study, parameters such as W/O ratio, temperature, time, nature of the emitting Ln^{3+} ion and alcohol carbon chain length, have been investigated in order to understand crystal growth and propose a rationale model for the crystal formation. Crystal geometry, phase and size are evaluated through Le Bail (http://www.xrd.us/services/quantificatin.htm) analysis from XRD patterns. Morphology of the materials was evaluated from transmission electron microscopy (TEM). Optical activity of the as-prepared materials was studied under 980 nm irradiation through a continuous wave diode laser pumped at different power densities. Color sensation of the emitted radiation is determined through the model provided by the Comission Internationale de l´Éclairage (CIE) in 1931[29]. If required, dispersion of solids was performed in cyclohexane solutions when covered with oleic acid and in water or ethanol after surface modification, as it will be explained later.

The stoichiometry of the synthesized compounds is $NaY_{1-x-y}Yb_xLn_yF_4$ with x=0.2 and y=0.02 in the case of doping with Er^{3+} or Ho^{3+} ions, and y=0.005 for Tm^{3+} ions. Pure α- and β-$NaYF_4$ crystals were also prepared as benchmarks of the two crystalline structures by controlling the temperature and time of the solvothermal treatment. The cubic structure was obtained at 150°C for 8 hours and the hexagonal one at 200°C for 48 hours, respectively.

Step 1. Synthesis and characterization of Y^{3+},Yb^{3+},Ln^{3+} stearates

The first step of the reaction is the formation of Y,Yb,Ln stearates. The preparation of the lanthanide stearates is reported later on.

Preparation of Y,Yb,Ln stearates

15 mmol stearic acid ($C_{17}H_{35}O_2$), with 3.9, 1, and 0.1 mmol Y,Yb, Er/Ho nitrates respectively or 3.975, 1 and 0.025 mmol Y,Yb,Tm nitrates and 100 mL absolute EtOH were placed into in a two neck round bottom flask. After 20 minutes under reflux (65ºC) and vigorous stirring, a clear and homogeneous solution was obtained. In the meanwhile, a soda solution was prepared with 15 mmol of NaOH, 5 mL of water and 10 mL of EtOH. The soda solution was then added dropwise into the clear refluxing lanthanide solution. The deprotonation of the stearic acid, provokes the formation of a non-soluble salt (mixed Y,Yb,Ln stearates) through the complexation of the metal cations in solution. The soda solution is carefully added dropwise in order to control the rate of the saponification process. Upon completion of the acid-base reaction, the temperature is raised to 80 °C and the reaction system is homogenized under vigorous stirring for 30'. The hot suspension is rapidly filtered under vacuum. The solid is washed twice with abundant EtOH and once with water to remove impurities and soluble byproducts. The product is finally dried at 75°C overnight and grinded with an agate mortar to be used as a powder for the following step.

Characterization of the mixed Y,Yb,Ln stearates product was performed through ATR-FTIR (Attenuated Total Reflection – Fourier Transform Infrared Spectroscopy) and TG-DTA (Thermo Gravimetry coupled to Differential Thermal Analysis). Samples were compared with pure stearic acid and similarly prepared sodium stearate. FTIR spectra were obtained in solid state under ATR conditions since ATR is a non-destructive technique (as compared to KBr pellets) and it is possible to recover sample after measurement to perform further analyses. TG-DTA analysis has been performed from room temperature to 900°C at a heating rate of 10°C/min under air atmosphere. Due to the very poor crystallinity of the solid, XRD (x-ray diffraction) analysis is discarded as structural technique of choice, and both alternative techniques are useful to determine the composition and the structure of the stearate salts which are going to be used successively in the solvothermal step, whose scope is the preparation of the UC nanomaterials.

ATR-FTIR provides enough structural information thanks to the determination of the main vibrations for the Y,Yb,Ln stearates. These vibrations are found between 1500 and 800 cm^{-1}, but probably the most significant vibration from the structural point of view is the one associated to the coordination sphere around the metal centers, i. e. the $(R\text{-}CO_2)_3$-M structure.

TG-DTA, instead has a more compositional role, since the thermal behavior is related with the mass loss during heat treatment and its thermal transitions. The mass loss is mostly driven by the decomposition of organic constituents, while the thermal transitions may involve the metal centers and the strength with which is bound to the stearate ion.

1) ATR-FTIR

Figure 2.9 shows the ATR-FTIR spectra of the three samples: stearic acid, sodium stearate and mixed lanthanide stearate precursor (note that only the results for the Y-Yb-Er $(St)_3$ precursor are presented in this section because the discussion is similar for Y-Yb-Tm and Y-Yb-Ho stearates).

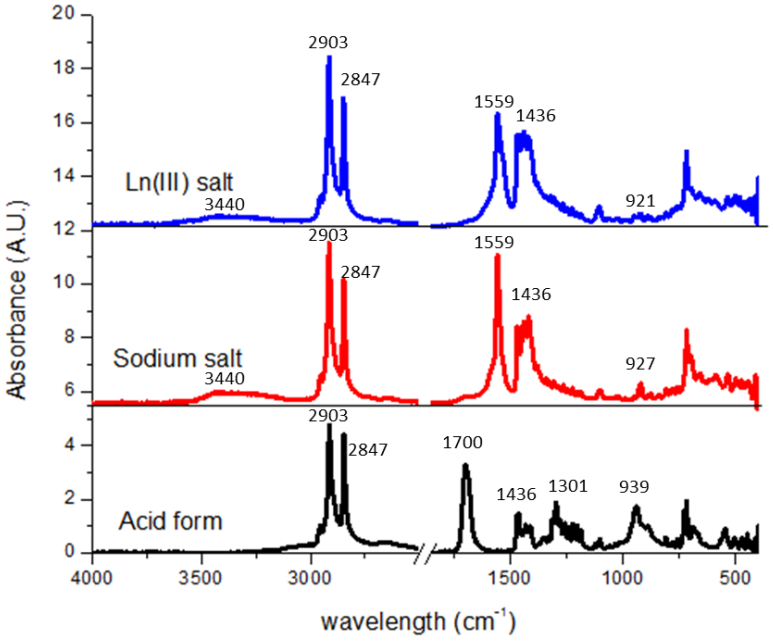

Figure 2.9: ATR-FTIR spectra of stearic acid **(black line)**, sodium stearate **(red line)** and $Ln(St)_3$ (Y-Yb-Er stearate) **(blue line)**.

Comparing the three IR spectra there are few differences that underline the compositional features of the products:

a) the stearate salts show residual crystallization water/solvent since a weak, broad band appears at 3440 cm^{-1} (stretching vibration of hydroxyl) and is not seen in the acid form (solid as well).
b) The C-H stretches at 2847 cm^{-1} appear to become slightly less intense in stearate salts and when the carboxylate is bound to a metal center.
c) The stretching vibration of carbonyl peak shows the usual shift between acid form and salts that is detected in other organic acids[30]: in the acid form it takes place at 1700 cm^{-1}, while in the salt forms it shifts to (asymmetric stretching vibrations) 1559 cm^{-1}. Similar shifts have been previously detected between the acid form and the derived complexes from organic ligands such as in the work of Papageorgiou and coworkers[30,31]. Figure 2.10 shows a sketch of the $Y(Ln)(St)_3$ chemical structure.

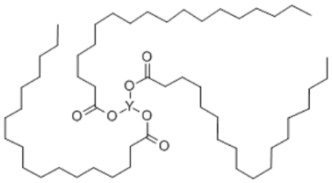

Figure 2.10. Chemical structure of $Y(St)_3$

d) The peak multiplet at 1436 cm^{-1}, due to C-O (symmetric stretching vibrations) of the carbonyl shows much higher intensities in the salts because of the higher dipole moment of the deprotonated carboxylic group. The band found at 1301 cm^{-1} in the carboxylic acid form is not seen in any of the metal salts. Therefore, it may be linked with the deprotonation of the carboxylic group, and this may confirm the higher intensity stretches at 1436 cm^{-1} for the metal salts forms. In other words, the band at 1301 cm^{-1} is due to a particular vibration of the C-O-H of the carboxylate group, but the higher intensities at 1436 cm^{-1} result from C-O-M higher stretching forces, eliminating the H-bonding between the C=O and C-O in the CO_2H groups.
e) The *fingerprints* IR zone (usually the one below 1000 cm^{-1} up to 400 cm^{-1}) shows diminished intensity and a limited shift of the peak at 939 cm^{-1} which is found at 927 and 921 cm^{-1} (out-of-plane bending vibration of hydroxyl) respectively for the Na^+ and Ln^{3+} salts. The shift is due to bending vibrations of hydroxyl moieties. and shows higher energy for the Ln^{3+} form of the stearate as compared to sodium or hydrogen bound

carboxylate. Probably these vibrations are due to the mayor quantity of water in the $Ln(St)_3$ or because the water is more tightly bound to metal moieties in $Ln(St)_3$ than in the $Na(St)_3$ and, clearly is much more visible in the acid because the carboxylic acid moiety.

2) TGA-DTA

The results of TGA and DTA analysis for the three analyzed samples are shown in Figure 2.11.

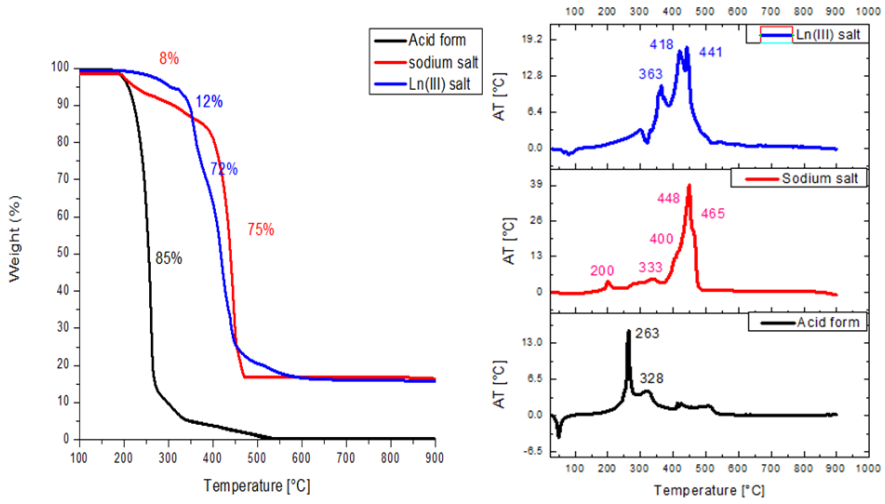

Figure 2.11: TGA and DTA curves of stearic acid **(black)**, sodium stearate **(red)** and $Ln(St)_3$ (Y-Yb-Er stearate) **(blue)**

The overall trend in the TGA curves consists on a significant weight loss due to the combustion of organic moieties in the three samples, which are associated to exothermic peaks in the DTA curves. However, the stearic acid decomposes much faster. Around 85% of its mass is burned in one step at around 265ºC, as registered in the DTA curve (exo peak), and the residual 15% of weight is progressively decomposed below 500ºC. It is important to note that the stearic acid is a pure organic compound that completely decomposes at the end of the analysis, and that it is solid at room temperature that melts at ~60ºC (endothermic peak without weight loss in TG).

On the contrary, the sodium and mixed lanthanide stearates have the most important weight loss at higher temperatures (between ~350 ºC and ~450ºC). Considering both TGA and DTA curves, it is noticeable that the sodium salt has some gradual decompositions (~15% of weight loss in total) at 200ºC,

278ºC and 333ºC (three exo peaks), but the most important process of combustion takes place at 450ºC, associated to a weight loss of 68%.
In the case of the mixed lanthanide stearate, it shows better thermal stability (up to 300ºC). Then, the organic combustion occurs in a stepwise way: there is mainly a three-step weight loss of 74% in total, accompanied of three exothermic peaks at 355, 420 and 440 ºC. This thermal behavior underlies a more complex combustion process for the mixed lanthanide precursor related to the different affinities of the stearate ligand for the three different cations composing the salt.

A last remark, the respective 18% and 17% of weight remaining at the end of the analysis for the sodium and lanthanide salts, corresponds to the respective metal oxides formed after decomposition of the stearate ligand. In the case of NaSt the percentage fits quite well with the expected final amount of Na_2O (20.2%) but in the case of Ln(III)St_3 the experimental amount is lower than expected (27%). This data reveals that a non-negligible amount of byproducts such as sodium stearate (not too much since the TGA-DTA analysis should show it) or even lanthanide hydroxide compounds are included in the precursor. The missing amount of lanthanides oxide can be due to the great sensitivity to moisture of the $Ln(NO_3)_3$ salts which did not permit an accurate weighing of lanthanide ions, since the overall weight is tampered by a great amount of water. However, Yan and co-workers found that the composition of NaYF4:Yb/Er nanocrystals varied with the reaction time via thermal decomposition of the lanthanide trifluoroacetate precursor[32] and Yi and colleagues reported a similar phenomenon when preparing NaYF4:Yb/Er nanocrystals in the presence of ethylenediaminetetraacetic acid by a hydrothermal method.[32] In the latter case, this effect was ascribed to the change in composition to different coordination abilities of lanthanides to EDTA, thus affecting supersaturation and precipitation processes which are the key to the formation of nanocrystals under such synthetic processes.[32] To rationalize the lack of accurate elemental Ln measurements, Liu and coworkers pointed out[32]: *"Presently, the dopant concentration of UC nanocrystals is typically estimated from the amount of the lanthanide precursors added to the solution, assuming that all the lanthanides are homogeneously doped into the nanocrystals after the reaction."*[32]

The results coming from the analysis of the IR spectra and of the thermal analysis show an effective coordination between the stearate and the lanthanide ions and therefore the solid stearate mixed salt can be used as lanthanide precursor for the successive solvothermal formation of the UC $NaYF_4$:Yb,Ln nanoparticles.

The principal feature of this compound as UCNPs precursor is the poor crystallinity, which may suppose a low-ordering of the solid with a random dispersion of the lanthanide within it. Moreover, a non-negligible quantity of byproducts can be still trapped within the solid. A more exhaustive analysis of the precursor could clarify its composition but this is not the goal of this study. Furthermore, at this moment of the thesis, we are reproducing the synthetic procedure published by M. Wang *et al.* in Materials Letters 63 (2009) 325–327.

It is important to mention that the presence of Na stearate in the lanthanide precursor may affect (increasing) the total quantity of sodium in the synthesis, since the solvothermal protocol uses NaF as source of sodium and fluorine for the formation of the UCNPs. This excess of sodium would favor the formation of cubic crystals, as mentioned in the introduction. Therefore, a detailed study of the conditions for the formation of high-quality UCNPs, with pure hexagonal lattices must be performed in order to understand the role of various parameters influencing the solvothermal formation of the crystals, as well as an analysis of the optical activity of the as-prepared crystals and derivation of the emission mechanisms for each of the parameter analyzed in this study. The study of synthetic parameters such as reaction temperature and time, nature of the lanthanide (active ions), influence of the W/O ratio and the length of the alcohol chain used as co-solvent, is useful in the definition of model for the formation of crystals under solvothermal synthesis.

Step 2. Solvothermal treatment

The second step is the solvothermal treatment of a pseudo-microemulsion containing all the chemical elements to make the formation of $NaYF_4$:Yb,Ln nanocrystals with the up-converting properties. A general description of the synthetic procedure is shown below.

Preparation of $NaYF_4$:Yb,Ln nanocrystals

In a general procedure, 20 mL of water, 10 mL of oleic acid, and 30 mL of ethanol were mixed at high speed stirring to get a water/oil/alcohol 3-components pseudo-emulsion. Then, 1.9156 g of the as-synthesized Y,Yb,Ln stearate and 0.4200 g of NaF were added. The mixture was stirred for 15 min, transferred to a 123 mL Teflon-lined acid digestion Parr autoclave, sealed, and solvothermally treated at different temperature (between 150 and 200 °C) for different reaction times (8 h, 16 h, 24 h or 48 h) in an oven. After cooling, the precipitate (nanocrystals of $NaY_{0.78}F_4$:$Yb_{0.20}$,Er/$Ho_{0.02}$ or $NaY_{0.795}F_4$:$Yb_{0.20}$,$Tm_{0.005}$) were separated by centrifugation, washed with ethanol and water for four and two times, respectively, and then dried at 60 °C for 12 h *(yield: 0.1466 g, ~71%)*.

The experimental conditions of the solvothermal treatment were changed and products were studied using various characterization techniques such as XRD (x-ray diffraction), TEM (Transmission Electron Microscopy), and spectrofluorometry, to understand the effects of the reaction parameters on the formation of crystals and on their optical activity. This study is explained in next section 2.2.

Different reaction temperatures, from 150°C to 200°C, and four reaction times, 8h, 16 h, 24 h and 48 h, for the solvothermal treatment were chosen as conditions of study for the determination of the crystalline phase. Composition of the emulsion was also varied to understand the formation of the crystals within different emulsion conditions. In all cases, the total volume of the emulsion was kept constant (60 mL) but the relative volume of the three components was varied. Furthermore, different lanthanide activators were chosen as Er, Ho and Tm (Er and Ho in 2% molar ratio and Tm in 0.5% molar ratio, replacing Y atoms in all cases; Yb molar ratio was constant at 20%). The ionic radii and size of the doping lanthanides has also an influence on the hexagonal vs cubic stabilization. Finally, the alcohol chain length was also changed from ethanol (2 C atoms) to butanol (4C atoms) to see their effects on the emulsions and on the product crystallinity.

2.2 Influence of reaction conditions on nanocrystals formation

2.2.1. Reaction temperature and time

The conditions of the solvothermal treatment, i. e. temperature and time of residence at that temperature are critical factors driving the formation of the α and β phases in the $NaYF_4$:Yb,Ln materials. First, time and temperature were established for the preparation of pure $NaYF_4$ as benchmarking conditions. The first essayed conditions were the ones reported by Wang[24], 150°C for 8 hours. However, our results disagreed with the ones appeared in the reported manuscript. Under these conditions, our system exhibited pure cubic (α) phase, as shown in Figure 2.12 right (JCPDS card 06-0342 pattern). As previously mentioned, the hexagonal phase is obtained under thermodynamic conditions. Therefore, the temperature and time of the solvothermal treatment was increased and, after several tests, pure hexagonal β phase was found at 200°C for 48 h. The experimental and theoretical XRD patterns are shown in Figure 2.12 left (JCPSD cards 016-0334). These two reaction conditions were found to be the ones to independently get the two lattices as single phase. Between these conditions, a mixture of both α and β crystals was obtained.

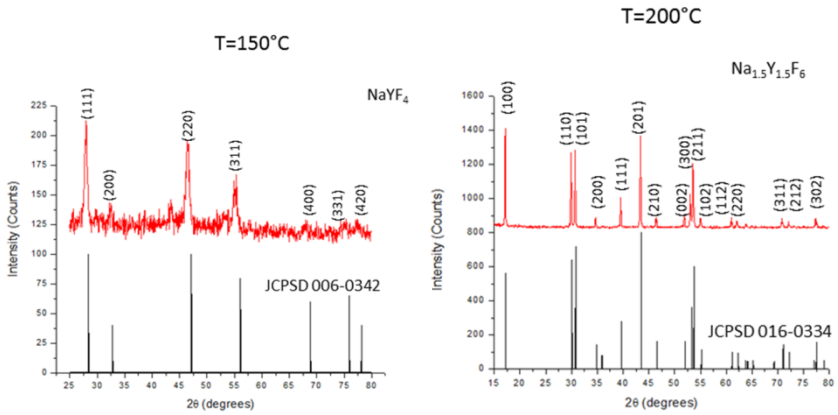

Figure 2.12: ***left*** **-** pure hexagonal $NaYF_4$ prepared by solvothermal synthesis at 200°C and 48 h and ***right*** **-** pure cubic phase prepared after 150°C and 8h of synthesis. Miller indices for the crystal planes and JCPDS standard patterns are included for each structure.

Once established the limiting boundaries of temperature and time for the solvothermal synthesis, it is important to determine how doping influence the formation of the

hexagonal crystals, which is the targeted phase (the most optically efficient). Therefore, lanthanide-doped $NaYF_4$ syntheses have been performed at 8, 24, 36 and 48 hours at 200°C degrees. Figure 2.13 summarizes the results from the powder XRD patterns and their quantitative profile analysis from Le Bail refinements.

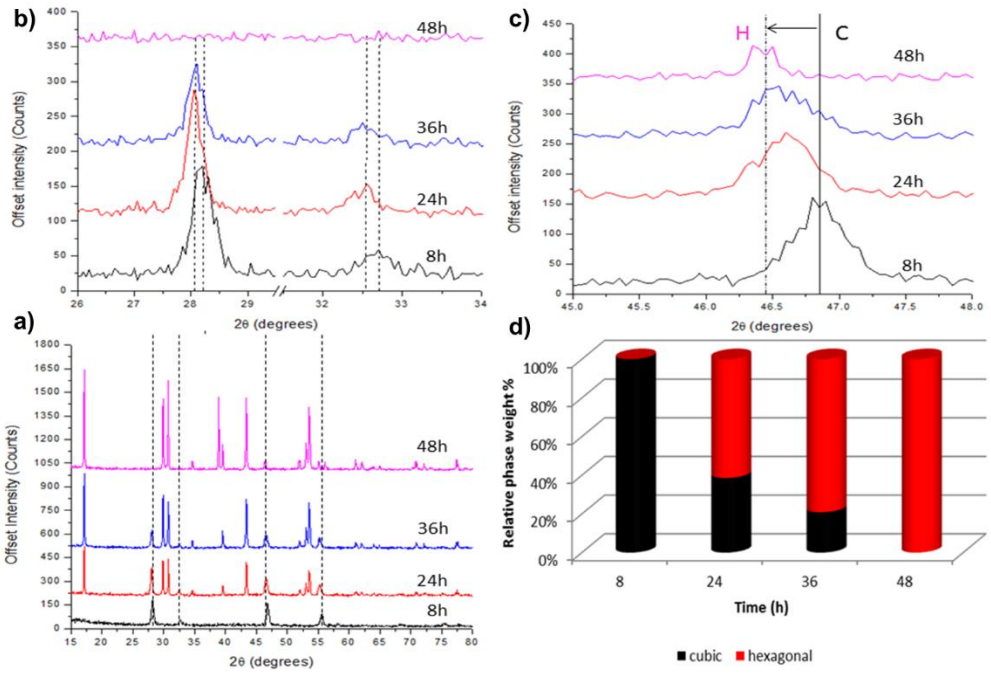

Figure 2.13: XRD patterns of the products obtained at 200°C with different reaction times: a) Full spectra; b) Enlargement of the spectra showing the (111) and (200) peaks from cubic phase; c) Enlargement of the spectra with a shift from cubic (220) peak to the hexagonal (210) peak; d) Graphical representation of the hexagonal to cubic ratio with reaction time.

Le Bail profile analysis (http://www.xrd.us/services/quantificatin.htm) is a quantitative phase analysis from XRD patterns of polycrystalline materials. It is a simple, yet powerful, method to quantify relative crystal phases or crystalline and amorphous amounts in multiphasic or poorly crystalline mixtures. The method relies on the simple relationship:

$$W_P = \frac{S_P(ZMV)_P}{\sum_{i=1}^{n} S_i(ZMV)_i} \qquad (2.2)$$

where W is the relative weight fraction of phase p in a mixture of n phases, and S, Z, M, and V are, respectively, the Rietveld scale factor, the number of formula units per

cell, the mass of the formula unit (in atomic mass units) and the unit cell volume (in $Å^3$). The advantages of this quantitative analysis include:

- The calibration constants are computed from reliable structural data, rather than by laborious experiments
- All reflections in the pattern are explicitly included for calculation
- The effects of preferred orientation and extinction are reduced, since all reflection types are considered
- Crystal structural and peak profile parameters, particle statistics, microabsorption, etc. are refined as part of the same analysis.

The XRD patterns of Figure 2.13 reveal a gradual conversion from the cubic lattice to the hexagonal one in the system treated at 200ºC with increasing time of solvothermal treatment from 8 to 48 hours.

This conversion is clearly observed in the changes of (111) and (200) planes (XRD peaks located at 28° and 32.5°) of the cubic structure. These peaks show a slight shift to lower angles (higher d-spacing), concomitantly to a diminution in intensity with increasing reaction time (Figure 2.13b). These diffraction lines disappear in the pattern of the powder prepared after 48 h of synthesis, sign that the cubic phase is no longer present, and two new peaks appears at 30º and 30.7º (from (110) and (101) planes) from the hexagonal structure. Further proof of the phase transition is found from the shift of the (220) plane position (peak located at 46.9°, from the powder prepared after 8h of treatment) of the cubic lattice towards the position of the hexagonal peak (210), which appears in the pattern of the powder prepared after 48 hours of treatment (Figure 2.13c). The profile of this peak for the patterns taken after 24 and 36 hours indicates that mixed α + β phases are formed, with different relative quantities, as confirmed from the full profile quantitative analysis. The results of this analysis are graphically represented in Figure 2.13d.

This experiment has proven that the kinetically stable cubic phase transforms into hexagonal structure when the system operates under thermodynamic regime. Thus, reaction time and temperature will be fixed to 48 hours and 200°C (conditions to form pure hexagonal crystals) and other parameters will be varied towards understanding nucleation and growth of nanocrystals.

The β-$NaYF_4$ sample prepared under these selected conditions shows large-spanned crystals, with irregular shape and sizes ranging from 200 to 400 nm (see Figure 2.14).

These sizes are too large for most of the biological and technological applications. A suitable range of size would be between 15 and 80 nm[20,33,34] in order to get a good compromise between optical UC efficiency (which increases with size) and dispersibility (much easier in small nanoparticles). In this view, our further attempts will try to reduce size of the crystals maintaining the pure hexagonal phase, through modification of other reaction parameters.

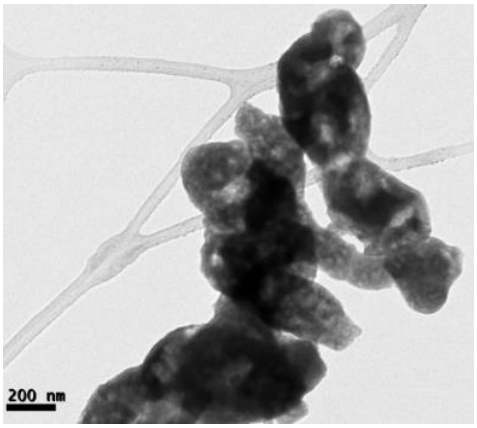

Figure 2.14: TEM image of the β-$NaYF_4$ crystals prepared at 200°C and 48 hours.

2.2.2. W/O ratio from pseudo-emulsions

The synthetic route chosen for the preparation of pure β-$NaYF_4$:Yb,Ln NPs makes use of pseudo-emulsions. The composition of the three-component mixture determines the nature of the micelles, which acts as template for the nucleation and growth of nanomaterials. The standard procedure (described in the blue frame, step 2) is based on a pseudo-emulsion of 10 mL of oleic acid, 20 mL of water and 30 mL of ethanol, but a poor control of the crystal formation was demonstrated (undefined morphology and large particle size of 200-400 nm). With view of a better control on the crystal formation process, this section explores the influence of the W/O ratio, and next section (2.2.3), the nature of the alcohol on the structural features.

Pseudo-ternary emulsion systems are generally composed of two insoluble liquids and a third one soluble in both liquids, which helps the mixing of the other two components. The formation of micelles is settled while stabilizing the mixture. To achieve the micellar system, amphiphilic substances are widely used since they promote one-phase emulsions that contains liquids that, otherwise, will not mix[23]. Several surface tension-active substances can be exploited depending on the nature of the emulsions: surfactants[35], alcohols[36], water-soluble polymers (such as

polyethylenglycol (PEG) or polyvinylpirrolidone (PVP))[37] and so on. These substances present, generally, a polar head and a large hydrophobic tail which help mixing the more polar solvents such as water with apolar organic solvents. These micellar systems are widely found in creams, gels, and many other products with industrial and commercial value.

In our work, the pseudo-emulsion composed of Water/Oleic acid/Ethanol (with oleic acid as oil phase) is used as template to limit the growth of the crystals, and also as source of ligands (oleates) that form organic coatings around the surface of the nanomaterials. Furthermore, this particular composition has a good resistance to high temperature and pressure[3].

In this study, samples of $NaYF_4$:Yb,Er (because the optical activity was further evaluated) with different water to oil (W/O) ratios (φ) were prepared according to the optimized conditions of reaction time and temperature (200ºC for 48h). The definition of W/O ratio is

$$\varphi = \frac{V_W}{V_{OA}} \cdot 100 \qquad (2.3)$$

Note that $V_W + V_{OA} = 30\ mL\ and\ V_{tot} = 60\ mL$ (ethanol volume was kept constant), in order to maintain similar filling factors which would significantly affect the nanomaterials preparation.

The values of the studied W/O ratios were 12.5% ≤ φ ≤ 87.5%. Relative amounts for each component is presented in Table 2.2, where values of φ, volumes of the emulsions components and the relative molar fractions (χ) are listed.

φ (W/O, %)	**V_{water} (mL)**	**χ_{water}**	**V_{EtOH} (mL)**	**χ_{EtOH}**	**V_{OA} (mL)**	**χ_{OA}**
0.0	0.00	0.00	30.00	0.858	30.00	0.142
12.5	3.75	0.263	30.00	0.643	26.25	0.094
33.3	10.00	0.490	30.00	0.459	20.00	0.051
41.7	12.50	0.550	30.00	0.410	17.50	0.040
50.0	15.00	0.598	30.00	0.371	15.00	0.031
58.3	17.50	0.638	30.00	0.338	12.50	0.024
66.7	20.00	0.672	30.00	0.311	10.00	0.017
87.5	26.25	0.736	30.00	0.259	3.75	0.005
100.0	30.00	0.764	30.00	0.236	0.00	0.000

Table 2.2: water to oil ratios, volumes and molar fractions of the various components in the pseudo-emulsions. The φ ratios at 0 and 100% were calculated for completion.

Figure 2.15 presents the ternary diagrams relative to the different amounts of water, oleic acid and ethanol. The red line connecting the squares define the oil and water boundary in changing the W/O ratio, since the alcohol volume quantity is held constant. The green arrows pointing the calculated extremes representing 0% water and 0% oleic acid have been added to complete the water/ oil boundary. These points have not been experimentally explored, due to change in reaction medium: these represent 2-components mixtures instead of 3-components ones, therefore changing synthetic reaction medium.

Under low water content, the 3-components emulsion mixes completely, up to a maximum: at φ=33.3% liquid-liquid boundaries (or turbidity) are not detected at naked eye. Beyond this point, and increasing the amount of water and reducing the amount of oil, the formation of turbidity is observed.

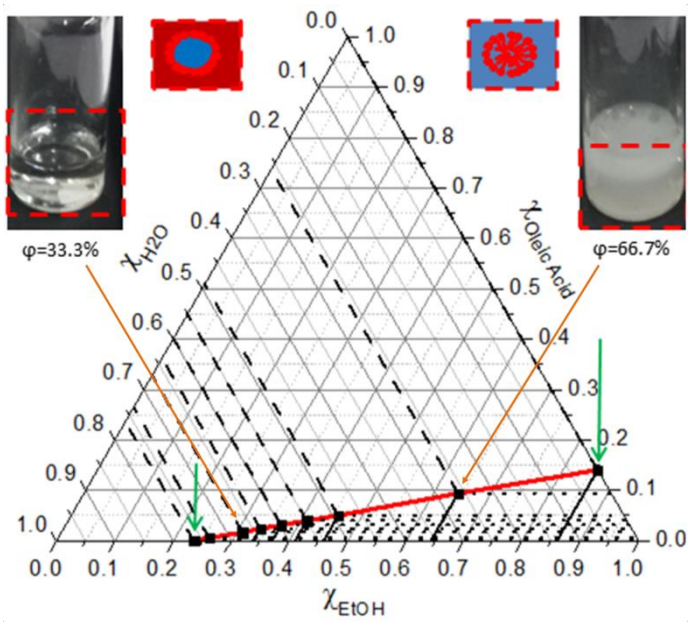

Figure 2.15: Ternary phase diagram showing the emulsions prepared in this study. The green arrows indicate the calculated points. *Inset:* (Left) the sample of standard procedure with W:O:E 1:2:3 (volume ratio) as representative water in oil emulsion; (Right) the sample of W:O:E 2:1:3 (volume ratio) as representative oil in water emulsion.

This visual change is associated to the transformation from inverse micelles (water into oil) to direct micelles (oil into water) as shown in Figure 2.15. In the first case, the tails of the fatty acids are joint together in a homogeneous organic medium and

the heads form small pools of water, where the crystal is expected to grow confined (see left inset of Figure 2.15). On the other hand, large amounts of water the organic tails are joined together forming the apolar micelles, while the carboxylic polar heads points outwards in a more watery medium (see left inset of Figure 2.15). Under these conditions, the confinement of the water for the formation of the nanocrystals is much less effective and it is expected that larger-spanned crystals are formed, with a major probability of exhibiting hexagonal phase, which is the most usual phase in large crystals.

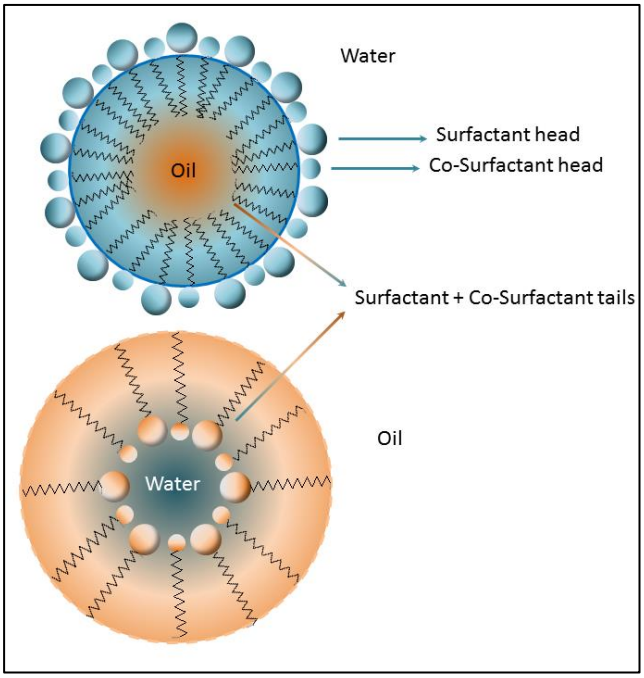

Figure 2.16: Formation of (a) direct micelles in O/W dispersions and (b) inverse micelles in W/O dispersions of 3-component mixtures.

The water to oil ratio is therefore a critical parameter for the formation of the nuclei and crystal growth, as well as the stabilization of either cubic or hexagonal phase. Thus, a complete study on XRD and TEM was performed on the samples with φ=12.5%, 33.3%, 41.8%, 50%, 58.3%, 66.7% and 87.5%. Figure 2.17 shows the XRD patterns of all these samples and a selection of the most representative TEM images for fixed W/O ratios.

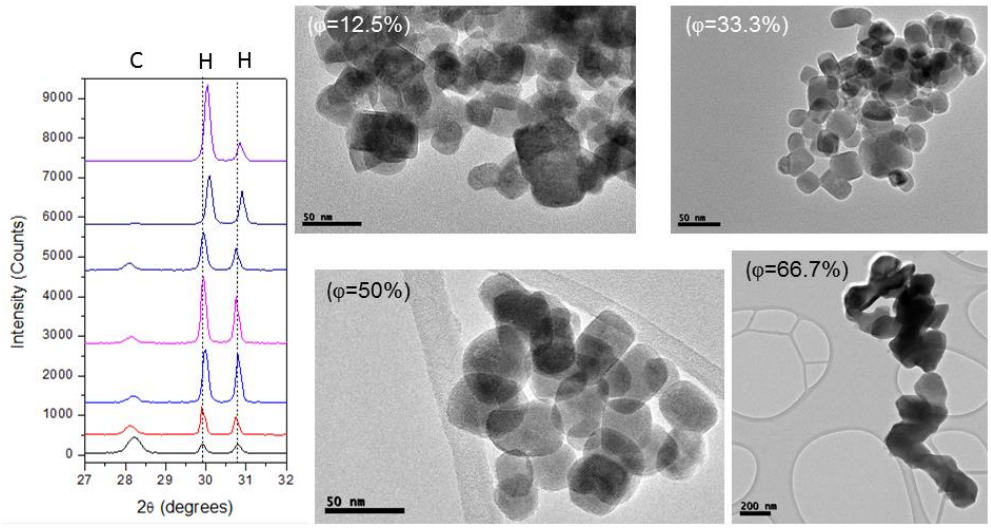

Figure 2.17: XRD and a selection of TEM images of W/O and O/W synthesized nanocrystals.

From XRD results, it can be stablished 3 different regions: (i) at low water content ($\varphi \leq 33.3\%$) the samples exhibit a significant amount of cubic phase; (ii) at intermediate water content ($41.7\% \leq \varphi \leq 58.3\%$) the hexagonal phase greatly predominates even though some remaining cubic crystals are present; (iii) at large water content ($\varphi \geq 66.7\%$), only hexagonal phase is present. Therefore a continuous increase of the water/oil ratio pushes towards the formation of hexagonal crystals (as hypothesized above), and concomitantly an increase in size of the crystals is found, as illustrated in the TEM images of Figure 2.17. Another interesting feature is that, at very large amounts of water and very little oil, it is possible to find a hexagonal to hexagonal transition. The relative intensity of the peaks at 30° and 30.7° degrees (planes 110 and 101 respectively) dramatically changes as proof of the modified hexagonal crystal structure. It has been claimed[38,39] that in pure fluorite-like crystals order-disorder lattice atom placements can occur and it is described as hexagonal to hexagonal transition at relatively high temperatures and pressures; this explanation may fit perfectly the observation of our findings, even though, however, it is not aim of this work to prove or disprove this theory.

Average crystallites size analyses were performed on the XRD patterns through Scherrer's relation

$$\tau = \frac{K\lambda}{\beta \cos\theta} \qquad (2.4)$$

where K is a dimensionless shape factor, with a constant value of about 0.9 and β is the line broadening, using, respectively, the (111) and (100) peaks at 27° and 17° for cubic and hexagonal cells. It was observed that the two crystal structures grow with different pace (see Figure 2.18). At very low water content (φ =12.5%), the average crystallites of both phases have similar size (around 3.5 nm); but quickly the hexagonal crystals show larger sizes than the cubic for a defined φ. The cubic crystals grow with a slower pace as compared to the hexagonal counterpart. Moreover, for φ ≥58.3% the cubic phase vanishes and only large β-crystallites are found. The hexagonal phase reaches a maximum around 14 nm, and then stabilizes at very high water contents. This can be attributed to stabilization of the crystallites following the order-disorder transition between hexagonal lattices.

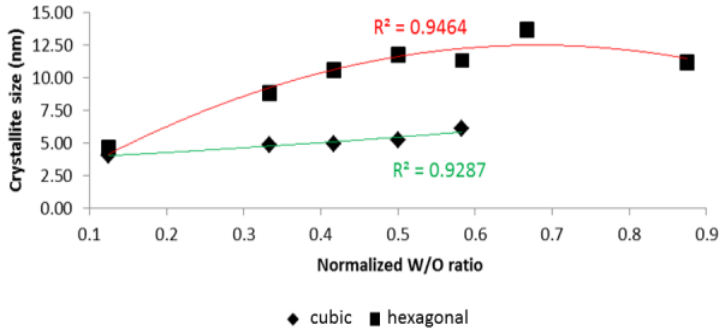

Figure 2.18: Scherrer's average crystallite size for α- (green) and β- (red) phases in function of the water fraction.

Concerning particle size analyzed by TEM (and not the average crystallite responsible for the XRD patterns), it can be noticed that at low W/O ratios, the crystals show cubic morphology with sizes ranging from 20 to 40 nm and some bigger distorted particles probably formed from two or more merged cubic nanocrystals. At higher W:O ratios (1.75:1.25), the crystals are more rounded a sizes comprised between 50 nm and 70 nm. At the highest W:O ratio (2:1), the crystals exhibit hexagonal shape (with some heterogeneous morphology) and sizes of 150-200 nm.

Summarizing the principal results from this section, low W/O ratio normally form purely α, or mixed α and β phases crystals with average diameter ranging from 20 to 40 nm; aggregation of crystals increases accordingly to the water content. The increase in aggregation results in sintering of larger-sized crystals, which are the derivation of many nanocrystals fused together. Consequent to this enlargement of the crystals, pure hexagonal lattices are found. The spatial constriction of the crystals in

direct emulsions is not so effective in forming small up-converting nanomaterials with pure hexagonal structures.

The polydispersity and heterogeneity of the deriving nanocrystals is a difficult issue to overcome even though the use of microemulsions. At least, the use of inverse emulsions provides mixed α+β nanocrystals with sizes under 50 nm, which is an interesting result for technological purposes. On the other hand, O/W emulsions, while forming pure hexagonal crystals, produce large sized crystals, which are not of interest for our purposes.[3,24,25] Therefore, for the rest of the study, UCNPs will be prepared under solvothermal conditions only under W/O conditions, in order to be applied toward advanced optical applications.

Comparing hexagonal crystals prepared at φ=66.7% and 87.5%, under same relative doping concentrations of lanthanide ions, and synthetic conditions, provokes an hexagonal to hexagonal transition phase that can be explained through an order-disorder transition in hexagonal structures. Analogous results were found in pure $NaYF_4$ under heavier conditions of temperature and pressure and under synchrotron light[38,39]. These experiments, as well as the change in alcohol carbon tail are crucial for understanding crystals formation and permit to draw a proof-based model that explains the crystal formation under those conditions.

2.2.3. Alcohol chains length in pseudo-microemulsions

The use of different alcohols plays an important co-solvent role on the stability of the prepared emulsions. It is long known that short chained alcohols have a partially disruptive effect on the stability of the emulsions and alter the monomers-micelle equilibrium[40]. On the other hand, however, large alkyl-chained alcohols act, sometimes, as surfactant and increase micelle stability [40]. Their concentration, as well as the nature of their carbon backbones (linear alkyl chains versus ramifications), affects the whole ternary mixture, changing the energy of formation (or disruption) of micelles.[40,41] More frequently, the use of large alkyl alcohols is used for the preparation of inverse emulsions, because of their surfactant activity, placing their polar heads sticking together with the polar carboxylic groups within pools of water, while the relatively large tails blend between the fats tails, forming a uniform medium, as shown in Figure 2.19.[40,42] The use of large-tailed alcohols usually enhances the compactness of the micelles, and so, their stability. This effect results in a shifting of the monomer-micelle equilibrium, toward the formation of the products.[43,44]

Alcohol chain lengths can have an effect on the formation of different geometry of micelles.[40–42,44,45] Therefore it is important to evaluate morphology, crystallinity and relative phase (or mixture of phases) of the obtained powders and the crystal relative size.

Taken this into account, alcohol chain lengths were tested in an effort to understand how different alkyl chain would affect $NaYF_4$:Yb,Er crystal formation. The linear tails were changed between 2 C atoms and 4 Carbon atoms (i.e. Ethanol, 1-Propanol and 1-Butanol). Obviously, since the lowest-sized crystals were prepared under inverse-emulsions conditions (φ=33.3%), therefore the alcohol chain length was changed under these water-to-oil conditions, and its volume was constant (30 mL). Table 2.3 reports the volumes and molar fractions (χ) of the alcohols – based emulsion at φ = 33.3%.

Alcohol	$\mathbf{V_{water}(mL)}$	χ_{water}	$\mathbf{V_{Alcohol}(mL)}$	$\chi_{Alcohol}$	$\mathbf{V_{Oleic\ Acid}(mL)}$	$\chi_{Oleic\ Acid}$
EtOH	10	0.490	30	0.459	20	0.051
1-PrOH	10	0.546	30	0.400	20	0.057
1-BuOH	10	0.585	30	0.351	20	0.064

Table 2.3: Volumes and molar fractions (X_i) of the pseudo-emulsions.

During the synthesis, an increasing turbidity of the ternary mixture was observed, mainly due to the greater insolubility of the larger-chained alcohols in water. Figure 2.19 shows the ternary diagram for EtOH, 1-PrOH and 1-BuOH inverse emulsions with φ = 33.3%. Insets show relative images of these emulsions. We have to take into account that the volume of alcohol in the synthesis is very high and it makes a significant change on the nature of the pseudo-emulsion.

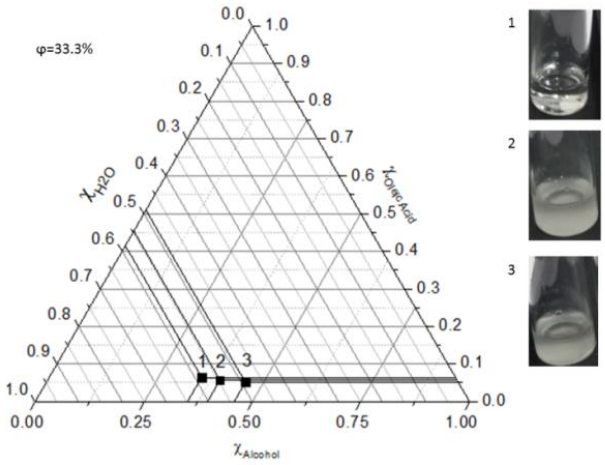

Figure 2.19: Ternary phase diagram for inverse emulsion with different alcohols: **1)** W:O:E 1:2:3; **2)** W:O:1-P 1:2:3; 3 W:O:1-B 1:2:3.

The XRD patterns of the as-prepared $NaYF_4$:Yb,Er samples exhibited in all cases a predominant hexagonal β-phase, but with some different α-to-β ratio depending on the nature of the alcohol (see Figure 2.20). Indeed, longer the chain length is, higher the hexagonal phase.

TEM images of the three samples revealed important differences in particle size and morphology. EtOH inverse emulsions promote the formation of 20-40nm-sized (in average) pseudo-cubic nanocrystals, as described before. However, 1-PrOH leads to heterogeneous morphologies and sizes, including undefined-shape particles between 20 to 80 nm and large submicrometric rods, which result from uncontrolled growth of the crystals. Finally, 1-BuOH induces the formation of μm-sized rods, deriving from a different geometry of the micelles and the extensive epitaxial growth of the $NaYF_4$ structure.

This behavior responds to a completely different nature of the micellar system. The EtOH helps the stabilization of pseudo-spherical micelles or droplets of water inside the organic matrix, where the small nuclei growth up to a limited size. Some coalescence of micelles can be responsible for the apparition of several particles with slightly higher size. However, in the presence of 1-PrOH and especially in 1-BuOH, the micelles are not stable anymore and the system rearranges as big laminar structures, in which micrometric crystals are formed. Furthermore, the trend in which the cubic phase quantity declines in favor of the hexagonal follows the order EtOH >

1-PrOH > 1-BuOH, confirming that the larger is the crystal, the more hexagonal is the crystal phase.

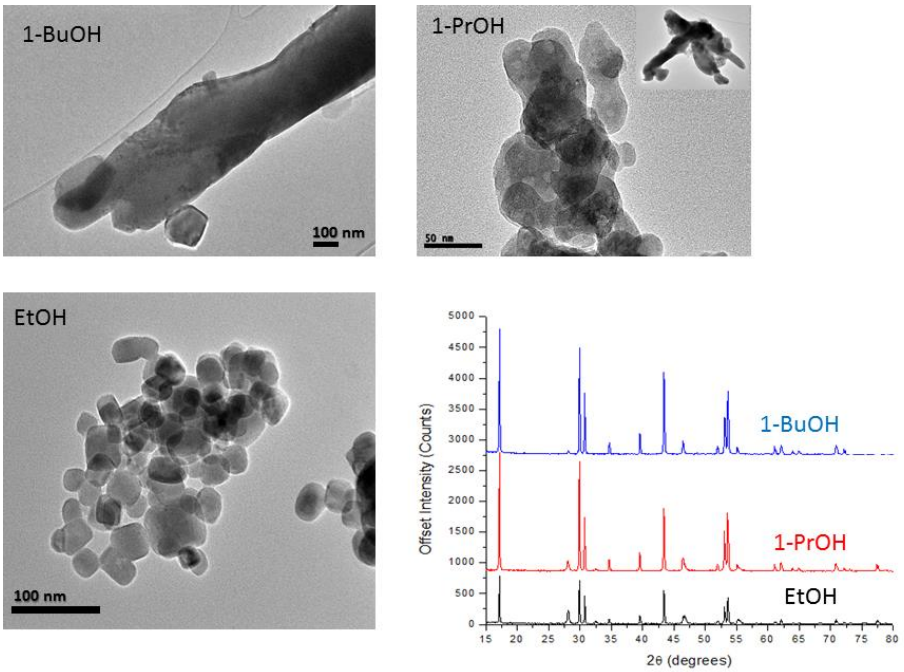

Figure 2.20: XRD and TEM images of nanocrystals prepared with EtOH, PrOH and BuOH

2.2.4. Influence of the emitting Ln(III) ions on the formation of nanocrystals

Analogously to the other parameters analyzed up to now, preparation of $NaYF_4$:Yb,Tm and $NaYF_4$:Yb,Ho in inverse emulsions was studied with the goal of tuning the color of the emissions and to investigate if there is some effect on the crystal formation driven by the lanthanide nature, as stated by F. Wang (Figure 1.24 from Chapter 1.[46]

The samples doped with thulium or holmium were prepared under the same reaction conditions used for $NaYF_4$:Yb,Er, and XRD patterns and TEM images of these samples are compared in Figure 2.17. The morphology of the crystals is similar but Tm-based nanoparticles are smaller in size, between 15 and 25 nm, as compared to Er and Ho-doped ones (20-40 nm in average). Furthermore, XRD of Tm^{3+}-doped up-converter reveals a higher percentage of cubic phase in this sample as compared to Ho^{3+} and Er^{3+} -doped samples. Indeed, the intensity of the cubic/hexagonal peaks

decreases in the order Tm > Ho > Er, and this result agrees with the aforementioned dependence of the stability of α or β phases with the size of the nanocrystal. Furthermore, according to the general trend of phase transition from cubic to hexagonal as a function of ionic radius (or polarizability) of the lanthanide dopant ions[46], Tm^{3+} has higher tendency than Er^{3+} and Ho^{3+} towards cubic phase, which is consistent with our experimental observations.

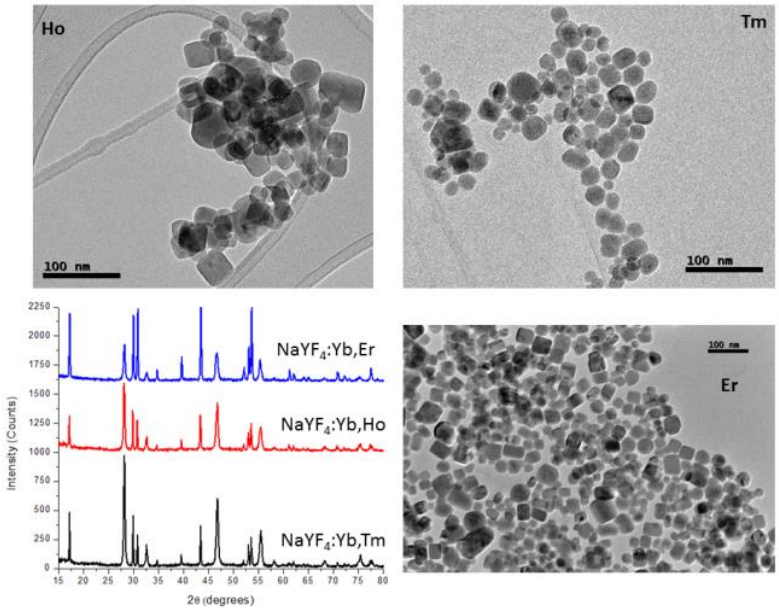

Figure 2.21: Yb^{3+}/Ln^{3+} patterns for respectively Tm^{3+}, Er^{3+} and Ho^{3+} doped $NaYF_4$ nanocrystals and relative TEM images.

In Figure 2.20, the particle size distributions of the Er^{3+} and Tm^{3+} doped crystals (Ho^{3+} doped nanocrystals size distribution is very close to Er^{3+} doped one) estimated from TEM images are presented. The graphics clearly shows that most of the nanocrystals for the thulium system range from 10 to 30 nm and, in the case of the erbium and holmium doped systems, the diameter of nanocrystals ranges mostly from 20 to 50 nm. The mean value was 22 ± 8 nm and 37 ± 12 nm for Tm- and Er-doped $NaYF_4$ nanoparticles, respectively.

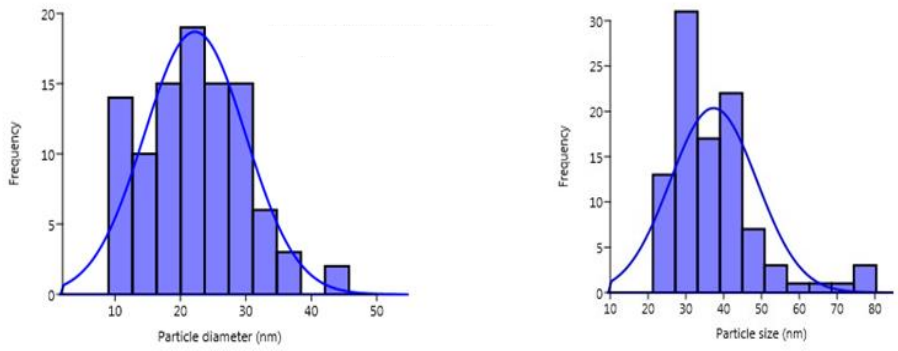

Figure 2.22: Particle size distribution of $NaYF_4$:Yb,Tm (left) and $NaYF_4$:Yb,Er (right) NPs.

2.2.5. Analysis of the optical response

The analysis of the optical activity will use fluorescence spectroscopy principles and the color sensation theory to describe the experimental findings and associate the variation of color coordinates for the emission spectra of the UC solvothermal-prepared phosphors. In this section, the effects of the different synthetic parameters on the optical response of the $NaYF_4$:Yb,Er system will be analyzed.

The up-converting processes that lead to the visible emissions (mainly in the green and red regions) of nano-sized $NaYF_4$:Yb,Er upon NIR excitation are very well known and described in Chapter 1[47]. The emission intensities and the ratios of the various emissions depends on the doping levels, excitation power, preparation temperature and time, organic impurities and nature of the matrix host. In this study, the concentration of the dopants (2% Er and 20% Yb molar ratio), the excitation power and the presence of oleate molecules at the surface of the crystals were kept constant. However, the presence of α and/or β-$NaYF_4$ crystal structures and the crystal size will affect the phonon energy and the number of defects, which can alter the green-to-red ratio of the erbium UC photoluminescence.

The electronic transitions of Er^{3+} ions responsible for the green emissions are $^2H_{11/2}\rightarrow{}^4I_{15/2}$ (at 523 nm) and $^4S_{3/2}\rightarrow{}^4I_{15/2}$ (at 546 nm); while the red one (centered at 656 nm) is originated from the $^4F_{9/2}\rightarrow{}^4I_{15/2}$ transition. All those three transitions come from the relaxation of ladder-arranged excited states of Er^{3+} ions, upon pumping photons from the $^2F_{5/2}$ excited state of Yb^{3+} ions, that arise from the sequential absorption of NIR (980 nm) photons. As aforementioned, all the parameters studied

in the crystal engineering of the nanostructured $NaYF_4$:Yb,Er had an influence on the red to green intensity relations.

For instance, the water-to-oil ratio controls the α/β phase quantities, the morphology and size of the crystals, which directly relates with lattice phonon energy and therefore vibrational, non-radiative emissions. Figure 2.23 shows the UC photoluminescence spectra of the $NaYF_4$:Yb,Er nanocrystals prepared with different W/O ratios upon excitation at 980 nm (1W laser). The green-to-red ratios (G/R) were calculated by integrating the spectral intensity of the green ($^2H_{11/2}\rightarrow{}^4I_{15/2}$ at 523 nm and $^4S_{3/2}\rightarrow{}^4I_{15/2}$ at 546 nm) and the red ($^4F_{9/2}\rightarrow{}^4I_{15/2}$ at 656 nm) emissions.

A general trend was observed (Figure 2.23): the green-to-red ratio increases from ~0.6 to ~3.5 with the increase of W/O ratio, hence with more hexagonal character of the crystal powders. During the cubic-to-hexagonal transition, an atom-lattice rearrangement modifies the inter-atomic distances between Yb and Er ions. Therefore, the most important mechanisms involved in the up-conversion processes for our chemical composition (ESA and ETU contributions) are affected, providing different green-to-red ratios. It is interesting to notice that samples exhibiting pure β-hexagonal phase (φ=66.7% and 87.5%) shows a similar value of G/R, which could be the maximum value (around 3.2) that can be reached under our experimental conditions.

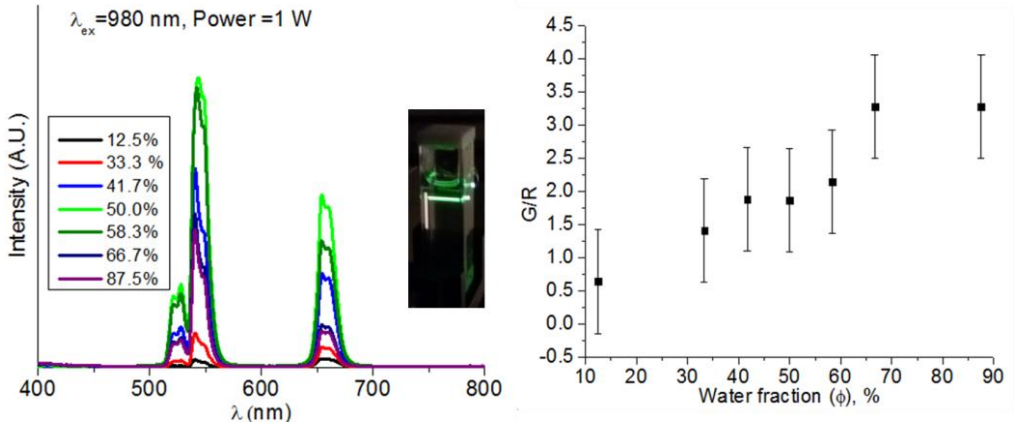

Figure 2.23: Up-conversion fluorescence spectra (λ_{exc}= 980 nm and pump density: 105 W/cm^2) of the Er,Yb-doped $NaYF_4$ samples prepared with different W/O ratio. Inset: Representation of the relative ratio of the areas for green and red emissions. Error bars are represented by the standard deviation.

The mechanisms mentioned in the first chapter, draw general schemes for the proposed mechanism of emission. These mechanisms are most likely the one happening in up-converting nanocrystals (non TTA), in which, for example, green and red emissions are often simultaneously obtained in Yb^{3+}–Er^{3+} co-doped systems with an overall yellow output. Yellow and blue colors are commonly observed in Yb^{3+}–$Ho^{3+}$and Yb^{3+}–Tm^{3+}co-doped systems as well, as a result of multiple, simultaneous transition. Each of them is governed by a multi-photon absorption mechanism. Alteration of the emissions intensities and fine tuning of the color output is one of the primary efforts in science in order to meet the requirements of various optical technologies, such as light emitting displays and multiplexed biological labeling, meaning that it is possible to manipulate emission mechanism to tune the outcoming visible light.[48,49] However, to do so, many tricks can be used in order to manipulate the optical output main color, including Ln concentrations and crystal structure manipulations.

As seen in the first chapter, $NaYF_4$:Yb,Er shows two distinct crystal structures, whose emission depends both on the local crystal field of the lanthanide which partially allows the parity 4f-4f forbidden emissions through odd-parity configurations and the spatial distances between sensing and actuating ions, which modifies the mechanisms underlying the main color of the emission.[48] It is known that α- and β- $NaYF_4$:Yb,Er have distinct emission efficiency and colors, with α-structures that often presents main emission in the red region of the visible spectrum, while β-structures show main emission in the green region of the visible spectrum.[48]

Known that $NaYF_4$ structures present different emission colors and efficiency, it looks obvious that each structure will present different emission intensity relations, which can be tuned upon manipulation of the mechanism of emission.[48] It is well known that $f_{g/r}$ is influenced by several factors, such as doping levels, excitation density, preparation temperature, oxygen impurities, crystallinity, surface ligands, and defects.[49]

In α- $NaYF_4$:Yb,Er it has been noticed that the G/R ratio decreases correspondently to an increase of size of the nanoparticles. It was suggested by Suyver and coworkers[50] that the saturation of emissions that takes place at high power densities proves that the up-conversion process in α- $NaYF_4$:Yb,Er is a sensitized up-conversion process involving $Yb^{3+}$and Er^{3+} rather than a purely ESA- type process involving only Er^{3+}.[50] However, Mai and coworker point out that the non-radiative decay of such

nanocrystals might be partially correlated with the influence between the surface defect, ligands, and surface Er^{3+} ions. As the ratio of the surface defects increases with decreasing size of the nanocrystals, the non- radiative decay is enhanced.[49] Quantitatively, it was found that shrinking crystal surface from about 13 to nearly 5, the $f_{g/r}$ was diminishing from 0.63 to 0.13 in α- $NaYF_4$:Yb,Er nanocrystals, and this result was addressed to few factors such as inclusion of oxygen atoms (partial oxygenation) to multiple surface defects.[49]

The same group describe the change in $f_{g/r}$, for β- $NaYF_4$:Yb,Er nanocrystals, under an excitation of 980 nm which reveal an increase of the ratio concomitant with the increase in the size of the nanocrystals. This result can be linked to a change in mechanism, passing from low pumping to high pumping density provoked from a pure 2-photon emission (low pumping density) to a partial 3-photon mechanism (high pumping density). The change in emission mechanism was proved by pump-power experiments.[49] In this article is described that on the basis of compositional optimization for such nanocrystals, the intensity ratio of green to red emission ($f_{g/r}$) reaches a maximum of about 30.

Comparing those results with our findings, we report that we found for nearly pure cubic crystals values were about the same found from Mai and coworkers[49] ($f_{g/r} \sim 0.5$) at very low water fractions. However it rapidly increases with the purification of phase and the switching from reverse to direct micelles, and with their consequent increase of size. This can be either due to a change in the emission mechanism or to a better distribution of sensing and actuating lanthanides within the crystals. However, we suggest that both the increasing in size and the consequent purification of crystal phase have a larger impact on the alteration of the G/R ratio because of the increasingly smaller number of surface defects and larger amount of actuating lanthanides *pro capita* within the crystals and not on the surface (quenched).

The color coordinate diagram (CIE1931) of the previous spectra is depicted in Figure 2.24. There is a clear tendency: the UC emission color of the sample prepared with the lowest W/O ratio (φ=12.5%) is red (sample with the smallest particle size and the highest amount of cubic phase) and continuously goes towards greener colors, as the hexagonal phase and crystal size increases. As expected, a similar position in the diagram is found for the pure hexagonal samples of φ=66.7% and 87.5%. The small variation of these two last samples can be attributed to the hexagonal-to-hexagonal crystal variation upon the order-disorder transition mentioned previously.

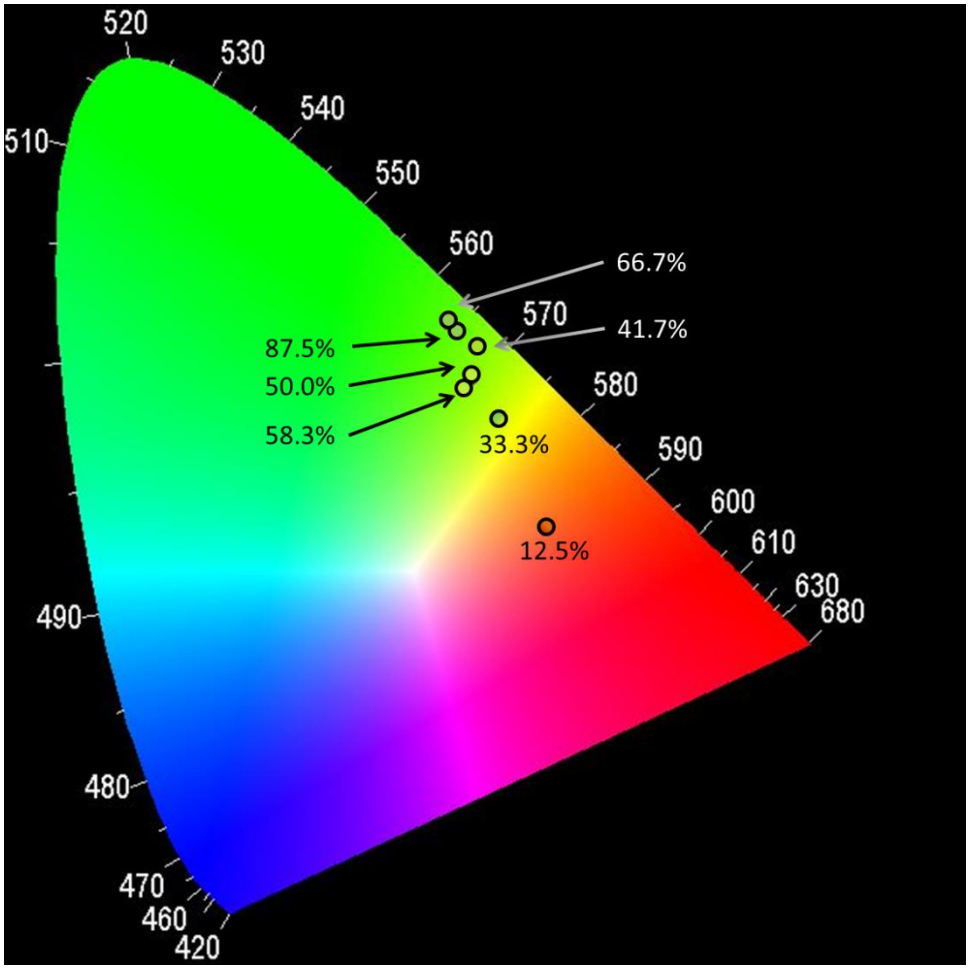

Figure 2.24: CIE 1931 color diagram for the various W/O ratios-prepared $NaYF_4$:Yb,Er nanocrystals.

The most important feature in the analysis of the UC emission spectra of the crystals, prepared with different alcohols as co-solvents, is the relation of the size and crystalline phase to their fluorescence. Figure 2.21 shows the up-converting spectra of the solids prepared using EtOH, 1-PrOH and 1-BuOH, the relative TEM images and the relative CIE 1931 color coordinates. Note that the pump power was adapted in order not to saturate the detector. Furthermore, the relative intensity of the spectra, (even using the same concentration of nanocrystals in suspension) is affected not only by the optical efficiency of each sample, but also by the tendency of crystals to

deposit (especially important effect in BuOH-sample) at the bottom of the vial or cuvette.

The results from the optical response agree well with the previous conclusions: the greater the crystal size and the hexagonal phase, the higher the green-to-red ratio and consequently, greener the color of the emission. The precise values of the green to red ratio are 1.5, 2.9 and 3.0 for the EtOH-, 1-PrOH-, and 1-BuOH-prepared crystals, respectively. Therefore, the visual color in the CIE 1931 diagram go from green-yellow to a green.

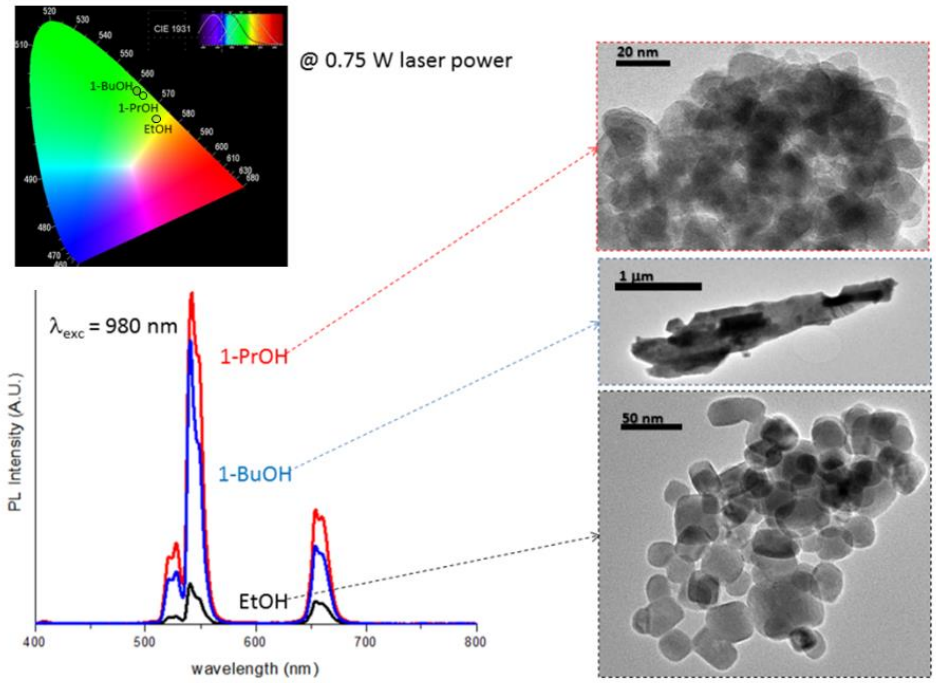

Figure 2.25: Up-conversion spectra and a selection of TEM images for the EtOH, 1-PrOH and 1-BuOH solvothermal-prepared solids. On the inset the CIE1931 color coordinates for the spectra of $NaYF_4$:Yb, Er under different co-solvent taken at 0.75 W.

Tuning the main emission for $NaYF_4$:Yb,Ln was performed using different elements (and relative quantities) as actuators. The extended light emitting elements, such as Tm^{3+}, Ho^{3+} and Er^{3+} ions, were incorporated as Ln ions in order to modulate the green, red and blue regions of the visible spectrum. Both Er^{3+} and Ho^{3+} codoped

nanocrystals emits mostly in the green region of the spectrum, while Tm-codoped crystals emits mainly in the blue region. The three UC PL spectra and the transitions attribute to each emission bands are shown in Figure 2.26.

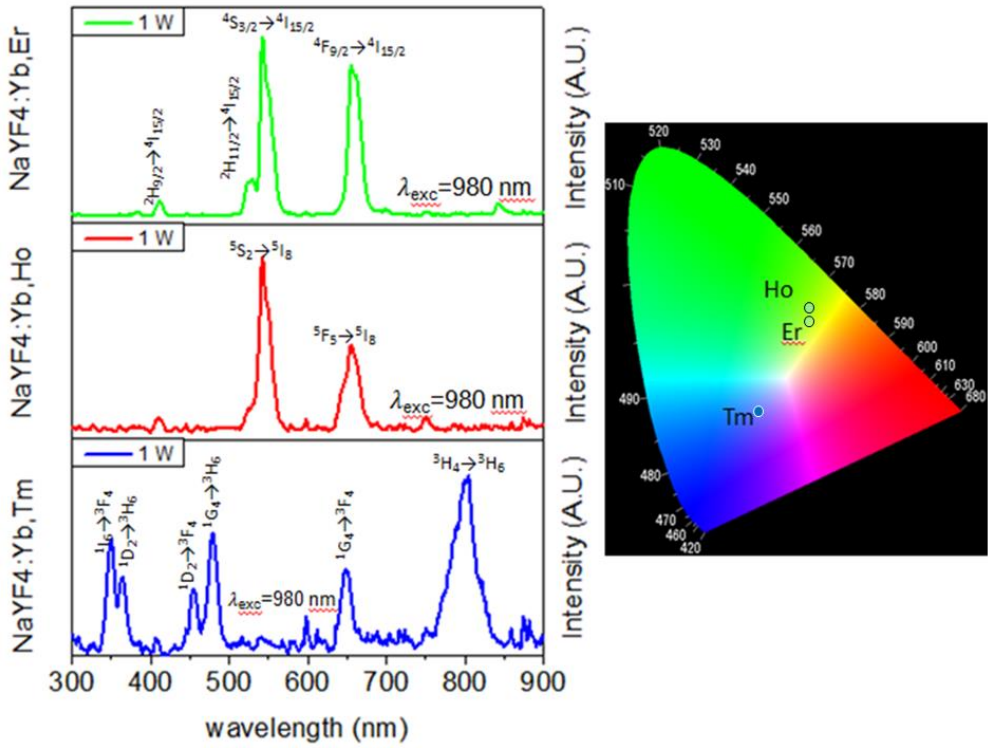

Figure 2.26: Photoluminescence spectra (λ_{exc}=980nm, 1W) of the up-converting nanocrystals: **1** Yb,Er; **2** Yb,Ho; **3** Yb,Tm-doped $NaYF_4$. CIE 1931 XYZ color coordinates are shown: the color coordinates were obtained at the same lasing power of the spectra.

Pump-power experiments on the solvothermal-prepared $NaYF_4$:Yb,Ln nanocrystals doped with Er, Ho and Tm have been performed in order to go further in the UC mechanisms of each system. The equation (1.1) of the Introduction chapter relates the intensity of one particular emission band (which varies with the laser pump power) with the number of photons absorbed by the sensing ions responsible for this emission. Thus, the slope of a log–log plot of intensity *vs.* excitation power density will provide the number of photons related with the UCPL. The results are shown in Figure 2.27.

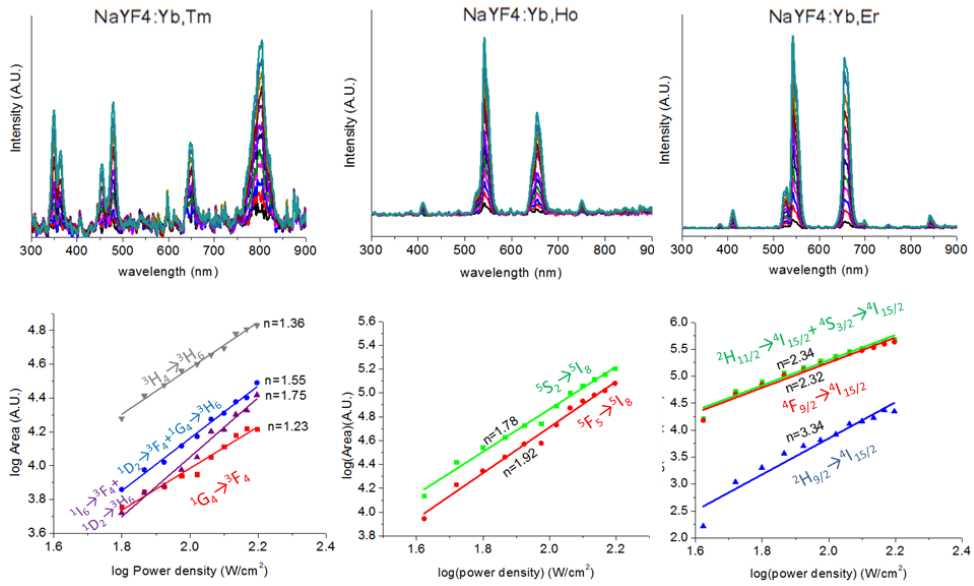

Figure 2.27: (Upper) Up-converting stacks of spectra for nano-$NaYF_4$:Yb,Tm, $NaYF_4$:Yb,Ho and $NaYF_4$:Yb,Er; **(Lower)** log–log plots of intensity *vs.* excitation power density for plots of Ho, Er and Tm-doped systems.

The slope for the green and red emissions of Er^{3+} and Ho^{3+} based up-converters show slopes close to 2, and the slope of the blue emission of the Er^{3+} doped crystals is close to 3 (as seen in the Figure 2.25); indicating that the UC mechanisms pass through a 2- or 3-photon absorption process, as ideally expected.

It turns out to be more critical the explanation of the experimental results for the Tm-based up-converters. Ideally, the slopes of the UV (around 350 nm) and blue (around 450 nm) emissions should be around 3, since the high energy of the emitted light for these Tm^{3+} emissions depends mainly on 3-photon absorption process. However, the experimental slopes are closer to 2. Instead, for the red (650 nm) and NIR (800 nm) emissions, the slopes can quite correctly describe the ideal 2-photon absorption process. The slopes that diverge greatly from the ascribed number of photons underlay significant limitations attributed to, probably, the polydispersity of the crystals and, also, to the difference in emission efficiency between hexagonal and cubic structures in $NaYF_4$:Yb,Ln. The significantly smaller crystal size and the high presence of cubic phase in Yb,Tm-doped UCNPs than in Yb,Er/Ho-doped NPs, can be an important issue on the detection of the number of photons. It is possible that the reduced number of active Tm^{3+} ions per particle (just 0.5% of Tm instead of 2% in Er

and Ho-doped NPs) and its smaller size increases the surface to volume ratio and the amount of defects. Therefore, those factors affect greatly the slopes for Tm-based UC processes.

2.2.6. Nucleation and growth model for solvothermal synthesis of UCNPs

Vast literature on diverse nanoparticles prepared via solvothermal routes is reported[20,28,33,34]; however when comes to up-converting nanocrystals, and in particular $NaYF_4$:Yb, Ln, only micro-sized and sub-micro sized crystals are generally found [19,8,51], or very small, cubic ones. The synthetic route that was followed in this study was taken from one of the first articles reporting the formation of pure hexagonal, highly-crystalline, bright, nano-sized (average size of ~25 nm) up-converting $NaYF_4$ crystals via solvothermal approach.[24] Despite numerous attempts of reproducing the same exact reaction, the pure hexagonal phase was not reached; therefore, a complete study of the different solvothermal conditions was performed. Furthermore, the nucleation and growth model proposed in that report, which is based on the formation of nanoparticles at the *solid–liquid* interface (with *solid phase*: mixed Y,Yb,Ln-stearate precursor, and *liquid phase*: the water-ethanol-oleic acid solution), was somehow limited.

According to the results of this PhD thesis, a more plausible explanation of the crystal formation will be proposed in this section. Briefly, the mixed metal stearates, in contact with the triphasic emulsion, dissolve and dissociate as charged species. Then, the lanthanide ions together with the fluoride and sodium ions previously dissolved in water start to form the first nuclei of α-$NaYF_4$:Yb,Er in the water phase. Then, a controlled growth of the crystals in the polar medium takes place, and after a critical size, the α-nanocrystals transform into β-nanoparticles.

The optimized synthesis was mainly focused in the water:oil ratio of 1:2 (φ=33%) because *inverse micelles* (small droplets of water in the oil phase) are formed, providing a spatial confinement for the nucleation and growth of the crystals. Even if several synthetic parameters have been evaluated, pure hexagonal phase was never completely reached. Furthermore, the particle size distribution was not so narrow than the one obtained by the most used thermal decomposition synthetic procedure. Nevertheless, the size of the crystals was adjusted to a distribution between 20 nm

and 50 nm, at least less than 80 nm, which was one of the goals that were attempted during this project, and their luminescence was more than acceptable.

The model presented here proposes the formation of nanoparticles with sized below 100 nm, through inverse micelles at low W/O ratios; on the contrary, at high water content, the formation of direct micelles takes place, so losing spatial constriction and large crystals are found. The former case generally produces mixed α+β phases with 70-80% hexagonal nanocrystals, and the later conditions provide 100% hexagonal crystals but with sizes of larger than 200 nm. A schematic representation of this model is shown in Figure 2.28.

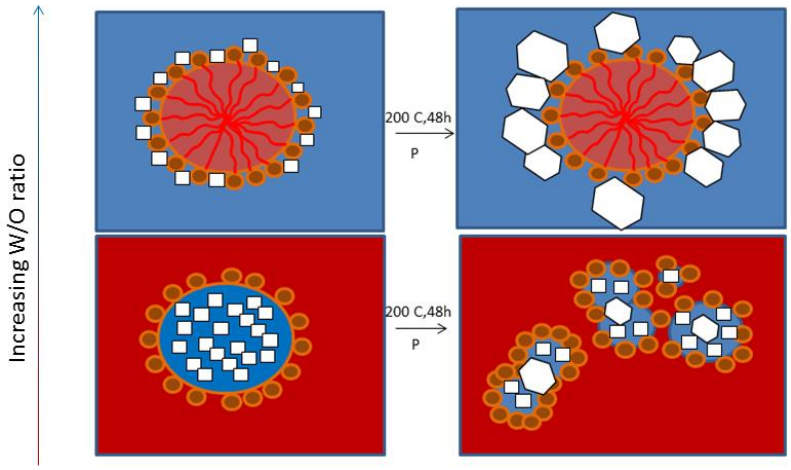

Figure 2.28: Direct (upper diagram) and inverse (lower diagram) micelle formation at high and low water-to-oil ratios. Blue and red are water and oil phases, respectively; orange spheres represent polar heads, and the white squares and hexagons represent α- and β-$NaYF_4$ crystals.

The use of ethanol, at low W/O ratios helps the mixing of the tri-phasic emulsion. On the other hand, at high W/O ratios, the ethanol contributed to a disruptive effect on the micellar structuration, leaving oleic acid monomers in the aqueous medium and not as micelles[36,40,42]. This effect can lead to uncontrolled crystal growth and polydispersity. Then, crystals fuse together under the conditions of high pressure and temperature, and epitaxial growth of the crystals.

The formation of "*direct*" or "*inverse*" micelles explains, therefore, both the size and the phase of the crystals. At low W/O ratios, under which the formation of inverse micelles confines water "micro-pools" within the polar heads that clusters around, where the ions *"meet"* and form kinetically stable crystal germs first (cubic) which,

successively grow until an hexagonal lattice is formed. If the aqueous medium is highly confined in inverse micelles, some cubic crystals do not reach the critical size to form hexagonal nanocrystals, maintaining the cubic structure due to a distribution of sizes of the micelles.

Under high W/O ratios, the formation of direct micelles clusters the tail of the lipids (OA molecules) and maintains the polar heads toward the water medium, which is found in larger quantity. The water phase contains all the ions (Na^+, F^-, Y^{3+}, Yb^{3+} and Ln^{3+} ions) necessary to form the cubic crystal germs, under the solvothermal conditions, and these small nuclei grow and coalesce giving to large hexagonal lattices because of the lack of space confinement.

In the optimized conditions (low W/O ratio, with *inverse micelles*), the nucleation of crystals takes place in the water micelles but in the water-oil interlayer[14,18,24]. In that case, two different mechanisms can be simultaneously responsible for the crystal growth and cubic-to-hexagonal transformation.

The first one implies that α-crystallites incorporate ions (Na^+, F^-, Y^{3+}, Yb^{3+} and Ln^{3+} ions) with the stoichiometric ratio at the surface, giving an epitaxial growth of the crystal lattice. At a certain point, the diameter of the crystals increases as much as that the cubic to hexagonal transition is the only way to lower the energy of the crystals at the pressure and temperature conditions (Figure 2.29, mechanism 1).

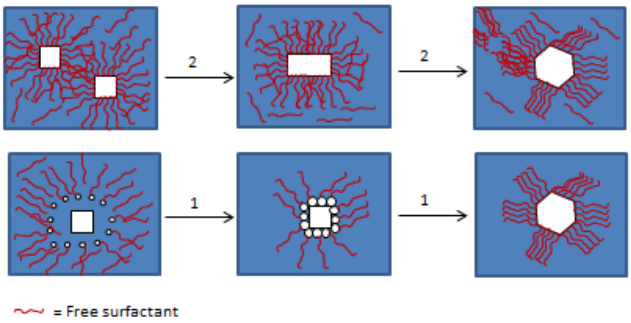

Figure 2.29: Mechanisms of formation of cubic to hexagonal transitions for the formation of hexagonal crystals (1) addition of extra ions within cubic germs; (2) two cubic germs that fuse together and transform into hexagonal crystals to lower their energy

In that case, the size of the crystals (α or β) are limited by the diameter of the micelles and also to the amount of ions dissolved in the same micelle to growth. However,

since the solvothermal reaction is assumed to be a dynamic system (even if the reactors have no stirring), there is another possibility for the crystal growth: coalescence. In essence, two or more cubic crystals can coalesce and form larger crystals which quickly transforms into hexagonal lattice due to energetic stabilization (mechanism 2 in Figure 2.29). Both competitive mechanisms are possible and cannot be discarded in the explanation for the formation of mixed-phases solids.

This model of nucleation and growth provides an alternative mechanism to the one reported by the authors[24] and reflects in more accurate the experimental evidences. Other authors[18,23,52] already pointed out that it was not possible to obtain pure hexagonal UC $NaYF_4$:Yb,Ln at temperatures lower than 180°C under similar solvothermal conditions, because the thermal energy fed and the relative autogenous pressure are not strong enough to ensure the cubic-hexagonal phase transition. This work disproves, then, the findings reported by the authors of our protocol, in which the β-crystal formation was carried at 150°C for 8 hours.

The alcohols chain length also affects the stability of emulsions and ultimately the crystal formation, as shown in Figure 2.30. The increase in the alcohol chain length alters the micellar geometry and gives to small (few nm) isolated particles in the case of using EtOH, more aggregated particles for the synthesis with 1-PrOH, and micrometric *sintered* rods when using 1-BuOH. The hexagonal character was increasing with the particle size. The formation of large rods can derive from an *"indefinite"* epitaxial growth or from a change in geometry of the inverse micelles, from spherical to tubular/laminar. 1-PrOH may enhance the number of micelles containing smaller crystals and has the effect of making them stuck together, resulting in rod-like aggregates of nanoparticles. It can be considered as an intermediate result between the mixed phase nanoparticles (EtOH) and the pure hexagonal large microrods (1-BuOH).

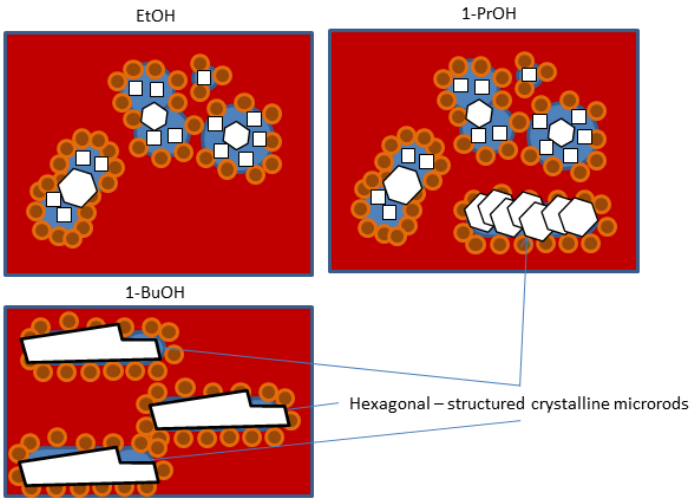

Figure 2.30: Effect of alcohol chain length on the nucleation and growth of the crystals.

2.3. Surface modification of solvothermal-prepared UCNPs

This solvothermal route leaves the crystals covered with an oleic acid layer which hinders bio-chemical applications since does not permit their dispersability in water. To switch between hydrophobic and hydrophilic surfaces, especially for bio-medical applications, several surface modification strategies have been developed in literature, from ligand exchange[53,54] to core- shell and core-multiple shells[49,54–56]. Attempts to switch surfaces of nanomaterials were performed in this PhD thesis using a protocol reported by Van Veggel *et al*[54]. The procedure is included in the blue frame.

Surface modification of $NaYF_4$:Yb,Ln

First, a suspension of 1% in weight of oleic acid-coated UCNPs in toluene was prepared. 200 μL of this solution were added to a 5 mL solution 1:1 of dichlorometane (DCM) and dimethylformamide (DMF), in which 75 mg of polyvynilpirrolidone (PVP) (a water-soluble polymer) were previously dissolved. The clear solution is refluxed for 6 hours at 80°C, after which 60 mL of diethyl ether was added to induce precipitation. The water-soluble particles are centrifuged at 4500 rpm for 5 minutes, and washed with ether.

This protocol permits, as well, prepare core-shell architectures from the PVP-grafted UCNPs, and cover them with a thin shell of SiO_2 using TEOS (tetraethoxysilane) as starting precursor. To achieve this goal, the PVP-decorated UCNPs recovered from the centrifuge are dissolved in 6.5 mL of absolute ethanol, in which 280 μL of concentrated NH_3 and 65 μL of 10% weight TEOS in EtOH were mixed. The system was stirred overnight, then centrifuged at 4500 rpm for 5 minutes and washed with ethanol.

The same procedure was used to make a second shell of Phenyl-SiO_2 (core:shell:shell Ln,Yb:$NaYF_4$@SiO_2@Ph-SiO_2) for usage in analytical applications. For the second layer, a mixture 3:1 wt/wt of Phenyl-triethyloxysylane (PTEOS) and TEOS was used. Then, 33 μL of this mixture were added to a 6.5 mL EtOH dispersion of the as-prepared core-shell system, under reflux at 100°C for 2 days, to ensure complete attachment of the silica shells to the particles.

The as-prepared particles were characterized by FTIR and TEM in order to make sure that the ligand exchange was successfully performed without affecting other structural parameters, and their up-converting properties were further analyzed.

FTIR spectra of the UCNPs coated with different ligands and shells are shown in Figure 2.31.

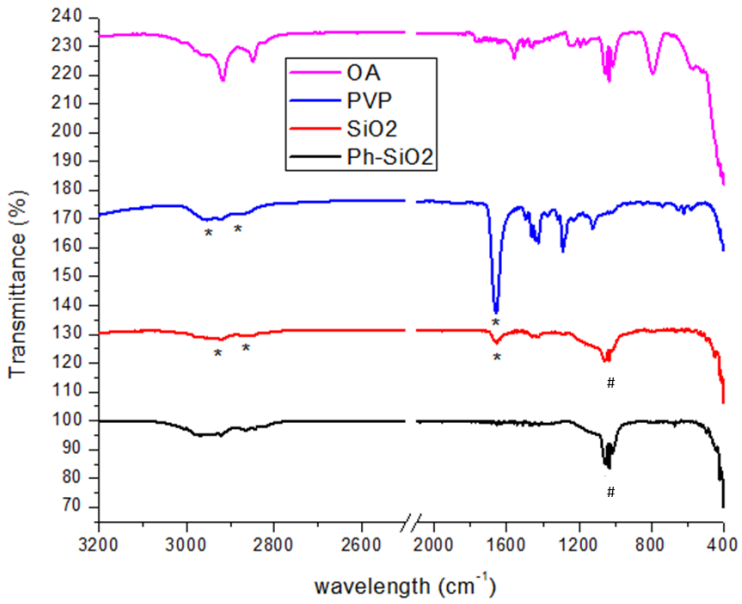

Figure 2.31: FTIR spectra of the UCNPs coated with Oleic Acid (pink line), with PVP (blue line), with a shell of SiO_2 (red line) and with two shells Ph-SiO_2@SiO_2 (black line). Asterisks are the vibrations of the PVP which are visible also in the SiO_2 coated ones. Hashes are the Si-O-Si vibration of SiO_2.

The comparison between the pink (OA-UCNPs) and blue (PVP-UCNPs) FTIR spectra reveal that the exchange from oleic acid to PVP is complete in the first step of the protocol. In fact, no peaks derivable from the oleic acid moieties were found in PVP-coated UCNPs. Furthermore, the presence of PVP molecules is confirmed by the strong peak of the carbonyl at around 1665 cm^{-1} that is absent in OA-coated UCNPs. The spectrum of Ln,Yb:$NaYF_4$@SiO_2 (red line) shows the characteristic Si-O-Si stretching bands at around 1050-1100 cm^{-1}, confirming the formation of the silica shell around the up-converter core, although some residual PVP units are still entrapped in the solid. The UCNPs with the second shell prepared from TEOS and PTEOS show a cleaner FTIR spectrum, with a more pronounced Si-O-Si vibration, and the complete removal of residual PVP molecules. The most intense bands associated to the phenyl group, i.e. the CH stretching at 3080–3010 cm^{-1} and the C=C

stretching in the region 1625–1430 cm^{-1}, are not easy to detect, probably due to the low concentration of phenyl species in the solid.

Images taken with a transmission electron microscopy (TEM) (Figure 2.32) show that the UCNPs were homogeneously coated with a small shell (~2 nm thickness) of PVP polymer after the first ligand exchange treatment as shown in the inset from Figure 2.32 left. However, TEM images reveals that the experimental procedure for the silica coating requires significant improvement, since instead of having a nice core-shell architecture, the system is better described as aggregates of amorphous silica, in which the UCNPs are entrapped. Despite of the aggregation, however, surface modification shows no alteration of the UCNP crystallinity and helps to render them soluble in water or polar solvents.

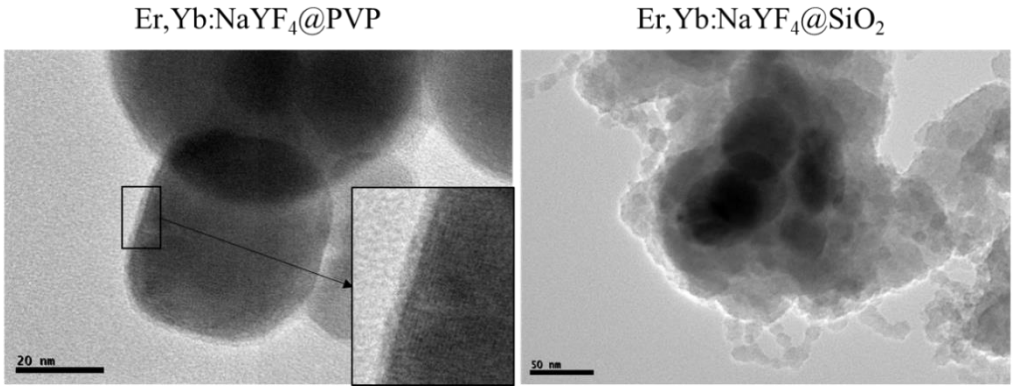

Figure 2.32: Electron microscopy images of the UCNPs after ligand exchange with PVP and after coating with SiO_2.

Finally, the up-conversion photoluminescence of the surface modificated Er,Yb:$NaYF_4$ samples dispersed in a polar solvent such as EtOH was performed upon irradiation at 980 nm with 2W laser power. The UCPL spectra of all samples show the characteristic emission profile of Er transitions previously described. The most important effect on the optical response is the significant enhancement of the PL intensity in all the spectral range when the sample is coated with SiO_2 and Ph-SiO_2/SiO_2. The substitution of organic ligands (both OA and PVP) by inorganic shells that prevents the quenching effect from CH and OH species as well as the decrease in the surface defects would explain the clear improvement of the emission intensity. In fact, we can notice that the Er,Yb:$NaYF_4$@SiO_2 sample has a lower emission intensity than the sample with double silica coating, which can be attributed to the presence of residual PVP molecules. So, even if the core-shell architecture was not properly

developed, the silica "coating" or imbibition offers benefits to the up-converter nanoparticles. However, another point that is also important to mention here is that the systems with the more hydrophilic shells (increasing in the order OA<PVP<SiO_2<SiO_2@Ph-SiO_2) provide a more stable suspension in the solvent and avoid the issues of sedimentation during the optical measurement.

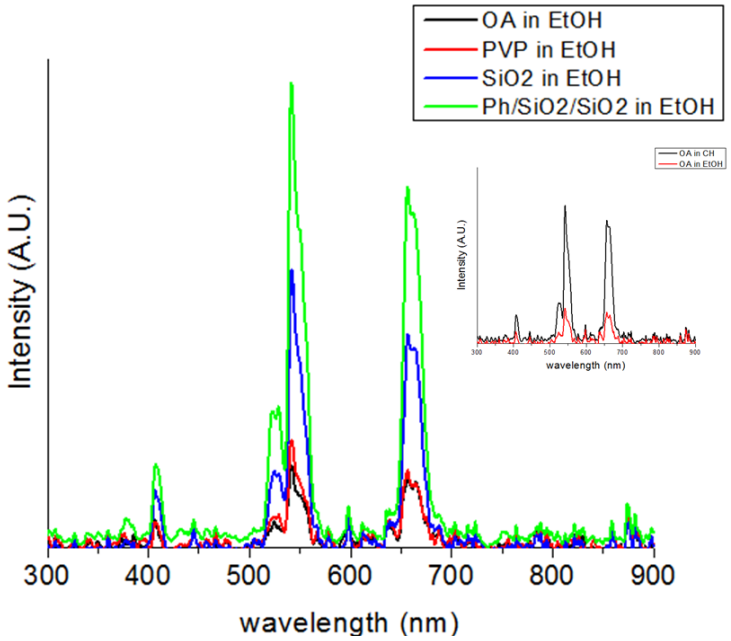

Figure 2.33: Emissions of $NaYF_4$:Yb,Er covered with different layers and dispersed in EtOH. Inset: intensity relation between OA coated UCNPs in cyclohexane (black) and EtOH (red) ($\lambda_{exc.}$=980 nm and 2 W laser power).

Therefore, when comparing the UC spectra of OA-coated nanoparticles dispersed in cyclohexane with the same concentration, a significant improvement (between 3 and 4 times) of the optical signal is detected. So, in conclusion, the intensity of the UC luminescence is affected by so many parameters that it is not always an easy task to analyse it in a simple way.

As conclusion of this section, surface modification of UCNPs is important for dispersing crystals in different solvents in sight of the application that is needed. In this study, the protocol for PVP ligand exchange was successful but further studies are still necessary to optimize the process of silica coatings in these solvothermal

prepared UCNPs. These issues are still ongoing and will be continued to pursue optimization of the process.

2.3 Conclusions

The aims of this work was first to shed light on the formation of β-$NaYF_4$:Yb, Ln (Ln= Er, Ho, Tm) nanocrystals under solvothermal conditions, establishing connections between crystal phase and size of the UCNCs with reaction parameters, as well as to study the structure(s) relations and relative optical activity.

Experimental findings shows that:

1) The reaction time and temperature, as well as O/W relations are critical parameters to control for the formation of UCNPs. The reaction conditions to get pure hexagonal structures requires at least 48 hours at 200°C. Below this time and/or temperature, cubic phase is always present. The study on the W/O ratio has demonstrated that low W/O ratios conduce to the generation of inverse micelles, which confines the spatial growth of the crystals, giving to nanoparticles between 20 and 50 nm mixed α,β-phase. In high W/O ratios, the larger content of water promotes the formation of direct micelles and larger crystals (between 200 and 400 nm) but pure hexagonal phase are formed. Alcohols, used as co-solvents within the emulsions have shown to have an effect in inverse-emulsion conditions: in fact, increasing the C-H linear chain from Ethanol to 1-BuOH, the nanoparticles show more aggregation and finally larger-spanned rods morphology. The formation of rods can be explained either through a change in emulsion geometry or through an increased epitaxial growth rate.
2) The optical UC response for the $NaYF_4$: Yb,Er system revealed that the more is the cubic character, the more intense the red emission are, meanwhile the green band increases with the hexagonal character.
3) The emissive properties of the up-converters can be tuned by changing the lanthanide ions; however, the particle size is affected by the nature and quantity of the lanthanide. In particular, $NaYF_4$:Yb,Ho and $NaYF_4$:Yb,Er prepared under same conditions show almost the same size, while $NaYF_4$:Yb,Tm are significantly smaller.

This study shows one of the first examples on the solvothermal preparation of up-converting nanoparticles of sizes comprised between 20 and 50 nm with strong up-

converting activity. This work can be used as a starting point for the future preparation of large quantities of pure hexagonal $NaYF_4$ nanocrystals.

.

2.4. Bibliography

(1) Walton, R. I. *Chem. Soc. Rev.* **2002**, *31*, 230–238.

(2) Chen, Z.; Tian, Q.; Song, Y.; Yang, J.; Hu, J. *J. Alloys Compd.* **2010**, *506* (2), 12–14.

(3) Wang, M.; Zhu, Y.; Mao, C. *Langmuir* **2015**, *31* (25), 7084–7090.

(4) Sun, Y.; Zhou, H. C. *Sci. Technol. Adv. Mater.* **2015**, *16* (5).

(5) Hongren, L.; Feng, L.; Aimin, D. *Luminescence* **2015**, *30* (6), 740–744.

(6) Riman, R. E.; Suchanek, W. L.; Lencka, M. M. *Ann. Chim. Sci. des Mater.* **2002**, *27* (6), 15–36.

(7) Demazeau, G. *Res. Chem. Intermed.* **2011**, *37* (2–5), 107–123.

(8) Zhuang, J.; Liang, L.; Sung, H. H. Y.; Yang, X.; Wu, M.; Williams, I. D. *Inorg. Chem.* **2007**, *46* (13), 2324–2329.

(9) Schreiber, D. R.; Pitzer, K. S. *Int. J. Thermophys.* **1988**, *9* (6), 965–974.

(10) Rao, C. N. R.; Vivekchand, S. R. C.; Biswas, K.; Govindaraj, A. *Dalt. Trans.* **2007**, No. 34, 3728.

(11) Lee, S. H.; Kang, M.; Cho, S. M.; Han, G. Y.; Kim, B.; Yoon, K. J.; Chung, C. *Photochem. Photobiol.* **2001**, *146*, 121–128.

(12) Dunne, P. W.; Lester, E.; Walton, R. I. *React. Chem. Eng.* **2016**, *1* (4), 352–360.

(13) Tatarova, E.; Dias, A.; Henriques, J.; Abrashev, M.; Bundaleska, N.; Kovacevic, E.; Bundaleski, N.; Cvelbar, U.; Valcheva, E.; Arnaudov, B.; Do Rego, A. M. B.; Ferraria, A. M.; Berndt, J.; Felizardo, E.; Teodoro, O. M. N. D.; Strunskus, T.; Alves, L. L.; Gonçalves, B. *Sci. Rep.* **2017**, *7* (1), 1–16.

(14) Wang, X.; Zhuang, J.; Peng, Q.; Li, Y. *Nature* **2005**, *437* (7055), 121–124.

(15) Wang, L.; Li, Y. **2006**.

(16) Gersten, B. *Chemfiles* **2005**, *5* (No. 13), 11–13.

(17) Zhang, F. *Photon Upconversion Nanomaterials*; 2015.

(18) Li, C.; Quan, Z.; Yang, J.; Yang, P.; Lin, J. *Inorg. Chem.* **2007**, *46* (16), 6329–6337.

(19) Tan, M. C.; Al-Baroudi, L.; Riman, R. E. *ACS Appl. Mater. Interfaces* **2011**, *3* (10), 3910–3915.

(20) Zhang, F.; Li, J.; Shan, J.; Xu, L.; Zhao, D. *Chem. - A Eur. J.* **2009**, *15* (41), 11010–11019.

(21) Wang, L.; Li, Y. **2007**, No. 27, 727–734.

(22) Zhang, M.; Fan, H.; Xi, B.; Wang, X.; Dong, C.; Qian, Y. *J. Phys. Chem. C* **2007**, *111*, 6652.

(23) Ledoux, G., Joubert, M.F., Mishra, S. 2016; pp 35–54.

(24) Wang, M.; Liu, J. L.; Zhang, Y. X.; Hou, W.; Wu, X. L.; Xu, S. K. *Mater. Lett.* **2009**, *63* (2), 325–327.

(25) Wang, M.; Li, M.; Yang, M.; Zhang, X.; Yu, A.; Zhu, Y.; Qiu, P.; Mao, C. *Nano Res.* **2015**, *8* (6), 1800–1810.

(26) Tian, G.; Gu, Z.; Zhou, L.; Yin, W.; Liu, X.; Yan, L.; Jin, S.; Ren, W.; Xing, G.; Li, S.; Zhao, Y. *Adv. Mater.* **2012**, *24* (9), 1226–1231.

(27) He, M.; Huang, P.; Zhang, C.; Chen, F.; Wang, C.; Ma, J.; He, R.; Cui, D. *Chem. Commun.* **2011**, *47* (33), 9510.

(28) Zhai, X.; Wang, Y.; Liu, X.; Liu, S.; Lei, P.; Yao, S.; Song, S.; Zhou, L.; Feng, J.; Zhang, H. *ChemPhotoChem* **2017**.

(29) Smith, T., Guild, J. **1931**, *73*.

(30) Papageorgiou, S. K.; Kouvelos, E. P.; Favvas, E. P.; Sapalidis, A. A.; Romanos, G. E.; Katsaros, F. K. **2010**, *345*, 469–473.

(31) Kojima, Y. **1970**, *27* (1964).

(32) Liu, X.; Deng, R.; Zhang, Y.; Wang, Y.; Chang, H.; Huang, L.; Liu, X. *Chem. Soc. Rev.* **2015**, *44* (6), 1479–1508.

(33) Haase, M.; Schäfer, H. *Angew. Chemie - Int. Ed.* **2011**, *50* (26), 5808–5829.

(34) Shan, J.; Ju, Y. *Nanotechnology* **2009**, *20* (27), 275603.

(35) Xin, X.; Zhang, H.; Xu, G.; Tan, Y.; Zhang, J.; Lv, X. *Colloids Surfaces A Physicochem. Eng. Asp.* **2013**, *418*, 60–67.

(36) Dickinson, E.; Golding, M. *J. Colloid Interface Sci.* **1998**, *197* (1), 133–141.

(37) Wang, Z.; Song, J.; Zhang, S.; Xu, X. Q.; Wang, Y. *Langmuir* **2017**, *33* (36), 9160–9169.

(38) Grzechnik, A.; Bouvier, P.; Crichton, W. A.; Farina, L.; Köhler, J. *Solid State Sci.* **2002**, *4* (7), 895–899.

(39) Grzechnik, A.; Bouvier, P.; Mezouar, M.; Mathews, M. D.; Tyagi, A. K.; Köhler, J. *J. Solid State Chem.* **2002**, *165* (1), 159–164.

(40) Birdi, K. S. *Colloid Polym. Sci.* **1982**, *260* (6), 628–631.

(41) Shan, S.; Wang, X.; Jia, N. **2011**, 3–7.

(42) Mathew, D. S.; Juang, R. S. *Sep. Purif. Technol.* **2007**, *53* (3), 199–215.

(43) Sanchez-Dominguez, M.; Pemartin, K.; Boutonnet, M. *Curr. Opin. Colloid Interface Sci.* **2012**, *17* (5), 297–305.

(44) Capek, I. *Adv. Colloid Interface Sci.* **2004**, *110* (1–2), 49–74.

(45) Debuigne, F.; Jeunieau, L.; Wiame, M.; Nagy, J. B. *Langmuir* **2000**, *16* (20), 7605–7611.

(46) Wang, F.; Han, Y.; Lim, C. S.; Lu, Y.; Wang, J.; Xu, J.; Chen, H.; Zhang, C.; Hong, M.; Liu, X. *Nature* **2010**, *463* (7284), 1061–1065.

(47) Ramasamy, P.; Manivasakan, P.; Kim, J. *RSC Adv.* **2014**, *4* (66), 34873–34895.

(48) Dong, H.; Sun, L.-D. D.; Yan, C.-H. H. *Chem Soc Rev* **2015**, *44* (6), 1608–1634.

(49) Mai, H. X.; Zhang, Y. W.; Sun, L. D.; Yan, C. H. *J. Phys. Chem. C* **2007**, *111* (37), 13721–13729.

(50) Suyver, J. F.; Aebischer, A.; García-Revilla, S.; Gerner, P.; Güdel, H. U. *Phys. Rev. B - Condens. Matter Mater. Phys.* **2005**, *71* (12), 1–9.

(51) Dyck, N. C.; Van Veggel, F. C. J. M.; Demopoulos, G. P. *ACS Appl. Mater. Interfaces* **2013**, *5* (22), 11661–11667.

(52) Chang, H.; Xie, J.; Zhao, B.; Liu, B.; Xu, S.; Ren, N.; Xie, X.; Huang, L.; Huang, W. *Nanomaterials* **2015**, *5*, 1–25.

(53) Wilhelm, S.; Kaiser, M.; Wurth, C.; Heiland, J.; Carrillo-Carrion, C.; Muhr, V.; Wolfbeis, O. S.; Parak, W. J.; Resch-Genger, U.; Hirsch, T. *Nanoscale* **2015**, *7* (4), 1403–1410.

(54) Johnson, N. J. J.; Sangeetha, N. M.; Boyer, J.-C.; van Veggel, F. C. J. M. *Nanoscale* **2010**, *2* (5), 771.

(55) Hirsh, D. A.; Johnson, N. J. J.; Van Veggel, F. C. J. M.; Schurko, R. W. *Chem. Mater.* **2015**, *27* (19), 6495–6507.

(56) Dong, H.; Sun, L.-D.; Wang, Y.-F.; Xiao, J.-W.; Tu, D.; Chen, X.; Yan, C.-H. *J. Mater. Chem. C* **2016**, *4* (19), 4186–4192.

Chapter 3

Applications of solvothermal-prepared $NaYF_4$:Yb,Ln UCNPs

3.1 IR light-harvesting hybrid soft materials

3.1.1. Introduction and motivation

Up-converting nanoparticles have a long list of applications presented in literature: in biological[1], biochemical[2–5], medicinal[6–9] and pharmacological[10] field of science, as well as in technological fields such as forensic[11,12], temperature control[3,1314], photocatalysis[15], solar cells and photovoltaics[16], sensors[3,13,17], hybrid optical systems[18], and so on. Nevertheless, the development of transparent and easy-to-shape materials showing multiple light conversion effects remains a challenge for the deployment of new technologies in the fields of light emitting diodes[19] field-emission displays[20], plasma display panels[21] and luminescent solar concentrators (LSCs)[22]. In these fields of application, transparent hybrid materials exhibiting the unique properties of the up-converting systems have been investigated in the last decade[23].

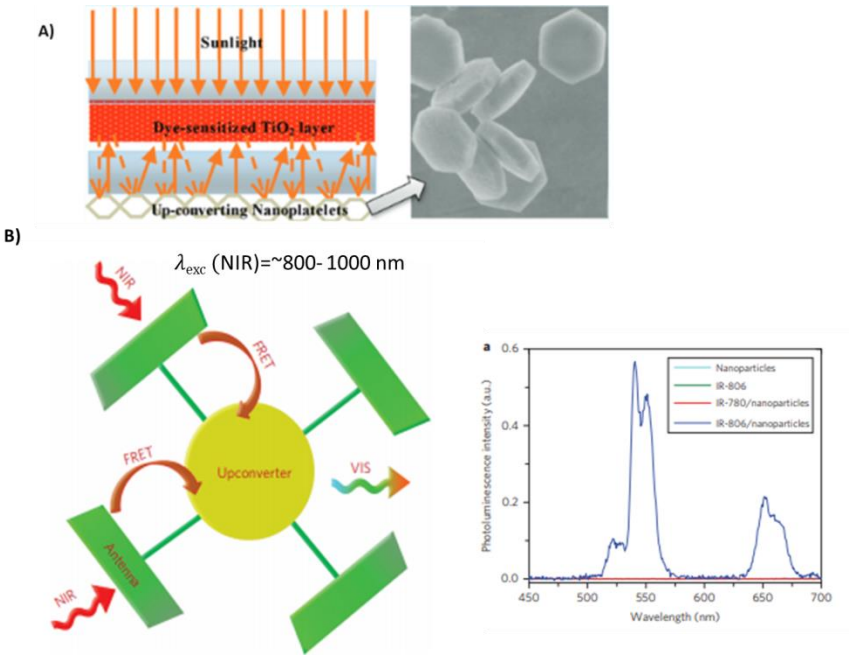

Figure 3.1. A) UCNPs nanoplatelets used for light harvesting in DSSC solar cells[16] and **B)** broad band IR **(left)** NIR absorption of antenna complex – coated UCNPs and their visible emission. Notice the steep increment in visible emission under a fairly low concentration of IR harvesting molecules **(right)**[24].

Embedding inorganic nanocrystals within an organic matrix had conferred to conventional materials a new dimension that offers new possibilities for exploiting novel applications[24–27]. To date, it is relatively recent the discovery of hybrids formed by organo or hydrogels trapping various optically active, inorganic nanocrystals. Organic and supramolecular gels have been proved to be interesting scaffolds for the entrapment of luminescent inorganic nanoparticles thanks to their properties: self-organization, gel-to-sol low temperature transition and reversibility, high solubility of the monomers in a large list of solvents with different polarity, and so on[28–31] (see Figure 3.2).

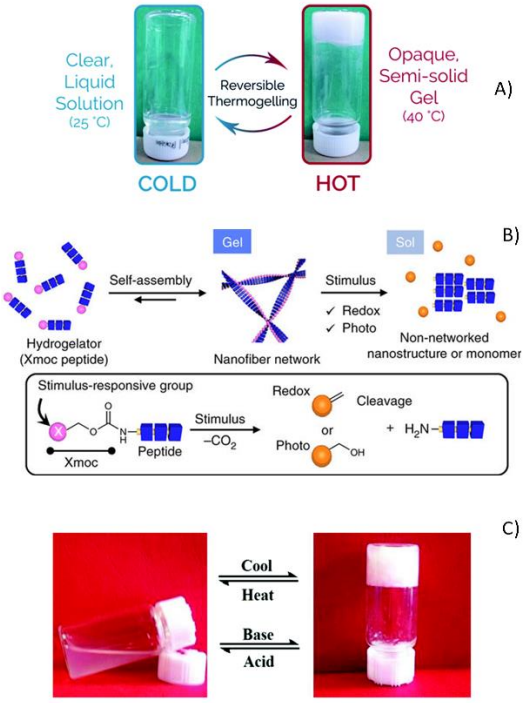

Figure 3.2. Basic properties of transparent supramolecular gels

Trapping photoluminescent nanocrystals within supramolecular gels has gained attention for the new interactions of the compounds with the light. Various kind of inorganic nano-phosphors have been found embedded within the organic matrix: from quantum dots (QDs) to SPR (Au, Ag, etc…) nanoparticles[29,32–35]. Moreover, recently, gels have been used in light and energy harvesting, either alone or with an inorganic moiety trapped within the fibers network[36–39]. Intercalation of inorganic emitters

within an organic matrix has shown a whole new type of materials, with interactions with light that differ from the standalone starting materials. As an example, it has been reported that the Au nanoparticles' plasmon quenches the emission of the DDOA (2,3-DidecyloxyAnthracene) when embedded in this fluorophore-based gels.[40] These hybrid materials have shown great potential as candidates for biological and industrial applications thanks to their low cytotoxicity[28] and high biocompatibility[41], in the first case, and as templates for the fabrication of organic electronic devices in the second case[42].

Despite of the huge amount of combinations to exploit up-conversion, very few works of hybrid complex gels entrapping these nanophosphors were reported in literature. The first article reported an homogeneous entrapment of up-converting $NaYF_4$:Yb,Er and $NaYF_4$:Yb,Tm nanocrystals in polypeptides, to tune the RGB emissions. In this case, the transparent gel acts as a passive scaffold for the homogeneous dispersion of the nanophosphors. The second paper goes more into the details on the possible mechanisms of an energy transfer between the emissions of UCNPs $NaYF_4$:Yb,Tm, and a matrix gel composed of 1-cyano trans-1,2-bis(3′,5′-bistrifluoromethyl-biphenyl)ethylene (CN-TFMBE). This compound was both a monomer that formed a fibrillary gel and a fluorophore capable of absorbing the UV radiations from the Yb,Tm-doped systems upon NIR irradiation. Results of this article have shown that the particles are found externally attached to the gel's fibers but not within the gel matrix; it is mentioned, but not explained the mechanism with which the gel matrix can act as a Rayleigh scattering network, as compared to a solution of UCNPs under the same conditions of irradiation.

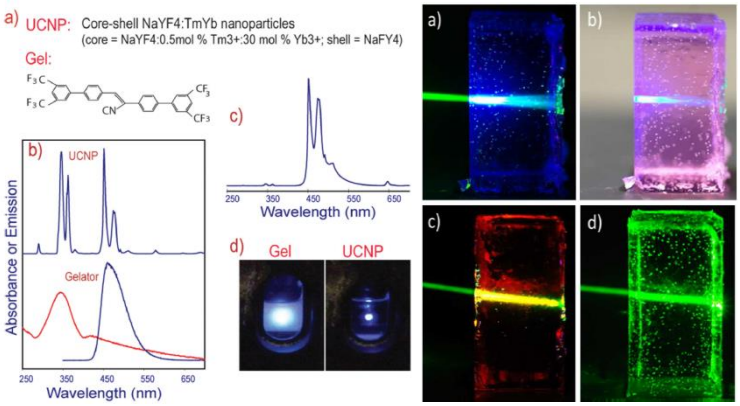

Figure 3.3. Images from reports about soft hybrid systems with up-conversion effects. **Left)** a) The chemical structure of the gelator and the UCNPs used to prepare the supramolecular

gel. b) UV–vis absorption (in red) and emission (λ exc = 348 nm). Furtjer details in Tong *et al.*[43] (**Right**) Pictures of free-standing PVOH-HMDI/DMF/DMSO organogels irradiated with a 2 mW green HeNe laser at 543 nm (power density = 350 mW cm^{-2}). The sample shown in a) and b) contains PdMesoIX ($2 \cdot 10^{-5}$ M) and DPA (10^{-2} M) and emitted a clearly visible blue upconverted light, even under ambient illumination. The samples shown in c) and d) contain only PdMesoIX (c, $2 \cdot 10^{-5}$ M) or DPA (d, 10^{-2}M) and display diffracted porphyrin phosphorescence (c) or excitation light (d)[44].

These supramolecular gels show great promises for the up-conversion applications (Figure 3.3) that their chemical nature may bring: self-healing, self-assembling materials, with new optical properties can be used as sensors, optical traps, drug delivery media (pH-driven) and scaffold for retaining of optical emitters for photodynamic therapies. However, despite these advantages, TTA upconverting complex systems show limited use since **a)** they are poorly soluble in water – which limits their use in biomedicine, **b)** although the up-conversion process is efficient, the metal complex acting as annihilator is will greatly reduce efficiency over time due to degradation of the organic matter, **c)** fairly higher energy irradiation sources (usually in the visible) and **d)** photobleaching over time.[45–48] Up-converting nanocrystals – containing gels show much more promises thanks to their robustness (no photobleaching for hours), low excitation source and ease of surface manipulation which can *'tune'* their dispersability in different solvents. Furthermore, their use in biomedicine has a rather large history in the scientific literature. Also, their intense emissions can be tuned from blue to red to green[49] depending on the crystal structure and hence the mechanisms underlying the principal emissions.[50,51]

Driven by the possibilities of manipulating IR radiation using UCNPs in soft materials, this chapter of the PhD thesis addresses the synthesis and characterization of a new hybrid supramolecular system based on a fibrillary network embedding the up-converters previously prepared by the optimized solvothermal route. This soft system is able to absorb both UV and NIR radiations and convert into visible emissions, what could be of interest to explore new areas of application in energy, photonics, photocatalysis, sensors, and so forth.

In particular, an organogel made of a fluorescent supramolecular network containing naphthalimide (NAF)-based fibers and nano-sized $NaYF_4$:Yb,Tm crystals has been chosen as ideal candidate to study the encapsulation of the up-converters, which should have improved stability towards UCNPs aggregation. On the other hand, the optical communication between the organic gel and the nanocrystals is expected. The

choice of $NaYF_4$:Yb,Tm is not casual: the 1,8-naphthalimide unit introduced in the gelator monomer is a well-known fluorophore[52] presenting light absorbance at λ_{max} = 340 nm and emission at λ_{max} = 410 nm, as shown in Figure 3.4b). NAF-based hybrid gels could then be excited by the UV emissions of Tm^{3+} ions (emission band at ~350 nm), upon 980 nm irradiation (Figure 3.4a)). Furthermore, the fluorophore would emit in a region (around 410 nm) where the UCNPs do not emit. A last aspect that will be addressed is the reversibility of the sol-gel transition and their optical response during that process.

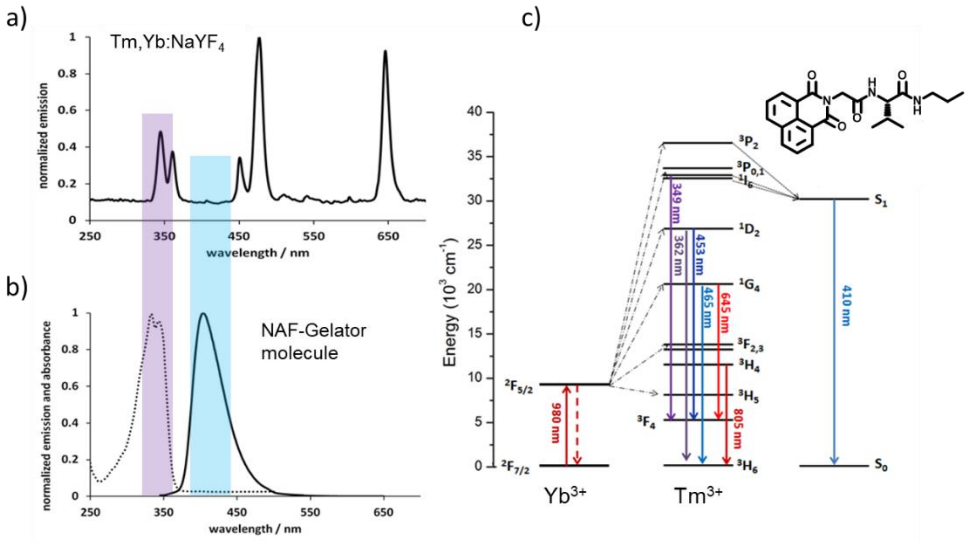

Figure 3.4: a) Emission spectrum of the $NaYF_4$:Yb,Tm powders prepared by solvothermal route. **b)** Absorption (dashed line) and emission (solid line) of the pure NAF-based gel upon λ_{exc}=340 nm. c) Jablonski diagram for the electronic transitions associated to the UC system of Yb^{3+}/Tm^{3+} pair and the energy transfers to the NAF chromophore.

3.1.2. Synthetic procedure

The synthesis of the hybrid supramolecular gel is described in the blue frame.

Preparation of the hybrid NAF-gels-UCNPs

The hybrid system was prepared as follows: 20 mg of UCNPs (Tm,Yb:$NaYF_4$) were suspended in 2 mL of butanol and sonicated for 5 min in a screw-capped vial. Then, $6x10^{-3}$ mmol of the organic gelator molecules were added and the closed system heated to 80 ºC until it was completely solubilized. The system was left cool down until room temperature for 10 minutes and the hybrid gel was formed. The samples were prepared in cylindrical glass vials with different sizes, and the gel dimensions ranged from 10-15 mm diameter and 5-20 mm height.

Figure 3.5 shows the synthetic procedure to produce the UC hybrid system. In essence, the monomer (or gelator molecule) represented with a red dot/square has the ability to self-assembly into long fibers, and includes the 1,8-naftalimide unit, which is a chromophore responsible for the optical communication between the matrix and the UCNP. The UCNPs are simply entrapped in the gel matrix during gelification.

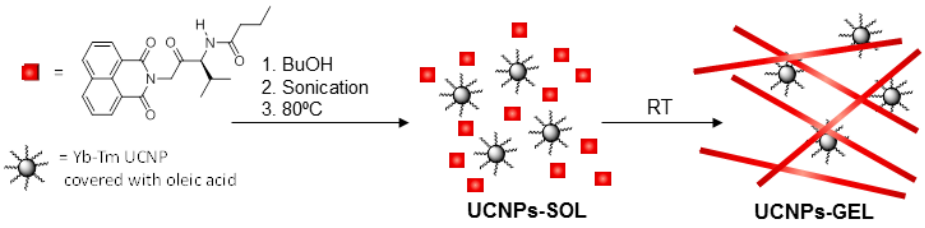

Figure 3.5: scheme of the sol- gel formation of the hybrid system

In few minutes, the composite hybrid gel containing the up-converting nanoparticles trapped was obtained. The gels were translucent as can be seen in the inverted vial from Figure 3.4 under visible light. Upon UV and IR irradiation, an intense fluorescence of the material is detected at naked eye (Figure 3.6).

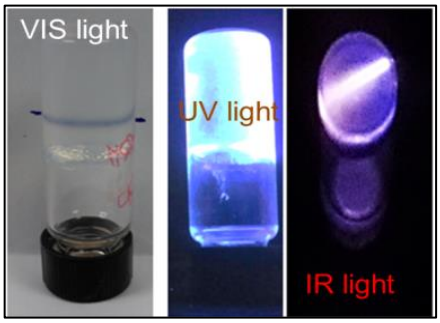

Figure 3.6: Photographs of the hybrid soft UC system under visible light, UV light (UV lamp) and NIR diode laser (980 nm)

3.1.3. Results and discussion

The structure of the hybrid gels were analyzed with OsO_4 staining-TEM to check if the microstructure of the gel is affected by the presence of the nanoparticles. Different photoluminescence (PL) measurements were performed to study the optical communication between the two constituents of the hybrid system. Temperature dependent PL experiments have been performed in order to determine a gel-sol transition and luminescence has been evaluated through the range of temperature used (10-90°C).

Transmission electron microscopy of the xerogel revealed the usual entanglement of micrometric fibers observed commonly in supramolecular gels and also the homogeneous dispersion of the UCNPs within the gel matrix, as shown in Figure 3.7. The thickness of the fibers depends on the cooling speed during the gel formation.

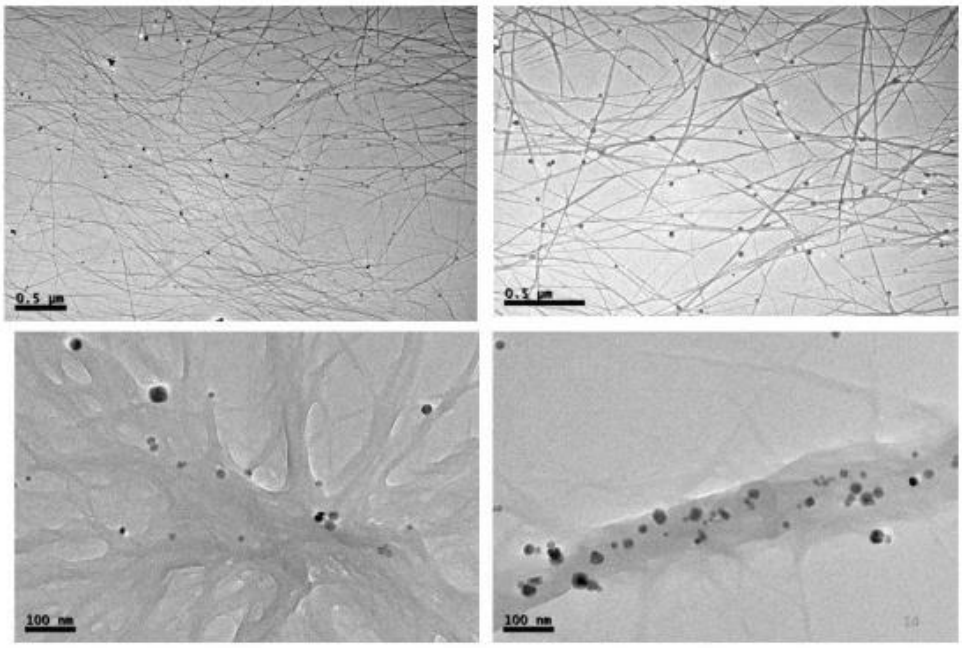

Figure 3.7: TEM images of $NaYF_4$:Yb, Tm UCNPs within the gel network and/or fibers

Very little aggregation of the phosphors was seen, and therefore we can be safe to assume that light scattering was not observed because of large objects were found within the fiber network.

The hypothesis of optical communication between the NIR-activated nanoparticles and the chromophore unit of the supramolecular gel was followed by fluorescence spectroscopy (Figure 3.8). The system responded as initially foreseen: upon excitation at 980 nm, the UV bands from Tm^{3+} ions disappear from the emission spectrum. Furthermore, a new band around 410 nm (from the chromophore) appears when the UCNPs are embedded within the gel network. The intensity of this band is low, but this is attributed to the low quantum yield of naphtalimide unit. This result is a confirmation that an energy transfer occurs and that the UCNPs are always nearby the organic chromophore.

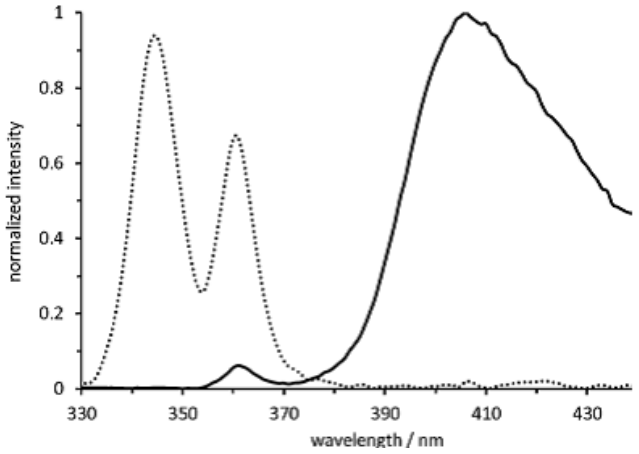

Figure 3.8: Overlay of the emission spectra of pure Tm,Yb:$NaYF_4$ nanocrystals (dotted line) and the UC hybrid gel (upon 980 nm excitation). Intensity at λ_{max} for both systems is normalized to 1.

In order to understand if the transfer is reversible, few thermal cycles with temperatures between 15 and 90°C were performed through a Peltier system, equipped with water circulation cooling system. The recorded intensity shows that the gel emission is temperature dependent, as seen in Figure 3.7. Interestingly, the hybrid system only originates IR-promoted emission at 410 nm in the gel state, being this process cancelled when the gel is disassembled at 80 ºC, a behavior directly related to the aggregation induced emission properties of the organogelator compound.

The system showed good reversibility and several heating-cooling cycles could be performed, restoring the upconversion to 410 nm at low temperatures (Figure 3.9). Consequently, the system formed by UCNPs-gel constitutes a thermally regulated light upconverting soft material.

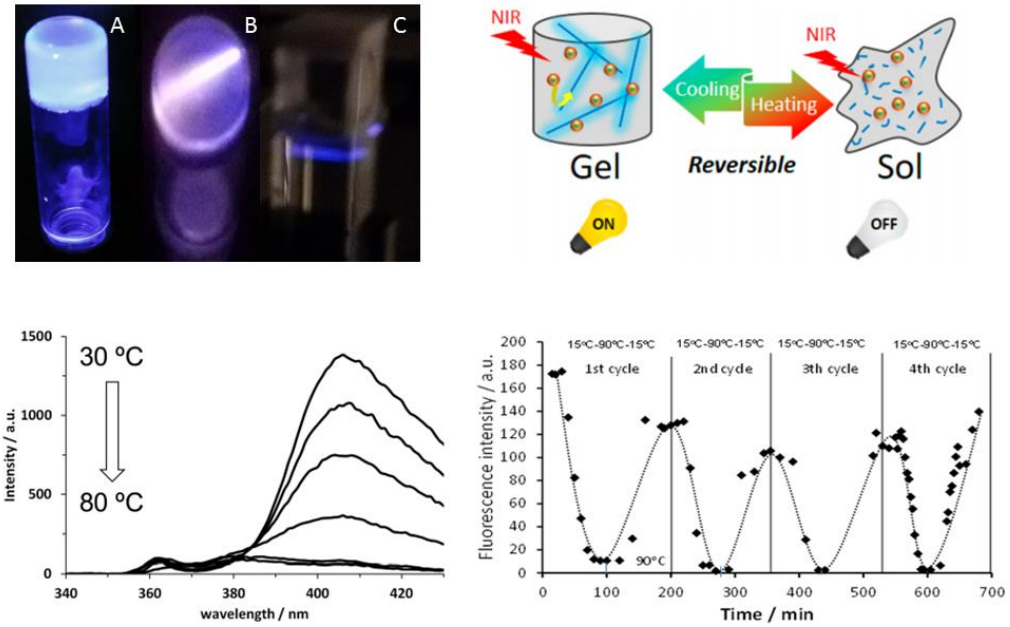

Figure 3.9: (top left) A: Naf-based gel under UV light; **B:** Naf-based composite emission under 980 nm irradiation and **C:** sol emission of the UCNPs at 980 nm irradiation (high temperature); **(top right):** scheme for the temperature dependent UC PL emissions for the hybrid UCNP-gel system; **(down left):** 410 nm emission of the Naphtalimide emitters in Naf-UCNPs composites and **(down right)** Reversibility of the emission intensity with several cycles of cooling and heating between 15 and 90°C.

This reversibility of the organic fluorophore of the gel with relatively small range of temperature may open several different scenarios for exploitation of this effect, as for example in temperature sensors, biological applications and bacterial cleaning of surfaces.

It is important to remark that the light emitted by UCNPs at ca. 350 nm is absorbed by NAF chromophore either when the hybrid system is in the gel state (at 30ºC-assembled) or in the sol state (80ºC-disassembled). This fact has implications for the mechanism of energy transfer taking place in the system. At 80ºC the fibers are disassembled and spatial proximity between UCNPs and naphthalimide units is precluded, discarding a dipole-dipole energy transfer mechanism like resonance energy transfer (RET).[53] Therefore, a photon reabsorption process, also known as inner filter effect, emerges as the most plausible mechanism for energy transfer between UCNPs both in gel and solution states although RET can't be discarded to

take place in the former case. The inner filter effect has been used in sensing applications based on UCNPs.

Concomitantly, it has been found a 475 nm Tm^{3+} emission band increase, which depends on the sol-gel transition. Variable temperature studies were carried out for suspensions of the UCNPs in butanol in the presence and absence of NAF organomolecule. Figure 3.10 represents the variation in intensity of the 475 nm Tm^{3+} emission with temperature.

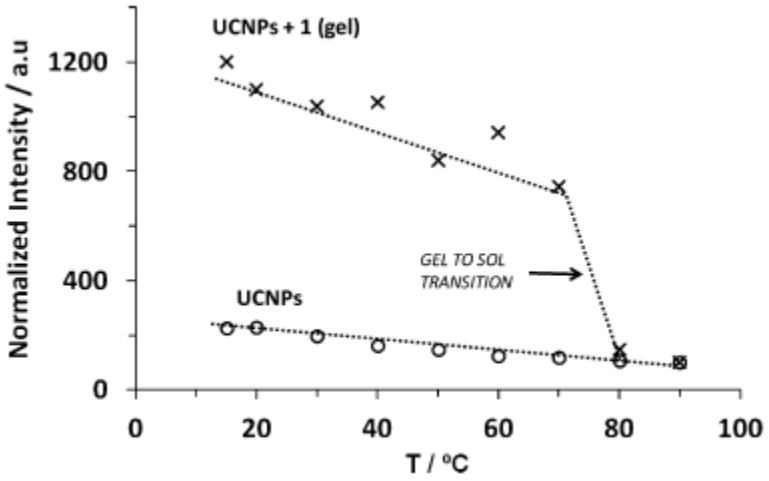

Figure 3.10: Variable temperature study of the emission intensity at 475 nm of UCNPs (suspended in butanol) and hybrid UCNPs-gel. Values are normalized taking as reference the intensities measured at 90 °C for both systems (λ_{exc} = 980 nm).

Clearly, an about 6-fold increment of intensity is found for the emission at 475 nm. This can be explained considering the gel as scattering matrix that permits the light to travel through the fibers and reaching further particles, which ultimately and simultaneously emit.

With these promising results, some other hybrid gels including UCNPs were prepared with NH_2-NAF-based fibers but using erbium ions instead of thulium ions. The choice of the lanthanide and the amino-derived chromophore corresponds to the overlap between the absorption of the amino-NAF and the blue emission of the erbium ions from the UCNPs. In this gel, the energy transfer was not so evident as in the previous hybrid system because of the low intensity of the blue emission in the $NaYF_4$:Yb,Er crystals (see Figure 3.11). In this case, the emission appearing around 405 nm from the $^2H_{9/2} \rightarrow {}^4I_{15/2}$ transition disappears when the UCNPs are embedded in

the hybrid gel. These results proofs that there is an optical communication, however, it is difficult to follow all the previous studies with this system.

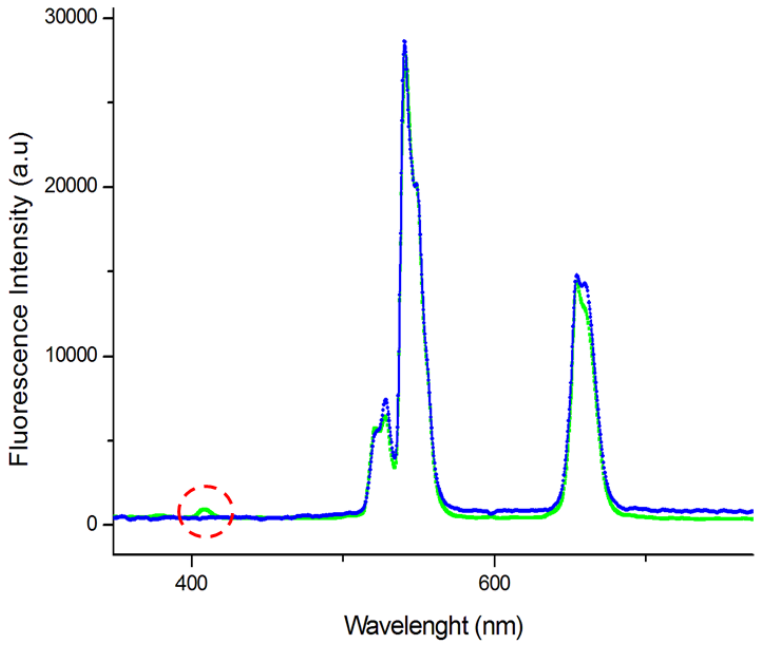

Figure 3.11: Normalized spectra of $NaYF_4$:Yb,Er suspension (green) in 1-BuOH and within the NH_2-Naf gel (blue). **Cirlce** shows energy transfer between the $^9H_{11/2} \rightarrow {}^4I_{15/2}$ and the gel matrix under 980 nm irradiation

Probably the most striking result from this NH_2-NAF gel trapping Er-doped UCNPs is the huge scattering effect of the fibrillary network responsible for the transport of IR energy to UCNPs and the bulb-like green emission of the whole gel, as shown in Figure 3.11. This effect was not so intense in the system with NAF and Tm-doped nanocrystals. A possible explanation for this special scattering effect would be on the structural arrangement of the matrix and the distribution of the UCNP within the gel. TEM analysis showed how the fibers are cross-linked like "stars", instead of long fibers, and the UCNPs are not well dispersed but aggregated and entrapped unhomogeneously within the branched structure, as seen in Figure 3.12. Probably, the aggregation of the nanoparticles increases the emission intensity and also the branched structure helps to scatter the light, giving to the special high emitting soft material. Some repeated cycles of high and low laser output was performed in both

hybrid systems (with thulium/NAF and erbium/NH_2-NAF), and the effect was fully reversible (Figure 3.12).

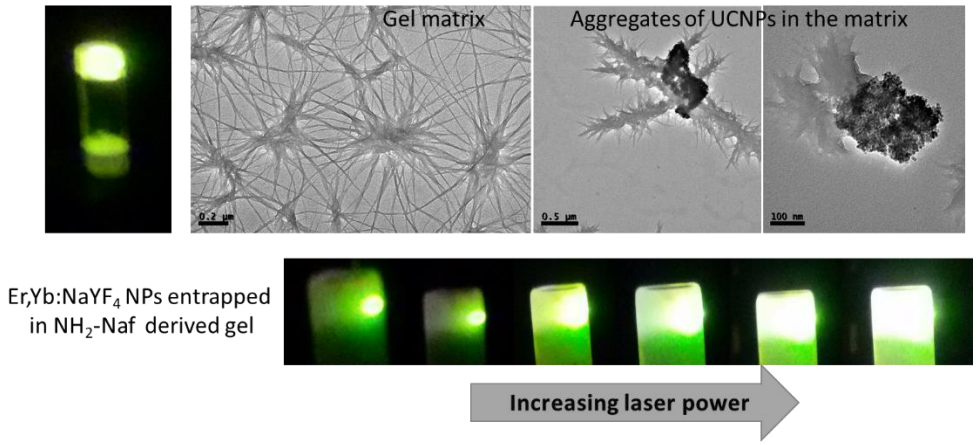

Figure 3.12: Images of the hybrid NH_2-NAF and $NaYF_4$:Yb,Er gel: the green emission of the gel (in a inverted vial), TEM images from different parts or the gel system and the dependence of the emitted light with the laser power (λ_{exc}=980 nm).

A keynote worth to add is that, despite of the IR radiation, which increments temperature itself, no degradation/dissolution of the gel or solvent evaporation was observed even at very high power densities.

3.2 Glycolipids-based vesicles entrapping UCNPs

3.2.1. Introduction and motivation

Encapsulation of various inorganic nanocrystals[10,54–59] in vesicles of various nature, from biopolymers[54–56,59] to surfactant-based systems[57–59], has been one of the mayor discovery in biotechnology, because of the vast potentialities as drug delivery and imaging carriers for the vesicles. These vesicular systems are capable to keep matter within their hydrophobic core and to travel around water-based systems. Their assembly/disassembly is an easy process and most of the time is reversible.[60]

The use of biosurfactants in non-deterging, materials science related applications is a recent research field that takes into account the astonishing and multivalent, yet unknown, properties of some of these compounds. In particular, bio-surfactants such as glycolipids have been studied for surface functionalization and/or encapsulation of different nanoparticles (iron oxide,[61] gold nanoparticles[62], etc.). Sophorolipids (SL),

which are biologically-derived glycoconjugates with a well-defined molecular structure have several advantages over other bio-surfactants. These compounds, whose open acidic form is highly suitable for nanoparticle stabilization[63], are readily obtained by a fermentation process of the yeast Candida bombicola (polymorph Starmerella bombicola) in large amounts. The final carbohydrate coated nanoparticles represent interesting potentially biocompatible materials for biomedical applications.

With these applications in mind, a study focused on the formation and stability in water medium of bio-surfactant based vesicles[60,63] to trap oleic acid-coated up-converting nanoparticles has been performed.

3.2.2. Synthetic procedure

Encapsulations of oleic acid capped nanocrystals were performed in water, medium used to prepare the vesicles which formation is granted upon steady changes of pH, using glycolipids as starting precursors after few pH manipulations. The glycolipids were supplied by the laboratory "Laboratoire de Chimie de la Matière Condensée de París". The chemical structure of the glycolipid is represented in Figure 3.13.

The synthetic procedure cannot be included in this PhD Thesis because the protocol was developed by another research group and it is not allowed to report it in this Thesis (it is under process of patenting/publication).

The pH changes promote onion-like multi-walled vesicles that present hydrophobic volume able to encapsulate the UCNPs either within the hydrophobic core or anchored between neighboring vesicles. The results were analyzed with XRD, cryo-TEM, up-converting luminescence and DLS measurements. For this study, Yb,Er UCNPs were chosen as luminescent materials of choice because of the strong green and red emission of the Er ion.

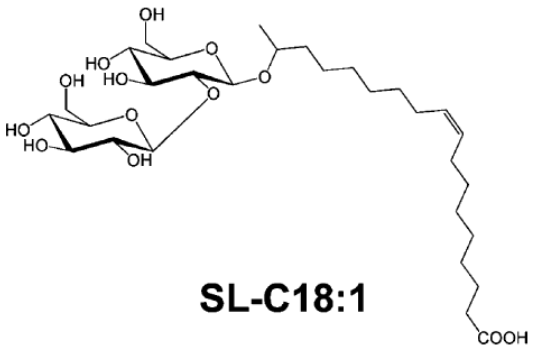

Figure 3.13. Chemical structure of the glycolipid employed for the study.

3.2.3. Results and discussion

In order to make the XRD measurements of the encapsulated nanoparticles, these have been lyophilized under low temperature and pressure. In the XRD patterns of Figure 3.14, we can observe that the UCNPs do not lose their crystallinity (mixed cubic and hexagonal phases) when encapsulated in the glycolipid vesicles, despite the pH manipulations. The cryo-TEM image shows the onion-like structure of the vesicles with some UCNPs entrapped inside the vesicles and in between the vesicles.

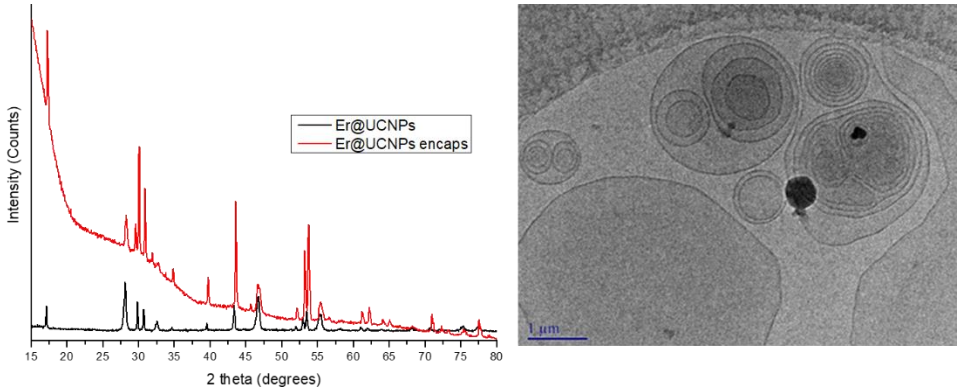

Figure 3.14: ***Left:*** XRD patterns of the as – prepared UCNPs and after encapsulation; ***Right:*** cryo-TEM of the glycolipid-based vesicles.

After all the pH manipulations made for the encapsulation, a ligand exchange between the free glycolipids and the oleic acid moieties on the surface of the nanoparticles might be induced. To ensure that no exchange occurred, DTA experiments were made on the particles after being free from vesicles thanks to a drastic pH change. Figure 3.15 resumes the DTA curves.

The DTA curves are pretty clear: a ligand exchange can be excluded because the as-prepared UCNPs and the *"freed"* UCNPs present a very similar thermal behavior (exothermic decomposition of oleic acid molecules between 200 and 350 ºC), whilst the glycolipids show three intense peaks at higher temperatures (between 350 and 550ºC) where the UCNPs do not provide any thermal process.

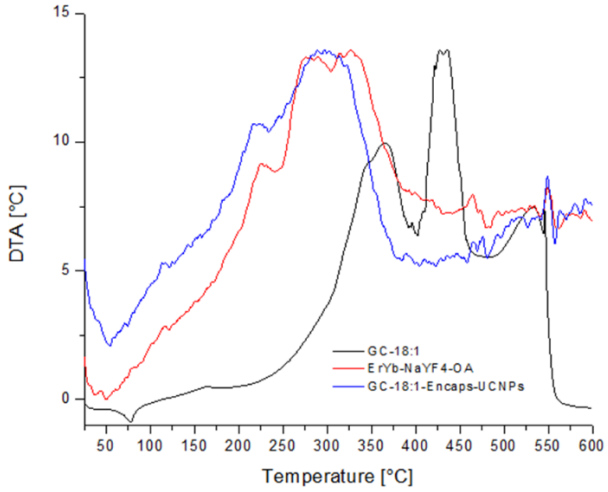

Figure 3.15: DTA curves of the GC-18:1 glycolipid (black), the as-prepared UCNPs (red) and the "*free*" particles *after* several pH manipulations.

Once verified some important points, it was interesting to study the stability of the vesicles including the UCNPs in water. DLS measurements have shown that the entrapment of OA –coated UCNPs is stable and there is no degradation over long periods of time (1h), for both the Er,Yb- and Tm,Yb- doped UCNPs, as shown in Figure 3.16.

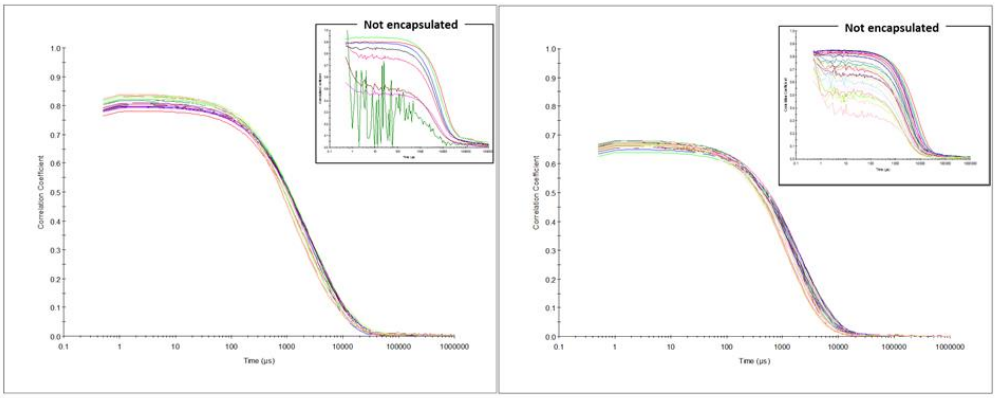

Figure 3.16: DLS kinetic experiments correlograms in 1h 30'. **left:** encapsulated $NaYF_4$:Yb,Er; inset is representing the correlogram of the bare UCNPs in water; **right:** encapsulated $NaYF_4$:Yb,Tm; inset is representing the correlogram of the bare UCNPs in water.

The "fresh" OA-coated UCNPs in water have no long-life and very quickly correlograms are no longer showing the same distribution of sizes (see the insets of Figure 3.16). This result is mainly due to the fact that OA-capped UCNPs are quickly precipitating and the process shows that increasingly fewer particles are found in solution until the correlogram no longer shows relation between size and time of detection. On the other side, the encapsulated UCNPs show correlograms that are consistent with the same size after more than 1 h and 30' of suspension.

The systems showed very nice up-conversion emission upon excitation at 980 nm (Figure 3.17).

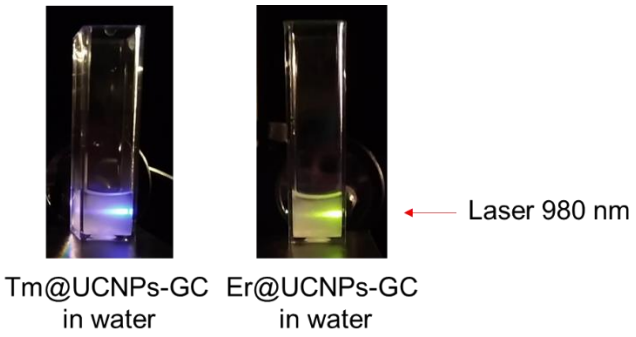

Figure 3.17. Photographs of the Tm- and Er- doped UCNPs encapsulated in the vesicles

The stability of the suspensions of the encapsulated UCNPs was therefore studied analyzing the intensity of the up-converting spectra with time upon different forced sedimentation conditions. The first experiment consist on the use of forced sedimentation (of the particles) at different centrifugal speeds for 30". The second experiment was done using 2000 rpm for different times, from 30" to 5'. After each centrifugation the surnatants were taken and the spectra recorded under focalized 980 nm continuous wave laser excitation were registered. Figure 3.18 represents the spectra deriving from the two experiments and their relative decay of the green and red emissions (measured from the area of the bands) with time.

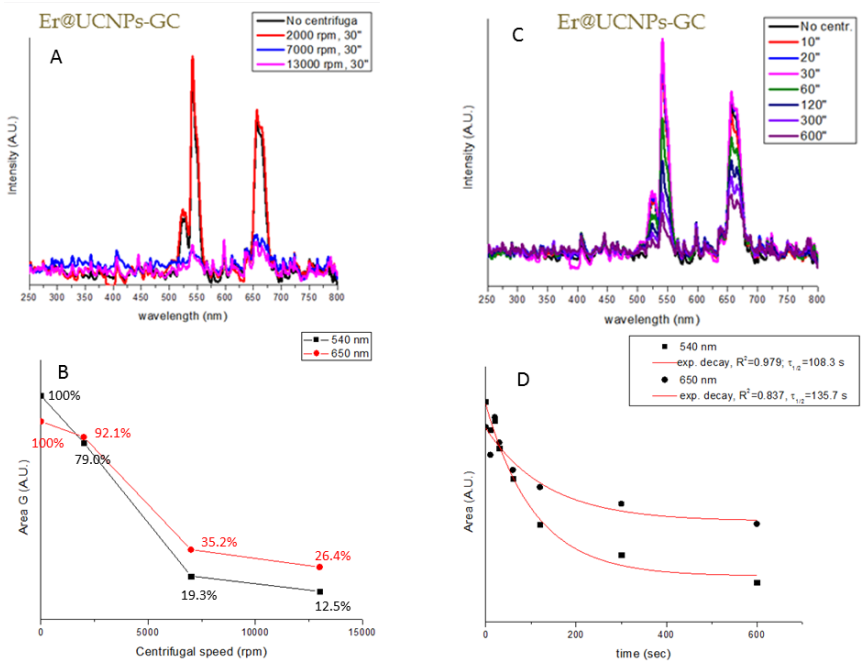

Figure 3.18: Up-conversion spectra (A,C) and decay curves (B,D) of the encapsulated Er,Yb-$NaYF_4$ NPs with different centrifugal speeds and different times.

This experiment has shown that while the increase in centrifugal speed enhances greatly the signal loss due to precipitation of the UCNPs, the time has not as the same impact: in fact the decays over time of the signal with time are much smoother as compared to the increase in centrifugal speed. However both experiments show that the encapsulation of the OA-coated UCNPs within the vesicles is quite good and the system is stable even at lower centrifugal speeds.

To address stability, kinetic experiments of *free fall* sedimentation have been performed on the same samples. Figure 3.19 shows the spectra derived from such kinetic experiments.

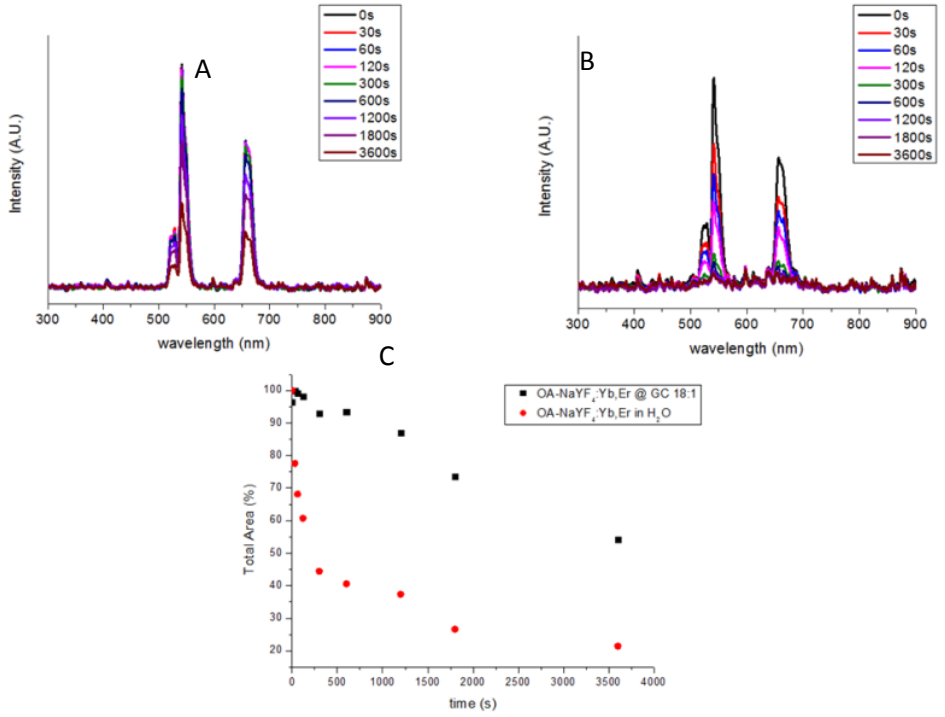

Figure 3.19: A) and B) UC spectra registred at 980 nm excitation during the "*free fall*" experiment of the encapsulated UCNPs and water-dispersed OA – coated UCNPs; C) total intensity decay of the encapsulated (black) and dispersed (red) OA-UCNPs.

This experiment confirm again that encapsulation of the particles is a fairly robust process: leaving the precipitation process of the nanoparticles alone let, after 1 h of measurement more than 50% of the total intensity of the UC signals, while at the same time, the free fall of the OA-coated UCNPs falls below 30%. It is already known that OA – coated UCNPs prefer to disperse in low-polarity or non-polar solvents but in this case it has been a good reference system, in water, to prove that encapsulation still works even after 1 h of continuous laser measurement.

As a conclusion, the encapsulation of non-water dispersable crystals (oleic acid coated UCNPs) is a powerful method for delivering UCNPs as biolabels through animal's cell membranes: the rate of free fall precipitation of UCNPs is low. In fact

after 1h and 30’ of kinetics, is still detectable more than 50% of the total signal. In comparison, water-dispersed, non-encapsulated particles, lead to a low 20% signal intensity detection, meaning that the precipitation of the UCNPs is much faster due to the coating of Oleic Acid (OA) on their surface which is highly hydrophobic, and does not allow for long-lived dispersions in water. Centrifugation (called forced precipitation method) has shown relative stability of the UCNPs, both under low to high rpm ranges and at 2000 rpm up to 5’. In both cases, the signal shows a slow decay, meaning stability of the complex vesicles-UCNPs, which is also confirmed from the correlograms obtained from DLS kinetic experiments. At high speed (low time) or long time at low speed particles fall and therefore, a more significant loss in signal intensity is found. Despite of it, the effect of the centrifugal revolution rate has a more pronounced effect as compared to the time-dependent centrifugation experiment. A plausible explanation of it can be described if it is assumed that, under high centrifugal speed the vesicles physically break or fall apart, letting the UCNPs precipitate; at low speed, however, this happens in a very light way, and the complex system resist up to longer times under fixed speed (2000 rpm).

Despite these results, research on understanding the trapping of UCNPs by glycolipids needs to undergo further experiments, in fact at the very moment it has been hard to understand where the UCNPs were placed, if within the vesicles or between them. Therefore, this research is still going on.

3.3 Conclusions

Formation of the gels has shown a good inclusion of the UCNPs within the Naf-based gel fibers and an effective energy transfer, dependent on the temperature-driven gel-sol transition, which shows that the 350 nm emission from Tm^{3+} ions in the UCNPs activated by IR light is absorbed by the fluorophore, which shows a broad band peaked at 407 nm. Attempts done with $NaYF_4$:Yb,Er in NH_2-Naf-based fibers have shown more cluster-like distribution of the particles within the gel, but they present an intense bulb-like emission in the whole hybrid material upon NIR irradiation.

Encapsulation of the UCNPs in vesicles of bio-surfactants has been performed in view of bioapplications. The effective entrapment was corroborated by DLS kinetic experiments, which has shown nearly-equal correlograms for more than 1h and 30'. Furthermore, the UCNPs do not lose their crystallinity despite of the pH manipulations required for the formation of the composite UCNPs-glycolipid vesicles. UC luminescence decrease has been used as a featured signal to detect the stability of the suspensions. *"Free fall"* experiments shows that the UCNPs encapsulated in vesicles were giving more than 50% of the total UC signal after 1h 30', while the emission of the OA-coated UCNPs was reduced as low as 20%. To deepen into the stability of the composite UCNPs-vesicles in water, experiments of *forced sedimentation* were performed with different centrifugal speeds and times. The main conclusion is that the suspension is more sensitive to the revolutions than the time of centrifugation.

3.4 Bibliography

(1) Hischemöller, A., Nordmann, J., Ptacek, P., Mummenhoff, K. & Haase, M. In-vivo imaging of the uptake of upconversion nanoparticles by plant roots. *J. Biomed. Nanotechnol.* **5,** 278–284 (2009).

(2) Zhang, C., Sun, L., Zhang, Y. & Yan, C. Rare earth upconversion nanophosphors: Synthesis, functionalization and application as biolabels and energy transfer donors. *J. Rare Earths* **28,** 807–819 (2010).

(3) Hao, S., Chen, G. & Yang, C. Sensing using rare-earth-doped upconversion nanoparticles. *Theranostics* **3,** 331–345 (2013).

(4) Wilhelm, S. Perspectives for Upconverting Nanoparticles. *ACS Nano* **11,** 10644–10653 (2017).

(5) Wang, M., Abbineni, G., Clevenger, A., Mao, C. & Xu, S. Upconversion nanoparticles: Synthesis, surface modification and biological applications. *Nanomedicine Nanotechnology, Biol. Med.* **7,** 710–729 (2011).

(6) Wen, H. Q. *et al.* Sequential Growth of NaYF4:Yb/Er@NaGdF4 Nanodumbbells for Dual-Modality Fluorescence and Magnetic Resonance Imaging. *ACS Appl. Mater. Interfaces* **9,** 9226–9232 (2017).

(7) Wolfbeis, O. S. An overview of nanoparticles commonly used in fluorescent bioimaging. *Chem. Soc. Rev. Chem. Soc. Rev* **44,** 4743–4768 (2015).

(8) Wilhelm, S. *et al.* Water dispersible upconverting nanoparticles: effects of surface modification on their luminescence and colloidal stability. *Nanoscale* **7,** 1403–1410 (2015).

(9) Muhr, V., Wilhelm, S., Hirsch, T. & Wolfbeis, O. S. Upconversion nanoparticles: From hydrophobic to hydrophilic surfaces. *Acc. Chem. Res.* **47,** 3481–3493 (2014).

(10) Zhao, J., Yang, H., Li, J., Wang, Y. & Wang, X. Fabrication of pH-responsive PLGA (UCNPs / DOX) nanocapsules with upconversion luminescence for drug delivery. *Sci. Rep.* 1–11 (2017). doi:10.1038/s41598-017-16948-4

(11) Wang, M. *et al.* NIR-induced highly sensitive detection of latent fingermarks by NaYF<inf>4</inf>:Yb,Er upconversion nanoparticles in a dry powder state. *Nano Res.* **8,** 1800–1810 (2015).

(12) You, M. *et al.* Inkjet printing of upconversion nanoparticles for anti-counterfeit applications. *Nanoscale* **7,** 4423–4431 (2015).

(13) Tian, X., Wei, X., Chen, Y., Duan, C. & Yin, M. Temperature sensor based on ladder-level assisted thermal coupling and thermal-enhanced luminescence in NaYF4:Nd3+. *Opt. Express* **22,** 30333–30345 (2014).

(14) Vetrone, F. *et al.* Temperature sensing using fluorescent nanothermometers. *ACS Nano* **4,** 3254–3258 (2010).

(15) Gonell, F. *et al.* Photon up-conversion with lanthanide-doped oxide particles for solar H 2 generation. *J. Phys. Chem. C* **118,** 11279–11284 (2014).

(16) Shan, G., Assaaoudi, H. & Demopoulos, G. P. Enhanced Performance of Dye-Sensitized Solar Cells by Utilization of an External , Bifunctional Layer Consisting of Uniform β -NaYF 4 : Er 3 + / Yb 3 + Nanoplatelets. 3239–3243 (2011). doi:10.1021/am200537e

(17) Vilela, P., Brown, T., Muskens, O. L. & Kanaras, A. G. Highly Sensitive DNA Sensor Based on Upconversion Nanoparticles and Graphene Oxide. (2015). doi:10.1021/am507591u

(18) Wang, F. *et al.* Simultaneous phase and size control of upconversion nanocrystals through lanthanide doping. *Nature* **463,** 1061–1065 (2010).

(19) Coe-sullivan, S., Woo, W., Steckel, J. S., Bawendi, M. & Bulovi, V. Tuning the performance of hybrid organic / inorganic quantum dot light-emitting devices. **4,** 123–130 (2003).

(20) Vier, E. & Ronda, C. R. Recent achievements in research on phosphors for lamps and displays. **74,** 49–54 (1997).

(21) Kim, C. *et al.* Phosphors for plasma display panels. **311,** 33–39 (2000).

(22) Fernandes, M. *et al.* Green Li+ - and Er 3+ -doped poly (ε -caprolactone)/ siloxane biohybrid electrolytes for smart electrochromic windows. *Sol. Energy Mater. Sol. Cells* **123,** 203–210 (2014).

(23) Julián-lópez, B., Gonell, F. & Lima, P. P. Easily processable multimodal spectral converters based on metal oxide / organic — inorganic hybrid nanocomposites. *Nanotechnology* **26,** 405601

(24) Zou, W., Visser, C., Maduro, J. A., Pshenichnikov, M. S. & Hummelen, J. C. Broadband dye-sensitized upconversion of near-infrared light. *Nature Photonics* **6,** 2–6 (2012).

(25) Budijono, S. J. *et al.* Synthesis of stable block-copolymer-protected NaYF 4:Yb 3+, Er 3+ up-converting phosphor nanoparticles. *Chem. Mater.* **22,** 311–318 (2010).

(26) J. C. Boyer, N. J. J. Johnson, F. C. J. M. V. V. Upconverting Lanthanide-Doped NaYF 4 - PMMA Polymer Composites Prepared by in Situ Polymerization. *Chem. Mater.* **21,** 2010–2012 (2009).

(27) Binnemans, K. Lanthanide-Based Luminescent Hybrid Materials. *Chem. Rev.,* **109,** 4283–4374 (2009).

(28) Weiss, R. G. The Past, Present, and Future of Molecular Gels. What Is the Status of the Field, and Where Is It Going? (2014). doi:10.1021/ja503363v

(29) Banerjee, S., Das, R. K. & Maitra, U. Supramolecular gels ' in action ' †. 6649–6687 (2009). doi:10.1039/b819218a

(30) Steed, J. W. Supramolecular gel chemistry : developments over the last decade. 1379–1383 (2011). doi:10.1039/c0cc03293j

(31) Hirst, A. R., Escuder, B., Miravet, J. F. & Smith, D. K. Gel Materials High-Tech Applications of Self-Assembling Supra- molecular Nanostructured Gel-Phase Materials : From Regenerative Medicine to Electronic Devices Angewandte. 8002–8018 (2008). doi:10.1002/anie.200800022

(32) Cametti, M. Dzolic, D. New frontiers in hybrid materials : noble metal nanoparticles – supramolecular gel systems generate materials of macro dimensions whose properties. 8273–8286 (2014). doi:10.1039/c4cc00903g

(33) Coates, I. A. & Smith, D. K. Hierarchical assembly — dynamic gel – nanoparticle hybrid soft materials based on biologically derived building blocks. 6696–6702 (2010). doi:10.1039/c0jm01166e

(34) Nanda, J., Adhikari, B., Basak, S. & Banerjee, A. Formation of Hybrid Hydrogels Consisting of Tripeptide and Di ff erent Silver Nanoparticle-Capped Ligands: Modulation of the Mechanical Strength of Gel Phase Materials. (2012). doi:10.1021/jp306262t

(35) Sangeetha, N. M. & Maitra, U. Supramolecular gels: functions and uses. *Chem. Soc. Rev.* **34,** 821–836 (2005).

(36) Rao, K. V., Datta, K. K. R., Eswaramoorthy, M. & George, S. J. Light-harvesting hybrid hydrogels: Energy-transfer-induced amplified fluorescence in noncovalently assembled chromophore-organoclay composites. *Angew. Chemie - Int. Ed.* **50,** 1179–1184 (2011).

(37) Ajayaghosh, A., Praveen, V. K. & Vijayakumar, C. Organogels as scaffolds for excitation energy transfer and light harvesting. *Chem. Soc. Rev.* **37,** 109–122 (2008).

(38) Rao, K. V., Datta, K. K. R., Eswaramoorthy, M. & George, S. J. Light-harvesting hybrid assemblies. *Chem. - A Eur. J.* **18,** 2184–2194 (2012).

(39) Sugiyasu, K., Fujita, N. & Shinkai, S. Visible-light-harvesting organogel composed of cholesterol-based perylene derivatives. *Angew. Chemie - Int. Ed.* **43,** 1229–1233 (2004).

(40) Sangeetha, N. M. *et al.* Hybrid materials combining photoactive 2,3-didecyloxyanthracene physical gels and gold nanoparticles. *Chem. Mater.* **21,** 3424–3432 (2009).

(41) Du, X., Zhou, J., Shi, J. & Xu, B. Supramolecular Hydrogelators and Hydrogels : From Soft Matter to Molecular Biomaterials. (2015). doi:10.1021/acs.chemrev.5b00299

(42) Bardelang, D. *et al.* Interfacing supramolecular gels and quantum dots with ultrasound: Smart photoluminescent dipeptide gels. *Adv. Mater.* **20,** 4517–4520 (2008).

(43) Tong, X., Xiang, J., Shi, F. & Zhao, Y. Near-Infrared Light-Sensitive Supramolecular Gel with Enhanced Visible Light Upconversion. *Adv. Opt. Mater.* **4,** 1392–1396 (2016).

(44) Lee, S. H., Ayer, M. A., Vadrucci, R., Weder, C. & Simon, Y. C. Light upconversion by triplet–triplet annihilation in diphenylanthracene-based copolymers. *Polym. Chem.* **5,** 6898–6904 (2014).

(45) Sternlicht, H., Nieman, G. C. & Robinson, G. W. Triplet-triplet annihilation and delayed fluorescence in molecular aggregates. *J. Chem. Phys.* **38,** 1326–1335 (1963).

(46) Zhao, J., Ji, S. & Guo, H. Triplet–triplet annihilation based upconversion: from triplet sensitizers and triplet acceptors to upconversion quantum yields. *RSC Adv.* **1,** 937 (2011).

(47) Singh-Rachford, T. N. & Castellano, F. N. Photon upconversion based on sensitized triplet-triplet annihilation. *Coord. Chem. Rev.* **254,** 2560–2573 (2010).

(48) Duan, P., Yanai, N., Nagatomi, H. & Kimizuka, N. Photon upconversion in supramolecular gel matrixes: Spontaneous accumulation of light-harvesting donor-acceptor arrays in nanofibers and acquired air stability. *J. Am. Chem. Soc.* **137,** 1887–1894 (2015).

(49) Huang, X. Tuning the size and upconversion luminescence of NaYbF_4:Er^3+/Tm^3+ nanoparticles through Y^3+ or Gd^3+ doping. *Opt. Mater. Express* **6,** 2165 (2016).

(50) Dong, H., Sun, L.-D. D. & Yan, C.-H. H. Basic understanding of the lanthanide related upconversion emissions. *Nanoscale* **5,** 5703–5714 (2013).

(51) Haase, M. & Schäfer, H. Upconverting nanoparticles. *Angew. Chemie - Int. Ed.* **50,** 5808–5829 (2011).

(52) Duke, R. M., Veale, E. B., Pfeffer, F. M., Kruger, P. E. & Gunnlaugsson, T. Colorimetric and fluorescent anion sensors: an overview of recent developments in the use of 1,8-naphthalimide-based chemosensors. *Chem. Soc. Rev.* **39,** 3936 (2010).

(53) Riuttamaki, T., Hyppanen, I., Kankare, J. & Soukka, T. Decrease in luminescence lifetime indicating nonradiative energy transfer from upconverting phosphors to fluorescent acceptors in aqueous suspensions. *J. Phys. Chem. C* **115,** 17736–17742 (2011).

(54) Yan, B., Boyer, J. C., Branda, N. R. & Zhao, Y. Near-infrared light-triggered dissociation of block copolymer micelles using upconverting nanoparticles. *J. Am. Chem. Soc.* **133,** 19714–19717 (2011).

(55) Xu, H. *et al.* Polymer encapsulated upconversion nanoparticle/iron oxide nanocomposites for multimodal imaging and magnetic targeted drug delivery. *Biomaterials* **32,** 9364–9373 (2011).

(56) Shah, S. *et al.* Hybrid upconversion nanomaterials for optogenetic neuronal control. *Nanoscale* **7,** 16571–16577 (2015).

(57) Yuan, Y., Min, Y., Hu, Q., Xing, B. & Liu, B. NIR photoregulated chemo- and photodynamic cancer therapy based on conjugated polyelectrolyte–drug conjugate encapsulated upconversion nanoparticles. *Nanoscale* **6,** 11259–11272 (2014).

(58) Hu, W. *et al.* Water-soluble conjugated polyelectrolyte brush encapsulated rare-earth ion doped nanoparticles with dual-upconversion properties for multicolor cell imaging. *Chem. Commun.* **49,** 9012 (2013).

(59) Bagheri, A., Arandiyan, H., Boyer, C. & Lim, M. Lanthanide-doped upconversion nanoparticles: Emerging intelligent light-activated drug delivery systems. *Adv. Sci.* **3,** (2016).

(60) Baccile, N., Babonneau, F., Jestin, J., Pehau-Arnaudet, G. & Van Bogaert, I. Unusual, pH-induced, self-assembly of sophorolipid biosurfactants. *ACS Nano* **6,** 4763–4776 (2012).

(61) Maharjan, P. P. *et al.* Photovoltaic devices and characterization of a dodecyloxybenzothiadiazole-based copolymer. 6856–6863 (2013). doi:10.1039/c3cp51070k

(62) Barrientos, Á. G., De la Fuente, J. M., Rojas, T. C., Fernández, A. & Penadés, S. Gold glyconanoparticles: Synthetic polyvalent ligands mimicking glycocalyx-like surfaces as tools for glycobiological studies. *Chem. - A Eur. J.* **9,** 1909–1921 (2003).

(63) Baccile, N., Noiville, R., Stievano, L. & Bogaert, I. Van. Sophorolipids-functionalized iron oxide nanoparticles. *Phys. Chem. Chem. Phys.* **15,** 1606–1620 (2013).

Chapter 4

Microwave Assisted Synthesis of UCNPs and Optical Activity Assessment

4.1 Introduction to microwave interaction with matter and motivation

Microwave-assisted synthesis of inorganic crystalline materials is a relatively recent route, which provides numerous advantages, such as more homogeneous heating[1], limited reaction times[2], relatively high yields[3,4], ease of scaling – up[3,4] and so forth. The interaction of radiation with matter is already well known, since radiation is composed of alternating electric and magnetic fields, matter will interact with those, causing dielectric or diamagnetic losses to be transformed into heat. Dielectric losses can be attributed to a re-distribution of charges or to charge polarization of the solid. The loss attributed to dielectric polarization can be divided into several components that depend on the fact that atoms are charged particles, such as: electronic polarization, dipole polarization, atomic polarization and interface polarization. This can be resumed as:

$$\alpha_t = \alpha_e + \alpha_d + \alpha_a + \alpha_i \qquad (4.1)$$

Where α_t is the total dielectric loss, α_e is the electronic polarization, α_d is the dielectric polarization, α_a is the atomic polarization and α_i is the interface polarization. Each contribution is frequency – dependent and happens on reaching such frequency. Figure 4.1 describes the polarization mechanisms and the relative frequency-dependent spectrum.

Polar molecules, under irradiation of light, tend to rotate when coupling their dipolar momentum to the magnetic field of the incident radiation. Since the electric and magnetic fields are alternating in microwaves, this dipolar moment will change continuously at the frequency of the microwave, and therefore the continuous alternation of the fields gives continuous rotation to polar molecules (e.g. water) which are generally used as solvents. When high conductivity materials (such as metals) are present in the reaction vessels, the absorption of microwave electric fields will be transformed into heat due to their high electric conductivity, giving a boost in the reaction temperature. Sometimes it is possible to produce solid state reactions adding catalytic quantities of metals under microwave irradiation. The quicker and higher is the absorption of microwave of a material, the more it will heat.

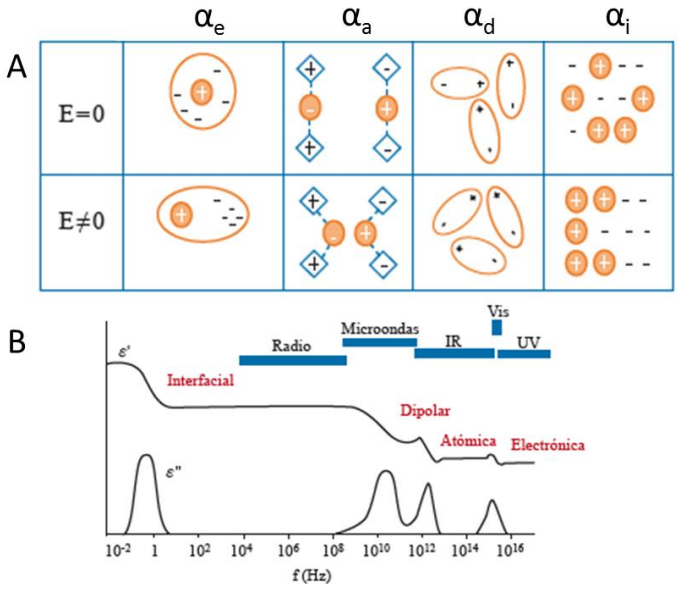

Figure 4.1: Polarization mechanisms **(A)** and frequency-dependence of the dielectric losses **(B)**[5]

The rate of absorption of microwave radiation is described in terms of electrical power per volume:

$$P_a = \omega \cdot \varepsilon_o \cdot \varepsilon_{eff} \cdot E_{rms}^2 + \omega \cdot \mu_0 \cdot \mu_{eff} \cdot H_{rms}^2 \quad (4.2)$$

where ω is the angular frequency (2πυ),ε_0 is the vacuum electrical permittivity, ε_{eff} is the effective relative dielectric loss ($\varepsilon_{polarization}+\varepsilon_{conduction}$), E_{rms} is the effective value of the internal electric field, μ_0 is the vacuum magnetic permittivity and μ_{eff} is the effective relative magnetic loss and H_{rms} is the effective value of the internal magnetic field. The main factor that a material must possess, for an efficient heating is to have an ε_{eff} comprised between 10^{-2} and 5; materials with very low ε_{eff} ($<10^{-2}$) have little or no possibility of heating while materials with $\varepsilon_{eff} > 5$ will heat only on the surface and not in the bulk.

There are several reasons why heating through microwave is desirable when synthesizing nanomaterials:

1. *Microwave is a very penetrating radiation:*

when using conventional heating, energy is transferred to the material by convection and conduction, and this generally creates heat gradients; nonetheless in microwave heating the heat is transferred to the system by molecular interactions with the electromagnetic field. Figure 4.2 shows these different ways of heating.

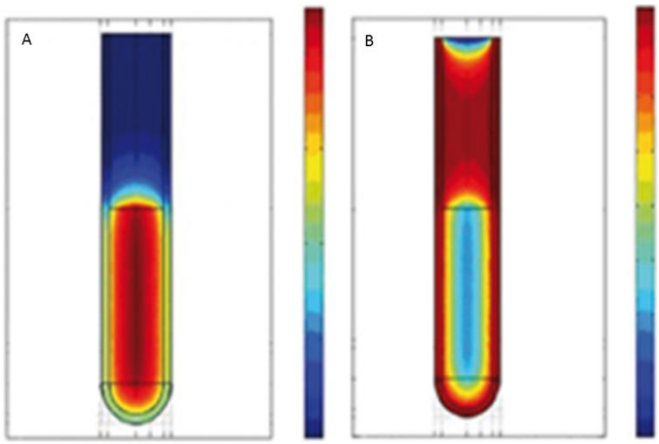

Figure 4.2: microwave (A) vs conventional (B) heating. Color bar is temperature, increasing from blue to red. Adapted from Prado Gonjal and Morán[5]

The depth reachable by microwave radiation varies depending on the heated material y other factors such as dielectric and diamagnetic losses, temperature, conductivity, frequency and power of the microwave radiation, and size and density of the heated materials.

2. *Fast heating method:*

The use of microwaves significantly reduces the reaction time of the synthesis with respect to conventional methods, maintaining properties and most of the times improving them. Nonetheless, it is worth reminding to be careful not to create hot spots during this fast heating cycle. Some authors reports increment between 10 and 1000 times of reaction kinetics when using microwave reactions.

3. *Selective heating of the materials*

Microwaves can be used to selectively heat materials, which is not usually possible with conventional heating. As said above, depending on the nature of the materials to be heated, some strong couplers that will absorb (and increment temperature during microwave irradiation) can be used, until auto-heating of the desired material is achieved.

4. Non – thermal effects

Several anomalies due to irradiation with microwaves are called non-thermal effects and include everything that is different from the conventional heating and that cannot be foreseen or easily explained by just looking at the heating profiles between the microwave heating and conventional one.

Microwave heating of solutions is becoming the method of choice production of a variety of nanoparticles, thanks to its easy scaling-up and focused, uniform heat flux on the reaction tubes[2–5]. This technique has been successfully proven in the preparation of nano- and micro-sized inorganic crystals, including simple and mixed metal oxides but also metal fluorides.

The synthesis of up-converting $NaYF_4$:Yb,Ln by microwave techniques has been already described in literature, however, either uniform but cubic single-phase $NaYF_4$ crystals or less uniform mixed cubic and hexagonal phases. Therefore, it is of interest, thanks to the multiple advantages offered by microwave heating, to foster this synthetic route for the preparation of pure hexagonal $NaYF_4$:Yb, Ln UCNPs with bright emissions. In this chapter, we present a study addressed to reach pure hexagonal $NaYF_4$:Yb,Ln (where Ln is Er, Tm, and Tb) nanocrystals by using the reproducible, quick and easy microwave approach.

4.2 Synthetic procedure

Several synthetic conditions for the preparation of UC nanoparticles were attempted, and crystallinity, relative crystal phase, and size have been routinely studied by TEM technique. TEM was the technique of choice for characterization of the products due to the limited amount of sample obtained in each MW-synthesis, which offered a better description than XRD.

A preliminary study of the synthetic parameters, including different precursor salts, nature of solvents, microwave conditions, etc… was performed for the sample $NaYF_4$:Yb,Er as a reference system. In some cases, a mixture of solvents were necessary to avoid fast boiling or dramatic changes of the reactants concentrations. Furthermore, post-synthetic coating of the resulting UCNPs were also performed.

Table 4.1 resumes the different tests performed and the outcomes obtained.

Sample Code	Y and Ln Precursors	Solvent mixture composition	V (mL)	MW parameters	PST	Size (nm)	Crystal phase
S1	$Y,Yb,Er(St)_3$	W:EtOH 1:4	3	30',300W, 80°C,12 bar	1. OA 2.No PST 3.Cytrate	10-15	Fm-3m (α)
S2	$Y,Yb,Er(St)_3$	W:EG 1:4	3	30',300W, 150°C,12 bar	1. OA 2.No PST	10-15	Fm-3m (α)
S3	$Y,Yb,Er(St)_3$	W:BA 1:4	3	300W, 12 bar 5',60°C/10',180°C	1. OA 2.No PST	10-40	Fm-3m (α)
S4	$Y,Yb,Er(Ac)_3$	W:EtOH 1:4	3	30',300W, 80°C,12 bar	1. OA 2.No PST	15-20	Fm-3m (α)
S5	$Y,Yb,Er(Ac)_3$	W:EG 1:4	3	30',300W, 150°C,12 bar	1. OA 2.No PST	15-20	Fm-3m (α)
S6	$Y,Yb,Er(Ac)_3$	W:BA 1:4	3	300W, 12 bar 5',60°C/10',180°C	1. OA 2. No PST 3. PVP	x=15 y=60	P-6 or $P6_3/m$ (β)

Table 4.1: Different synthetic tests performed to prepare pure hexagonal up-converting nanoparticles through microwave irradiation.

In the table, St stands for Stearate ($C_{18}H_{35}O_2^-$) anion, Y^{3+}, Yb^{3+}, and Er^{3+} concentration were respectively 78, 20 and 2% molar; PST is the acronym of post-synthetic treatment performed in order to coat nanoparticles (using as coating agents: oleic acid, OA, or polyvinylpyrrolidone, PVP), EG stands for Ethylene glycol and BA stands for benzylalcohol. The latter solvent is widely used in microwave and solvothermal procedures either as solvent or as oxidation[6] /reduction[7] reagent for the preparation of metal[7] or metal oxides[1,8,9] nanoparticles. Sodium fluoride, as for the solvothermal synthesis, was used as source of sodium and fluorine ions.

The optimized procedure is detailed later on, in a blue frame but in a typical synthesis, the Y and lanthanide precursors were emulsified in a polar solvent different from water, while NaF was dissolved in water. Then, the mixture of both solutions (emulsion) is subjected to microwave treatment. Different conditions of power, pressure, temperature and time were tested, including one-step and two-steps heating processes. In the reaction tubes, depending on the solvents mixture, white precipitates or bulky gels (trapping the UCNPs particles within the organic gel) were obtained. The powdered solids were recovered by centrifugation but the polymeric bulky/gel systems were not easy to manipulate and therefore they were placed in a water bath at 80ºC to keep them as solution for further analysis. The characterization of their size, shape and crystallinity of the solids was done by TEM.

A selection of the most representative TEM images and relative SAED diffraction patterns from different samples are summarized in Figure 4.3.

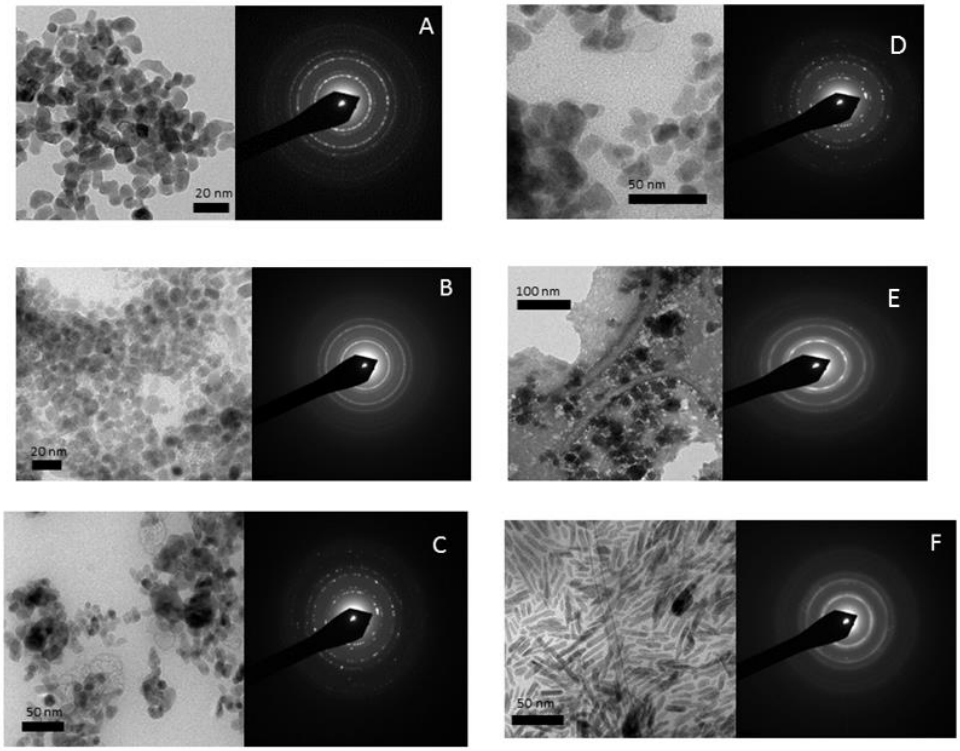

Figure 4.3: TEM and SAED images from the microwave-synthesized UCNPs: **A)** S1 **B)** S2, **C)** S3, **D)** S4, **E)** S5, **F)** S6. SAED images show distances corresponding to corresponding to cubic lattices in particles (from A to E); and to a pure hexagonal lattice in rods (F).

Stearate-based emulsions (images A, B and C from Figure 4.3) have proven the formation of small nanoparticles, especially those prepared with EtOH and EG (10-15 nm), and more heterogeneous distribution of size for the samples prepared with benzyl alcohol (between 10 and 40 nm). In all cases, the samples showed pure cubic structures, no matter the mixture of solvent used.

Reactions performed with acetates in mixture of water/ethanol 1:4 or water/EG 1:4 (images D and E from Figure 4.3) have shown the formation of nanoparticles with irregular shape and sizes similar to the ones formed by stearates (15-20 nm), but also pure cubic structure. In the last sample, the solvent mixture gel and form a hard gel/plastic matrix which traps the particles, and therefore the particles can be seen as darker spots in an organic matrix.

Sample S6 (image F from Figure 4.3), prepared with benzyl alcohol and metal acetates, is composed of highly uniform nanorods (UCNRs) of 14 nm diameter x 50 nm length, of pure hexagonal $NaYF_4$. Several attempts have shown that this morphology is reproducible using same heating-MW conditions and regardless the chemical nature and quantity of actuators. Therefore, this procedure was selected for the rest of the study. The details of the procedure are found in the blue frame.

Microwave-assisted UC Nanorods (UCNRs) formation

The stoichiometry of the different compositions prepared by this microwave route is: $NaY_{0.8-x}Yb_{0.20}Ln_xF_4$ with x=0.02 for Ln:Er^{3+} and Tb^{3+} and x=0.005 for Ln:Tm^{3+}.

In a typical synthesis, 0.415 g of $Y(Ac)_3$, 0.140 g of $Yb(Ac)_3$ and 0.014 g of $Tb(Ac)_3$ were dispersed in 2.25 mL of benzyl alcohol by stirring at 60ºC until good homogenization. In another vial, 0.084 g of NaF were dissolved in 750 µl of MilliQ water (18.2 MΩ). Both solutions were mixed and sonicated for few seconds to give a complete emulsion. The emulsified mixture is then inserted in the microwave reactor (CEM Discovery SP-X model) and heated first 5' at 60°C to completely homogenize the precursor mixture and, then, heated at 180°C for 10 minutes to induce nucleation and crystal growth. The system is cooled until 55°C under gentle N_2 flow and then left until reaching room temperature.

The bare or "fresh" UCNRs were collected by addition of absolute EtOH to the reaction tube. The product was washed four times with EtOH to remove the excess of organics and recovered by centrifugation (5000 rpm for 10 min). The reproducibility of the protocol was confirmed up to 5 times, obtaining similar results in all cases. The synthesis yield was estimated to be ~ 85%.

The great advantage in the use of microwave heating is to post-synthetic coat the nanoparticles' surface, with custom-prepared surfactants, able to bind the surface of the particle. In fact, the prepared nanoparticles are still reactive up to half an hour after the end of the MW heating, and this reactivity permits the surfactants to be grafted onto the surface. This post-synthetic coating allows the material to be ready for solvent-selective dispersions, and subsequent uses in sight of the desired fate for the UCNR.

However, to preserve the surface reactivity for the post-treatment coating, the tube samples must be kept at 80°C (in a water bath) until the selected coating agent was inserted and let react through sonication.

To prove the possibility of preparing solvent-selective dispersion, and to use hydrophobic and hydrophilic-capped UCNRs, the reaction batch is divided in three parts equally (around 1 mL each). The first batch is coated with 500 µL of 90% oleic acid, the second one is coated with 500 µL of a PVP aqueous solution (100 mg of PVP (polyvynilpirrolidone) in 1 mL water), and the third one was left uncoated to prove reactivity of naked UCNRs, which would have allowed for aggregation and/or coalescence of the nanorods. The crystals were collected by centrifugation and washed repeatedly with EtOH and acetone to remove most of the organics and leave only the coated and uncoated rods. Figures 4.4 and 4.5 resume the procedure and results for the preparation and functionalization of the nanorods.

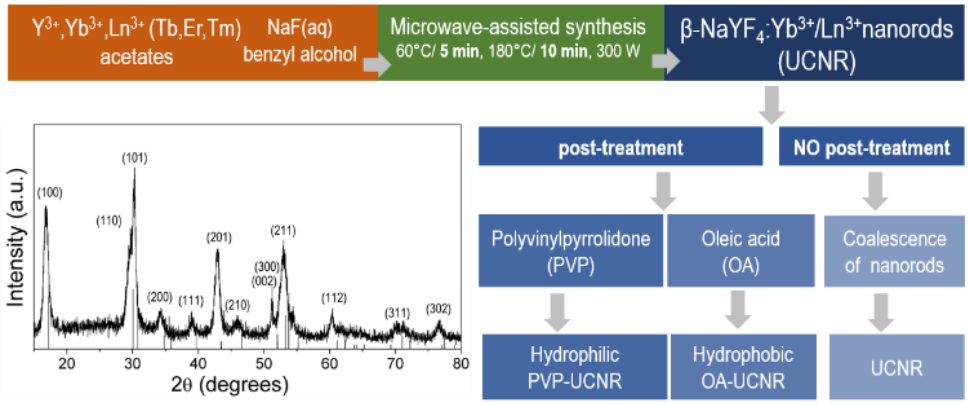

Figure 4.4: Synthetic route of the synthesis of pure hexagonal $NaYF_4$:Yb, Ln nanorods and route for post-synthetic coating. Inset is the XRD pattern, the relative hkl indices and the JCPSD 016-0334 used as reference for the experimental XRD pattern.

Multiple syntheses were performed in order to have an acceptable sample to be run under polycrystalline XRD instrumentation. The experimental pattern was compatible with a pure hexagonal structure obtained from the JCPDS 016-0334 (specially revealed by the presence of (100) peak at around 16º), therefore clearing once and for all that the structure of the crystals was fully hexagonal.

The anisotropic growth of the hexagonal particles into rods is generally explained as an epitaxial growth on the more energetic 0001 plane that tends to accumulate ions

and lead to a preferred direction of growth for the crystals. The reduced size, however, is a sign that the quick quench of temperature after microwave annealing, and the rapid and homogeneous heating provided by the microwaves (which is far faster than a solvothermal synthesis) allow to stop the growth at the nanoscale, rather than leaving crystals to an uncontrolled enlargement.

Dimensions of the UCNR were of 14 nm x 50 nm in average as shown by TEM (Figure 4.5 d) and little polydispersity is found. However, as the TEM clearly shows, the acetone-dispersed naked rods aggregated and coalesced, and finally precipitated (Figure 4.5 a and f)

However, the PVP-water dispersions and the OA-cyclohexane dispersion show fairly-separated rods (Figure 4.5b and c) and do not present precipitation at all (Figure 4.5.f). The addition of coatings of various nature do not destroy their hexagonal lattice (Figure 4.5 d).

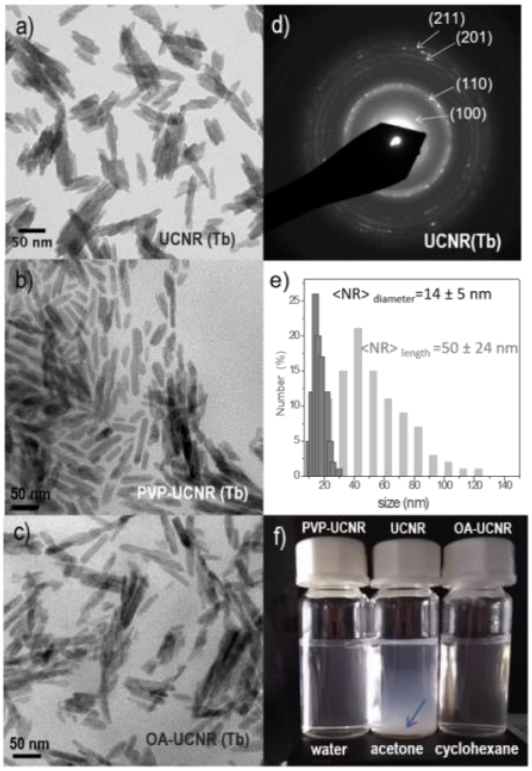

Figure 4.5: TEM images for the PVP, OA coated and uncoated nanorods **(A,B,C)**, SAED diffractogram **(D)**, size distribution for widths and lengths **(E)** and dispersion of the nanorods

in three different solvents **(F)**. Noticeable is the precipitation of the uncoated rods in acetone due to coalescence (as can be seen in the TEM image **(A)**)

The rods presents uniform shape and are fairly monodisperse, meaning that the reaction medium and the uniform heating promotes the uniform crystallization. The ease of coating demands a quick action to avoid coalescence and amplifies the range of commercial and applicable opportunities for these materials, which can be dispersed in polar solvents as well as in non-polar solvents.

To test reproducibility of the synthetic method and to tune emissions, several actuators, such as Er, Tb, and Tm were employed in similar fashion to prepare nanorods. UC emissions from nano-$NaYF_4$:Yb,Tb has been rarely studied, and only a couple of examples have been found in literature. Moreover, the most relevant of those was based on samples composed of cubic (or mixed cubic and hexagonal) nanostructures.[10,11]

The disinterest for the optical UC activity of Yb,Tb relies to the lack of ladder-like excited energy levels of the Tb ion, and therefore, the mechanism of cooperative sensitization that must occur has a very low probability, especially when exciting with a low-energy source as NIR photons. However, this mechanism can be observed in the MW prepared UC nanorods. The cooperative sensitization mechanism, at relatively high temperatures happens because Tb ion has emissions that comes directly either from the $^5D_3$ and $^5D_4$ to the ^7F_J manifold (J=6,5,4,3). The energetic distance between the excited and ground states make it possible to get emissions only if two Yb^{3+} nearby the same Tb actuator absorb simultaneously the IR photons and directly transfer the absorbed energy the actuating Tb^{3+} ions. Since the probabilities of these transitions are so poor it is of help that this reaction has offered pure hexagonal, monocrystalline structures, keeping in mind that cubic structures are much less emissive as compared to pure hexagonal ones in up-converting $NaYF_4$ hosts[11–14]. Monocrystalline structure increases the probability of finding the emitting path over the non-radiative ones.

To test optical activity of the nanorods, UC emission spectra have been recorded using an infrared laser diode (model RLTMDL-980-2W, Roithner LaserTechnik, 980 nm ± 5 nm, 2 W continuous waveform, stability <5%, laser head 141 × 46 × 73 nm) as the pump source and the emission spectra were measured at 1 W output with a focus lens, providing 105 W cm^{-2} optical power density on the sample. A StellarNet EPP2000-UV−vis spectrometer was employed for the fluorescence detection in the

visible region. Figure 3.6 shows the up-converting spectra of the Er and Tm, and, suprising, the manifold of emissions from Tb is also detected, as consequence of the cooperative sensitization of the Yb ions.

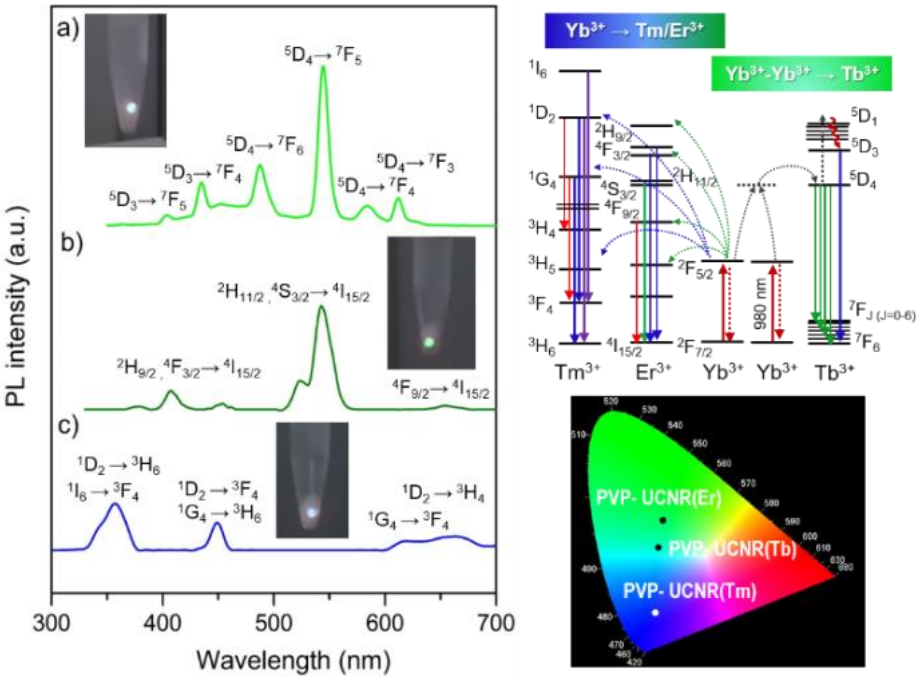

Figure 4.6: Up-converting optical spectra and relative images of the emitted light (left) a) Yb,Tb:$NaYF_4$, b) Yb,Er:$NaYF_4$ and c) Yb,Er:$NaYF_4$. Dieke diagram showing the energy transfer (upper right) and relative CIE emission colors of the relative upconverting nanorods (UCNRs) PVP-coated.

4.3 Conclusions

In conclusion, the emulsions of Ln(acetates) in benzylalcohol (BA) are very stable; upon the addition of a water solution of NaF it forms crystalline germs that grow anisotropically with limited sizes upon the fast and localized microwave heating. The fast reaction permits an easy routine scaling through multiple consequent syntheses. The opportunity offered from the reaction in customize the surface coating of the NR a posteriori, gives freedom of choice for the possibility of choice of the solvent for stable dispersions. Coalescence of uncoated particles has revealed post-reaction

activity of the crystals. Moreover, the change of actuators do not change the morphology and the crystal phase (pure hexagonal of the nanorods), but only the length. Thus, tuneable visible colours can be readily prepared by rational selection of the doping ions. Owing to their small size, excellent crystallinity and good dispersibility, these nanorods could be used for a wide range of application. Therefore, it is expected that this simple and ultrafast route to prepare the so-used $NaYF_4$ nanocrystals will be useful for the community working on up-conversion nanomaterials.

4.4 Bibliography

(1) Bondioli, F.; Ferrari, A. M.; Leonelli, C.; Siligardi, C.; Pellacani, G. C. *J. Am. Ceram. Soc.* **2001**, *84* (11), 2728–2730.

(2) Bilecka, I.; Niederberger, M. **2010**, *2* (8).

(3) Baghbanzadeh, M.; Carbone, L.; Cozzoli, P. D.; Kappe, C. O. *Angew. Chemie - Int. Ed.* **2011**, *50* (48), 11312–11359.

(4) Rao, K.; Vaidhyanathan, B. *Chem. Mater.* **1999**, 882–895.

(5) Prado-Gonjal, J.; Morán, E. *An. Quím* **2011**, *107*, 129–136.

(6) Bilecka, I.; Elser, P.; Niederberger, M. *ACS Nano* **2009**, *3* (2), 467–477.

(7) Aliofkhazraei, M. In *Handbook of Nanoparticles*; 2015; pp 1–1426.

(8) Bilecka, I.; Elser, P.; Niederberger, M. *ACS Nano* **2009**, *3* (2), 467–477.

(9) Corradi, A. B.; Bondioli, F.; Focher, B.; Ferrari, A. M.; Grippo, C.; Mariani, E.; Villa, C. *J. Am. Ceram. Soc.* **2005**, *88* (9), 2639–2641.

(10) Liang, H.; Chen, G.; Li, L.; Liu, Y.; Qin, F.; Zhang, Z. *Opt. Commun.* **2009**, *282* (14), 3028–3031.

(11) Prorok, K.; Gnach, A.; Bednarkiewicz, A.; Stręk, W. *J. Lumin.* **2013**, *140*, 103–109.

(12) Haase, M.; Schäfer, H. *Angew. Chemie - Int. Ed.* **2011**, *50* (26), 5808–5829.

(13) Dong, H.; Sun, L.-D.; Yan, C.-H. *Chem. Soc. Rev.* **2015**, *44* (6), 1608–1634.

(14) Dong, H.; Sun, L.-D. D.; Yan, C.-H. H. *Nanoscale* **2013**, *5* (13), 5703–5714.

Chapter 5

Conclusions

5.1 Conclusions

The aims of this work was first to shed light on the formation of β-$NaYF_4$:Yb, Ln (Ln= Er, Ho, Tm) nanocrystals under solvothermal conditions, establishing connections between crystal phase and size of the UCNCs with reaction parameters, as well as to study the structure(s) relations and relative optical activity.

Experimental findings shows that:

1) The reaction time and temperature, as well as O/W relations are critical parameters to control for the formation of UCNPs. The reaction conditions to get pure hexagonal structures requires at least 48 hours at 200°C. Below this time and/or temperature, cubic phase is always present. The study on the W/O ratio has demonstrated that low W/O ratios conduce to the generation of inverse micelles, which confines the spatial growth of the crystals, giving to nanoparticles between 20 and 50 nm mixed α,β-phase. In high W/O ratios, the larger content of water promotes the formation of direct micelles and larger crystals (between 200 and 400 nm) but pure hexagonal phase are formed. Alcohols, used as co-solvents within the emulsions have shown to have an effect in inverse-emulsion conditions: in fact, increasing the C-H linear chain from Ethanol to 1-BuOH, the nanoparticles show more aggregation and finally larger-spanned rods morphology. The formation of rods can be explained either through a change in emulsion geometry or through an increased epitaxial growth rate.
2) The optical UC response for the $NaYF_4$: Yb,Er system revealed that the more is the cubic character, the more intense the red emission are, meanwhile the green band increases with the hexagonal character.
3) The emissive properties of the up-converters can be tuned by changing the lanthanide ions; however, the particle size is affected by the nature and quantity of the lanthanide. In particular, $NaYF_4$:Yb,Ho and $NaYF_4$:Yb,Er prepared under same conditions show almost the same size, while $NaYF_4$:Yb,Tm are significantly smaller.

This study shows one of the first examples on the solvothermal preparation of up-converting nanoparticles of sizes comprised between 20 and 50 nm with strong up-converting activity. This work can be used as a starting point for the future preparation of large quantities of pure hexagonal $NaYF_4$ nanocrystals.

Secondly, particular applications of the solvothermal UCNPs have been addressed:

(i) The study demonstrates a good inclusion of the UCNPs within the Naf-based gel fibers and an effective energy transfer, dependent on the temperature-driven gel-sol transition which shows that the 350 nm emission from Tm^{3+} ions in the UCNPs activated by IR light is absorbed by the fluorophore, which shows a broad band peaked at 407 nm. Attempts done with $NaYF_4$:Yb,Er in NH_2-Naf-based fibers have shown more cluster-like distribution of the particles within the gel, but they present an intense bulb-like emission in the whole hybrid material upon NIR irradiation.

(ii) Encapsulation of the UCNPs in vesicles of bio-surfactants has been performed in view of bioapplications. The effective entrapment was corroborated by DLS kinetic experiments, which has shown nearly-equal correlograms for more than 1h and 30'. Furthermore, the UCNPs do not lose their crystallinity despite of the pH manipulations required for the formation of the composite UCNPs-glycolipid vesicles. UC luminescence decrease has been used as a featured signal to detect the stability of the suspensions. *"Free fall"* experiments shows that the UCNPs encapsulated in vesicles were giving more than 50% of the total UC signal after 1h 30', while the emission of the OA-coated UCNPs was reduced as low as 20%. To deepen into the stability of the composite UCNPs-vesicles in water, experiments of *forced sedimentation* were performed with different centrifugal speeds and times. The main conclusion is that the suspension is more sensitive to the revolutions than the time of centrifugation.

Finally, this work identifies a new methodology for the formation of pure hexagonal $NaYF_4$:Yb,Ln nanocrystals through MW-assisted synthesis. A preliminary study has performed to find the optimal conditions of reaction (solvent, temperature, time, precursors…) for the formation of pure β-$NaYF_4$ crystals. Benzyl alcohol, acetate precursors and a two-steps MW-heating ramp were found to be the ideal conditions to obtain the desired crystal structure. The morphology of the material was in form of nanorods of 15 nm x 50 nm dimensions. The proposed route permits a versatile and fast post-synthetic coating that permit ease of dispersion in various solvents. Optical activity of the nanorods is good, and also it is worth noticing that under NIR irradiation is possible to observe the cooperative sensitization mode of the Yb^{3+} ions to stimulate the emissions of the $^5D_4$ and $^5D_3$ excited states of Tb^{3+} ions to the ^7F_J (J = 2,3,4,5,6,) manifold at room temperature. This is one of the first examples reported of such optical phenomenon in pure hexagonal $NaYF_4$ crystals.

Appendix 1

Metrics

1. Powder X-ray Diffraction

For the solvothermal synthesis and the microwave nanorods, the instrument used was D4 Endeavor, Bruker-AXS, with a Bragg-Brentano (θ/2θ) geometry, copper x-ray source and diffracted axis monochromator and spark detector. It was used under these conditions: 15-80° angles range, 0.05°/sec step, 1.5 sec accumulation. The goniometer was controlled with the D4 Endeavor from Bruker AXS (See Figure A-1). For the Le Bail quantitative Analysis, the MAUD program was used [http://maud.radiographema.com/].

Figure A-1: The D4 Endeavor powder diffraction instrument from Bruker AXS

2. Transmission electron microscopy

Solvothermal – prepared nanocrystals and the hybrid gels were analyzed with a JEOL 2100 equipped with a LaB_6 electron gun with a working voltage of 200 KV, and images were detected with a CCD camera of 11 Mpixels from Gatan, model Orius. (see Figure A-2 left) To obtain visibility for the organic fibers, OsO_4 staining was performed over the samples. The particles were suspended with an opportune solvent and few drops of the dispersion were deposited over carbon-coated copper or nickel grids. They were let dry and then analized.

Microwave-prepared nanorods were analyzed with a JEOL JEM-1210 electron microscope, operating at 120 kV (see Figure A-2 right). The 120 KV JEOL 1210 TEM features a high angular range (Tilt X= ± 60°, Tilt Y= ± 30°) with a resolution below 3.2 Å. The transmission electron microscope service is equipped with an analytical specimen holder, double tilt (Tilt X=± 60^o, Tilt Y=± 30^o) GATAN 646 and a CCD camera ORIUS 831 SC 600, GATAN.

The modality of preparation for the nanorods samples was analogous to the one used for the nanoparticles, but using different solvents: the OA- coated nanorods were dispersed in cyclohexane, the non-coated were dispersed in acetone and the PVP-coated were dispersed in EtOH for quicker drying. The mean diameter and polydispersity of each system were determined by counting and sizing over 100 rods (or particles) from TEM images.

Figure A-2: (Left) JEOL 2100 (UJI) and (Right) JEOL 1210 microscopes (ICMAB-CSIC)

3. Optical spectroscopy

The pump source for all the luminescence measurements was an infrared laser diode RLTMDL-980-2W module (980 nm ± 5nm, 2 W cw, stability <5%, laser head 141x46x73 nm) from Roithner LaserTechnik (see Figure A-3). The laser has a variable (tunable) output from 0.3 to approx. 2.4 W, with a power density range that goes from 31 to 252 W/cm^2 on the sample, after focusing of the laser axis.

Figure A-3: RLTMDL-980 nm-2W module Roitner LaserTechnik

For the pump-power measurements on the solvothermal-prepared nanoparticles, dispersions of 10 mg/mL were used, and the luminescence detected between 31 and 157 W/cm^2 for the Yb/Ln doped $NaYF_4$ (Ln=Er, Ho, Tm) and 52 and 210 W/cm^2 for the different alcohol-prepared nanoparticles. The detector used was a fiber optic Black Comet CXR, (StellarNet), with a spectral range between 220 and 1100 nm, with an optical resolution of less than 1 nm with a slit of 25 µm.

The same setup was used for the determination of the emission intensities (kinetic and forced sedimentation experiments) of the encapsulated nanoparticles at 105 W/cm^2.

For the optical analysis of the hybrid gels, emissions were recorded using a JASCO FP-8300 fluorimeter detector (equipped with a Peltier thermal system, coupled with water cooling, temperature range 15-90°C). Figure A-4 shows a diagram of the apparatus.

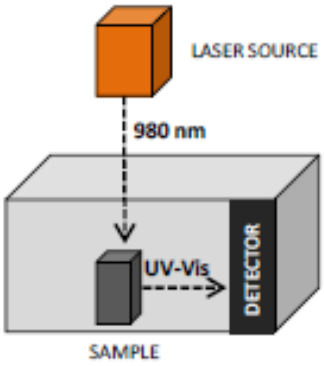

Figure A-4: Measurement set-up for the hybrid gels.

The same setup was used for the detection of the luminescence of the nanorods prepared via microwave. Dispersions were prepared in water or cyclohexane depending on the coating chosen, at concentration of 10 mg/mL.

4. pH measurements

The pH for the encapsulation was measured through a Crison 20 electronic pH meter. The formation of glycolipids vesicles was performed in water; same solvent was used to disperse and encapsulate the OA-coated UCNPs.

5. DLS measurements

DLS measurements of the kinetics for the encapsulated UCNPs and non-encapsulated UCNPs were performed through a NanoZetaSizer (Malvern) with a particle range size of 0.3 nm – 10 μm, temperature range 0-90°C (see Figure A-5).

Figure A-5: Malvern NanoZS instrument

Dispersions of the glycolipids, UCNPs, and glycolipids-encapsulated UCNPs were made in water. Encapsulated UCNPs were prepared as follows. 5mg of glycolipids GC18:1 were emulsified in 1 mL of water, and 5 mg of UCNPs were put before every pH change.

6. Thermal analysis (TGA/DSC)

TGA/DSC thermal analyses were performed through a simultaneous instrument TG-STDA Mettler Toledo model TGA/SDTA851e/LF/1600. Temperatures were taken in

O_2 atmosphere between room temperature and 600°C or 900°C. DSC- measurements were performed through a Mettler Toledo model DSC2 with heat flow measurement. It has a power inlet of 400W and sample holder with a ceramic sensor FRS6 and resolves up to 0.04 µW. It can heat up to 700ºC. Rate of heating up to 100ºC/min. Figure A-6 show the two instruments used for the thermal analysis.

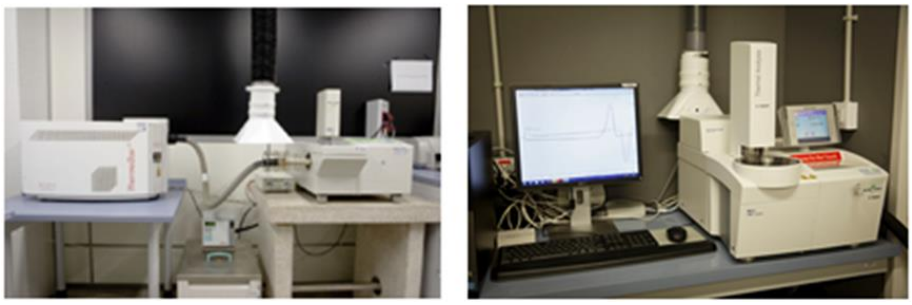

Figure A-6: TGA instrument (left) and DSC instrument (right) used for the thermal analysis

7. ATR-FT-IR studies

FT-IR was performed through a FT/IR-6200 (Jasco). It can go from about 8000 cm^{-1} to 400 cm^{-1} (see Figure A-7). Maximum resolution is of 0.25 cm^{-1} and a signal to noise ratio of 45000:1. An ATR stage was used for detecting vibrations on solid samples.

Figure A-7: FT-IR and microscope JASCO FT/IR 6200

THE JOURNAL OF PHYSICAL CHEMISTRY C

Article

pubs.acs.org/JPCC

Multimodal Light-Harvesting Soft Hybrid Materials: Assisted Energy Transfer upon Thermally Reversible Gelation

Carles Felip-León,[†,§] Fabrizio Guzzetta,[†,‡,§] Beatriz Julián-López,*[,†,‡] Francisco Galindo,*[,†] and Juan F. Miravet*[,†]

[†]Department of Inorganic and Organic Chemistry, Universitat Jaume I, Avda. Sos Baynat s/n, 12071 Castellón, Spain

[‡]Institute of Advanced Materials (INAM), Universitat Jaume I, Avda. Sos Baynat s/n, 12071 Castellón, Spain

Supporting Information

ABSTRACT: Multimodal light-harvesting soft systems able to absorb UV-to-NIR radiations and convert into visible emissions have drawn much attention in the last years in order to explore new areas of application in energy, photonics, photocatalysis, sensors, and so forth. Here, we present a new hybrid system combining a supramolecular photonic gel of naphthalimide-derived molecules self-assembled into fibers and upconverting $NaYF_4$:Yb/Tm nanoparticles (UCNPs). The hybrid system presented here manipulates light reversibly as a result of an optical communication between the UCNPs and the photoactive gel network. Upon UV irradiation, the system shows the characteristic emission at 410 nm from the photoactive organogelator molecule. This emission is also activated upon 980 nm excitation thanks to an efficient energy transfer from the UCNPs to the fibrillary network. Interestingly, the intensity of this emission is thermally regulated during the reversible assembly or disassembly of the organogelator molecules, in such a way that gelator emission is only observed in the aggregated state. Additionally, the adsorption of the UCNPs with the supramolecular gel fibers enhances their emissive properties, a behavior ascribed to the isolation from solvent quenchers and surface defects, as well as an increased IR light scattering promoted by the fibrillary network. The reported system constitutes a unique case of a thermally regulated, reversible, dual UV and IR light-harvesting hybrid soft material.

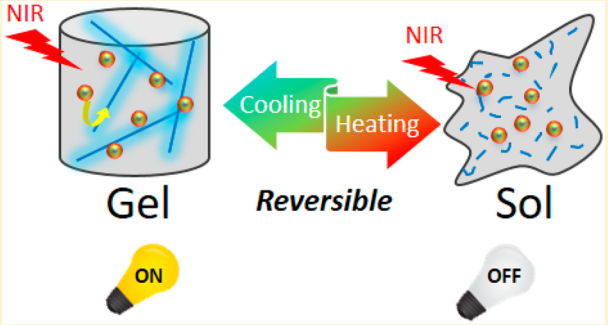

INTRODUCTION

Supramolecular gels based on self-assembled fibrillary networks are soft materials with significant advantages when compared to polymeric analogues such as intrinsic reversibility, stimuli responsiveness, and superior biocompatibility.[1−4] The increasing attention paid to supramolecular gels is related to their applicability as new soft materials in areas such as molecular electronics, controlled release, tissue engineering, or catalysis, among others.[2−7] Several approaches have addressed the inclusion of photonic functionalities into supramolecular gels.[8] For example, gels with chromophore units have been used as photocatalysts[9,10] and excitation energy transfer has been studied in supramolecular gels formed by photoactive fibers which contained entrapped dyes.[11−15] Recently, we reported orthogonal fibrillization of two fluorescent supramolecular gelators.[16] Additionally, supramolecular gels have been used as photon upconversion matrixes based on the triplet−triplet-annihilation mechanism via organic molecules.[17,18] Some studies have also been devoted to hybrid systems of noble (Ag and Au) metallic nanoparticles (NPs) and supramolecular networks.[19] In this case, supramolecular gels act as scaffold to support the NPs,[20−22] which in some of cases were prepared in situ,[23−26] and can find application as antibacterial soft materials[26−29] or catalysts.[30] Some studies have evaluated the influence of the molecular gel network in the photoluminescence of NPs.[31−34] Core/shell semiconductor nanocrystals of CdSe/ZnS, or quantum dots (QDs), have been incorporated into molecular gels, affording an improvement in emission quantum yields[35] and have been used as sensors of nitric oxide.[36]

In this work, a soft hybrid system based on IR light upconverting $NaYF_4$:Yb/Tm nanoparticles (UCNPs) and a fluorescent supramolecular network containing naphthalimide-derived molecules is described. Bulk upconverting lanthanide-based crystals have been known for decades, but there has been a resurgence of their study associated with the preparation of upconverting nanoparticles (UCNPs) about one decade ago.[37,38] Manipulation of IR radiation using UCNPs has been found to be of much interest because the UV−vis output can be used to promote several chemical processes or to develop a number of applications in the fields of lighting and displays, energy, photocatalysis, sensing, bioanalytics, and theranostics.[39−45] To our knowledge, only two reports concerning the inclusion of UCNPs in self-assembled organogels are available

Received: June 30, 2017
Revised: September 11, 2017
Published: September 13, 2017

DOI: 10.1021/acs.jpcc.7b06441
J. Phys. Chem. C 2017, 121, 21154−21159

in the literature. UCNPs could be dispersed in a supramolecular gel matrix formed by a peptide derivative, reinforcing the gel structure.[46] However, the gel matrix was acting as a passive scaffold. In another report, a photoactive supramolecular gel formed by a derivative of *trans*-stilbene experienced energy transfer from UCNPs.[47] Unlike the results reported here, the reversibility of the hybrid gel was not studied and the emission of gelator overlapped with that of the UCNPs. In this work, there is an optical communication between the UCNPs and the organic chromophore, and the light manipulation process is found to be fully reversible and associated with the assembly/disassembly of the gel. Furthermore, the gel provides much improved stability toward aggregation to the UCNPS.

EXPERIMENTAL SECTION

The synthesis of the hybrid supramolecular gel is fully described in the Supporting Information file (SI). In a typical procedure, the organogelator molecule (labeled as compound **1**) and the upconverting $NaYF_4$:Yb/Tm nanoparticles (20%-Yb and 0.5%-Tm molar ratio replacing yttrium ions in the lattice, labeled as UCNPs) were first prepared. The hybrid system (UCNPs-1gel) was prepared as follows: 20 mg of UCNPs was suspended in 2 mL of butanol and sonicated for 5 min in a screw-capped vial. Then, 6×10^{-3} mmol of compound **1** were added and the closed system heated to 80 °C until it was completely solubilized. The system was left to cool down until room temperature for 10 min, and the hybrid gel was formed. The samples were prepared in cylindrical glass vials with different sizes, and the gel dimensions ranged from 10 to 15 mm diameter × 5−20 mm height.

The characterization by high-resolution transmission electronic microscopy (HRTEM) was carried out on a JEOL- 2100 LaB_6 microscope, at an accelerating voltage of 200 kV, with an Inca Energy TEM 200 (Oxford) energy dispersive X-ray spectroscope (XEDS). The gel samples were deposited over Ni grids coated with a carbon film before TEM observation. The absorption spectra were measured on a Cary 500 Scan UV−vis−NIR spectrophotometer (Varian) equipped with an integrating sphere. The upconversion spectra were measured using an infrared laser diode (model RLTMDL-980-2W, Roithner LaserTechnik, 980 nm ± 5 nm, 2 W continuous waveform, stability <5%, laser head 141 × 46 × 73 nm) as the pump source. The emission spectra were measured at 1 W output with a focus lens, providing 105 W cm^{-2} optical power density on the sample. A StellarNet EPP2000-UV−vis spectrometer was employed for the fluorescence detection in the visible region. Additional experiments on the hybrid system were carried out in a transparent cuvette using the setup shown in the SI using a spectrofluorimeter JASCO FP-8300.

RESULTS AND DISCUSSION

Compound **1** (see Figure 1) is a low molecular weight gelator derived from 1,8-naphthalimide chromophore. When compound **1** is dissolved in a hot solution of butanol and the clear solution is left to cool down to room temperature, supramolecular gels are formed. The minimum concentration required for gelation (mgc) was 5 mM with a transition from gel to solution (T_{gel}) taking place at 65 °C using a vial inversion test. Transmission electron microscopy of the xerogel revealed the usual entanglement of fibers observed commonly in supramolecular gels (Figure S1, Figure S1 from Supporting Information file). The 1,8-naphthalimide unit introduced in the

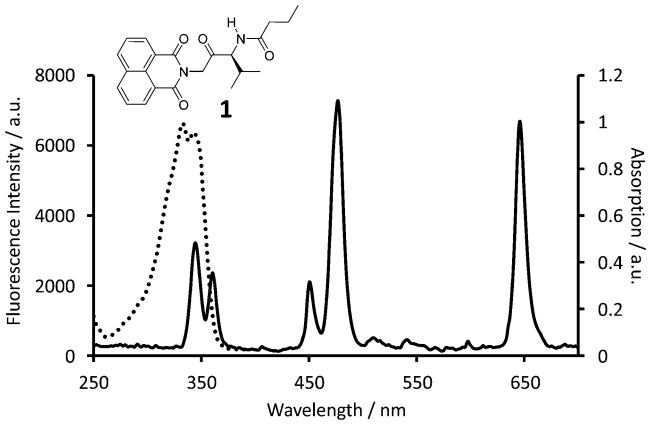

Figure 1. Overlaid absorption spectrum of compound **1** in butanol (dotted line) and emission spectrum of UCNPs (λ_{exc} = 980 nm, 105 Wcm^{-2} optical power density).

gelator is a well-known fluorophore,[48] presenting light absorbance at λ_{max} = 335 nm and emission at λ_{max} = 410 nm (see Figure 1 and Figure S2). $NaYF_4$:Yb^{3+}/Tm^{3+} upconverting nanocrystals (UCNPs) prepared following a simple solvothermal procedure (see SI)[49] produce different emissions with maximum intensity at wavelengths of 345, 355, 450, 475, and 650 nm (Figure 1) upon excitation at 980 nm. The hybrid system UCNPs-1gel was designed in such a way that the absorption of the gelator overlaps with the two emission bands of the UCNPs located at ca. 350 nm (Figure 1), and an energy transfer from the UCNPs to the chromophoric residue could take place (see adapted Jablonsky diagram in Figure S8).

Examination of the fluorescent properties of the pure gel formed by compound **1** revealed a strong aggregation induced emission effect upon excitation with 335 nm light.[50] This means that when the gel is heated from 20 to 80 °C a dramatic decrease of the 410 nm emission is observed, associated with a progressive gel disassembly (Figure 2). This behavior is

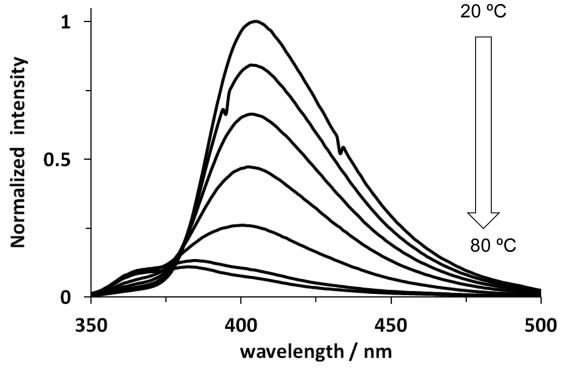

Figure 2. Variable temperature study of the emission spectra of the gel of compound **1** (λ_{exc} = 335 nm). Intensity at λ_{max} is normalized to 1 for the spectrum at 20 °C.

opposite to that observed by a 4-amino-1,8-naphthalimide analogue which was studied by us recently.[16] Under 980 nm excitation, the pure gel did not exhibit any emission.

The hybrid system containing the UCNPs within the fibrillary network has a good translucent/transparent (depending on the concentration of UCNPs and the cooling rate of the gel) appearance. Figure 3 left shows the picture of the hybrid UCNPs-1gel under natural, UV, and NIR light. Electron

DOI: 10.1021/acs.jpcc.7b06441
J. Phys. Chem. C 2017, 121, 21154−21159

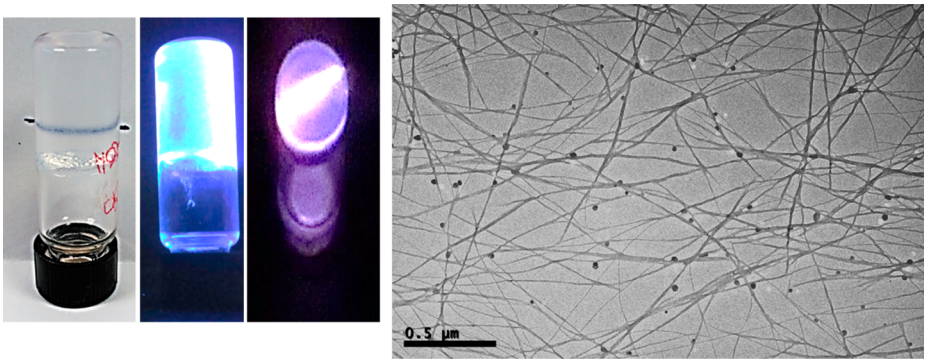

Figure 3. (Left) Pictures of the hybrid UCNPs-1 gel under natural light, UV lamp excitation, and 980 nm laser irradiation. (Right) Transmission electron microscopy image of the hybrid UCNPs-1 gel.

microscopy revealed that the hybrid material is formed by thin self-assembled fibers isolated and well-dispersed UCNPs mostly stacked at the surface of the fibers (Figure 3 right). It could be argued that the solvophobic oleic acid units covering the UCNPs provide anchorage points to the surface of the fibers as described, for example, for the interaction with polymers.[51,52]

Next, the emission of UV−vis light upon irradiation of the UCNP-loaded gels with 980 nm IR light was studied. It was found that the emission of the UCNPs at ca. 350 nm disappears and the emission band at 410 nm emerges (Figure 4). This is a consequence of the overlapped emission of the UCNPs and the absorption of compound **1**, as expected.

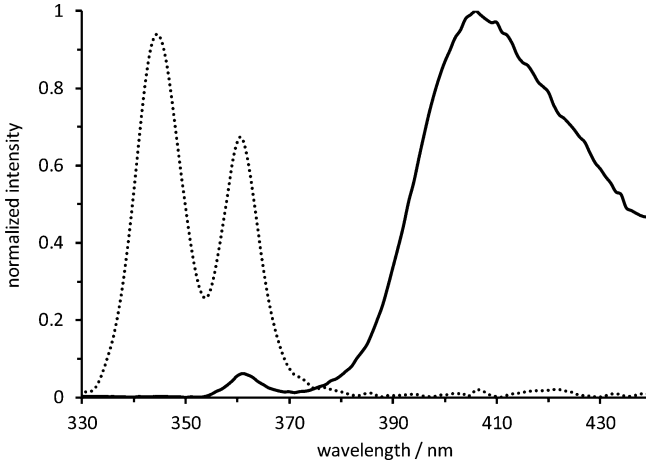

Figure 4. Overlay of the emission spectra of UCPNs (dotted line) and hybrid UCNPs-1 gel (upon 980 nm excitation). Intensity at λ_{max} for both systems is normalized to 1.

Interestingly, the hybrid system only originates IR-promoted emission at 410 nm in the gel state (Figure 5), with this process being canceled when the gel is disassembled at 80 °C, a behavior directly related to the aggregation induced emission properties of compound **1**. The system showed good reversibility and several heating−cooling cycles could be performed, restoring the upconversion to 410 nm at low temperatures. Consequently, the system formed by UCNPs-1gel constitutes a thermally regulated light upconverting soft material.

It is important to remark that the light emitted by UCNPs at ca. 350 nm is absorbed by compound **1** when the hybrid system is either in the gel state (at 30 °C-assembled) or in the sol state (80 °C-disassembled) (see Figure 5). This fact has implications

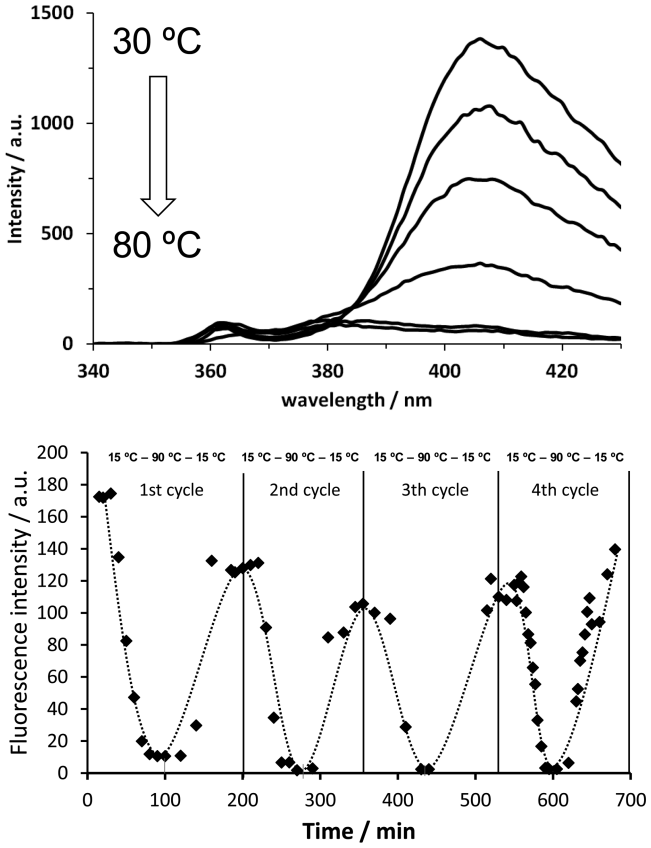

Figure 5. Top: Variable temperature study of the emission spectra of the hybrid UCPNs-1gel (λ_{exc} = 980 nm). Bottom: Variation of the emission intensity at 410 nm for the hybrid system UCNPs-1 upon heating−cooling cycles. The dotted line is used as a guide to the eye (λ_{exc} = 980 nm).

for the mechanism of energy transfer taking place in the system. At 80 °C the fibers are disassembled and spatial proximity between UCNPs and naphthalimide units is precluded, discarding a dipole−dipole energy transfer mechanism such as resonance energy transfer (RET).[53] Therefore, a photon reabsorption process, also known as the inner filter effect, emerges as the most plausible mechanism for energy transfer between UCNPs in both gel and solution states although RET cannot be discarded to take place in the former case. The inner filter effect has been used in sensing applications based on UCNPs.[54]

DOI: 10.1021/acs.jpcc.7b06441
J. Phys. Chem. C 2017, 121, 21154−21159

Aside from the previous results, it is noteworthy that the emission intensity of the UCNPs in the presence of the supramolecular gel is clearly improved. Variable temperature studies were carried out for suspensions of the UCNPs in butanol in the presence and absence of compound **1**. As can be seen in Figure 6, the emission of the UCNPs at 475 nm

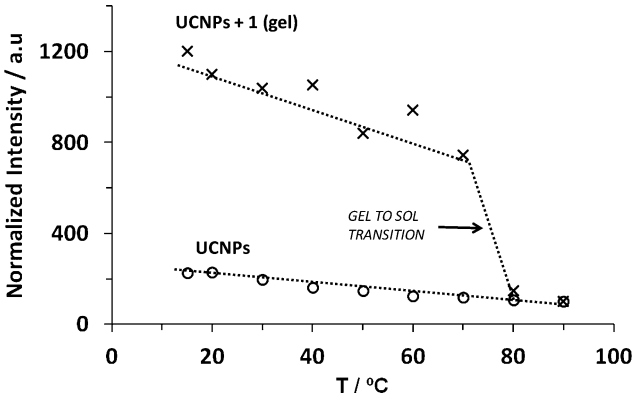

Figure 6. Variable temperature study of the emission intensity at 475 nm of UCNPs (suspended in butanol) and hybrid UCNPs-1 gel. Values are normalized taking as reference the intensities measured at 90 °C for both systems (λ_{exc} = 980 nm).

measured in the range 20−90 °C varies weakly, being moderately higher at low temperatures. However, in the presence of gelator 1 a very notable dependence with temperature was detected. It is important to recall that in the range 20−90 °C a progressive thermal disassembly of the gel network takes place and the system is converted from a gel to a solution. For the sake of comparison, it was decided to analyze the behavior of both samples, with and without gelator, normalizing the results to the emission intensity measured at 90 °C for pure UCNPs. This seems reasonable because in both cases free and disperse UCNPs and no aggregates are present. In this way, the fluorescence intensity at 20 °C in the presence of the gelator is much higher than that observed in the presence of UCNPS alone, with a 6-fold increase (Figure 6).

The process was found to be reversible and after a heating−cooling cycle, the emission was restored to initial values. These results indicate an improvement of the lanthanide nanocrystals emission ascribable to their interaction with the fibrillar network. A plausible rationale for this behavior is based on the partial isolation from the solvent experienced by the UCNPs upon adsorption on the gel fibers, avoiding in this way strong quenching effects from the high vibrational states of the hydroxyl groups of butanol. Such quenching effects have been demonstrated unequivocally in the case of water molecules and other alcohols.[55,56] It is also important to mention that the fibrillary network avoids the clustering of the UCNPs, leading to a more homogeneous and uniform luminescent material. Additionally, the scattering of IR light in the supramolecular gel could also enlarge the interaction of the laser with the UCNPs, contributing to the observed emission.[47]

CONCLUSIONS

We present a new hybrid system combining a supramolecular photonic gel of naphthalimide-derived molecules self-assembled into fibers and upconverting $NaYF_4$:Yb/Tm nanoparticles (UCNPs). The hybrid system presented here manipulates light reversibly as a result of an optical communication between the UCNPs and the photoactive gel network. Radiative excitation energy transfer occurs very efficiently affording a transformation of the light emitted from the nanoparticles. Upon NIR radiation, the UCNP's emission overlapping the absorption of the gel chromophore is removed and a new emission from the 1,8-napthalimide acceptor appears at 410 nm. This fact corresponds to a light-harvesting process. This process is only active in the form of gel as a result of the aggregation induced emissive properties of the supramolecular gelator. Reversible gel disassembly is promoted by temperature changes, giving place to a temperature regulated tunable photonic soft material. Additionally, the interaction of the UCNPs with the self-assembled fibers fosters the emissive relaxation pathways more than nonradiative decays. This fact is accompanied by a greater exposure of the NIR radiation from the gel scattering, originating an outstanding improvement of the emission intensity. This effect can also be ascribed to isolation from the solvent of the nanoparticles upon interaction with the gel fibers together with IR light scattering produced by the self-assembled gel network. Hybrid UCNPs-gel systems such as those described here are envisaged to be used in applications related to IR-based sensing or light manipulation in general, especially taking into account the possibility of their miniaturization in the form of micro-/nanogels for biomedical applications.

ASSOCIATED CONTENT

Supporting Information

The Supporting Information is available free of charge on the ACS Publications website at DOI: 10.1021/acs.jpcc.7b06441.

Experimental details regarding UCNPs and gelator preparation as well as hybrid gel formation and its fluorescence studies (PDF)

AUTHOR INFORMATION

Corresponding Authors

*(B.J-L.) E-mail: julian@uji.es.
*(F.G.) E-mail: franciso.galindo@uji.es.
*(J.F.M.) E-mail: miravet@uji.es.

ORCID

Beatriz Julián-López: 0000-0003-1019-776X
Francisco Galindo: 0000-0003-0826-6084
Juan F. Miravet: 0000-0003-0946-3784

Author Contributions

§C.F.-L. and F.G. contributed equally.

Notes

The authors declare no competing financial interest.

ACKNOWLEDGMENTS

Ministerio de Economía y Competitividad of Spain (grants CTQ2015-71004-R and MAT2015-64139-C4-1-R) and Universitat Jaume I (grants P1.1B2015-76 and P1.1B2014-21) are thanked for financial support. C.F.-L. thanks Ministerio de Economía y Competitividad of Spain for a FPI fellowship. F.G. thanks Generalitat Valenciana for a Santiago Grisolia fellowship. Technical support from SCIC of University Jaume I is acknowledged.

REFERENCES

(1) Hirst, A. R.; Escuder, B.; Miravet, J. F.; Smith, D. K. High-tech applications of self-assembling supramolecular nanostructured gel-

DOI: 10.1021/acs.jpcc.7b06441
J. Phys. Chem. C 2017, 121, 21154−21159

phase materials: From regenerative medicine to electronic devices. *Angew. Chem., Int. Ed.* **2008**, *47*, 8002−8018.
(2) Banerjee, S.; Das, R. K.; Maitra, U. Supramolecular gels 'in action'. *J. Mater. Chem.* **2009**, *19*, 6649−6687.
(3) Steed, J. W. Supramolecular gel chemistry: developments over the last decade. *Chem. Commun.* **2011**, *47*, 1379−1383.
(4) Weiss, R. G. The past, present, and future of molecular gels. what is the status of the field, and where is it going. *J. Am. Chem. Soc.* **2014**, *136*, 7519−7530.
(5) Terech, P.; Weiss, R. G. Low molecular mass gelators of organic liquids and the properties of their gels. *Chem. Rev.* **1997**, *97*, 3133−3159.
(6) Dawn, A.; Shiraki, T.; Haraguchi, S.; Tamaru, S.-i.; Shinkai, S. What Kind of "Soft Materials" Can We Design from Molecular Gels? *Chem. - Asian J.* **2011**, *6*, 266−282.
(7) Escuder, B.; Rodriguez-Llansola, F.; Miravet, J. F. Supramolecular gels as active media for organic reactions and catalysis. *New J. Chem.* **2010**, *34*, 1044−1054.
(8) Babu, S. S.; Praveen, V. K.; Ajayaghosh, A. Functional π-gelators and their applications. *Chem. Rev.* **2014**, *114*, 1973−2129.
(9) Weingarten, A. S.; Kazantsev, R. V.; Palmer, L. C.; McClendon, M.; Koltonow, A. R.; Samuel, A. P. S.; Kiebala, D. J.; Wasielewski, M. R.; Stupp, S. I. Self-assembling hydrogel scaffolds for photocatalytic hydrogen production. *Nat. Chem.* **2014**, *6*, 964−970.
(10) Weingarten, A. S.; Kazantsev, R. V.; Palmer, L. C.; Fairfield, D. J.; Koltonow, A. R.; Stupp, S. I. Supramolecular packing controls H-2 photocatalysis in chromophore amphiphile hydrogels. *J. Am. Chem. Soc.* **2015**, *137*, 15241−15246.
(11) Ajayaghosh, A.; Praveen, V. K. pi-organogels of self-assembled p-phenylenevinylenes: Soft materials with distinct size, shape, and functions. *Acc. Chem. Res.* **2007**, *40*, 644−656.
(12) Vijayakumar, C.; Praveen, V. K.; Ajayaghosh, A. RGB emission through controlled donor self-assemble and modulation of excitation energy transfer: A novel strategy to white-light-emitting organogels. *Adv. Mater.* **2009**, *21*, 2059−2063.
(13) Babu, S. S.; Praveen, V. K.; Ajayaghosh, A. Functional pi-gelators and their applications. *Chem. Rev.* **2014**, *114*, 1973−2129.
(14) Desvergne, J.-P.; Olive, A. G. L.; Sangeetha, N. M.; Reichwagen, J.; Hopf, H.; Del Guerzo, A. Self-assembling and light-harvesting properties of fluorescent linear condensed aromatic gelators. *Pure Appl. Chem.* **2006**, *78*, 2333−2339.
(15) Del Guerzo, A.; Olive, A. G. L.; Reichwagen, J.; Hopf, H.; Desvergne, J. P. Energy transfer in self-assembled n -acene fibers involving $\geq$ 100 donors per acceptor. *J. Am. Chem. Soc.* **2005**, *127*, 17984−17985.
(16) Felip-León, C.; Díaz-Oltra, S.; Galindo, F.; Miravet, J. F. Chameleonic, light harvesting photonic gels based on orthogonal molecular fibrillization. *Chem. Mater.* **2016**, *28*, 7964−7972.
(17) Duan, P.; Yanai, N.; Nagatomi, H.; Kimizuka, N. Photon upconversion in supramolecular gel matrixes: Spontaneous accumulation of light-harvesting donor-acceptor arrays in nanofibers and acquired air stability. *J. Am. Chem. Soc.* **2015**, *137*, 1887−1894.
(18) Duan, P.; Yanai, N.; Nagatomi, H.; Kimizuka, N. Photon upconversion in supramolecular gel matrixes: Spontaneous accumulation of light-harvesting donor−acceptor arrays in nanofibers and acquired air stability. *J. Am. Chem. Soc.* **2015**, *137*, 1887−1894.
(19) Cametti, M.; Džolić, Z. New frontiers in hybrid materials: Noble metal nanoparticles-supramolecular gel systems. *Chem. Commun.* **2014**, *50*, 8273−8286.
(20) Coates, I. A.; Smith, D. K. Hierarchical assembly - Dynamic gel-nanoparticle hybrid soft materials based on biologically derived building blocks. *J. Mater. Chem.* **2010**, *20*, 6696−6702.
(21) Nanda, J.; Adhikari, B.; Basak, S.; Banerjee, A. Formation of hybrid hydrogels consisting of tripeptide and different silver nanoparticle-capped ligands: Modulation of the mechanical strength of gel phase materials. *J. Phys. Chem. B* **2012**, *116*, 12235−12244.
(22) Chakrabarty, A.; Maitra, U.; Das, A. D. Metal cholate hydrogels: Versatile supramolecular systems for nanoparticle embedded soft hybrid materials. *J. Mater. Chem.* **2012**, *22*, 18268−18274.
(23) Chakrabarty, A.; Maitra, U. Organogels from dimeric bile acid esters: In situ formation of gold nanoparticles. *J. Phys. Chem. B* **2013**, *117*, 8039−8046.
(24) Lu, J.; Wu, J.; Ju, Y. Tuning the aggregation mode to induce different chiralities in organogels of mono- and bis-triterpenoid derivatives and the preparation of gold nanoparticles for use as a template. *New J. Chem.* **2014**, *38*, 6050−6056.
(25) He, H.; Chen, S.; Tong, X.; Chen, Y.; Wu, B.; Ma, M.; Wang, X.; Wang, X. Strong and fast-recovery organic/inorganic hybrid AuNPs-supramolecular gels based on loofah-like 3D networks. *Soft Matter* **2016**, *12*, 957−964.
(26) Das, D.; Maiti, S.; Brahmachari, S.; Das, P. K. Refining hydrogelator design: Soft materials with improved gelation ability, biocompatibility and matrix for in situ synthesis of specific shaped GNP. *Soft Matter* **2011**, *7*, 7291−7303.
(27) Dutta, S.; Kar, T.; Mandal, D.; Das, P. K. Structure and properties of cholesterol-based hydrogelators with varying hydrophilic terminals: Biocompatibility and development of antibacterial soft nanocomposites. *Langmuir* **2013**, *29*, 316−327.
(28) Mandal, S. K.; Brahmachari, S.; Das, P. K. In situ synthesised silver nanoparticle-infused L-lysine-based injectable hydrogel: Development of a biocompatible, antibacterial, soft nanocomposite. *ChemPlusChem* **2014**, *79*, 1733−1746.
(29) Shome, A.; Dutta, S.; Maiti, S.; Das, P. K. In situ synthesized Ag nanoparticle in self-assemblies of amino acid based amphiphilic hydrogelators: Development of antibacterial soft nanocomposites. *Soft Matter* **2011**, *7*, 3011−3022.
(30) Nanda, J.; Biswas, A.; Adhikari, B.; Banerjee, A. A gel-based trihybrid system containing nanofibers, nanosheets, and nanoparticles: Modulation of the rheological property and catalysis. *Angew. Chem., Int. Ed.* **2013**, *52*, 5041−5045.
(31) Sangeetha, N. M.; Bhat, S.; Raffy, G.; Belin, C.; Loppinet-Serani, A.; Aymonier, C.; Terech, P.; Maitra, U.; Desvergne, J. P.; Del Guerzo, A. Hybrid materials combining photoactive 2,3-didecyloxyanthracene physical gels and gold nanoparticles. *Chem. Mater.* **2009**, *21*, 3424−3432.
(32) Das, R. K.; Bhat, S.; Banerjee, S.; Aymonier, C.; Loppinet-Serani, A.; Terech, P.; Maitra, U.; Raffy, G.; Desvergne, J. P.; Del Guerzo, A. Self-assembled composite nano-materials exploiting a thermo reversible n-acene fibrillar scaffold and organic-capped ZnO nanoparticles. *J. Mater. Chem.* **2011**, *21*, 2740−2750.
(33) Roy, S.; Banerjee, A. Amino acid based smart hydrogel: Formation, characterization and fluorescence properties of silver nanoclusters within the hydrogel matrix. *Soft Matter* **2011**, *7*, 5300−5308.
(34) Yamamoto, K.; An, Z.; Saito, N.; Yamaguchi, M. Fluorescent gold nanoparticles: Synthesis of composite materials of two-component disulfide gels and gold nanoparticles. *Chem. - Eur. J.* **2013**, *19*, 10580−10588.
(35) Wadhavane, P. D.; Galian, R. E.; Izquierdo, M. A.; Aguilera-Sigalat, J.; Galindo, F.; Schmidt, L.; Burguete, M. I.; Pérez-Prieto, J.; Luis, S. V. Photoluminescence enhancement of CdSe quantum dots: A case of organogel-nanoparticle symbiosis. *J. Am. Chem. Soc.* **2012**, *134*, 20554−20563.
(36) Wadhavane, P. D.; Izquierdo, M. A.; Galindo, F.; Burguete, M. I.; Luis, S. V. Organogel-quantum dots hybrid materials displaying fluorescence sensitivity and structural stability towards nitric oxide. *Soft Matter* **2012**, *8*, 4373−4381.
(37) Heer, S.; Lehmann, O.; Haase, M.; Güdel, H. U. Blue, green, and red upconversion emission from lanthanide-doped $LuPO_4$ and $YbPO_4$ nanocrystals in a transparent colloidal solution. *Angew. Chem., Int. Ed.* **2003**, *42*, 3179−3182.
(38) Yan, C.; Zhao, H.; Perepichka, D. F.; Rosei, F. Lanthanide ion doped upconverting nanoparticles: synthesis, structure and properties. *Small* **2016**, *12*, 3888−3907.
(39) Zhou, B.; Shi, B.; Jin, D.; Liu, X. Controlling upconversion nanocrystals for emerging applications. *Nat. Nanotechnol.* **2015**, *10*, 924−936.

DOI: 10.1021/acs.jpcc.7b06441
J. Phys. Chem. C 2017, 121, 21154−21159

(40) Gonell, F.; Haro, M.; Sánchez, R. S.; Negro, P.; Mora-Seró, I.; Bisquert, J.; Julián-López, B.; Gimenez, S. Photon up-conversion with lanthanide-doped oxide particles for solar h_2 generation. *J. Phys. Chem. C* **2014**, *118*, 11279−11284.
(41) Tang, Y.; Di, W.; Zhai, X.; Yang, R.; Qin, W. NIR-responsive photocatalytic activity and mechanism of $NaYF_4$:Yb,Tm@TiO_2 core−shell nanoparticles. *ACS Catal.* **2013**, *3*, 405−412.
(42) Sedlmeier, A.; Achatz, D. E.; Fischer, L. H.; Gorris, H. H.; Wolfbeis, O. S. Photon upconverting nanoparticles for luminescent sensing of temperature. *Nanoscale* **2012**, *4*, 7090−7096.
(43) Sedlmeier, A.; Gorris, H. H. Surface modification and characterization of photon-upconverting nanoparticles for bioanalytical applications. *Chem. Soc. Rev.* **2015**, *44*, 1526−1560.
(44) Chen, G.; Qiu, H.; Prasad, P. N.; Chen, X. Upconversion nanoparticles: Design, nanochemistry, and applications in theranostics. *Chem. Rev.* **2014**, *114*, 5161−5214.
(45) Chatterjee, D. K.; Gnanasammandhan, M. K.; Zhang, Y. Small upconverting fluorescent nanoparticles for biomedical applications. *Small* **2010**, *6*, 2781−2795.
(46) Wu, J.; Tian, Q.; Hu, H.; Xia, Q.; Zou, Y.; Li, F.; Yi, T.; Huang, C. Self-assembly of peptide-based multi-colour gels triggered by up-conversion rare earth nanoparticles. *Chem. Commun.* **2009**, 4100−4102.
(47) Tong, X.; Xiang, J.; Shi, F.; Zhao, Y. Near-infrared light-sensitive supramolecular gel with enhanced visible light upconversion. *Adv. Opt. Mater.* **2016**, *4*, 1392−1396.
(48) Duke, R. M.; Veale, E. B.; Pfeffer, F. M.; Kruger, P. E.; Gunnlaugsson, T. Colorimetric and fluorescent anion sensors: an overview of recent developments in the use of 1,8-naphthalimide-based chemosensors. *Chem. Soc. Rev.* **2010**, *39*, 3936−3953.
(49) Wang, M.; Liu, J.-L.; Zhang, Y.-X.; Hou, W.; Wu, X.-L.; Xu, S.-K. Two-phase solvothermal synthesis of rare-earth doped $NaYF_4$ upconversion fluorescent nanocrystals. *Mater. Lett.* **2009**, *63*, 325−327.
(50) Mei, J.; Leung, N. L. C.; Kwok, R. T. K.; Lam, J. W. Y.; Tang, B. Z. Aggregation-induced emission: Together we shine, united we soar! *Chem. Rev.* **2015**, *115*, 11718−11940.
(51) Yi, G.-S.; Chow, G.-M. Water-soluble $NaYF_4$:Yb,Er(Tm)/$NaYF_4$/Polymer core/shell/shell nanoparticles with significant enhancement of upconversion fluorescence. *Chem. Mater.* **2007**, *19*, 341−343.
(52) Wu, T.; Boyer, J.-C.; Barker, M.; Wilson, D.; Branda, N. R. A "plug-and-play" method to prepare water-soluble photoresponsive encapsulated upconverting nanoparticles containing hydrophobic molecular switches. *Chem. Mater.* **2013**, *25*, 2495−2502.
(53) Riuttamäki, T.; Hyppänen, I.; Kankare, J.; Soukka, T. Decrease in luminescence lifetime indicating nonradiative energy transfer from upconverting phosphors to fluorescent acceptors in aqueous suspensions. *J. Phys. Chem. C* **2011**, *115*, 17736−17742.
(54) Sun, L.-N.; Peng, H.; Stich, M. I. J.; Achatz, D.; Wolfbeis, O. S. pH sensor based on upconverting luminescent lanthanide nanorods. *Chem. Commun.* **2009**, 5000−5002.
(55) Liu, C.; Wang, H.; Li, X.; Chen, D. Monodisperse, size-tunable and highly efficient β-$NaYF_4$:Yb,Er(Tm) up-conversion luminescent nanospheres: controllable synthesis and their surface modifications. *J. Mater. Chem.* **2009**, *19*, 3546−3553.
(56) Boyer, J.-C.; Manseau, M.-P.; Murray, J. I.; van Veggel, F. C. J. M. Surface modification of upconverting $NaYF_4$ nanoparticles with PEG−phosphate ligands for NIR (800 nm) biolabeling within the biological window. *Langmuir* **2010**, *26*, 1157−1164.

DOI: 10.1021/acs.jpcc.7b06441
J. Phys. Chem. C 2017, 121, 21154−21159

THE JOURNAL OF PHYSICAL CHEMISTRY Letters

Letter

Cite This: J. Phys. Chem. Lett. 2017, 8, 5730-5735

pubs.acs.org/JPCL

Ultrafast Synthesis and Coating of High-Quality β-$NaYF_4$:Yb^{3+},Ln^{3+} Short Nanorods

Fabrizio Guzzetta,[†] Anna Roig,*[,‡] and Beatriz Julián-López*[,†]

[†]Institute of Advanced Materials (INAM), Universitat Jaume I, Av. Sos Baynat s/n, 12071 Castellón, Spain

[‡]Institut de Ciència de Materials de Barcelona (ICMAB-CSIC), Campus de la UAB, 08193 Bellaterra, Spain

Supporting Information

ABSTRACT: An ultrafast route to prepare up-converting single β-phase $NaYF_4$:Yb^{3+},Ln^{3+} (Ln: Er, Tm, or Tb) short nanorods (UCNRs) of high quality was developed. This new procedure affords reactive-surface nanorods that are easily coated by direct injection of suitable capping ligands. Thus highly crystalline nanorods with excellent UC fluorescence and good solvent-selective dispersion are obtained, which represents a significant advance in the field and enlarges their use for biomedical and other technological applications. Unlike other methodologies, the short reaction time provides a kinetic control over crystallization processes, and the β-phase and rod morphology is preserved regardless of the optically active Ln^{3+} ion. The UC emission was finely tuned by using the most popular Yb^{3+}/Tm^{3+} and Yb^{3+}/Er^{3+} pairs. More importantly, UCNRs doped with the unusual Yb^{3+}/Tb^{3+} pair, with no ladder-like energy levels, provided a nice emission upon near-infrared excitation, which constitutes the first example of phonon-assisted cooperative sensitization to date in pure β-$NaYF_4$ nanocrystals.

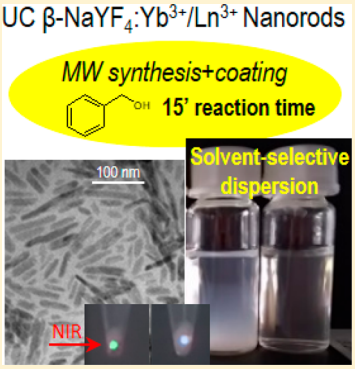

Lanthanide-codoped β-$NaYF_4$ nanocrystals (Ln^{3+}: Er, Tm, Yb) are high-brightness near-infrared (NIR) to visible-light up-converters with great interest in technological applications across many fields such as photonics, security, sensors, energy, and biomedicine.[1,2] The key for their effective industrial integration in commercial devices will be the prospect to fabricate monodisperse high-quality nanocrystals with nanometric size (<100 nm), well-defined shape of pure hexagonal (β) phase, which affords the highest optical emission through a facile, cheap, and fast scalable synthetic route. Furthermore, a one-pot processing to make solvent-soluble dispersions of the nanoparticles is highly desirable.[3]

Up-converting nanoparticles (UCNPs) are routinely prepared by thermal decomposition,[4−7] coprecipitation,[8,9] and hydro- or solvothermal[10,11] routes. However, harsh conditions such as high reaction temperature (>300 °C) and pressure, long reaction times (6−48 h), or waterless oxygen-free conditions are usually required, hindering their industrial upscaling. Furthermore, $NaYF_4$ crystallizes first as a metastable cubic α-phase with very poor optical activity. The cubic-to-hexagonal conversion needs to overcome a high free-energy barrier,[12] and a subsequent fast growth of crystals occurs; thus mixtures of both phases are usually obtained, especially in the case of small nanoparticles.

Microwave-assisted (MW) synthesis has appeared as an attractive way to prepare monodisperse colloids with complex kinetic/thermodynamic control over crystallization processes.[13,14] Indeed, this route has already been employed to prepare different fluoride materials.[15−17] However, the accurate attribution of the crystalline phase is difficult in small nanocrystals and even sometimes avoided by the authors because it is a crucial issue in highly sensitive luminescent systems. Reports concerning UC $NaYF_4$ encompass either small nanoparticles (<8 nm) of the 10-times less efficient α-phase[18−20] and α/β mixtures[21] or pure β-phase prisms[20,22] and long wires[23] of micrometric size. Small nanorods of <100 nm, highly crystalline, and pure β-phase by using a mild and fast microwave route have never been reported to our knowledge.

An additional advantage of our MW protocol is that a functional coating can be added upon completion of the reaction.[24] This allows great versatility in designing stable colloids in solvents of different polarity in sight of the envisaged application. For example, in biologically relevant applications such as bioimaging, drug targeting, or nanothermometers, luminescent nanoparticles must be water-dispersible to be compatible under physiological conditions.[25] By contrast, other technological applications need their dispersion in low boiling solvents such as cyclohexane to make thin films in miniaturized designs. This is the case for solar cells, optoelectronic devices, or anticounterfeiting systems.[26,27]

Here we present a fast, energy-efficient, and versatile microwave route to successfully prepare pure β-$NaYF_4$:Yb^{3+},Ln^{3+} nanorods (NRs) surface coated for solvent-selective dispersions. Along with the so-characterized Er^{3+} and Tm^{3+} ions as Ln^{3+} activators, we focused also on Tb^{3+} ions because it shows an unusual upconversion process. The distinctive energy level structure of Tb ions does not match with the 980 nm excitation. However, the long-lived excited $^5D_4$

Received: September 18, 2017
Accepted: November 10, 2017
Published: November 10, 2017

DOI: 10.1021/acs.jpclett.7b02473
J. Phys. Chem. Lett. 2017, 8, 5730−5735

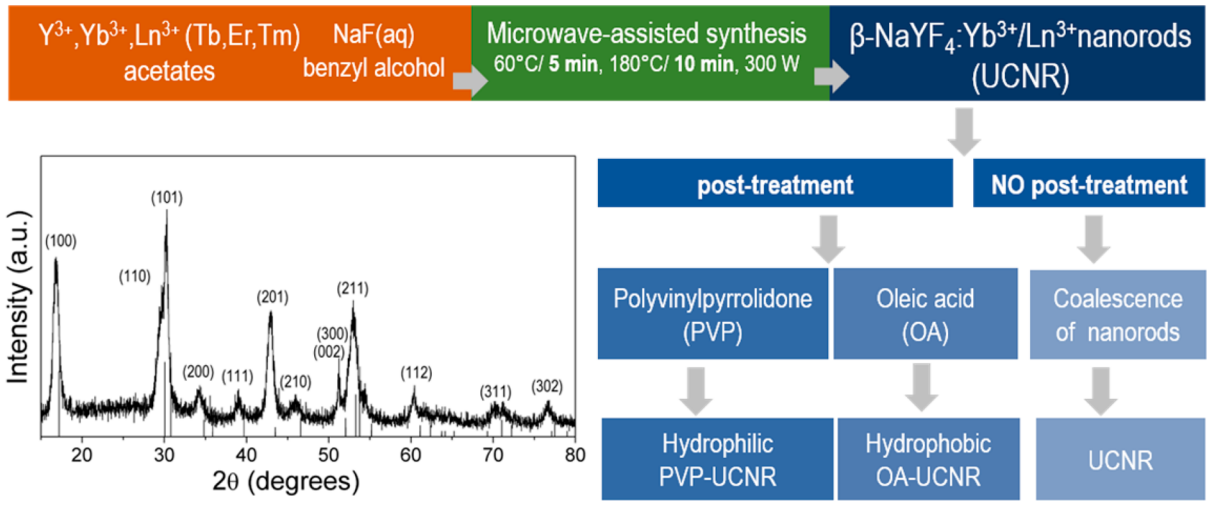

Figure 1. Schematic representation of the MW synthesis and post-treatment (PT) coating of the UCNR. XRD pattern of the β-$NaYF_4$:Yb,Tb^{3+} nanorods (β reference, JCPDS card 16-0334).

level can be populated based on the energy migration mechanism[28] in which two adjacent Yb^{3+} ions cooperatively sensitize one Tb^{3+} ion. This process has been demonstrated in Yb,Tb-codoped single crystals of $SrCl_2$[29] and ceramic glasses containing $LiYbF_4$,[30] $NaLuF_4$,[31] and $NaYF_4$[32] nanocrystals but very scarcely reported on $NaGdF_4$[33] and α-$NaYF_4$[34] nanoparticles. This approach can also be extended to other lanthanide ions such as Eu^{3+}, Dy^{3+}, or Sm^{3+} and afford tunable emissions spanning from the UV to the visible spectral region. Thus this simple and universal strategy to prepare NIR-activated fluorescent β-$NaYF_4$ nanorods represents a significant advance in the field.

Figure 1 summarizes the procedure to synthesize the up-converting nanorods; the details of the synthesis are included in the Supporting Information (SI). The precursors and solvent, F/Y ratio, and MW reaction conditions (T, t) have been judiciously modified to target nanometric dimensions and the single $P6_3/m$ hexagonal phase, as shown in the XRD pattern of Figure 1. The reaction conditions investigated to attain the pure β-phase are summarized in Table SI1 and Figure SI1. The optimized synthesis employs benzyl alcohol and lanthanide acetates as solvent and Ln^{3+} precursors, respectively.

Benzyl alcohol and benzyl mercaptan have previously been employed to prepare metal oxides[35] and sulfides[36] by nonaqueous routes with good results in controlling particle size but have never been tried for the synthesis of fluoride crystals. In such studies, the alcohol and mercaptan groups promoted the metal−oxygen−metal and metal−sulfur−metal bonds. The synthetic route reported here is not analogous because the main role of the benzyl alcohol is to act as a suitable solvent in terms of solubility in water (4 g/100 mL), thermal stability (boiling point of 205 °C), and probably as capping agent minimizing the nanocrystal aggregation. Although a detailed mechanistic study goes beyond the scope of this communication, the results will be shortly discussed.

The synthesis of the UC nanorods includes a preheating at 60 °C to completely dissolve the lanthanide acetates and the sodium fluoride in the benzyl alcohol/water mixture (4/1 molar ratio). The use of lanthanide acetates instead of stearates, which are salts commonly employed in the synthesis of lanthanide-doped fluoride nanocrystals,[37] favors the dissolution of the precursors without significant coordinating effect of the acetate ligand. After 5 min at 60 °C, the temperature is rapidly increased to 180 °C and kept for 10 min. In this step, the kinetically controlled nucleation of α-$NaYF_4$ seeds and the nanocrystal growth promoting the α-to-β phase[38] transformation takes place. Further growth of the thermodynamically favored β-$NaYF_4$ phase is drastically reduced by a fast cooling of the reactor.

We further take advantage of the particles surface reactivity just after the MW synthesis to graft hydrophilic, such as polyvinylpyrrolidone (PVP), or hydrophobic, such as oleic acid (OA), molecules on the particle's surface. A functional coating was formed by simple injection of the capping ligands into the reaction tubes, which were kept at 80 °C after the nanocrystals synthesis to better preserve their surface reactivity. We adopted this strategy instead of the addition of PVP or OA during the UCNRs synthesis because both molecules were demonstrated to suffer oxidation or degradation processes during the microwave treatment. The formation of PVP- and OA-capped UCNRs was verified by FTIR analysis (Figure SI2).[39−41]

Figure 2a shows a TEM image of the bare UCNRs doped with Tb, as an example. The particles exhibit an anisotropic morphology with rather uniform transversal size (or diameter) of ∼15 nm and a longitudinal size distribution ranging between 30 and 100 nm (Figure 2e). The rods appear stacked along the longitudinal axis, forming small aggregates of few NRs. In accordance to the XRD results, the diffraction rings of the SAED patterns for the UCNRs (Figure 2d) were indexed to the β-phase.

In comparison with previous reports in which MW routes are used to prepare small monodisperse α-$NaYF_4$ nanocrystals,[18] our synthesis of β-$NaYF_4$ nanorods provides larger but less uniform particle sizes. The larger sizes are beneficial for the UC photoluminescence because it is well-established that the particle size dramatically influences the nonradiative properties (multiphonon relaxation and energy transfer), reducing the UC efficiency drastically from values of 13 to 14% to 0.001% in Er,Yb:$NaYF_4$ particles of a few microns to a few nanometers (<8 nm). This effect is related to the presence of defects at the surface of the nanocrystals.[42,43] Regarding the less uniform morphology, we can find an explanation on the model of phase transition reported by Berry.[38] We hypothesize that the size polydispersity would be related to small differences in the

DOI: 10.1021/acs.jpclett.7b02473
J. Phys. Chem. Lett. 2017, 8, 5730−5735

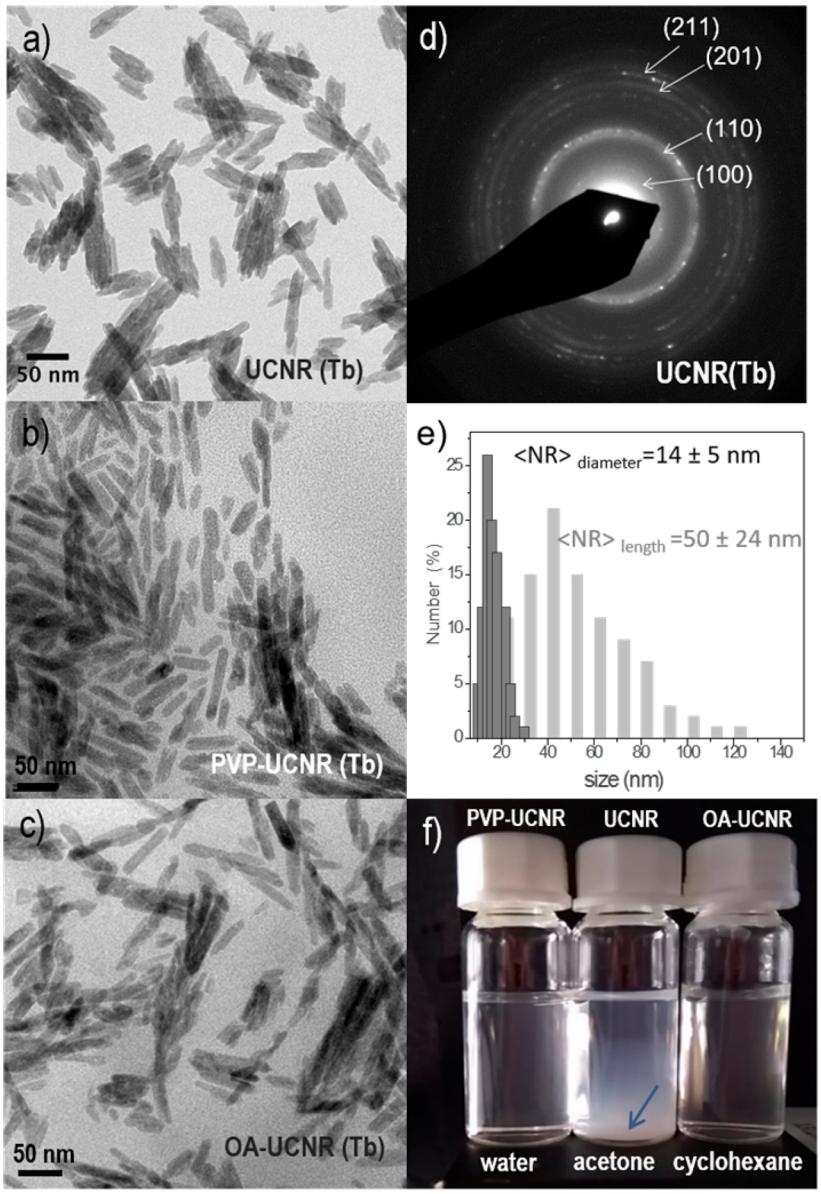

Figure 2. (a–c) TEM images of the bare, PVP-coated and OA-coated UCNRs, respectively. (d) SAED image from bare Tb-NRs. (e) Transversal and longitudinal size distribution of Tb-NRs. (f) Dispersion of the Tb-NRs in different solvents.

duration of the stage during which the α particle ripens, before β particles begin to appear. Therefore, it would be interesting to explore in the future if mild annealing conditions for a long time can be used to refine nanomaterials shape. Anyway, the described methodology provides pure hexagonal nanorods in extremely short time (15 min) with excellent up-conversion luminescence intensity.

After coating with PVP molecules (see Figure 2b), the small aggregates disappear and the nanorods are found isolated with an average inter-rods distance of ca. 8 nm, a distance compatible with a uniform PVP coating. In the case of OA-grafted NRs, the particles also appeared less aggregated than for the bare UCNR, but the inter-rod distance is not so evident (Figure 2c). Figure 2f depicts the nanoparticles stability in polar and nonpolar solvents. The as-obtained rods quickly sediment in all solvents (acetone is used here to illustrate this fact). In contrast, the rods coated with PVP are colloidally stable for months when dispersed in water; similarly, the particles coated with oleic acid remain well dispersed in cyclohexane.

Figure 3 shows that the hexagonal crystal phase and the rod-like morphology are maintained under the same reaction conditions independently of the emitting lanthanide ion employed (terbium, erbium, and thulium). This fact highlights the universal kinetic control of the crystal growth in this MW-assisted synthesis;, allowing us freedom of choice of multilined emissions. The Figure also evidences the lanthanide-doping-mediated crystal growth process reported by Wang,[44] where the dimensions of the NRs are little affected by the ionic radius and dipole polarizability of the substitutional dopant ion (increasing ionic radius or polarizability Tm < Er < Tb).

The MW-synthesized $NaYF_4$ nanorods exhibited excellent up-conversion emission. Figure 4 shows the photographs of the three-doped systems emitting visible light (mainly green and blue light at naked eye) upon 980 nm excitation. The UC emission spectra of PVP-coated nanorods are illustrated in Figure 4, left. The optical analysis was done in water suspensions for convenience because the emissions of the crystalline nanorods are hardly affected by the coating. The

DOI: 10.1021/acs.jpclett.7b02473
J. Phys. Chem. Lett. 2017, 8, 5730–5735

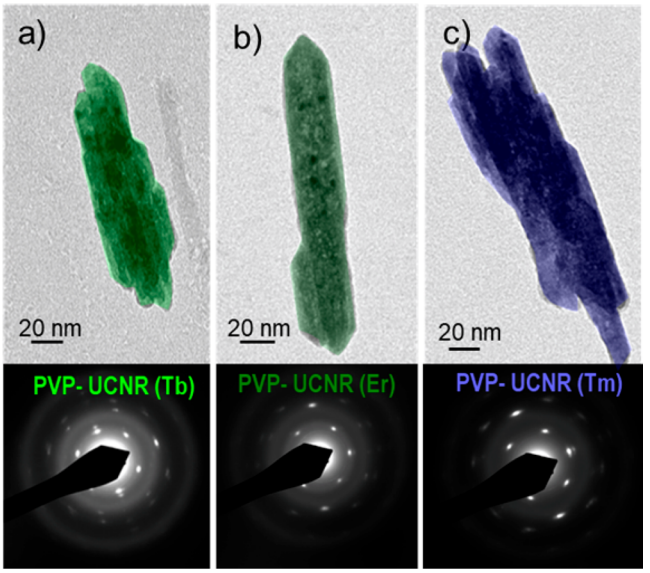

Figure 3. TEM images and SAED patterns of PVP-UCNRs doped with (a) Yb,Tb-, (b) Yb,Er-, and (c) Yb,Tm-$NaYF_4$ hexagonal nanorods.

spectra display the characteristic emission bands from the f–f electronic transitions of Tb^{3+}, Er^{3+}, and Tm^{3+} ions ascribed in the spectra upon NIR irradiation. These transitions correspond to the well-established UC mechanism for Er/Yb (two-photon absorption) and Tm/Yb (three-photon absorption) doping pairs,[45] in which the efficient upconversion is associated with their ladder-like arranged energy levels facilitating the successive photon absorption (Figure 4, right).

It is remarkable to see the intense manifold emissions from $^5D_4$,$^5D_3 \rightarrow {}^7F_J$ (J = 6, 5, 4, 3) transitions of Tb^{3+} generated by excitation of two Yb^{3+} ions and simultaneous energy transfer at the ground state $^7F_6$, which then populates the excited $^5D_4$ and $^5D_3$ levels.[34] To our knowledge, this is the first example of phonon-assisted cooperative sensitization in pure β-$NaYF_4$:Yb^{3+},Tb^{3+} to date.

The visible color emission is efficiently tuned by changing the activator ion (Tm, Tb, Er), spanning from blue to green shades, as represented in the color coordinates (Figure 4, right).

In summary, this work reports a ultrafast, cheap, and easily scalable microwave route to prepare pure hexagonal $NaYF_4$:Yb,Ln^{3+} nanorods of small size with strong upconversion luminescence. The process allows an easy coating with hydrophilic or hydrophobic molecules to render the rods dispersible in solvents of different nature. The crystal growth process is kinetically controlled by the short reaction time and permits the choice of multiple active ions (Er, Tm, Tb, etc.) without strongly affecting the nanorods crystallinity, morphology, or size. Thus tunable visible colors can be readily prepared by rational selection of the doping ions. Owing to their small size, excellent crystallinity, and good dispersibility, these nanorods could be used for a wide range of application.. Therefore, it is expected that this simple and ultrafast route to prepare the so-used $NaYF_4$ nanocrystals will be warmly

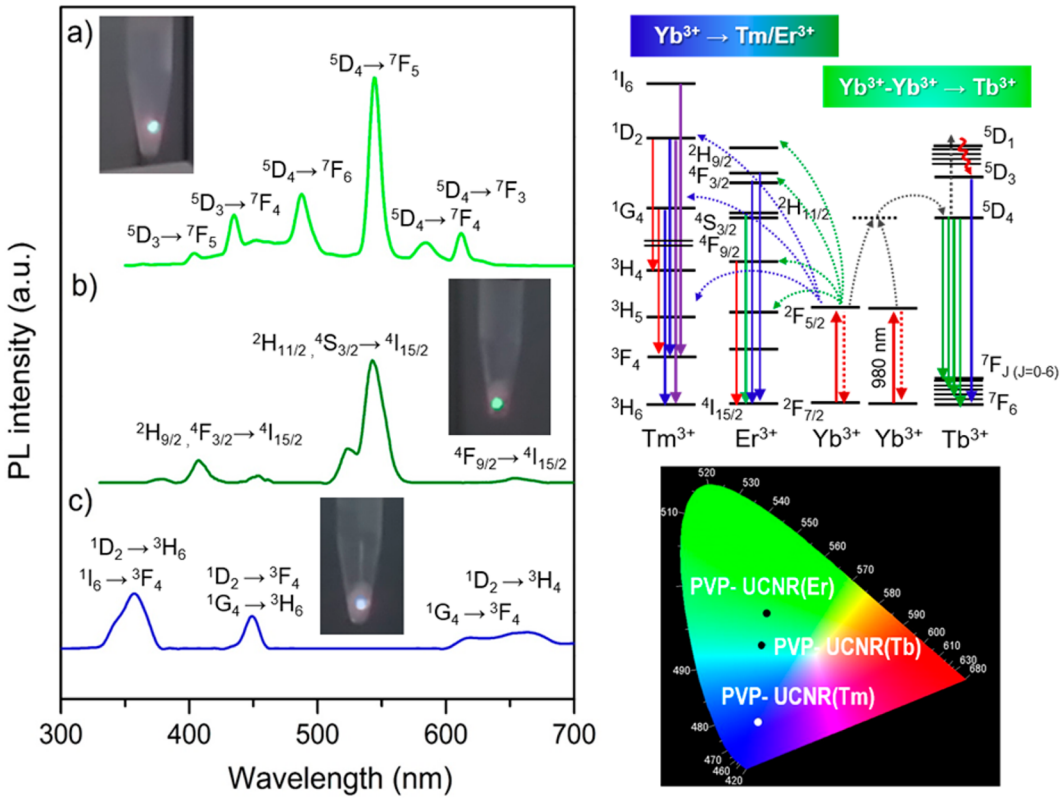

Figure 4. Left: Images of the emission in powdered samples and relative UC emission spectra for water suspensions of (a) PVP-UCNR(Tb), (b) PVP-UCNR(Er), and (c) PVP-UCNR(Tm) under 980 nm diode laser excitation. Right: Proposed energy-transfer mechanisms in the Yb:$NaYF_4$ nanorods codoped with Tm^{3+}, Er^{3+}, and Tb^{3+}. The full arrows represent photon excitation and emission processes, while dotted and dashed arrows represent energy transfer and multiphonon relaxation processes, respectively. Corresponding CIE chromaticity coordinates of the UCNRs.

DOI: 10.1021/acs.jpclett.7b02473
J. Phys. Chem. Lett. 2017, 8, 5730–5735

received by the big research community working on up-conversion nanomaterials.

■ ASSOCIATED CONTENT

Supporting Information

The Supporting Information is available free of charge on the ACS Publications website at DOI: 10.1021/acs.jpclett.7b02473.

Synthesis reactants, microwave-assisted synthetic route, surface coating, characterization techniques used, details of synthesis variations (including XRD results and TEM micrographs), as well as FTIR characterization of the UCNRs. (PDF)

■ AUTHOR INFORMATION

Corresponding Authors

*E-mail: julian@uji.es (B.J.-L.).
*E-mail: roig@icmab.es (A.R.).

ORCID

Fabrizio Guzzetta: 0000-0003-2253-8947
Anna Roig: 0000-0001-6464-7573
Beatriz Julián-López: 0000-0003-1019-776X

Notes

The authors declare no competing financial interest.

■ ACKNOWLEDGMENTS

This research was partially funded by the Spanish Ministry of Economy (MAT2015-64442-R, MAT2015-64139-C4-1-R, and SEV-2015-0496 projects, cofunded with European Social Funds) and Universitat Jaume I (P1B2014-21). F.G. thanks Generalitat Valenciana for his Grisolia Ph.D. Fellowship. We thank Olatz Arriga, nanoscience and nanotechnology student at the UAB, for her assistance in sample processing.

■ REFERENCES

(1) Nadort, A.; Zhao, J. B.; Goldys, E. M. Lanthanide upconversion luminescence at the nanoscale: fundamentals and optical properties. *Nanoscale* **2016**, *8*, 13099−13130.

(2) Zhou, J.; Liu, Q.; Feng, W.; Sun, Y.; Li, F. Upconversion luminescent materials: advances and applications. *Chem. Rev.* **2015**, *115*, 395−465.

(3) Zhou, B.; Shi, B.; Jin, D.; Liu, X. Controlling upconversion nanocrystals for emerging applications. *Nat. Nanotechnol.* **2015**, *10*, 924−936.

(4) Yi, G. S.; Chow, G. M. Synthesis of hexagonal-phase $NaYF_4$:Yb,Er and $NaYF_4$:Yb,Tm nanocrystals with efficient up-conversion fluorescence. *Adv. Funct. Mater.* **2006**, *16*, 2324−2329.

(5) Boyer, J. C.; Vetrone, F.; Cuccia, L. A.; Capobianco, J. A. Synthesis of colloidal upconverting $NaYF_4$ nanocrystals doped with Er^{3+}, Yb^{3+} and Tm^{3+}, Yb^{3+} via thermal decomposition of lanthanide trifluoroacetate precursors. *J. Am. Chem. Soc.* **2006**, *128*, 7444−7445.

(6) Li, D. D.; Shao, Q. Y.; Dong, Y.; Jiang, J. Q. A facile synthesis of small-sized and monodisperse hexagonal $NaYF_4$:Yb^{3+}, Er^{3+} nanocrystals. *Chem. Commun. (Cambridge, U. K.)* **2014**, *50*, 15316−15318.

(7) Yu, S.; Gao, X.; Jing, H.; Zhao, J.; Su, H. A synthesis and up-conversional photoluminescence study of hexagonal phase $NaYF_4$:Yb,Er nanoparticles. *CrystEngComm* **2013**, *15*, 10100.

(8) Heer, S.; Kompe, K.; Gudel, H. U.; Haase, M. Highly efficient multicolour upconversion emission in transparent colloids of lanthanide-doped $NaYF_4$ nanocrystals. *Adv. Mater.* **2004**, *16*, 2102−2105.

(9) Carling, C. J.; Boyer, J. C.; Branda, N. R. Remote-control photoswitching using NIR light. *J. Am. Chem. Soc.* **2009**, *131*, 10838−10839.

(10) Wang, L. Y.; Li, Y. D. $Na(Y_{1.5}Na_{0.5})F_6$ single-crystal nanorods as multicolor luminescent materials. *Nano Lett.* **2006**, *6*, 1645−1649.

(11) Wang, Y. H.; Cai, R. X.; Liu, Z. H. Controlled synthesis of $NaYF_4$: Yb, Er nanocrystals with upconversion fluorescence via a facile hydrothermal procedure in aqueous solution. *CrystEngComm* **2011**, *13*, 1772−1774.

(12) Mai, H. X.; Zhang, Y. W.; Si, R.; Yan, Z. G.; Sun, L. D.; You, L. P.; Yan, C. H. High-quality sodium rare-earth fluoride nanocrystals: Controlled synthesis and optical properties. *J. Am. Chem. Soc.* **2006**, *128*, 6426−6436.

(13) Baghbanzadeh, M.; Carbone, L.; Cozzoli, P. D.; Kappe, C. O. Microwave-assisted synthesis of colloidal inorganic nanocrystals. *Angew. Chem., Int. Ed.* **2011**, *50*, 11312−11359.

(14) Yu, S. M.; Hachtel, J. A.; Chisholm, M. F.; Pantelides, S. T.; Laromaine, A.; Roig, A. Magnetic gold nanotriangles by microwave-assisted polyol synthesis. *Nanoscale* **2015**, *7*, 14039−14046.

(15) Goetz, J.; Nonat, A.; Diallo, A.; Sy, M.; Sera, I.; Lecointre, A.; Lefevre, C.; Chan, C. F.; Wong, K. L.; Charbonniere, L. J. Ultrabright lanthanide nanoparticles. *ChemPlusChem* **2016**, *81*, 526−534.

(16) Li, F. F.; Li, C. G.; Liu, X. M.; Chen, Y.; Bai, T. Y.; Wang, L.; Shi, Z.; Feng, S. H. Hydrophilic, upconverting, multicolor, lanthanide-doped $NaGdF_4$ nanocrystals as potential multifunctional bioprobes. *Chem. - Eur. J.* **2012**, *18*, 11641−11646.

(17) Niu, N.; He, F.; Gai, S.; Li, C.; Zhang, X.; Huang, S.; Yang, P. Rapid microwave reflux process for the synthesis of pure hexagonal $NaYF_4$:Yb^{3+},Ln^{3+},Bi^{3+} (Ln^{3+} = Er^{3+}, Tm^{3+}, Ho^{3+}) and its enhanced UC luminescence. *J. Mater. Chem.* **2012**, *22*, 21613−21623.

(18) Wang, H. Q.; Nann, T. Monodisperse upconverting nanocrystals by microwave-assisted synthesis. *ACS Nano* **2009**, *3*, 3804−3808.

(19) Li, F.; Li, C.; Liu, J.; Liu, X.; Zhao, L.; Bai, T.; Yuan, Q.; Kong, X.; Han, Y.; Shi, Z.; Feng, S. Aqueous phase synthesis of upconversion nanocrystals through layer-by-layer epitaxial growth for in vivo X-ray computed tomography. *Nanoscale* **2013**, *5*, 6950−6959.

(20) Ullah, S.; Hazra, C.; Ferreira-Neto, E. P.; Silva, T. C.; Rodrigues-Filho, U. P.; Ribeiro, S. J. L. Microwave-assisted synthesis of $NaYF_4$:Yb^{3+}/Tm^{3+} upconversion particles with tailored morphology and phase for the design of UV/NIR-active $NaYF_4$:Yb^{3+}/Tm^{3+}@TiO_2 core@shell photocatalysts. *CrystEngComm* **2017**, *19*, 3465−3475.

(21) Mi, C.; Tian, Z.; Cao, C.; Wang, Z.; Mao, C.; Xu, S. Novel microwave-assisted solvothermal synthesis of $NaYF_4$:Yb,Er upconversion nanoparticles and their application in cancer cell imaging. *Langmuir* **2011**, *27*, 14632−14637.

(22) Som, S.; Das, S.; Yang, C. Y.; Lu, C. H. Enhanced upconversion of $NaYF_4$:Er^{3+}/Yb^{3+} phosphors prepared via the rapid microwave-assisted hydrothermal route at low temperature: phase and morphology control. *Opt. Lett.* **2016**, *41*, 464−467.

(23) Wawrzynczyk, D.; Piatkowski, D.; Mackowski, S.; Samoc, M.; Nyk, M. Microwave-assisted synthesis and single particle spectroscopy of infrared down-and visible up-conversion in Er^{3+} and Yb^{3+} co-doped fluoride nanowires. *J. Mater. Chem. C* **2015**, *3*, 5332−5338.

(24) Pascu, O.; Carenza, E.; Gich, M.; Estrade, S.; Peiro, F.; Herranz, G.; Roig, A. Surface reactivity of iron oxide nanoparticles by microwave-assisted synthesis; Comparison with the thermal decomposition route. *J. Phys. Chem. C* **2012**, *116*, 15108−15116.

(25) Su, Q. Q.; Feng, W.; Yang, D. P.; Li, F. Y. Resonance energy transfer in upconversion nanoplatforms for selective biodetection. *Acc. Chem. Res.* **2017**, *50*, 32−40.

(26) Chen, X.; Xu, W.; Zhang, L. H.; Bai, X.; Cui, S. B.; Zhou, D. L.; Yin, Z.; Song, H. W.; Kim, D. H. Large upconversion enhancement in the "islands" Au-Ag Alloy/$NaYF_4$: Yb^{3+}, Tm^{3+}/Er^{3+} composite films, and fingerprint identification. *Adv. Funct. Mater.* **2015**, *25*, 5462−5471.

(27) Fischer, S.; Frohlich, B.; Steinkemper, H.; Kramer, K. W.; Goldschmidt, J. C. Absolute upconversion quantum yield of beta-$NaYF_4$ doped with Er^{3+} and external quantum efficiency of upconverter solar cell devices under broad-band excitation considering spectral mismatch corrections. *Sol. Energy Mater. Sol. Cells* **2014**, *122*, 197−207.

DOI: 10.1021/acs.jpclett.7b02473
J. Phys. Chem. Lett. 2017, 8, 5730−5735

(28) Wang, F.; Deng, R. R.; Wang, J.; Wang, Q. X.; Han, Y.; Zhu, H. M.; Chen, X. Y.; Liu, X. G. Tuning upconversion through energy migration in core-shell nanoparticles. *Nat. Mater.* **2011**, *10*, 968−973.
(29) Salley, G. M.; Valiente, R.; Guedel, H. U. Luminescence upconversion mechanisms in Yb^{3+}-Tb^{3+} systems. *J. Lumin.* **2001**, *94*, 305−309.
(30) Chen, D.; Yu, Y.; Huang, P.; Weng, F.; Lin, H.; Wang, Y. Optical spectroscopy of Eu^{3+} and Tb^{3+} doped glass ceramics containing $LiYbF_4$ nanocrystals. *Appl. Phys. Lett.* **2009**, *94*, 041909.
(31) Wei, Y.; Liu, X.; Chi, X.; Wei, R.; Guo, H. Intense upconversion in novel transparent $NaLuF_4$:Tb^{3+}, Yb^{3+} glass−ceramics. *J. Alloys Compd.* **2013**, *578*, 385−388.
(32) Gao, Y.; Hu, Y.; Ren, P.; Zhou, D.; Qiu, J. Phase transformation and enhancement of luminescence in the Tb^{3+}-Yb^{3+} co-doped oxyfluoride glass ceramics containing $NaYF_4$ nanocrystals. *J. Eur. Ceram. Soc.* **2016**, *36*, 2825−2830.
(33) Dong, H.; Sun, L. D.; Wang, Y. F.; Xiao, J. W.; Tu, D. T.; Chen, X. Y.; Yan, C. H. Photon upconversion in Yb^{3+}-Tb^{3+} and Yb^{3+}-Eu^{3+} activated core/shell nanoparticles with dual-band excitation. *J. Mater. Chem. C* **2016**, *4*, 4186−4192.
(34) Liang, H.; Chen, G.; Li, L.; Liu, Y.; Qin, F.; Zhang, Z. Upconversion luminescence in Yb^{3+}/Tb^{3+}-codoped monodisperse $NaYF_4$ nanocrystals. *Opt. Commun.* **2009**, *282*, 3028−3031.
(35) Bilecka, I.; Djerdj, I.; Niederberger, M. One-minute synthesis of crystalline binary and ternary metal oxide nanoparticles. *Chem. Commun. (Cambridge, U. K.)* **2008**, 886−888.
(36) Ludi, B.; Olliges-Stadler, I.; Rossell, M. D.; Niederberger, M. Extension of the benzyl alcohol route to metal sulfides: "non-hydrolytic' thio sol-gel synthesis of ZnS and SnS_2. *Chem. Commun. (Cambridge, U. K.)* **2011**, *47*, 5280−5282.
(37) Wang, M.; Liu, J.-L.; Zhang, Y.-X.; Hou, W.; Wu, X.-L.; Xu, S.-K. Two-phase solvothermal synthesis of rare-earth doped $NaYF_4$ upconversion fluorescent nanocrystals. *Mater. Lett.* **2009**, *63*, 325−327.
(38) May, P. B.; Suter, J. D.; May, P. S.; Berry, M. T. The dynamics of nanoparticle growth and phase change during synthesis of β-$NaYF_4$. *J. Phys. Chem. C* **2016**, *120*, 9482−9489.
(39) Wang, M.; Dykstra, T. E.; Lou, X.; Salvador, M. R.; Scholes, G. D.; Winnik, M. A. Colloidal CdSe nanocrystals passivated by a dye-labeled multidentate polymer: Quantitative analysis by size-exclusion chromatography. *Angew. Chem., Int. Ed.* **2006**, *45*, 2221−2224.
(40) Wang, M.; Oh, J. K.; Dykstra, T. E.; Lou, X.; Scholes, G. D.; Winnik, M. A. Surface modification of CdSe and CdSe/ZnS semiconductor nanocrystals with Poly(N,N-dimethylaminoethyl methacrylate). *Macromolecules* **2006**, *39*, 3664−3672.
(41) Wang, M.; Felorzabihi, N.; Guerin, G.; Haley, J. C.; Scholes, G. D.; Winnik, M. A. Water-soluble CdSe quantum dots passivated by a multidentate diblock copolymer. *Macromolecules* **2007**, *40*, 6377−6384.
(42) Gargas, D. J.; Chan, E. M.; Ostrowski, A. D.; Aloni, S.; Altoe, M. V. P.; Barnard, E. S.; Sanii, B.; Urban, J. J.; Milliron, D. J.; Cohen, B. E.; Schuck, P. J. Engineering bright sub-10-nm upconverting nanocrystals for single-molecule imaging. *Nat. Nanotechnol.* **2014**, *9*, 300−305.
(43) Xue, X.; Uechi, S.; Tiwari, R. N.; Duan, Z.; Liao, M.; Yoshimura, M.; Suzuki, T.; Ohishi, Y. Size-dependent upconversion luminescence and quenching mechanism of $LiYF_4$: Er^{3+}/Yb^{3+} nanocrystals with oleate ligand adsorbed. *Opt. Mater. Express* **2013**, *3*, 989−999.
(44) Wang, F.; Han, Y.; Lim, C. S.; Lu, Y. H.; Wang, J.; Xu, J.; Chen, H. Y.; Zhang, C.; Hong, M. H.; Liu, X. G. Simultaneous phase and size control of upconversion nanocrystals through lanthanide doping. *Nature* **2010**, *463*, 1061−1065.
(45) Haase, M.; Schafer, H. Upconverting Nanoparticles. *Angew. Chem., Int. Ed.* **2011**, *50*, 5808−5829.

DOI: 10.1021/acs.jpclett.7b02473
J. Phys. Chem. Lett. 2017, 8, 5730−5735